Toward an Understanding of the Indirect Climatic Effect of Aerosols

Thesis by

Athanasios Nenes

In Partial Fulfillment of the Requirements

for the Degree of

Doctor of Philosophy

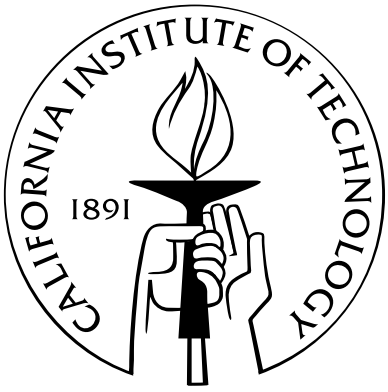

California Institute of Technology

Pasadena, California

2003

(Defended August 26, 2002)

All men by nature desire to know.

Aristotle (Metaphysics).

To my parents, Luz, and the memory of my grandfather.

Acknowledgements

I never thought that the years spent at Caltech would have such a profound effect on me. It is not only because of the quality and level of science that takes place here; that is well known. It is also the extraordinary people that I've gotten to know and become friends with, that have made these years special.

First, I would like to thank John Seinfeld for being a wonderful advisor. He gave me the opportunity to work in an exciting field, he let me choose my own research path, he has been very understanding and supportive during times of personal need, and always has been there to provide guidance and professional support. I couldn't ask for a better mentor and truly thank him for helping me realize a dream. I would also like to thank Rick Flagan for his help over the years, for all the interesting and challenging conversations, and for constantly reminding me what love for science is all about.

I would like to thank my friend and colleague Timothy Vanreken for all the fun we had throughout the difficult years of grad school, for not hating me too much when projects changed direction, and simply for being there when needed the most. Likewise, I would also like to thank Peter Adams for his friendship and help during all these years. Both of you guys have been like a "family away from home". I hope that will never change. I would also like to thank Serena Chung, for being such a great officemate, musical partner and friend. I would like to thank all of the other members of the Seinfeld group, and in particular, Patrick Chuang (who also showed me some excellent restaurants), Don Collins, Rob Griffin, Bill Conant, Julia Lu, Tracey Rissman, David Katoshevski, and Greg Roberts. I will always remember their friendship and have enjoyed working with them all.

There are also a few people outside of Caltech that I would like to thank. Spyros Pandis

has always generously offered help and advice whenever seeked for, and Bob Charlson, for our many long and interesting discussions.

Many people made sure my life here wasn't just science. Delores Bing and Allen Gross provided many opportunities to play music in the Caltech music program and the Occidental College Orchestra. I was fortunate to play with very talented musicians, particularly Alex Dunn and Todd Murphey. I thank them both for the many moments of beautiful music. I would also like to thank the St. Anthony's Greek Orthodox Church for entrusting me the role of organist during the past three years. Getting up at 8AM (give or take a few minutes) every Sunday morning wasn't always easy; nevertheless, it was well worth it. Getting to know the choir director, Dr. Dimitrios Antsos, was another stroke of luck. His friendship (and vast knowledge of music) is truly a treasure.

Of course, I cannot neglect to thank the "Latino crowd" for all the legendary parties, asados, dinners, Semana Latina's....

From thousands of kilometers away, I am grateful to my parents Theodosi and Maria, and my brothers Anastasio and Dimitri, for constantly providing love and support for as long as I can remember.

And finally, I would like to thank Luz. Her love, support and companionship has been a constant source of hope and inspiration.

Abstract

This thesis is motivated by the need to improve our understanding of the aerosol indirect effect. The activation of aerosol into cloud droplets has been extensively studied, using a comprehensive numerical cloud droplet activation model. Using this model, the effect of water vapor mass transfer limitations on the cloud droplet activation process was first studied; it was found that mass transfer limitations are important for activation under polluted conditions. The potential effect of (currently unresolved) "chemical effects" on cloud droplet number (e.g., the presence soluble gases and surface active species) was also assessed. It was seen that small changes in aerosol and gas-phase composition can have a strong effect on cloud droplet number, and should be included in future estimates of the aerosol indirect effect.

A comprehensive aerosol activation parameterization was developed for use in a first-principle assessment of the aerosol indirect effect. This new parameterization introduces the concept of "population splitting," in which the droplets are separated into two populations, each with its own growth characteristics. The effect of water vapor mass transfer limitations is explicitly introduced. The parameterization allows for treatment of chemical effects. The new parameterization shows excellent and robust agreement with a detailed numerical parcel model.

Previously unidentified mechanisms of aerosol-cloud interactions were also explored. Aerosol, when it contains black carbon, can absorb light and heat the droplet enough to affect its activation behavior. This can affect cloud properties in numerous and counterintuitive ways; black carbon heating can dissipate clouds, but may also increase cloud lifetime (and lead to a climatic cooling) by decreasing the probability of drizzle formation.

Finally, the performance of instruments used for measuring the concentration of cloud condensation nuclei (CCN) was assessed. Each design exhibits different limitations and sources of uncertainty, but all show decreased ability to measure CCN of low critical su-

persaturation ($< 0.1\%$). The performance of the instrumentation can be very sensitive to the operating conditions. Therefore, an in-depth theoretical understanding of the instrumentation is necessary; otherwise, CCN measurements may be subject to considerable uncertainty.

Contents

List of Figures

List of Tables

Chapter 1

Preface

1.1 Introduction

It is well established that suspended particulate matter, or aerosols, can have an important effect on the planetary radiative balance (Figure 1.1) and thus affect climate. These climatic effects are roughly classified into two categories. First is the "direct effect", which refers to the direct interaction of the aerosol particles with radiation (through scattering and absorption). Second is the so-called indirect effect, which is the change in cloud properties that result from changes in the aerosol, which serve as cloud condensation nuclei (CCN).

It is currently believed that the indirect effect tends to cool the planet through two mechanisms that act primarily upon liquid water boundary layer clouds. The "first" (or "Twomey," [156]) indirect effect is an increase in cloud droplet concentration that is a result of increased cloud condensation nuclei concentrations from anthropogenic emissions. The resulting clouds are believed to be more reflective, thus cool the planet. The "second" (or "Albrect," [10]) effect results from the increased lifetime (because the droplets that form tend to be smaller in size and thus decrease the probability of precipitation); this effect would increase the fractional planetary coverage, and also lead to a cooling effect. These are not the only aerosol-cloud interactions that can affect climate, nor do all such mechanisms cool the planet. For example, the so-called semi-direct effect, in which heating released by the short-wave absorbing aerosol (primarily black carbon) tends to impede cloud formation [61]; this leads to decreases in global cloud coverage, and planetary warming.

Evidence of the indirect effect can be found in many aspects of the climate system. Some of them are

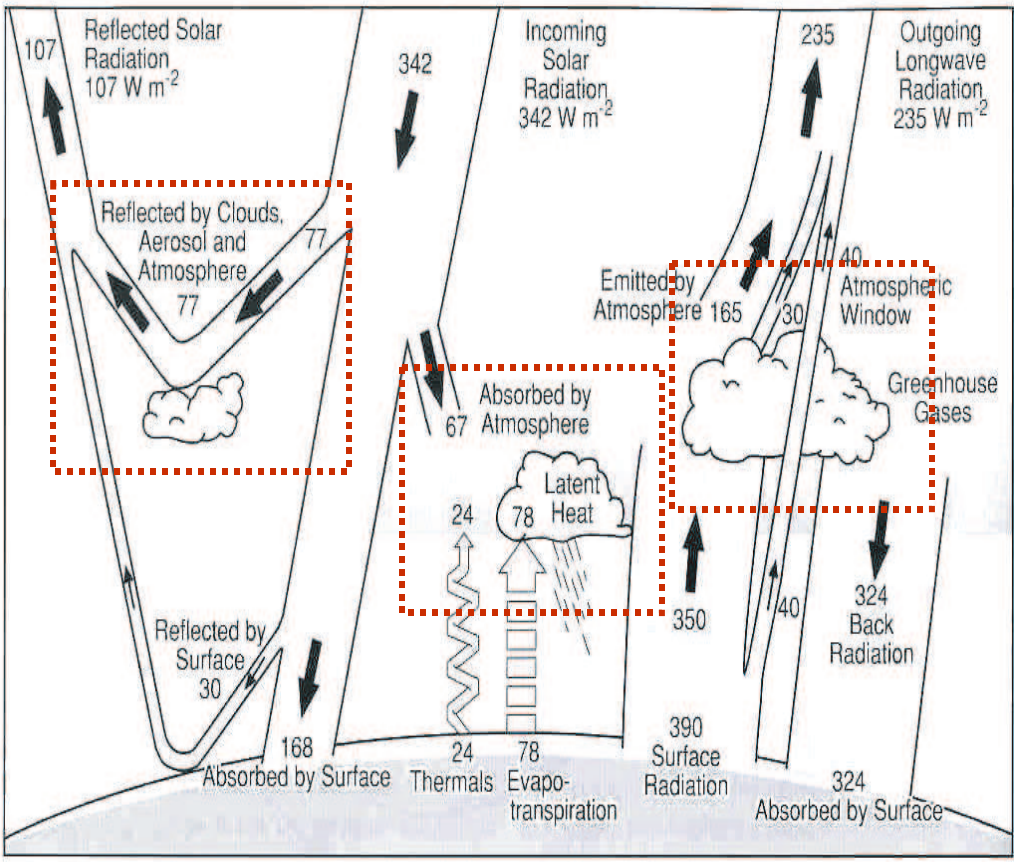

J.T. Houghton: "The science of climate change"

Figure 1.1: Radiative budget of Earth's climate. Red boxes indicate regions where clouds are influential [76].

Figure 1.2: Satellite picture at 3.5 μm wavelength of ship tracks off the West Coast of the United States [143].

- CCN concentrations are greater in continental air masses (exceeding 1000 cm^{-3}) than in the marine atmosphere (which rarely exceed 100 cm^{-3}). At the same time, continental clouds tend to exhibit greater cloud droplet number concentrations than marine clouds do. [127].

- Cloud droplet number concentrations tend to increase with increasing aerosol loading. This has been confirmed from modelling studies (e.g., [57, 117]) and from observations [128, 23].

- The existence of "ship tracks," linear features of high cloud reflectivity embedded within marine stratus clouds, are caused by aerosols emitted from ship exhausts (Figure 1.2).

1.2 Current estimates of indirect forcing

Figure 1.3 displays a quantitative comparison of each climatic forcing (including those from greenhouse gases and aerosol), [76]. Each climatic forcing is expressed as the global annual average change in the radiative balance at the top of the atmosphere. Estimates

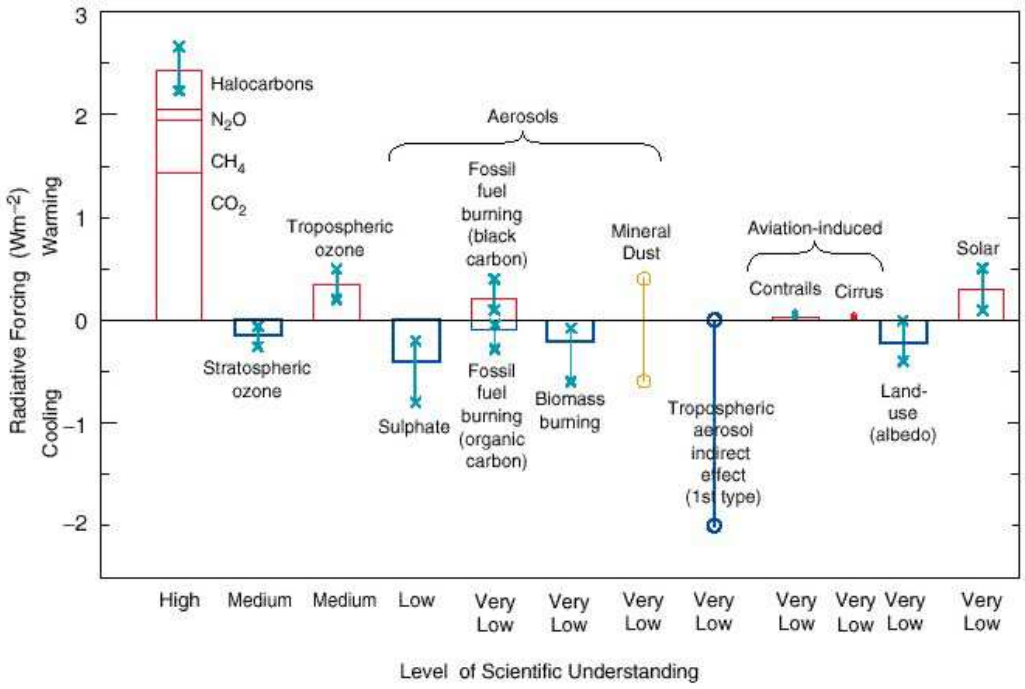

Figure 1.3: Global, annual-mean radiative forcings (Wm^{-2}) due to a number of agents for the period from pre-industrial (1750) to present (late 1990s). Bar heights indicate best estimate value; lack of a bar indicates no estimate is available. The vertical line about the rectangular bar with "X" delimiters indicates an estimate of the uncertainty range, for the most part guided by the spread in the published values of the forcing. A vertical line without a rectangular bar and with "O" delimiters denotes a forcing for which no central estimate can be given owing to large uncertainties. A "level of scientific understanding" index is accorded to each forcing, with high, medium, low and very low levels, respectively. (*Adopted from http://www.cmdl.noaa.gov/info/ipcc.html*)

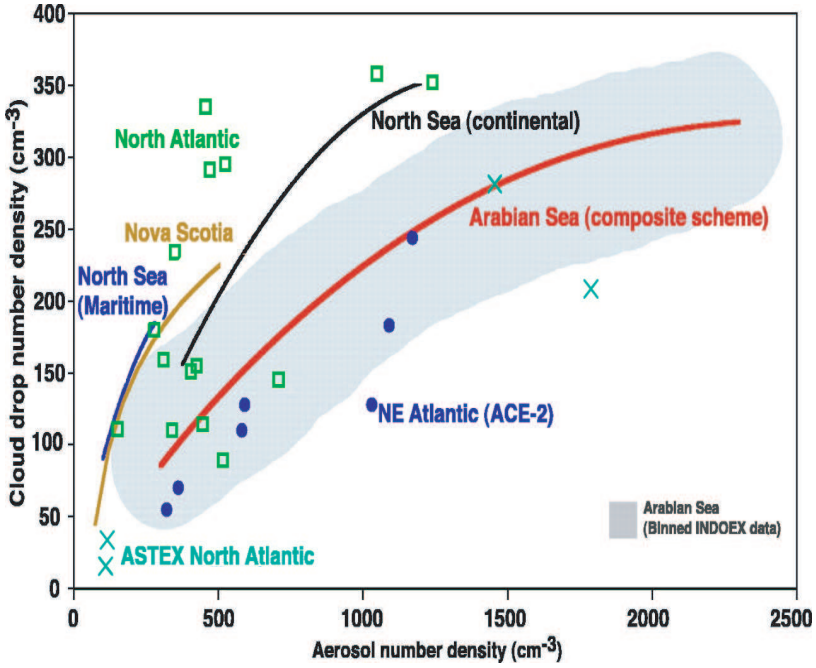

Figure 1.4: Empirical relationship between cloud droplet number and sulfate mass (adopted from [131]).

imply that the tropospheric aerosol might have a net global cooling effect of the order of the combined warming effect caused by greenhouse gases, which is estimated to be $+2.5(\pm 10\%)$ W m^{-2}. To date, the best estimate of the direct climatic forcing of sulfate aerosols lies in the range between -0.4 W m^{-2}, to within a factor of 2. The indirect forcing effect is believed to be negative in sign, but the present state of knowledge precludes even an estimate of the magnitude. The value indicated on the plot refers to the first indirect effect, while estimates of the second indirect effect are too uncertain even to be assigned a value by the IPCC [76].

To fully understand the indirect climate effect of aerosols, it is necessary to be able to relate changes in atmospheric aerosol properties to changes in cloud radiative properties. Key aerosol properties include particle size, number and composition; key cloud properties are droplet size, number, and cloud liquid water content. Most of the global aerosol models found in the literature explicitly resolve only aerosol mass from first principles, and cannot provide information for an explicit treatment of aerosol-cloud interactions. Because of this, empirical relations (such as that shown in Figure 1.4) have been used to relate aerosol number (or mass) with and droplet concentration. The first comprehensive study using correlations was done by [15]; predictions of global sulfate from two models were used to

predict cloud droplet number concentrations. The empirical approach, although a quick way to provide a rough estimate of the magnitude of the indirect effect and uncertainties [101, 83]; it is far from providing an estimate with high enough level of confidence. The empirical relationship itself is subject to high uncertainty, at least an order of magnitude; this is a result of the highly complex numerous processes of aerosol-cloud interactions which cannot be resolved through a simple correlation with one aerosol property. This is shown by the [83] study, where several different empirical relationships yielded estimates of the global annual average indirect forcing between -0.40 W m^{-2} and -1.78 W m^{-2}. Furthermore, the chemical composition and concentration of the aerosol, together with the underlying cloud dynamics, vary strongly with time and location, so that simulations using first principles seems to be the only viable route towards more confident estimates of the indirect effect.

Physically based approaches to address the aerosol indirect effect have also started to appear. For example, [21, 22] parameterized the sulfate production to preexisting particles by condensation of gas-phase sulfuric acid and aqueous oxidation of sulfur dioxide, and used that for their indirect forcing estimates. [101] and [58] have developed prognostic schemes of global cloud droplet number and used those to assess sulfate indirect effects. [53, 54] further introduced a modal aerosol microphysical algorithm to predict CCN concentrations and assess indirect effects. [140] introduced a physically based methodology for assessing the first and second indirect effects. All of these studies provide important contributions, but clearly a substantial amount of work needs to be done, before the confidence level in these global simulations is improved.

1.3 The challenges of indirect forcing

Understanding the indirect climate effect of aerosols requires establishing a link between changes in atmospheric aerosol properties to changes in cloud radiative properties. This is indeed a monumental task. Some of the major issues that involve aerosol-cloud interactions and their incorporation into GCMs are

- **The aerosol mass - aerosol number relationship.** Most GCMs handle aerosol on a mass basis, which is sufficient for direct forcing calculations, but cannot be used for indirect forcing. Aerosol number, size, and composition are the parameters that characterize the activation properties. The most comprehensive representation is a

size-resolved aerosol global simulation using a sectional approach. Such algorithms have started to appear (e.g., [159, 8]). The former study utilizes an algorithm that conserves mass, but not number; only [8] uses an algorithm that accurately and efficiently conserves aerosol number and mass concentrations, a prerequisite for reliable indirect forcing calculations. Further developments to include size resolved simulations of sea salt, mineral dust and carbonaceous aerosol would provide the information needed for an in-depth analysis of the contribution of each species to the indirect effect.

- **The treatment of cloud formation in global models.** This is probably the largest source of uncertainty surrounding indirect forcing of aerosols. Explicitly resolving cloud formation in global models is a task that far exceeds anything computationally feasible, as it covers a wide range of length scales: from hundreds of kilometers (which are relevant for large scale systems) down to meters (which are relevant for individual updrafts). The size of a typical global model grid cell is on the order of a hundred kilometers, and can only resolve the largest of cloud systems. Cloud-resolving large eddy simulations (LES) can possibly address these small length scales, but global models are far from being able to achieve this. As a consequence, global models heavily rely on parameterizations to account for all such sub-grid processes, such as cloud formation and aerosol-cloud interactions. Current parameterizations are very simplistic, and unable to capture the complexities of aerosol-cloud interactions. This is a particularly important issue in the aerosol indirect effect, as all its mechanisms act on subgrid scales.

- **The link between aerosol and cloud droplet formation.** This relationship has to consider a multitude of parameters that can affect the formation of cloud droplets, such as varying aerosol composition, and the behavior of complex (and poorly understood) carbonaceous aerosol. Furthermore, the treatment should allow for generalized representations of aerosol size and composition, and not rely on prescribed size distributions (e.g., lognormal). Essential is the ability to account for externally mixed aerosol; CCN that result from mixing of heterogeneous aerosol populations occurs frequently, and affects clouds that are most susceptible to changes in aerosol.

The challenges, however, are not limited to the theory and modelling of aerosol-cloud-climate interactions. There are many issues in the performance of the instrumentation used

to provide model input and also used for assessment of model performance. For example, the measurement of CCN concentrations is in itself a challenge; a theoretical understanding of the different measurement methodologies, in both their strengths and limitations, is essential for evaluating instrumental uncertainties.

1.4 Organization of Thesis

The motivation of this thesis is to improve our understanding of the complex and numerous mechanisms of aerosol-cloud-climate interactions, and the instrumentation used in CCN measurements. In Chapter 2, we study the dynamics of aerosol activation into cloud droplets, and study under which conditions mass transfer limitations on the growth of cloud condensation nuclei (CCN) may have a significant impact on the number of droplets that can form in a cloud. In Chapters 3 and 4, the sensitivity of cloud droplet number concentration to CCN chemical effects (such as dissolution of soluble gases and slightly soluble substances, surface tension depression by organic substances and accommodation coefficient changes) is assessed by using a cloud parcel model. Chapter 5 assesses the impact of biomass-burning aerosol on cloud properties in the Amazon Basin and identifies the physical and chemical properties of the aerosol that influence droplet growth. Chapters 6 and 7 study previously unidentified cloud microphysical effects of black carbon inclusions in cloud droplets. Chapter 8 develops a novel parameterization of cloud droplet activation intended for use in a global model. Chapter 9 theoretically analyzes the behavior and performance of four cloud condensation nucleus (CCN) instruments. Finally, Chapter 10 presents a summary and conclusions for the whole thesis.

Chapter 2

Kinetic limitations on cloud droplet formation and impact on cloud albedo

Note: This chapter appeared as reference [117].

2.1 Abstract

Under certain conditions mass transfer limitations on the growth of cloud condensation nuclei (CCN) may have a significant impact on the number of droplets that can form in a cloud. The assumption that particles remain in equilibrium until activated may therefore not always be appropriate for aerosol populations existing in the atmosphere. This work identifies three mechanisms that lead to kinetic limitations, the effect of which on activated cloud droplet number and cloud albedo is assessed using a one-dimensional cloud parcel model with detailed microphysics for a variety of aerosol size distributions and updraft velocities. In assessing the effect of kinetic limitations, we have assumed as cloud droplets not only those that are strictly activated (as dictated by classical Köhler theory), but also unactivated drops large enough to have an impact on cloud optical properties. Aerosol number concentration is found to be the key parameter that controls the significance of kinetic effects. Simulations indicate that the equilibrium assumption leads to an overprediction of droplet number by less than 10% for marine aerosol; this overprediction can exceed 40% for urban type aerosol. Overall, the effect of kinetic limitations on cloud albedo can be considered important when equilibrium activation theory consistently overpredicts droplet number by more than 10%. The maximum change in cloud albedo as a result of kinetic

limitations is less than 0.005 for cases such as marine aerosol; however albedo differences can exceed 0.1 under more polluted conditions. Kinetic limitations are thus not expected to be climatically significant on a global scale, but can regionally have a large impact on cloud albedo.

2.2 Introduction

Much of the uncertainty associated with quantifying the indirect climatic effect of aerosols originates in the complex relationship between aerosols and cloud droplets. Approximate analytical expressions that predict those aerosol particles that activate to form cloud droplets have been proposed for implementation in general circulation models (GCMs) [56, 99, 3]. These parameterizations generally rely on the assumption that particles are at equilibrium with the ambient (supersaturated) water vapor concentration until activated as cloud condensation nuclei (CCN). The number of droplets formed in a cloud can therefore be estimated from the number of CCN active at the maximum supersaturation in the cloud updraft. The problem of droplet nucleation parameterization is then reduced to the problem of determining the maximum supersaturation in the cloud parcel.

The assumption that all particles respond instantaneously to any changes in supersaturation leads to a problem: the amount of water absorbed by the largest aerosol particles when they activate can be larger than the amount of water vapor available in the cloud parcel. This problem, known for a long time, is not serious when predicting the number of droplets, because although not activated, these particles have an equilibrium saturation ratio very close to unity, as activated particles do. As a consequence, their growth can be parameterized as if they were activated. In addition, the number of large particles that give rise to this problem are usually negligible compared to the concentration of smaller particles of the distribution, so the errors in cloud droplet number overall are expected to be small.

The assumption of equilibrium, however, can lead to a discrepancy in droplet number as a result of mass transfer limitations. [22] have shown that under certain circumstances growth kinetics may retard the growth of CCN sufficiently to limit the number of activated droplets formed. By comparing the timescale for particle growth at equilibrium with that for actual condensational growth, [22] conclude that particles with critical supersaturation less than a threshold value do not have time to grow larger than their critical size, and thus

do not activate. This suggests that equilibrium models that diagnose droplet formation from maximum supersaturation may systematically overestimate the number of activated droplets formed. Such a systematic bias could have implications for estimates of indirect aerosol radiative forcing of climate. It is difficult, however, to draw firm conclusions simply from a comparison of timescales because growth kinetics depend on the full time history of supersaturation and particle growth. Furthermore, the timescales controlling the growth of the droplets change drastically as the populations grow. A more conclusive method of evaluating the importance of growth kinetics is obtained by explicitly simulating the kinetic growth process and then comparing the simulated number of droplets formed with that predicted by equilibrium theory for the same CCN concentration and maximum supersaturation.

Furthermore, it is incorrect to consider cloud drops as only those that are strictly activated (as defined by Köhler theory); the presence of large unactivated droplets cannot be neglected. This issue becomes even more important when slightly soluble substances are present in the aerosol [93]. The condensational growth of an aerosol population prescribes that particles with very large dry diameters, although not activated, lead to roughly the same size of activated droplets and thus belong to the cloud droplet population. With this in mind, one can define as CCN all particles that produce droplets that are larger than the smallest particle that is strictly activated. This cloud droplet definition differs slightly from that given by [123]; we do not consider as droplets all the particles that exceed their critical diameter or have a critical supersaturation lower than ambient supersaturation, but only those comparable in size to those that are strictly activated.

Based on the previous discussion, the inertial mechanism of [22] is believed not to contribute to any bias in the predicted droplet number when the equilibrium assumption is invoked. However, there are other kinetic limitation mechanisms that produce particles that are much smaller than activated drops; in this sense, these mechanisms act to decrease the number of cloud droplets from that predicted strictly on the basis of equilibrium activation. This study will focus mainly on these mechanisms.

In the sections that follow, the mechanisms that lead to kinetic limitations in cloud droplet formation are presented. The models used for evaluating kinetic effects are then described, together with the relevant criteria used for assessing the potential climatic importance of these effects. Finally, simulations are presented, for a variety of updraft conditions

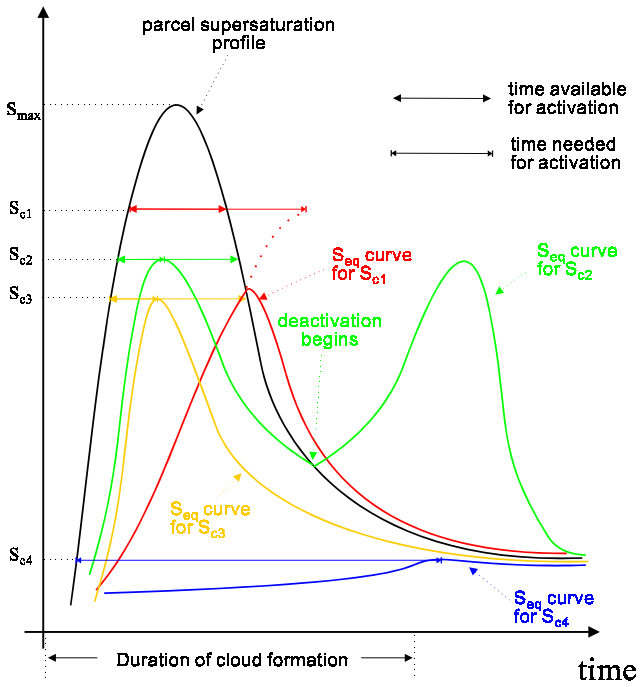

Figure 2.1: Illustration of the kinetic limitation mechanisms.

and aerosol types, from which conclusions can be derived regarding the effect of kinetic limitations on cloud droplet number concentration and albedo.

2.3 Kinetic limitation mechanisms

There are three kinetic limitation processes that can inhibit the formation of cloud droplets. These mechanisms will be explained with the help of Figure 2.1, which illustrates typical cloud parcel and droplet equilibrium supersaturation profiles (S and S_{eq}, respectively) as a function of cloud depth, as predicted by adiabatic parcel theory. Each aerosol equilibrium curve corresponds to particles containing a different amount of solute. The equilibrium curves vary with respect to cloud depth as a consequence of droplets changing size as they traverse through the cloud column. According to equilibrium activation theory, any particle with a critical supersaturation, S_c, less than the maximum supersaturation, $S_{\max}$, encountered in the parcel will activate. However, the time which particles are exposed to a supersaturation level is a crucial parameter; that time must be sufficiently long to allow the particle to reach its critical diameter. The droplet can be considered activated only

when the wet diameter exceeds its critical value. Furthermore, to ensure constant growth of the droplet, the ambient supersaturation should be high enough for activated droplets to continuously grow throughout the duration of cloud formation.

The yellow curve of Figure 2.1 represents an aerosol particle that activates and remains so throughout the entire time of cloud formation. The critical supersaturation of the particle, S_{c3}, is less than $S_{\max}$; the time needed for activation is also less than the time during which $S \geq S_{c3}$. When this particle activates, its equilibrium curve will be at a maximum (with $S_{eq} = S_c$); subsequently, the particle is activated and S_{eq} drops. As can be seen, the particle S_{eq} is always less than the parcel supersaturation, so the driving force for growth, $S - S_{eq}$, is always positive. This guarantees that the particle will remain activated throughout the cloud.

The same cannot be said for all the aerosol types depicted in Figure 2.1. The first mechanism that limits the formation of activated droplets is the inertial mechanism described by [22]. This mechanism is illustrated in Figure 2.1 for the particles with a critical supersaturation S_{c4} (blue curve). These particles have a large dry diameter and a very low critical supersaturation. The timescale of cloud formation is not sufficient for these particles to reach their critical diameter. Nonetheless, the driving force for growth is always positive, and these particles continuously grow, attaining a wet diameter similar (and actually larger) to those of the activated droplets. Thus, even though these particles do not activate, they cannot be distinguished from activated droplets, and so should be treated as such.

The red curve corresponds to a particle with a relatively high critical supersaturation, S_{c1}. The time during which $S > S_{c1}$ is not sufficient for activation. As a result, the particle initially grows, but subsequently evaporates to become an interstitial aerosol particle. This kinetic effect is the second of the three mechanisms identified, and is termed the "evaporation mechanism." Although this is an inertial mechanism (in the sense that small particles do not respond fast enough to changes in ambient supersaturation), a different name is assigned because the particles affected behave much differently than those subject to the inertial mechanism of [22].

Finally, some particles can initially activate but become interstitial aerosol through the third mechanism, the so-called "deactivation mechanism." This is illustrated in Figure 2.1 for particles of critical supersaturation S_{c2} (green curve). These particles are exposed to a supersaturation that exceeds their critical values sufficiently long to activate and do so

initially. However, after a while, the parcel supersaturation drops below the droplet S_{eq}. When this happens, the growth driving force, $S - S_{eq}$, becomes negative, and these droplets begin evaporating. The rate of evaporation can be quite fast, and the droplet may deactivate and become part of the interstitial aerosol, thus decreasing the number of cloud droplets. This mechanism is not a result of mass transfer kinetic limitation, but rather a dynamic effect arising from the limited available water vapor; water transfers from activated drops to other sizes that can still grow.

The deactivation and evaporation mechanisms render the affected aerosol much smaller than the activated droplet size, leading to considerably smaller contribution to cloud optical properties. On the other hand, whereas the inertial mechanism prevents droplets from activating, it does not produce droplets that are differentiated from other activated droplets as the other two mechanisms do. When using the equilibrium assumption, it is expected that the inertial mechanism does not lead to any bias in predicted droplet number. The same cannot be said for the evaporation and deactivation mechanisms, which tend to decrease the number of cloud droplets that are formed. Therefore using the equilibrium assumption in the presence of these two mechanisms will tend to overestimate the droplet number.

In summary, if kinetic limitations affect mainly larger particles (through the inertial mechanism), the equilibrium assumption should not induce a large error in predicted droplet number. However, if kinetic effects apply mainly to the smaller particles of a distribution, not only can the equilibrium assumption yield large error in predicted droplet number, but the droplet number will be sensitive to fluctuations in parcel supersaturation. Any factor that can influence supersaturation history (such as mode radius, number concentration, and updraft velocity) will, in turn, affect all the relevant timescales and thus the extent and type of kinetic limitations.

2.4 Measures of kinetic limitations

Assessing the effect of kinetic limitations on cloud droplet formation requires first the calculation of two quantities, N_{eq} and N_{kn}, the number concentrations of droplets based on equilibrium and kinetic approaches, respectively. N_{eq} is equal to the concentration of particles with critical supersaturation, S_c, less than or equal to the maximum supersaturation, S_{max}, achieved in the ascending air parcel (as calculated by the parcel model). N_{eq}

is based on the assumption that the particles that can activate do so instantaneously, and is the upper limit to the number of droplets that can be formed. N_{kn} is the actual droplet concentration, and is equal to the number of particles that are larger than the activated particle with the smallest dry diameter (i.e., that has a wet radius larger than its critical value). This number contains droplets that have a critical supersaturation less than the parcel maximum supersaturation but which are not larger than their critical size. Critical parameters are calculated from classical Köhler theory (e.g., [143]).

The importance of kinetic growth limitations on droplet formation will be measured in terms of both the activated droplet number and the cloud albedo. Based on the variation of N_{kn} and N_{eq} with cloud depth, z, one can define the total droplet ratio at any height z, $\alpha(z)$,

$$\alpha(z) = N_{kn}(z)/N_{eq}(z) \tag{2.1}$$

which expresses the ratio of actual droplet number to the maximum droplets attainable at a certain distance above cloud base. The droplet ratio includes both strictly activated and unactivated droplets. It is also useful, when assessing kinetic effects, to examine the portion of the droplet population that is strictly activated. For this purpose, the unactivation ratio, $\phi(z)$, defined as the fraction of droplets that are not activated, is used:

$$\phi(z) = N_{unact}(z)/N_{kn}(z) \tag{2.2}$$

where $N_{unact}(z)$ is the number of unactivated droplets in the distribution. For example, a $\phi(z) = 0.2$ means that 20% of the droplets are smaller than their activation diameter and thus are not strictly activated.

Profiles of $\alpha(z)$ and $\phi(z)$ can provide insight regarding the kinetic limitation mechanisms present. Figure 2.2 presents a qualitative sketch of the three types of $\alpha(z)$ profiles seen in the simulations. Each type represents a case where different kinetic limitation mechanisms are active. The "type 1" profile is observed when the inertial mechanism is the only type of kinetic limitation active. In this case, $\phi(z)$ initially attains large values that decreases further up in the cloud column (not shown), and $\alpha(z)$ approaches unity with increasing z. If the evaporation mechanism is active, $\alpha(z)$ initially increases and approaches an asymptotic value less than unity; the fraction that never activates are the small particles that evaporate.

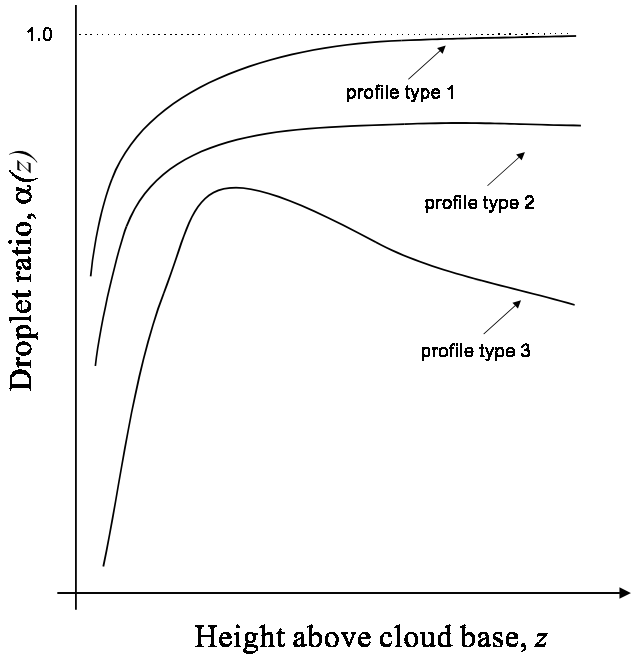

Figure 2.2: Illustration of the three types of droplet ratio profiles seen in the simulations.

This is the "type 2" profile of Figure 2.2. Finally, if the deactivation mechanism is present, then the droplet ratio would initially increase, reach a maximum, and then begin to decrease as particles evaporate and deactivate.

It is difficult to determine *a priori* when a discrepancy in cloud droplet number is important. Placed in the context of the effect on albedo, this issue becomes more straightforward; the discrepancy in droplet number can be considered significant when the albedo is biased by an amount comparable to the change induced by anthropogenic effects. Furthermore, GCMs currently implement a cloud drop number calculation for determining cloud albedo, so it is directly relevant to examine the potential error from the equilibrium activation assumption. In calculating cloud albedo, the cloud liquid water content and effective radius of the droplet distribution are used, with the assumption that the droplet distribution is narrow. Furthermore, the effect of interstitial aerosol on the liquid water content and optical properties are neglected.

2.5 Cloud parcel and albedo models

A cloud parcel model is the simplest tool that can be used to simulate the evolution of droplet distributions throughout a non-precipitating cloud column. These models predict a number concentration profile that starts from zero at cloud base and reaches an asymptotic value further up. In reality, droplet number and size are also affected by turbulent mixing and downdrafts, which cannot be correctly accounted for in a single parcel model. Near cloud base, where kinetic effects are strongest, droplets from upper levels tend to dry out and do not participate in the droplet distribution. Therefore, one would still expect a droplet number concentration that is zero at cloud base and quickly reaches an asymptotic value. Such distributions have been measured and predicted by more comprehensive models [29], so this variation in droplet number with cloud height must be considered when calculating optical properties. Finally, existing theoretical aerosol-cloud parameterizations in GCMs are based on adiabatic cloud parcel model equations, and so estimating cloud albedo sensitivity to kinetic effects is appropriately carried out using adiabatic parcel model calculations. In order to assess the differences arising from the kinetic and thermodynamic assumptions, a droplet growth model has been incorporated within the framework of an adiabatic parcel model.

2.5.1 Cloud parcel model

The adiabatic cloud parcel model is based upon the parcel model described by [127] and [143]. Conservation of heat and moisture for a rising air parcel can be expressed as

$$\frac{dT}{dt} = -\frac{gV}{c_p} - \frac{L}{c_p}\frac{dw_v}{dt} \tag{2.3}$$

$$\frac{dw_v}{dt} = -\frac{dw_c}{dt} \tag{2.4}$$

where T is the temperature of the air, V is the updraft velocity, and w_v and w_c are the mixing ratios of water vapor, and liquid water in the parcel, respectively.

In (2.4), the condensation rate for a population of water droplets consisting of N_i droplets of radius r_i, $i = 1...n$ can be expressed as

$$\frac{dw_c}{dt} = \frac{4\pi\rho_w}{\rho_a}\sum_{i=1}^{n} N_i r_i^2 \frac{dr_i}{dt} \tag{2.5}$$

where the particle growth rate is determined from,

$$\frac{dr}{dt} = \frac{G}{r}\left(S - S_{eq}\right) \tag{2.6}$$

with G given by

$$G = \frac{1}{\frac{\rho_w RT}{p_v^* D_v' M_w} + \frac{L\rho_w}{k_a' T\left(\frac{LM_w}{RT}-1\right)}} \tag{2.7}$$

The supersaturation S is given by $w_v/w_v^* - 1$. By integration of the supersaturation balance equation,

$$\frac{dS}{dt} = \frac{1}{w_v^*}\left[\frac{dw_v}{dt} - (S+1)\left(\frac{\partial w_v^*}{\partial T}\frac{dT}{dt} - \frac{\partial w_v^*}{\partial p_a}\rho_a g V\right)\right] \tag{2.8}$$

and the equilibrium supersaturation S_{eq} is given by Köhler theory,

$$S_{eq} = \exp\left(\frac{2M_w\sigma_w}{RT\rho_w r_i} - \frac{3n_s M_w}{4\pi\rho_w\left(r_i^3 - r_{dry,i}^3\right)}\right) - 1 \tag{2.9}$$

Here we have used the hydrostatic relation to relate changes in atmospheric pressure to vertical velocity in (2.8). D_v' in (2.9) is the diffusivity of water vapor in air, modified for noncontinuum effects,

$$D_v' = \frac{D_v}{1 + \frac{D_v}{a_c r}\sqrt{\frac{2\pi M_w}{RT}}} \tag{2.10}$$

where $a_c = 1.0$ is the condensation coefficient. k_a' in (2.7) is the thermal conductivity of air modified for noncontinuum effects,

$$k_a' = \frac{k_a}{1 + \frac{k_a}{a_T r\rho c_p}\sqrt{\frac{2\pi M_a}{RT}}} \tag{2.11}$$

where $a_T = 0.96$ is the thermal accommodation coefficient, and n_s in (2.9) is the number of moles of solute per particle,

$$n_s = \frac{4\rho_p \varepsilon \nu \pi d_i^3}{3M_s} \tag{2.12}$$

where d_i is the dry particle diameter, and

$$\rho_p = \left[(1-\varepsilon)/\rho_u + \varepsilon/\rho_s\right]^{-1} \tag{2.13}$$

is the mean particle density. Surface tension σ_w is expressed (in J m^{-2}) as a function of the parcel temperature T [143], $\sigma_w = 0.0761 - 1.55 \times 10^{-4}\,(T - 273)$. Other symbols are defined in the Appendix. Equations (2.3)-(2.8) constitute a closed system of ordinary differential equations that are solved numerically using the LSODE solver of [66].

2.5.2 Cloud albedo

Cloud albedo, R_c, is calculated based on the two-stream approximation of a non-absorbing, horizontally homogeneous cloud [94],

$$R_c = \frac{\tau}{7.7 + \tau} \tag{2.14}$$

where τ is the cloud optical depth,

$$\tau = \int_0^H \frac{3\rho_a w_L(z)}{2\rho_w r_{eff}(z)} dz \tag{2.15}$$

where $w_L(z)$ is the liquid water mixing ratio profile along the cloud column, calculated from the parcel model simulations (after transforming the Lagrangian solution into Eulerian form by setting $w_L(z) = w_L(t)$ at $t = z/V$).$\rho_w$is the water density, $\rho_a$is the air density and $r_{eff}(z)$ is the cloud droplet distribution effective radius,

$$r_{eff} = \frac{\int_0^\infty r^3 n(r) dr}{\int_0^\infty r^2 n(r) dr} \tag{2.16}$$

where $n(r)$ is the droplet size distribution. These expressions yield values for cloud albedo that are of reasonable accuracy for relatively thick clouds composed of narrow distributions of large droplets [63].

Assuming that the interstitial aerosol has a negligible amount of liquid water, and that the droplet population is effectively monodisperse, the expression for $r_{eff}(z)$ is given by

$$r_{eff}(z) = \frac{3w_L(z)}{4\pi N_i(z)\rho_w} \tag{2.17}$$

where $N_i(z)$ can be either $N_{kn}(z)$ or $N_{eq}(z)$. In the first case, the albedo calculated will be the "kinetic albedo," while the second will be the "thermodynamic albedo." The thermodynamic albedo tends to be higher than the kinetic albedo. This is because for the same amount of cloud liquid water, the number of droplets predicted is larger in the thermodynamic case, hence the effective radius according to (2.17) would be smaller than in the kinetic case.

The quantity used for assessing the importance of kinetic effects, in terms of cloud albedo, is the difference between thermodynamic and kinetic albedo. Because the thermodynamic albedo is larger than the kinetic (as explained before), this difference will be positive. Furthermore, since this difference depends on the cloud depth, we select the cloud depth for which this difference is maximum.

2.6 Simulation parameters

The importance of kinetic limitations depends on cloud thickness, updraft velocity, and aerosol characteristics. To explore the dependence on these parameters, we shall consider a range of values spanning observations of boundary layer clouds. This study does not examine all possible phenomena that influence aerosol activation behavior, such as changes in surface tension, and the presence of slightly soluble substances. For example, a decrease in surface tension (from surfactant species in the aerosol) should enhance kinetic effects, because a) the critical radius for activation becomes larger, so particles need more time to activate, and b) a larger fraction of the aerosol population can activate, so more particles compete for cloud water. Solution non-idealities are not considered; they do not have a significant impact since droplets dilute considerably under supersaturated conditions [164]. Finally, the effect of uncertainty in the accommodation coefficient is not examined.

2.6.1 Key parameters

Cloud thickness influences the transit time of air parcels rising through a cloud, and hence the time available for particle growth. Boundary layer clouds are typically 100-500 m thick, with most in the range of 200-400 m [118, 31, 42, 161]. To explore the dependence of kinetic effects on cloud thickness, we consider values ranging from 10 to 1000 m.

Updraft velocity influences both the transit time and the maximum supersaturation in a cloud updraft. The maximum supersaturation achieved is lower in weaker updrafts, so only particles with relatively low critical supersaturations can be activated. Observed updraft velocities in boundary layer clouds vary widely, but values derived from measured vertical velocity variance are typically 30-50 cm s^{-1} [118, 31, 43]. We explore the dependence on updraft by considering updraft velocities of 10, 30, 100, and 300 cm s^{-1}.

2.6.2 Aerosol characteristics

The dependence of kinetic effects on aerosol number concentration and mean radius will be explored by considering a variety of aerosol size distributions. We consider idealized size distributions in which the number concentration and mean radius are prescribed in order to clearly sort out the physics involved. We then consider size distributions that more closely approximate ambient distributions.

Size distributions are of the single or multiple lognormal form,

$$\frac{dn\left(r\right)}{d\ln r}=\sum_{i=1}^{n_m}\frac{N_i}{\sqrt{2\pi}\ln\sigma_i}\exp\left[-\frac{\ln^2\left(r/r_{g,i}\right)}{2\ln^2\sigma_i}\right] \tag{2.18}$$

where N_i is the aerosol number concentration, $r_{g,i}$ the number mode radius, σ_i is the geometric standard deviation for mode i, and n_m is the number of modes in the distribution. For single modes we consider a single value for $\sigma = 2$, but a wide range in number concentration (100-3000 cm^{-3}) and mode radius (0.02-0.1 μm). The range in mode radius and number concentration is appropriate for accumulation mode particles, which comprise most CCN. For multiple modes we have selected four of [160] trimodal representations, namely, the marine, clean continental, average background, and urban aerosol. The parameters of these four distributions are listed in Table 2.1. The size distributions refer to dry size, while the chemical composition of the aerosol is assumed pure ammonium sulfate.

In all kinetic simulations, particles are assumed initially to be in equilibrium with a

Table 2.1: Aerosol distribution parameters ($r_{g,i}$ in μm, N_i in cm^{-3}) [160]

Aerosol type	Nuclei Mode			Accumulation Mode			Coarse Mode		
	$r_{g,1}$	σ_1	N_1	$r_{g,2}$	σ_2	N_2	$r_{g,3}$	σ_3	N_3
Marine	0.005	1.6	340	0.035	2.0	60	0.31	2.7	3.1
Clean Continental	0.008	1.6	1000	0.034	2.1	800	0.46	2.2	0.72
Average Background	0.008	1.7	6400	0.038	2.0	2300	0.51	2.16	3.2
Urban	0.007	1.8	106000	0.027	2.16	32000	0.43	2.21	5.4

relative humidity of 98%. For the idealized size distributions, we consider 200 size bins spaced equally in log radius. Using a size range between about $D_{p,g}/10\sigma$ and $10\sigma D_{p,g}$ covers total particle number to within 10^{-7}%. The simulations exhibit little sensitivity with respect to initial relative humidity concentrations and denser discretization schemes.

2.7 Effect of kinetic limitations on cloud droplet number

We first explore the parametric dependence of kinetic limitations using the single lognormal size distributions. We then consider various multimode lognormal distributions that resemble ambient aerosol.

2.7.1 Single lognormal size distributions

From the simulations we calculate the $\alpha(z)$ and $\phi(z)$ profiles. The results of these simulations are summarized in Table 2.2, which gives the characteristics of these ratios for all the mode radii, number concentrations, and updrafts examined. As expected, the droplet ratio (for constant mode radius and number concentration) in most cases approaches an asymptotic value for large cloud depths. Kinetic effects become more apparent as updraft velocity decreases and aerosol concentrations increase. For a mode radius of 0.03 μm, the droplet number is reduced by 40% for an updraft velocity of 10 cm s^{-1} and an aerosol number concentration of 3000 cm^{-3}. In this particular example, the unactivation ratio $\phi(z)$ is close to zero. This means that most (more than 95%) of the cloud drops are activated. In this particular case, the droplet ratio profile is "type 3," so both evaporation and deactivation mechanisms are present.

Table 2.2: Characteristics of $\alpha(z)$ and $\phi(z)$ profiles for single lognormal aerosol distribution runs. $\alpha_{\max}$ is the maximum value of $\alpha(z)$, encountered at $z_{\alpha_{\max}}$ above cloud base.

$r_{g,i}$ (μm)	N_i (cm^{-3})	V (m s^{-1})	Profile type	$\alpha_{\max}$	$z_{\alpha_{\max}}$ (m)	α ($1000m$)	ϕ ($20m, 1000m$)
0.03	100	0.1	1	1.000	10	1.000	0.002, 0.000
0.03	100	0.3	1	1.000	20	1.000	0.006, 0.042
0.03	100	1.0	1	1.000	20	1.000	0.024, 0.026
0.03	100	3.0	1	1.000	20	1.000	0.095, 0.012
0.03	300	0.1	2	0.931	10	0.931	0.005, 0.000
0.03	300	0.3	3	1.000	10	0.948	0.008, 0.000
0.03	300	1.0	1	1.000	20	1.000	0.028, 0.000
0.03	300	3.0	1	1.000	20	1.000	0.095, 0.020
0.03	1000	0.1	3	0.918	10	0.768	0.014, 0.000
0.03	1000	0.3	3	1.000	10	0.936	0.019, 0.000
0.03	1000	1.0	2	0.956	10	0.956	0.037, 0.000
0.03	1000	3.0	1	1.000	20	1.000	0.103, 0.029
0.03	3000	0.1	3	0.815	10	0.589	0.052, 0.000
0.03	3000	0.3	3	0.922	10	0.713	0.050, 0.000
0.03	3000	1.0	3	0.944	10	0.889	0.066, 0.000
0.03	3000	3.0	3	1.000	20	0.961	0.141, 0.001
0.05	100	0.1	1	1.000	10	1.000	0.019, 0.042
0.05	100	0.3	2	0.974	10	0.974	0.032, 0.000
0.05	100	1.0	1	1.000	20	1.000	0.092, 0.013
0.05	100	3.0	1	1.000	20	1.000	0.231, 0.004
0.05	1000	0.1	3	0.857	10	0.668	0.159, 0.001
0.05	1000	0.3	3	0.948	10	0.847	0.154, 0.001
0.05	1000	1.0	2	0.970	20	0.970	0.177, 0.002
0.05	1000	3.0	1	0.985	20	0.985	0.323, 0.003
0.10	100	0.1	3	0.974	10	0.948	0.206, 0.005
0.10	100	0.3	1	1.000	10	1.000	0.244, 0.006

$r_{g,i}$ (μm)	N_i (cm^{-3})	V (m s^{-1})	Profile type	$\alpha_{\max}$	$z_{\alpha_{\max}}$ (m)	α ($1000m$)	ϕ ($20m, 1000m$)
0.10	100	1.0	1	1.000	20	1.000	0.386, 0.008
0.10	100	3.0	1	1.000	30	1.000	0.586, 0.009
0.10	300	0.1	3	0.908	20	0.774	1.000, 0.011
0.10	300	0.3	3	0.954	20	0.929	0.414, 0.014
0.10	300	1.0	1	1.000	20	1.000	0.422, 0.024
0.10	300	3.0	1	0.998	30	0.998	0.671, 0.018
0.10	1000	0.1	3	0.925	200	0.785	1.000, 0.034
0.10	1000	0.3	3	0.950	70	0.804	1.000, 0.033
0.10	1000	1.0	3	0.979	20	0.933	1.000, 0.036
0.10	1000	3.0	1	1.000	20	0.994	0.755, 0.040
0.10	3000	0.1	2	0.902	700	0.902	1.000, 0.133
0.10	3000	0.3	3	0.925	500	0.853	1.000, 0.102
0.10	3000	1.0	3	0.952	200	0.857	1.000, 0.086
0.10	3000	3.0	3	0.979	50	0.933	1.000, 0.083

The dependence of kinetic effects on N_i is further pronounced as mode radius increases. For example, the droplet ratio for an aerosol number concentration of 3000 cm^{-3} and a mode radius of 0.1 μm can be close to zero for a large portion of the cloud, because the time required for growth is very large for weak updrafts (this is also seen in $\phi(z)$, which ranges between 1.0 and 0.083). In this particular case, the $\alpha(z)$ profile is "type 2," so the evaporation mechanism is present. The fact that $\alpha(z)$ is maximum at 700 m above cloud base indicates that kinetic effects are very strong. This is not surprising, given the mode radius and concentration of particles. As updraft velocity increases, supersaturation, being the driving force for particle growth, also increases and activates particles lower in the cloud. The dependence on cloud thickness is also stronger for a mode radius of 0.1 μm than for 0.03 μm because a) maximum supersaturation is achieved further up from cloud base, and, b) the larger particles respond more slowly to variations in supersaturation. The deactivation mechanism is responsible for decreasing the droplet ratio for low updrafts and high number concentrations ($>$ 300 cm^{-3}). Another striking feature, as evidenced by $\phi(z)$, is that the inertial mechanism is negligible for particles of smaller modal diameter; in the larger size

distributions, roughly half of the particles are not activated during the first 50-100 m of the cloud. Despite the difference in modal size, the fraction of small particles that fail to activate is roughly the same at large cloud depths.

The simulations indicate that a large mode radius tends to accentuate kinetic effects. By examining $\alpha(z)$ and $\phi(z)$ as a function of mode radius for a number concentration of 100 cm^{-3}, we can see that evaporation and deactivation effects are negligible for all mode radii; most droplet ratio profiles are of type 1. Inertial effects (as shown by the value of $\phi(z)$ at 20 m) become increasingly important as mode radius increases. On the other hand, $\alpha(z)$ never drops below 0.95. This is an important point: for low concentration of particles, kinetic effects that influence droplet number are negligible regardless of particle diameter. The inertial mechanism is the only type of limitation experienced by these particles.

Kinetic effects are more prominent when the number concentration increases to 1000 cm^{-3}. When the concentration of particles is this high, $\alpha(z)$ profile types indicate that the deactivation and evaporation mechanisms are much more prominent than for a particle concentration of 100 cm^{-3}. This suggests that these kinetic limitation mechanisms are present primarily at high number concentrations.

2.7.2 Trimodal lognormal size distributions

From the previous section it is clear that kinetic limitations on droplet formation are important for high number concentrations, and large mean particle size can further enhance these effects. Although one can imagine combinations of number concentration and mean particle size that would yield significant kinetic limitations, such combinations may not be realistic. High particle concentrations are normally associated with small particle sizes, and vice versa. An assessment of the importance of kinetic limitations on ambient droplet formation should therefore consider size distributions that represent ambient aerosol. In doing so, we examine the trimodal lognormal fits to measured size distributions for a variety of aerosol types in Table 2.1.

Although the number concentration for the nuclei mode can be quite large, the particles are so small that the supersaturation necessary for activating them is never encountered within a cloud. Furthermore, the mean particle size of the coarse mode is large enough for significant kinetic effects, but the number concentrations are usually too small to have a significant impact on droplet number. Thus, the distribution characteristics of the accumu-

lation mode is expected to determine the kinetic effects of the aerosol types in Table 2.1.

Figure 2.3 shows $\alpha(z)$ and $\phi(z)$ as a function of updraft velocity and cloud thickness for the aerosol types shown in Table 2.1. Simulations reveal that kinetic effects for the marine aerosol are negligible regardless of updraft velocity and cloud thickness. This is not surprising, given that the number concentration of the accumulation mode, 60 cm^{-3}, is too low for kinetic effects to be important.

The accumulation mode number concentration for the clean continental aerosol is much higher, 800 cm^{-3}, so kinetic effects become evident at weak updraft velocities: $\alpha(z)$ is always below 0.85 for V=10 cm s^{-1}, and 0.95 for V=30 cm s^{-1}. Results for the clean continental aerosol are comparable to those illustrated in Table 2.1 for a number mode radius of 0.03 μm and a number concentration of 1000 cm^{-3}, but with kinetic effects being somewhat weaker because of the lower number concentration. The ratio $\phi(z)$, however, is low and the droplet ratio approaches an asymptotic value, so the aerosol is subject to the evaporation mechanism, as some of the particles fail to activate in the initial stages of cloud formation.

Kinetic limitations on droplet formation are quite important for the average background aerosol, which has an accumulation mode number concentration of 2300 cm^{-3}. The droplet ratio is a little over 0.8 for a 30 cm s^{-1} updraft, which is consistent with the single lognormal size distribution with the same number concentration. Although there are strong inertial effects in the coarse mode, its contribution to the total droplet number concentration is rather small. Because of this, $\phi(z)$ is low, less than 0.1 for cloud depths larger than 20 m, indicating that most of the droplets are strictly activated. For weak updrafts, because of the high concentration of accumulation mode particles, deactivation plays a significant role and reduces the droplet number by 20%. Overall, the aerosol seems to be subject to both deactivation and evaporation mechanisms, the degree to which depends on the updraft velocity.

With an accumulation mode number concentration of 32,000 cm^{-3}, one might expect substantial kinetic effects for the urban aerosol, and indeed this is the case. In fact, kinetic effects are so strong, that $\alpha(z)$ is zero until 70 m above cloud base. The activation ratio never exceeds 0.8, even for the strongest updrafts. The latter indicates that many particles fail to activate as the supersaturation decreases following the maximum supersaturation in all updraft cases examined. Inertial effects are also significant; even for clouds of 200 m

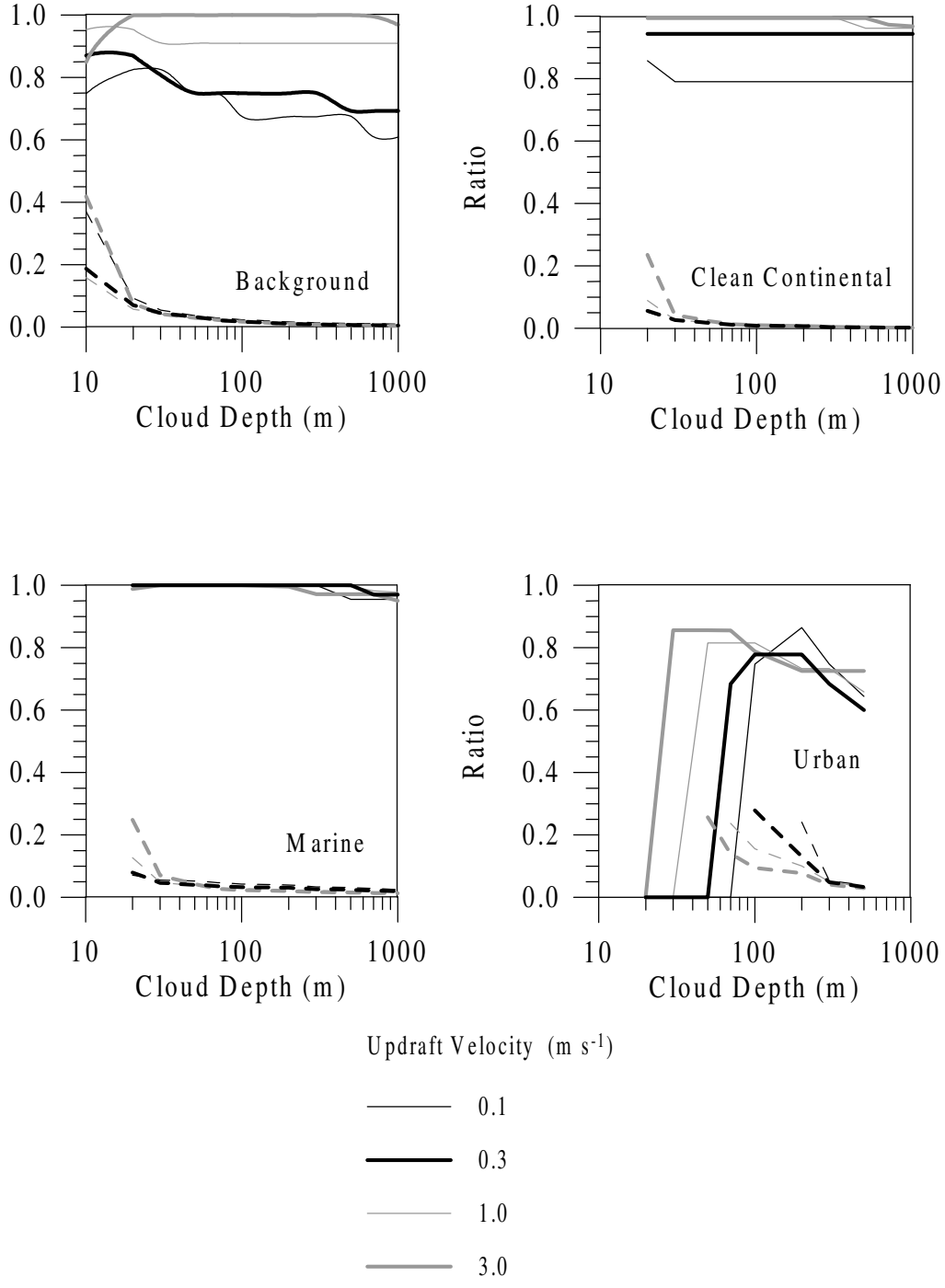

Figure 2.3: Droplet ratio as a function of updraft velocity and cloud thickness for the background, clean continental, marine, and urban distributions of Table 1. Solid lines represent the droplet ratio $\alpha(z)$, while dashed lines represent the unactivation ratio $\phi(z)$.

thickness, $\phi(z)$ is above 0.2. Finally, deactivation is also very strong since the decrease in $\alpha(z)$ after the maximum is about 20%.

2.8 Effect of kinetic limitations on cloud albedo

For very thin clouds (on the order of 10 m), the optical depth is small, so the albedo difference itself is small. As the cloud depth increases, so does optical depth. This initially leads to an increase in the albedo difference; after a certain point, the optical depth is so large, that the albedo difference begins to decrease. The point of maximum difference between thermodynamic and kinetic albedo is used for evaluating kinetic effects. A climatically important kinetic effect would be considered for a difference between kinetic and thermodynamic albedo larger than about 0.005; this albedo change, if relevant globally, could yield an uncertainty in radiative forcing comparable to that estimated for anthropogenic indirect aerosol radiative forcing [36]. It should also be noted that the maximum albedo difference in the simulations (both single mode and trimodal distributions) was encountered in the first 300 m of the cloud. As expected, increasing the kinetic effects in droplet number tends to shift the locus of the maximum higher up in the cloud.

2.8.1 Single lognormal size distributions

Since the difference between thermodynamic and kinetic cloud albedo depends on the difference in cloud droplet number, it is expected that the largest difference would be seen for high number concentrations. The discrepancy is also expected to be enhanced if the distribution has a large modal radius. This can be seen in the two top panels of Figure 2.4, which shows the maximum albedo difference, as a function of number concentration, for two modal radii. For a number mode radius of 0.03 μm (top left panel), there is large sensitivity of kinetic effects on albedo to number concentration. For low concentrations (100 cm^{-3}), kinetic limitations are not strong enough to yield a significant difference in cloud albedo; this difference becomes very large however, close to 0.05, when the concentration is around 3000 cm^{-3}. For a number mode radius of 0.1 μm (top right panel), these effects are enhanced considerably and the albedo difference approaches 0.7 for the lowest updraft and highest number concentrations. The cases where albedo difference is below 0.005 seem to be the same for both mode radius cases, when the number concentration is below 300 cm^{-3}.

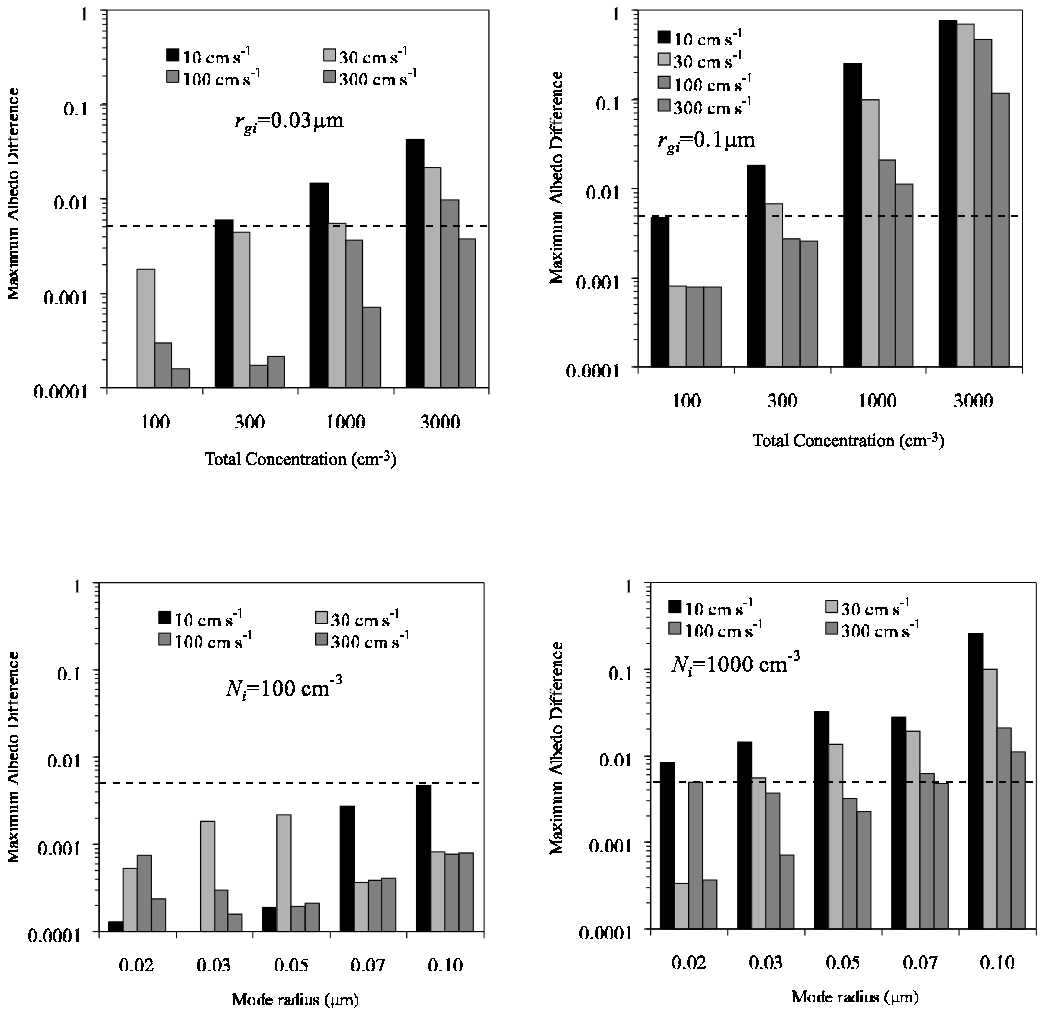

Figure 2.4: Maximum difference between thermodynamic and kinetic cloud albedo. The single mode lognormal distribution aerosol is used with (a) number mode radius 0.03 μm, (b) number mode radius 0.1 μm, (c) number concentration of 100 cm^{-3}, and (d) number concentration of 1000 cm^{-3}.

The above statements are further supported by the two bottom panels of Figure 2.4. These show the maximum albedo difference as a function of mode radius, for two number concentrations. Regardless of modal radius, when the concentration is 100 cm^{-3} (bottom left panel), the albedo difference is insignificant. However, when the concentration becomes 1000 cm^{-3}, kinetic effects are always significant. When the albedo difference is around 0.1, the effect of mode radius seems to be small.

By comparing Figure 2.4 with Table 2.2, we observe a consistent trend; the maximum albedo difference tends to exceed the 0.005 value whenever the droplet ratio consistently (that is, for all cloud depths) is below 0.9. This is an important point, since it provides a quantitative measure for when the bias in droplet number becomes important.

2.8.2 Trimodal lognormal size distributions

Figure 2.5 shows the maximum difference in cloud albedo between the thermodynamic and kinetic activation models, for the four lognormal distributions of Table 2.1. Albedo differences are shown for both the total number concentration in Table 2.1 and twice these values. The urban aerosol distribution exhibits the largest difference in albedo, which is expected, given that it is the distribution with the largest kinetic limitation effects in droplet number. Of the other aerosol classes, the largest sensitivity is experienced by the clean continental aerosol, where a doubling in concentration leads to a fivefold increase in albedo difference (at the highest updraft velocities). As in section 2.7.2, kinetic limitations become important for cloud albedo whenever $\alpha(z)$ is consistently below 0.9.

2.9 Summary and conclusions

There are three mechanisms that lead to kinetic limitations on cloud droplet formation. The first, identified by [22], and termed the *inertial mechanism*, arises when particles with critical supersaturation less than a threshold value do not have time to grow larger than their critical size and thus do not activate. In the second *deactivation mechanism*, activated droplets evaporate to form interstitial aerosol when the parcel supersaturation drops below the droplet equilibrium saturation ratio. In the third mechanism, the *evaporation mechanism*, particles that could potentially activate (because their critical supersaturation is low enough) evaporate to form interstitial aerosol because the time they are exposed to

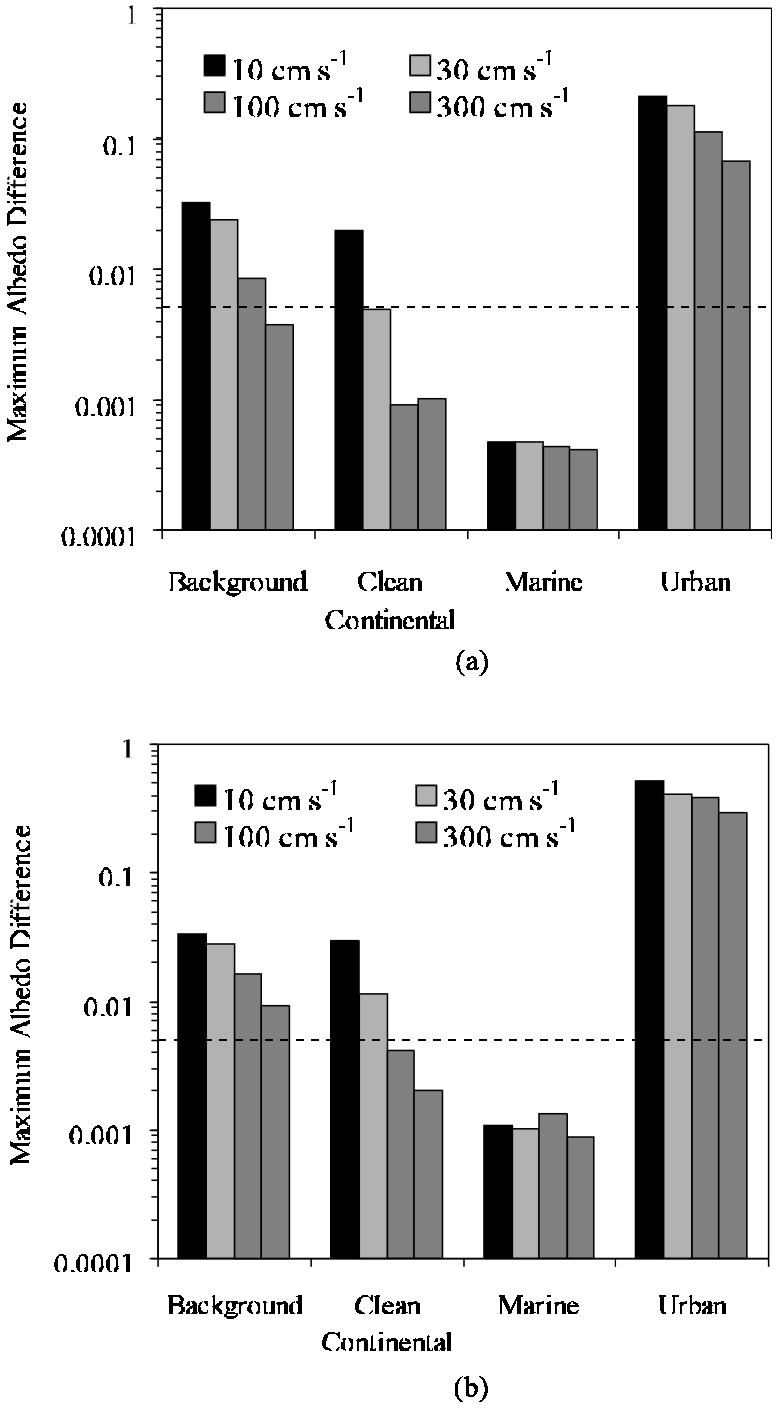

Figure 2.5: Maximum difference between thermodynamic and kinetic cloud albedo. The aerosol distributions in Table 2.1 are used with (a) given number concentrations, and (d) doubled number concentrations.

high supersaturation is not sufficient to reach their critical radius. Large particles, which are subject to the inertial mechanism, are also large enough to be considered cloud droplets even when they are not strictly activated. Particles, however, that are subject to the deactivation and evaporation mechanisms become much smaller than activated drops and hence should not be considered cloud droplets. Thus, if deactivation and evaporation significantly reduce the droplet number concentration, these processes should be accounted for in parameterizations of the activation process. The inertial mechanism, although a type of kinetic limitation, does not generate a discrepancy in cloud droplet number. Most of the discrepancy is a result of the smaller particles that fail to activate, through the two other mechanisms identified. This also implies that for cases where kinetic effects are significant, the droplet number is quite sensitive to fluctuations in supersaturation.

In terms of number of cloud droplets, the conditions most likely to yield considerable kinetic effects are those of high aerosol number concentrations. Weak updrafts and large mode radius tend to enhance kinetic effects. We have also investigated a variety of aerosol types to determine those subject to important kinetic effects under a variety of cloud formation conditions. We have found that urban aerosol is strongly affected by kinetic growth limitations, but relatively pristine marine aerosols are not. We have found that for most aerosols the percentage errors from neglecting kinetic effects are larger for weak updrafts than for strong updrafts, even though the residence time of air parcels in clouds is shorter for strong updrafts. However, absolute errors in droplet number are often largest for moderate updrafts because aerosol activation is inefficient for weak updrafts, and kinetic limitations are smaller for strong updrafts.

The conditions most likely to yield considerable differences in cloud albedo are similar to those for droplet number, i.e., weak updrafts, large mode radius, and high aerosol concentrations. Simulations indicate that the maximum albedo difference is less than 0.005 for marine aerosol (where kinetic limitations in cloud droplet number are also not significant). Albedo differences can, however, exceed 0.1 for urban aerosol.

By comparing the droplet ratio and albedo difference plots, it can be seen that kinetic effects become important whenever the droplet ratio is consistently below 0.9. Of the three kinetic limitation mechanisms, the evaporation and deactivation mechanisms can influence droplet number concentrations. However, the deactivation mechanism does not affect aerosol throughout the cloud and always appears together with the evaporation mech-

anism. So, it is believed that conditions that are conducive towards the appearance of the evaporation mechanism can lead to substantial kinetic effects. As a consequence, kinetic limitations are not expected overall to be climatically significant, but can have a noticeable local impact.

Existing parameterizations of aerosol activation in GCMs do not account for kinetic limitations. Because closed-form solutions of the activation process are not available, parameterizations can be fit to kinetic simulations. Future parameterizations should therefore be matched to kinetic simulations that extend beyond the point of maximum supersaturation, classify activated particles on the basis of their size rather than their critical supersaturation, and also account for fluctuations in cloud supersaturation.

2.10 Acknowledgments

This work was supported at PNNL by the NASA Earth Science Enterprise under contract NAS5-98072 and by the U.S. Department of Energy Atmospheric Radiation Measurement Program, which is part of the DOE Biological and Environmental Research Program. PNNL is operated for the DOE by Battelle Memorial Institute under contract DE-AC06-76RLO 1830. This work was supported at the California Institute of Technology by the Office of Naval Research.

2.11 Notation

a_c	condensation coefficient
a_T	thermal accommodation coefficient
c_p	specific heat of dry air at constant pressure
r_{dry}	particle dry radius
D_v	water vapor diffusivity in air
D'_v	water vapor diffusivity in air, corrected for noncontinuum effects
g	acceleration of gravity
G	particle growth parameter, as given by (2.7)
H	cloud thickness
k_a	thermal conductivity of air
k'_a	thermal conductivity of air, corrected for noncontinuum effects
L	latent heat of condensation of water
M_a	molecular weight of dry air
M_s	molecular weight of the solute
M_w	molecular weight of water
$n(r)$	number size distribution
n_m	number of modes in idealized lognormal distributions
n_s	number of moles of solute per particle
N	aerosol number concentration
N_{eq}	number concentration of particles with S_c smaller than or equal to $S_{\max}$
N_{kn}	number concentration of particles with dry radius larger than that of the smallest activated particle
N_{unact}	number concentration of large unactivated particles (with dry radius larger than that of the smallest activated particle, but with a wet radius less than the critical size)
p_a	air pressure
p_v^*	saturation vapor pressure of water
r	particle wet radius
$r_{g,i}$	number mode radius of lognormal size distribution
r_{eff}	size distribution effective radius
R	universal gas constant
R_c	cloud albedo

S	supersaturation
S_c	critical supersaturation for activating according to Köhler theory
S_{eq}	supersaturation in equilibrium with particle size
$S_{\max}$	maximum supersaturation in a cloud parcel
t	time
T	temperature of air parcel
V	parcel updraft velocity
w_v	water vapor mixing ratio in air parcel
w_c	cloud liquid water mixing ratio
w_v^*	p_v^*/p_a saturation mixing ratio of water
z	cloud depth as measured from cloud base (or where S=0%)
α	droplet ratio N_{kn}/N_{eq}
ε	mass fraction of soluble material in the dry particle
ν	number of ions the solute dissociates into in solution
ρ_a	density of air
ρ_w	density of water
ρ_p	mean density of particle
ρ_s	density of soluble component of particle
ρ_u	density of insoluble component of particle
σ	geometric standard deviation of the aerosol size distribution
σ_w	water surface tension
τ	optical depth
ϕ	unactivation ratio N_{unact}/N_{kn}

Chapter 3

Reshaping the theory of cloud formation

Note: Parts of this chapter appeared as reference [19].

3.1 Abstract

Clouds are the principal determinant of the albedo of Earth, are a major component of the hydrologic cycle, and are at the center of myriad biogeochemical processes, but they remain the most uncertain factor in forced climate change. Recent extensions of the traditional Köhler theory have shown the possible importance of water soluble gases, substances of partial solubility, surfactants, and condensation kinetics. When these factors are combined, significant changes of droplet populations and sizes occur, thereby altering cloud radiative forcing. While it is currently impossible to calculate the global impact of these additional activation effects because of a lack of data on atmospheric composition, sensitivity calculations indicate that realistic conditions representing anthropogenically perturbed environments result in albedo changes that are climatically significant, adding still more uncertainty to the forcing by modification of clouds. More broadly, inclusion of these new factors erases a conceptual boundary between what we call "cloud" and "aerosol" or "haze," and an "aerosol-cloud continuum" results in which subtle changes in thermodynamic state lead to substantial changes in cloud albedo.

3.2 Introduction

Clouds of water droplets in Earth's atmosphere are as intrinsic to our planet as is water itself. Droplet clouds are the single most important factor controlling the albedo of the Earth, covering, on average, about half of it with substantially higher reflectivity than that of most of the underlying surface. Possible anthropogenic influences on cloud properties and albedo, the so-called indirect climatic effect of aerosols, could constitute a potential major climate forcing (1). These influences are presently estimated to have a global mean ranging from 0 to -2.8 W m^{-2}, based either on the range of published estimates or on the range of forcings that results from the uncertainty of the parameters input to the models (1). Uncertainties in the influence of anthropogenic emissions on cloud albedo are far and away the largest in climate forcing, with a magnitude in the global mean comparable (but opposite in sign) to that calculated for greenhouse gases (about + 2.4 W m^{-2}).

Moreover, none of the estimates of indirect aerosol radiative forcing has yet included the combined influences of a number of recently identified chemical factors, each of which has been suggested to have possible global significance. Therefore, one purpose of this paper is to assess the sensitivity of cloud albedo to the combined set of chemical factors as a way to identify their potential importance to global climate. More broadly, our goal is to describe these new factors, in combination, in the context of the classical theory of cloud formation.

Scientific study of clouds is very old, with beginnings reaching back to Aristotle's *Meteorologica* (2), which included the notion of coalescence: "...so here the water floats on the air till a number of the small droplets coalesce to form large drops that fall." Modern scientific description of clouds and cloud formation began over a century ago with the recognition by Aitken (3) that cloud droplet formation requires airborne particles that serve as nuclei for water condensation. He went on to develop a variety of particle counters based on the condensation of water at substantial supersaturation (saturation ratios around 3). Many figures influential in the early fields of chemistry and physics provided much of the framework on which our current understanding of clouds is based, including Raoult, W. Thomson (Lord Kelvin), van't Hoff, and C. T. R. Wilson.

Nomenclature in this field also evolved based more on human observation than on exact physical/chemical theory. Terms like "cloud," "fog," and "haze" arrived in common usage independent of a thermodynamic basis.

The modern theory of cloud droplet formation was advanced by the Swedish scientist Hilding Köhler in the 1920s and 1930s (4). In that theory clouds consist of "activated" water droplets that grow spontaneously after they have reached a critical size, which occurs at a critical value of the supersaturation of water vapor. Köhler's theory provided a solid basis that has served the cloud physics and meteorology communities as the primary description of cloud formation for some 80 years. The first treatise on cloud microphysics by Mason in 1957 (5) has by now been joined by numerous others, all more or less following the traditional Köhler approach. Importantly, the notion that clouds consist of activated droplets is difficult to demonstrate by measurements, and there is no extensive data base to confirm that the assumption is generally true.

Recent attempts to understand quantitatively the effects of changing global aerosol levels on cloud properties and albedo have led to an examination of the relationships between cloud characteristics and those of the particles on which the cloud formed. Ambient data relating, for example, cloud droplet number concentrations to non-sea salt sulfate aerosol mass exhibit a large degree of variation (around a factor of 10) (6) that suggests cloud properties may not be controlled in as simple a manner as envisioned by Köhler some 80 years ago. Called into question are the long-held assumptions that clouds do not exist in a subsaturated environment and that the number of particles that do activate is controlled strictly by meteorological factors, such as the rate at which a rising parcel of air cools.

Köhler knowingly took the simplest case for analysis and assumed that the cloud condensation nucleus (CCN) is composed of a completely soluble salt and that it is in thermodynamic equilibrium until the point of spontaneous growth. Traditionally, it is assumed that a cloud forms only in a supersaturated water vapor environment, and, indeed, this is true for particles composed of completely soluble substances (with or without the presence of insoluble material).

However, it has recently become evident that chemical processes, compositional influences on physical properties, and kinetics also influence the formation of cloud droplets. These include the roles of soluble gases (7), partially soluble solutes (8), surface tension depression by organic substances (9), aqueous-phase chemistry (10), and slow condensation kinetics (11). These phenomena, originally unforeseen by Köhler, give rise to an expanded picture of cloud formation and suggest that additional types of information are needed to develop an ability to relate cloud droplet number concentration (and cloud albedo) to the

gases and aerosols in an increasingly anthropogenically perturbed atmosphere. It is currently not possible to estimate with confidence even what fraction of the world's clouds are affected by such factors.

3.3 Traditional Köhler theory of cloud formation

The basis of the traditional Köhler theory is the equilibrium of a small, aqueous solution droplet with humid air. The equilibrium condition is equality of the chemical potential of water between the aqueous phase and the vapor phase adjacent to the droplet surface (12). That condition may be expressed in terms of a relation between the ambient water saturation ratio S (relative humidity divided by 100%) and the droplet radius r:

$$S = a_w \exp\left[\frac{2\sigma\bar{v}_w}{R_g T r}\right] \tag{3.1}$$

where σ is the droplet solution surface tension, $\bar{v}_w$ is the partial molar volume of water in solution, R_g is the universal gas constant, T is temperature, and a_w is the water activity of the solution. For aqueous solutions,

$$a_w = \exp\left[-\frac{M_w \nu \Phi m}{1000}\right] \tag{3.2}$$

where M_w is the molecular weight of water, ν is the total number of ions produced by dissociation of one molecule of solute, Φ is the practical osmotic coefficient of the solution, and m is the solution molality. The product $\nu\ \Phi$ is often replaced by the van't Hoff factor i. An approximation frequently made is that the solution is dilute ($\Phi = 1$) (13), although this assumption does introduce some error (14). This error primarily affects the larger nuclei, since their molalities are higher at activation than smaller nuclei.

The presence of solute acts to lower the vapor pressure of water, while the droplet curvature tends to increase it (the latter being the so-called Kelvin effect and the former the so-called Raoult effect). The vapor pressure increase owing to droplet curvature is approximately proportional to the inverse of the droplet radius, and the vapor pressure reduction attributable to the solute is proportional to the inverse of droplet volume.

Expressing S as a function of droplet radius for a given initial salt crystal, one obtains an equilibrium curve (a "Köhler" curve) that increases steeply when S <1 and goes through

a maximum at some S above unity, the critical supersaturation, S_c (Figure 3.1). Droplets of radii left of S_c are intrinsically stable. The situation is fundamentally different to the right of the Köhler maximum. If the ambient S exceeds S_c, the droplet grows and then has its surface value of $S < S_c$, such that there is a gradient of water vapor causing water to diffuse to and condense on the droplet. As it grows, this effect accelerates, resulting in spontaneous growth.

When the ambient saturation ratio, S, crosses the critical supersaturation, S_c, of a given droplet and rapid condensation starts, according to traditional theory the droplet is said to be activated. According to traditional Köhler theory, atmospheric cloud formation takes place when S starts crossing the critical supersaturations of particles in the air. According to equilibrium theory, droplets formed on the largest salt crystals activate first, followed by activation of droplets containing less and less solute. The driving force for the increase of S is cooling caused usually by adiabatic expansion of rising air or by radiation.

Condensational depletion of water vapor and release of latent heat of condensation slow down the increase of S, and at some point (altitude) S reaches a maximum (Figure 3.1). In principle, all droplets with critical supersaturations below the maximum value of S achieved can activate to cloud droplets, although the diffusional growth of droplets may be sufficiently slow that all droplets with critical supersaturations below the maximum S will not have time to activate (11). The maximum value of S achieved in rising air, as well as the number, N, of activated droplets, thus results from a competition between the ambient cooling rate and condensational depletion of water vapor, which is affected by the number concentration, size distribution, and composition of the aerosol particles present.

3.4 Extended Köhler theory and its implications

Classical Köhler theory addresses activation of soluble salt particles. (It can be applied straightforwardly to include an insoluble solute as well.) Including the effects of soluble gases and partially soluble solutes gives the following expression for the equilibrium water saturation ratio (15),

$$S = \exp\left(\frac{2\sigma\bar{v}_w}{R_g T r} - \frac{i_s n_s}{n_w} - \frac{i_v n_v}{n_w} - \frac{i_{ss} n_{ss}}{n_w}\right) \tag{3.3}$$

where n_w, n_s, n_v, n_{ss} are the numbers of moles of water, soluble salt, soluble gases, and

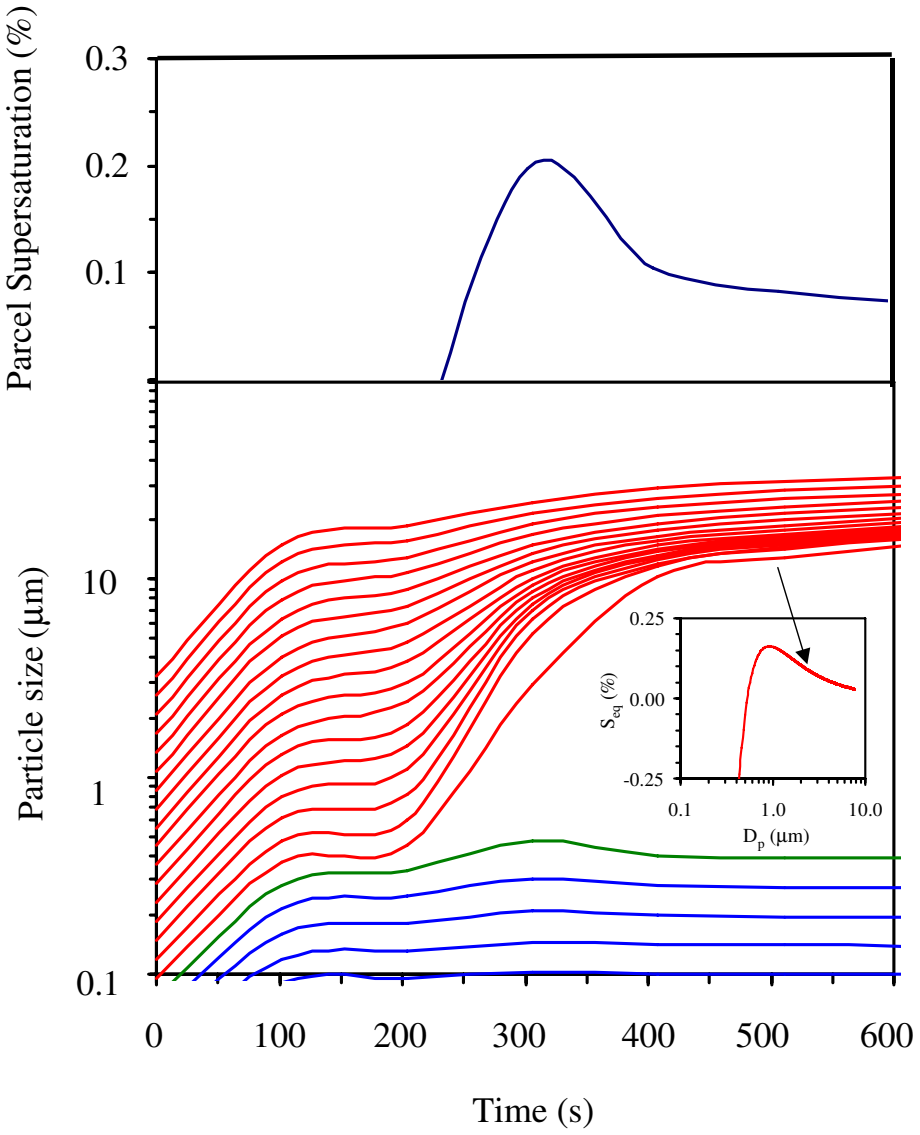

Figure 3.1: Typical parcel supersaturation and droplet growth profiles for a rising adiabatic cloud parcel. In this calculation, the parcel rises with a velocity of 0.1 m s^{-1}. The aerosol in the parcel has a typical marine size distribution and is composed entirely of $(NH_4)_2SO_4$. The initial parcel conditions are 98% relative humidity, 800 mbar pressure, and 283 K temperature. Red curves correspond to particles that form cloud droplets. Blue curves represent particles with critical supersaturation too high to activate. The green curve corresponds to a particle that could activate but is not exposed sufficiently long to a supersaturation to cause activation. The particle with the smallest dry size that activates into a cloud droplet has a dry diameter of 0.095 μm; its corresponding Köhler curve is shown in the insert.

partially soluble species, respectively; i_s, i_v, i_{ss} are the corresponding van't Hoff factors (the dilute approximation has been taken). Here n_{ss} can be calculated from the solubility of the partially soluble substance (8), while n_v is determined by an equilibrium relation similar in form to Equation (3.1) and a mass balance between the gas and aqueous phases.

Nitric acid (HNO_3) is perhaps the most important highly soluble trace gas in the atmosphere. Ample data exist establishing the importance of nitrate as a constituent of cloud and fog water in polluted air (16). In the presence of a water-soluble trace gas such as HNO_3, as the gas condenses into the droplet, the amount of dissolved solute increases, and the critical supersaturation for that droplet is lowered (17). In theory, HNO_3 at very low mixing ratios, on the order of 1 ppb and less, can influence cloud formation. At 1 atm and 273 K, 1 ppb corresponds to 2.7×10^{10} molecules cm^{-3}, which is equivalent to the number of molecules in 6300 $(NH_4)_2SO_4$ particles with a diameter of 0.1 μm. Depending on how it is dispersed over the aerosol population, a minute amount of soluble material can exert a considerable effect on the number of activated droplets. Moreover, Hegg (18) has shown that for acidic aerosols, absorption of NH_3 can play an even more important role in modifying activation behavior than HNO_3.

Highly soluble trace gases are not the only compounds that can alter activation behavior. Recent measurements have shown that 20 to 60% of the carbon mass in fine atmospheric aerosols consists of water-soluble organic compounds (WSOC) (19). Traditional individual compound analysis has generally not been able to identify all of the WSOC mass. Using a combination of chromatographic separation, organic functional group analysis, and total organic carbon analysis, Decesari et al. (20) have completely identified WSOC in a variety of fog/cloud samples. Neutral/basic compounds were found to consist of polyhydroxylated aliphatic compounds (mainly polyols and sugars). Mono- and dicarboxylic acids were principally hydroxylated aliphatic compounds, and polyacids were unsaturated compounds, both aliphatic and aromatic, with a minor content of hydroxyl groups.

Many organic aerosol compounds are surface active, and their presence can significantly affect the surface tension of cloud droplets (8). Lowering of surface tension owing to organic compounds will influence droplet activation and growth (21). Figure 3.2 shows measured decrease in surface tension of cloud/fog water samples, as a function of WSOC concentration (in terms of C). It is noteworthy that samples from completely different environments have been found to behave similarly with respect to surface tension lowering. Facchini et al.

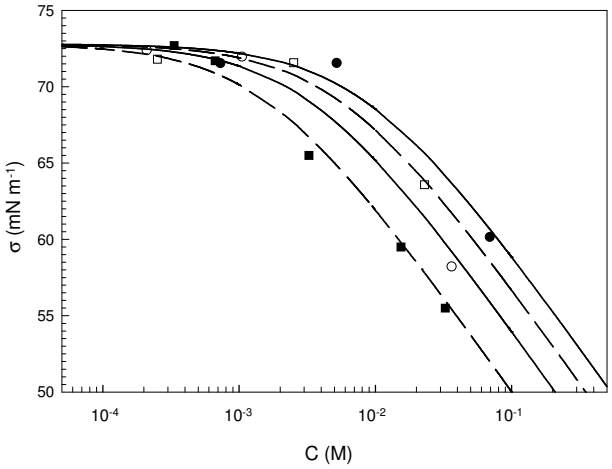

Figure 3.2: Surface tension decrease with respect to pure water as a function of water soluble organic carbon (WSOC) concentration (expressed as moles per liter of carbon) of cloud/fog water samples collected at Tenerife (Canary Islands) and in the Po Valley (Italy). The observed data are fitted by the empirical Szyszkowski-Langmuir equation (9), $\sigma = K - \beta T \ln(1 + \alpha C)$, where $K = 72.8$ kN m^{-1}, and C is the WSOC concentration (mol C L^{-1}). The values of the empirical parameters, β and α, are $\beta = 87$ kN m^{-1} K^{-1} and α(L mol^{-1}) is 179.9 for Po Valley 1, 628.1 for Po Valley 2, 302.1 for Tenerife 1, and 888.9 for Tenerife 2. Uncertainty associated with surface tension measurements is less than 0.5%, while WSOC concentration uncertainty does not exceed 4%.

(21) have shown that in the case of Po Valley fog water the polycarboxylic acid fraction (22) exhibits the most pronounced surface active behavior: four times higher than the mono- and dicarboxylic acid fraction and one order of magnitude higher than the neutral compound fraction. Dynamic surface tension measurements (23) of Po Valley fog samples indicate that the surfactants present are mainly soluble substances rather than insoluble film-forming ones (21).

For a particle of given dry size comprised of a mixture of insoluble and completely soluble salts, Köhler theory predicts that the critical supersaturation, S_c, increases with increasing mass fraction of the insoluble portion, that is, it is more difficult to activate the droplet. Similarly, when the solute is a mixture of partially and completely soluble substances, S_c increases with increasing mass fraction of the partially soluble substance, with its solubility determining the magnitude of S_c. If the surface tension of the droplet decreases as the substance dissolves, then S_c decreases. Thus, the presence of a partially soluble surfactant gives rise to two competing effects on the critical supersaturation: a decrease in S_c because

of the lowering of surface tension and an increase in S_c because not all the solute is dissolved in the aqueous phase. An overall decrease in S_c implies activation of more particles from a given aerosol distribution; if more particles compete for the available water vapor, the effective radius of the droplet distribution decreases, and the optical depth and albedo of the resulting cloud increase.

Whether cloud albedo actually increases or decreases in the presence of partially soluble substances, relative to that of a cloud formed on aerosol of a completely soluble solute of the same size distribution, depends on the relative magnitudes of the "surface tension" and "insolubility" effects. When insolubility effects dominate, the effective radius of the cloud droplets increases (because the same amount of liquid cloud water condenses on fewer droplets); when surface tension (and soluble gas) effects dominate, the reverse is true. Shifting the aerosol activation spectrum towards higher critical supersaturations increases the maximum S achieved in the cloud because fewer particles activate; this decreases the rate of water absorption in the early stages of cloud formation. In such a case, the ambient S increases accordingly until enough particles eventually activate to consume the available water vapor. The reverse effect occurs when the activation spectrum is shifted towards lower S_c, namely particles activate earlier, depressing the maximum value of S achieved in the cloud.

3.5 Effects of a soluble gas (HNO_3) on cloud formation

Figure 3.3 shows the behavior of ambient relative humidity (RH) during the simulated development of a radiation fog (a cloud formed at a low cooling rate) at two levels of ambient HNO_3. The "clean" case (HNO_3 = 0.1 ppb), the blue curves, exhibits a clear maximum in RH exceeding 100%, and thus the droplets are activated in the traditional sense. In the "polluted" case (HNO_3 = 30 ppb), the red curves, there is no RH maximum, but only an asymptotic limit of 100%. The droplet size distributions are shown after roughly ½ hour. The "clean" fog droplet concentration is 79 cm^{-3}; the "polluted" concentration is 166 cm^{-3} (24). Interestingly, in the polluted case the initial aerosol divides into two distributions, particles that do not grow substantially (not shown) and those that do, despite the fact that the ambient RH does not exceed 100%. This behavior is not in accordance with traditional Köhler theory and is a result of regions of unstable equilibrium arising because of the

dissolving HNO_3. Such behavior is not unique to nitric acid; it can arise in the presence of any highly soluble gas. Practically all of the more hygroscopic accumulation mode particles, as well as some of the less hygroscopic ones and more hygroscopic Aitken mode particles, "activate" in the polluted case. In the clean case, under the conditions considered here, only about one-half of the more hygroscopic accumulation mode particles activate.

Qualitatively similar behavior to that in Figure 3.3 can occur at lower HNO_3 mixing ratios, especially if other sources of soluble species are available, including NH_3, HCl, SO_2 + oxidants, organic acids in the gas phase, and partially soluble solutes instead of insoluble material (25).

A striking consequence of the presence of a soluble trace gas is that clouds or fogs with micrometer-sized droplets may exist even though the droplets have not undergone traditional activation and even though the ambient RH never exceeds 100%. Significant features of such "pollution clouds" compared with "clean clouds" are a higher droplet number concentration and a broader droplet size distribution.

One recent study reports a set of data that indicate the existence of substantial numbers of large fog droplets under conditions that are polluted but subsaturated (26). Using an instrumental method that measures the aerosol particle size associated with each droplet size class in clouds and fog, Frank et al. (26) show ambient droplet diameters as a function of the dry particle size. In an orographic cloud, they found droplets much larger than the critical size, up to a factor of ten. However, in a polluted fog, they found droplets that were of an order half the critical size. Importantly, these droplets were not tiny and had radii ranging up to 5 μm. The polluted fog had a much wider droplet spectrum than a traditional activated cloud, in accordance with the results shown in Figure 3.3. Additional data would be needed to reveal how often such "sub-activated" clouds and fogs exist and what the solutes are in them; however, these observations support the theory of the existence of clouds without supersaturation. Indeed, without data such as these, clouds or fogs that are dominated by unactivated droplets are visually indistinguishable from activated clouds. However, as will be seen below, differences in the droplet populations generated by subtle differences in thermodynamic state can lead to climatically significant changes in cloud albedo [see also (27)].

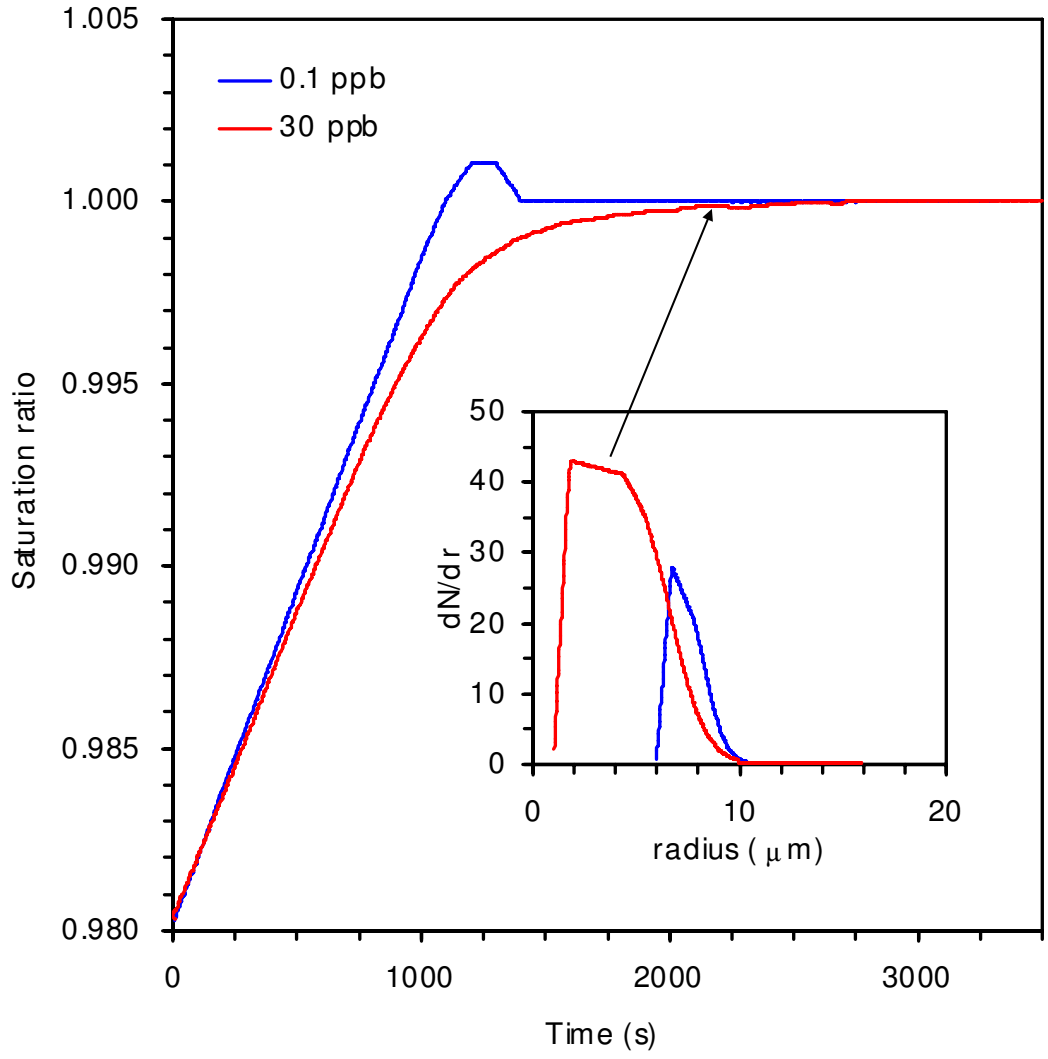

Figure 3.3: Ambient saturation ratio in two fog simulations, with gas-phase HNO_3 mixing ratios of 0.1 and 30 ppb, the former a "clean" case and the latter corresponding to polluted conditions. The ambient cooling rate is 1 K h^{-1}, corresponding to observations of radiative cooling during fog formation (32). Initial relative humidity is 98%, and initial aerosol size distributions are log normal, consisting of two modes, each having two submodes. Particles consist of ammonium sulfate and insoluble material, as discussed by Kulmala et al. (26). Values are shown in Table 3.1.

3.6 Alteration of cloud optical properties

It has been demonstrated that the presence of highly soluble gases, as well as insoluble and partially soluble aerosol substances, including those that alter the surface tension of the growing droplet, alter cloud formation in important ways. From a climatological point of view, an essential question is, what is the potential of these phenomena to affect cloud optical properties?

To examine this question quantitatively, we simulate cloud albedo and droplet number concentration relative to a base case in which the cloud is formed from an aerosol composed exclusively of soluble salt in the absence of volatile or partially soluble species. An adiabatic cloud parcel model (12) with explicit aerosol microphysics is a standard way to simulate cloud droplet formation, and we use such a model here (28). The resulting difference in cloud albedo, ΔR, for a cloud of given depth is a direct measure of activation effects on the optical properties of a cloud (29). Since albedo is a function of cloud depth, we calculate ΔR over a range of cloud depths and report the maximum magnitude (positive or negative) of ΔR, denoted ΔR^*. An absolute magnitude of ΔR^* exceeding 0.005 can be considered to be climatologically important; such an albedo change at a global scale could produce a change in radiative forcing comparable in magnitude to that currently estimated for anthropogenic indirect aerosol radiation forcing (9).

Figure 3.4 shows the predicted maximum albedo changes under typical convective marine cloud conditions. The presence of an insoluble core in the below-cloud aerosol can have a significant impact on cloud optical properties, particularly for weak updrafts. Although the maximum cloud supersaturation increases because the presence of an insoluble core increases the critical supersaturation of the aerosol, this increase in cloud supersaturation is not sufficient to compensate for the decrease in the number of cloud droplets formed, and the albedo actually decreases. As updraft velocity increases, cloud supersaturation increases, compensating more and more for the larger S_c of the droplets to the point where, for the conditions considered, the two effects essentially cancel each other out.

The presence of a water-soluble organic component in the marine aerosol, in the absence of any effect on surface tension, alters the activation behavior of the aerosol by adding solute to the aqueous phase as the droplet grows. This additional solute compensates for the decreasing inorganic fraction. As a consequence, the activation behavior of the aerosol, for

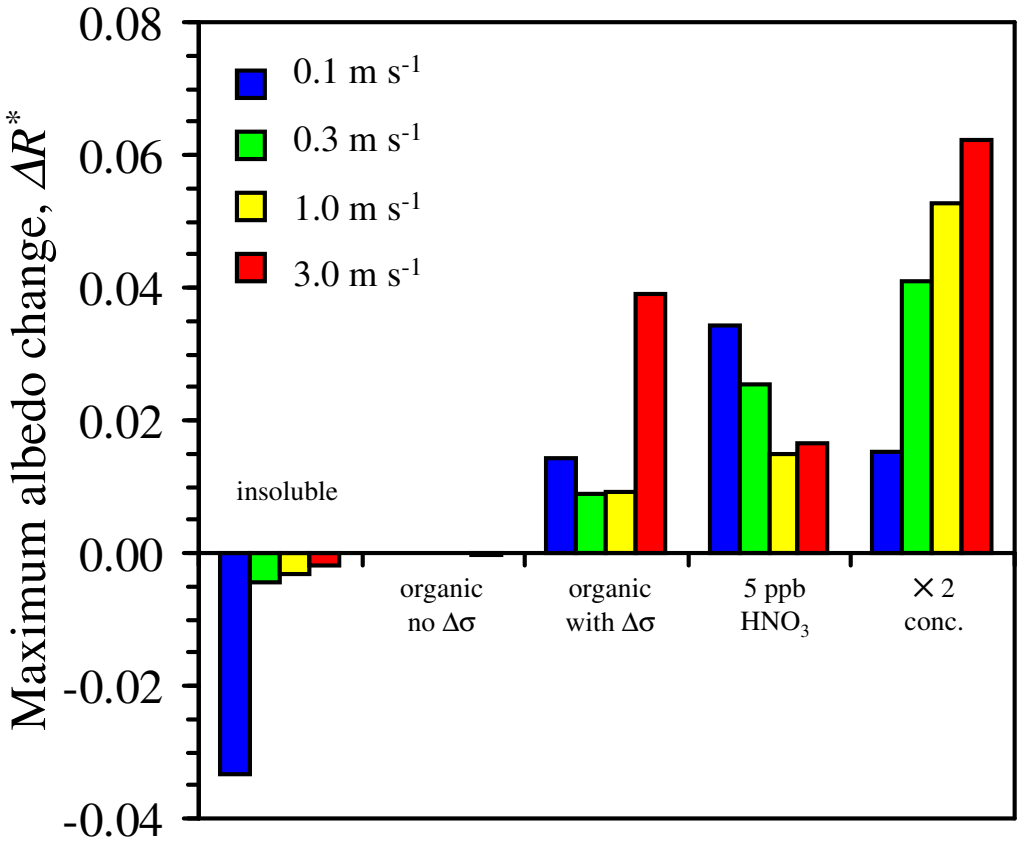

Figure 3.4: Maximum albedo difference with respect to the baseline simulation, for a convective marine cloud, (a) CCN containing 10% by mass insoluble material, (b) CCN containing 10% by mass of water-soluble organic carbon (no surface tension effects), (c) CCN containing 10% by mass of water-soluble organic carbon (with surface tension effects), (d) completely soluble inorganic aerosol, initial gas-phase HNO_3 at 5 ppb, and (e) completely soluble inorganic aerosol, with concentrations doubled. The organic fraction is assumed to be composed of 18% (by mass) levoglucosan ($C_6H_{10}O_5$, molar mass = 0.162 kg mol^{-1}, density = 1600 kg m^{-3}, van't Hoff factor = 1), 41% (by mass) succinic acid ($C_6O_4H_6$, molar mass = 0.118 kg mol^{-1}, density = 1572 kg m^{-3}, van't Hoff factor = 3), and 41% (by mass) fulvic acid [Suwanee River certified FA standards, US Geological Survey, Report 87-557, 1989] ($C_{33}H_{32}O_{19}$, molar mass = 0.732 kg mol^{-1}, density = 1500 kg m^{-3}, van't Hoff factor = 5).

the conditions of this simulation, does not substantially differ from that of pure ammonium sulfate. If surface tension is lowered in addition as the substance dissolves, S_c is further decreased in all of the particles, and the number of particles that can activate at any given supersaturation increases. For all updraft velocities, the number of activated droplets increases, and $\Delta R^* > 0$. Hence, when water-soluble organic carbon is present, its effect is of climatic importance regardless of updraft velocity.

The presence of HNO_3 dissolving in the droplets acts to increase the number of activated particles. For the conditions considered, at low HNO_3 levels (0.5 ppb), the relative increase in droplet number, $\Delta N/N_{base}$, ranges between 0 and 15%, increasing to 18 to 50% at $HNO_3 = 5$ ppb. Such an increase in droplet number concentration leads to a large, positive ΔR^*. The effect is most pronounced for weak updrafts when fewer droplets are formed; the available HNO_3 is partitioned amongst fewer droplets, so the amount of solute per droplet is larger. That the soluble gas effect is strongest for weak as opposed to strong updraft velocities is an important difference between condensable gas and other effects. Furthermore, at weak updraft velocities the timescale of the cloud activation process is longer, giving the soluble gas more time to diffuse to the droplets. As a result, the total amount of soluble material dissolved by the time activation ceases is larger.

Simply doubling the aerosol number concentration (the "Twomey effect") has a significant influence on both ΔN (not shown) and ΔR^*. It is interesting to note that doubling aerosol particle number concentration does not double droplet number concentrations; this behavior is a consequence of the nonlinear response of cloud parcel maximum supersaturation to changes in the aerosol size distribution. For the conditions considered here, $\Delta N/N_{base}$ ranges between 30% (for an updraft velocity of 0.1 m s^{-1}) and 85% (for 3 m s^{-1}). Maximum S drops roughly the same amount for all updraft velocities, between 21 and 25%.

Compared to marine clouds, activation effects under polluted conditions are much stronger, and all are of a climatically significant magnitude (Figure 3.5). An unexpected feature of the polluted case is that the presence of insoluble substances in the droplets leads to significantly smaller values of albedo and droplet number concentration changes than when those substances are partially soluble. This behavior is in marked contrast to the marine cloud case, in which ΔR^* and ΔN are maximum when the core is insoluble. The reason for this difference lies in the behavior of the maximum cloud supersaturation. While, for the conditions considered, S_{max} in the marine case increases by 1.9% when the aerosol

contains an insoluble core, S_{max} increases by as much as 43% under polluted conditions. In the presence of insoluble material, the polluted CCN spectrum shifts dramatically toward higher critical supersaturations. Because of this, very few particles absorb water at low supersaturations; only much later within the cloud, where S_{max} is considerably higher than when the core is entirely soluble, do enough particles activate so that S_{max} begins decreasing. Because S_{max} attains much higher values, particle sizes that normally would not activate do so. Still, not as many activate as in the totally soluble base case, and cloud albedo decreases. If the core is soluble, however, considerably more particles start absorbing water in the early stages of cloud formation. As a result, S_{max} does not increase as much as when the core is totally insoluble (for the conditions examined here about 14%, for a solute mass fraction of 0.5), and this is not sufficient to activate as many droplets as for the insoluble core. As a consequence, $\Delta R^* < 0$ also, and the albedo decrease is much larger than in the presence of an insoluble substance.

The increase in cloud albedo because of the presence of a condensable gas (HNO_3) is of lesser magnitude in the polluted case than under marine conditions. This difference is a consequence of the typically larger number concentration of particles present under polluted conditions, so that less solute condenses per particle. In continental clouds the total concentration of different acids and ammonia can be sufficiently high that the effect on albedo is very important (30), even more significant than under marine conditions.

Cold temperatures significantly enhance the soluble gas effect (7, 31). The colder the temperature, the lower is the absolute H_2O vapor concentration and the slower its diffusion to droplets. Consequently, a soluble gas has more time to dissolve during the cloud activation, leading to a larger amount of solute per droplet and increased activation compared with warmer conditions. Therefore middle-level clouds, such as altocumulus and altostratus, are potentially susceptible to the HNO_3 effect.

Most of the phenomena described above and summarized in Figure 3.5 for convective clouds are also prevalent in stratus clouds. At higher cooling rates, if 10% of the particle mass is insoluble, there are negligible effects on cloud albedo in both clean and polluted cases; not surprisingly, at 50% insolubility, effects on albedo are significant. Partial solubility can lead to compensation for the loss in activated droplet numbers as a result of the insolubility of the core, and if partial solubility is accompanied by surface tension lowering, then the loss of droplet number can actually be reversed, leading to an increase in cloud

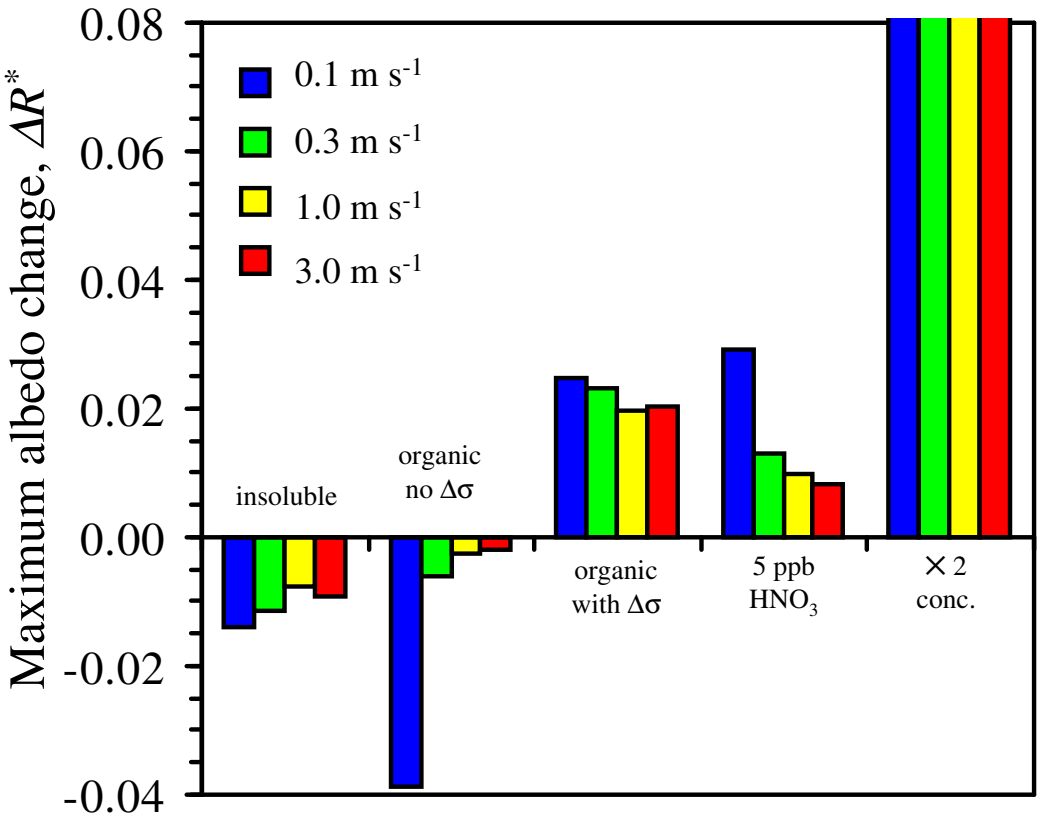

Figure 3.5: Maximum albedo difference with respect to the baseline simulation, for a convective urban cloud, (a) CCN containing 50% by mass insoluble material, (b) CCN containing 50% by mass of water-soluble organic carbon (no surface tension effects), (c) CCN containing 50% by mass of water-soluble organic carbon (with surface tension effects), (d) completely soluble inorganic aerosol, initial gas-phase HNO_3 at 5 ppb, and (e) completely soluble inorganic aerosol, with concentrations doubled. The organic fraction is assumed to be the same as for Figure 3.4.

albedo. At very low cooling rates, even 10% solute insolubility can lead to substantial effects on cloud optical properties. This is because the maximum supersaturation achieved in the cloud is so low that minute changes in activation behavior have a substantial effect on the number of droplets. As in the convective cloud case, the presence of a condensable gas leads to an increase of cloud albedo, at levels that are, in almost all cases, climatically important.

The effect of partially soluble surface-active organic species on CCN activation (and its subsequent effect on cloud albedo) depends on the concentration of the organic species, when the droplet is on the verge of activation. This concentration can be expressed in terms of the organic solubility and dry mass fraction (Figure 3.6). At the $\Delta R^* = 0$ line in Figure 3.6, the solubility and surface tension effects exactly compensate for each other, and the aerosol behaves as if it were composed of $(NH_4)_2SO_4$. To the left of this line, the presence of the organic is not sufficient to compensate for the decreased amount of inorganic solute, and cloud albedo decreases. To the right of the line, the reverse is true. At solubilities below 10^{-4} M, the substance behaves essentially as if it were insoluble. Depending on the organic mass fraction, at solubilities between 10^{-4} and 10^{-2} M, surface tension effects substantially change cloud optical properties, and climatically significant changes (compared to the baseline case) occur when solubility exceeds about 10^{-3} M. The change in surface tension when the droplet is close to its activated size governs the extent of the effect. This change, in turn, is a function of the dissolved organic concentration, which is maximum when the volume of water in the droplet is precisely that to completely dissolve the substance. Because of this, beyond about 10^{-2} M, increasing solubility does not have an additional significant affect on cloud albedo.

3.7 Conclusions

To assess the importance of the indirect climatic effect of aerosols, one seeks a reliable connection between cloud droplet population and a prognostic variable from global aerosol models. We have addressed here the question of how much of that connection might depend upon physical and chemical cloud activation effects, including variations in aerosol chemical composition, solute water solubility, solute surface tension lowering, and condensation of gaseous solutes. Lack of data on these activation effects poses additional uncertainty beyond

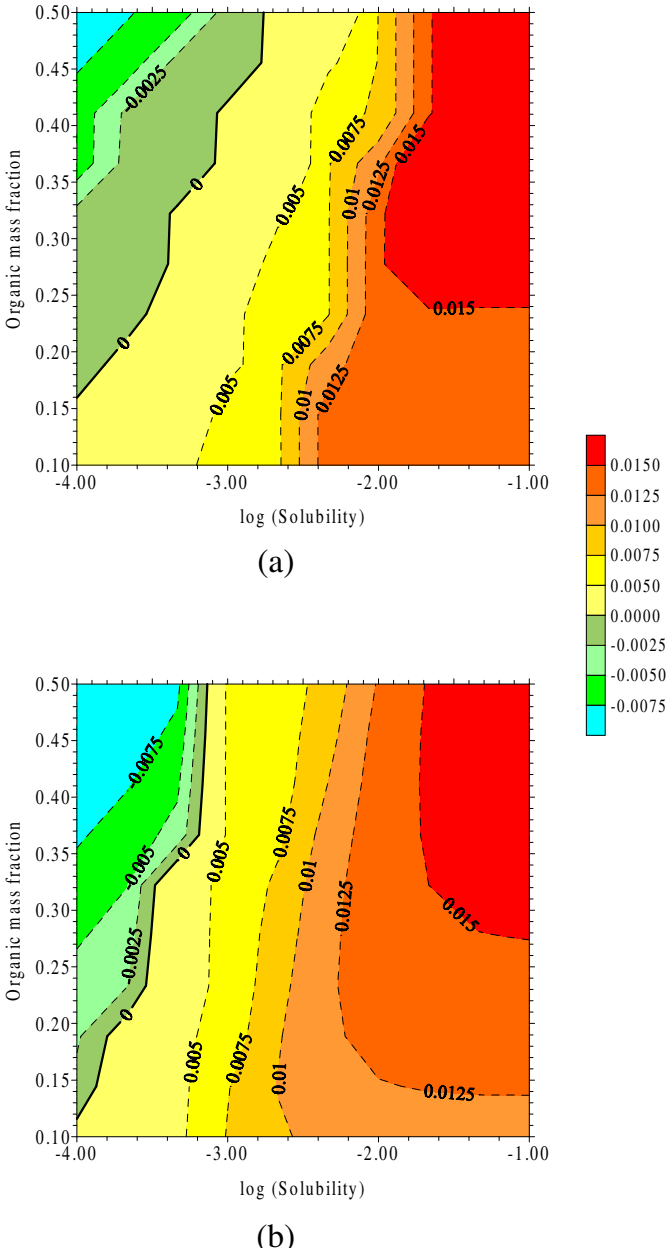

Figure 3.6: Isopleth contours of maximum albedo difference with respect to the logarithm of solubility (moles L^{-1}) and organic mass fraction of aerosol. Surface tension effect is as described in the caption of Figure 3.2. The organic fraction is assumed to be the same as for Figure 3.4. Marine (a) and urban (b) convective clouds with an updraft velocity equal to 1 m s^{-1} are assumed in these calculations.

that already recognized by the IPCC, making the largest uncertainty in calculating climate forcing even larger. However, we also can identify possible causes for the observed variations in ambient observations of cloud droplet and aerosol parameters.

The presence of insoluble substances in atmospheric aerosol can have a substantial impact on cloud droplet number, the fraction activated, and cloud albedo. The presence of partially or completely soluble substances, accompanied by surface tension lowering, can lead to significant effects as well. Generally speaking, the lowering of surface tension associated with a dissolving substance has a stronger effect on cloud properties than the fact that the substance itself is only partially soluble, given that a majority of these substances are surface-active. All activation effects exhibit strong dependence on the magnitude of updraft velocity. The dissolution of a soluble gas like HNO_3 during cloud formation can have a large impact on cloud droplet number concentration, the fraction activated, and cloud albedo. In contrast to the other activation effects, higher updraft velocities (and, as a consequence, higher droplet concentrations) diminish this effect; the reason for this is that less solute is introduced per droplet, because of both increased droplet concentration and a shorter activation period.

For typical marine clouds, climatically important effects can result from the presence of insoluble solutes, partially soluble surfactants, and condensable gases. For more anthropogenically perturbed conditions, all activation effects are potentially of climatic significance.

As predicted by Köhler some 80 years ago, droplet activation constrains the supersaturation of water vapor that can be reached in the atmosphere, which depends on the amount and chemical composition of the solute in the underlying aerosol population. Given sufficient solute or enough depression of surface tension (or a combination of the two), the supersaturation achieved in a given atmospheric physical cooling situation will decrease. At high levels of aerosols and gas solutes and for low cooling rates, strict activation is not necessary for the formation of a visible cloud; indeed, a continuum exists from ambient aerosol to wetter and wetter particles to unactivated clouds to activated ones. What is seen in the atmosphere as "cloud" can, in reality, be a collection of large numbers of droplets ranging from fully activated to unactivated. "Haze" particles, generally considered tiny interstitial aerosol particles among fully mature, activated cloud droplets, can, indeed, be as large as the activated cloud droplets themselves. While traditional CCN consist of high solubility

solutes as envisaged by Köhler (like NaCl in trade wind cumuli), it is becoming increasingly clear that the presence of other solutes in anthropogenically influenced regimes can exert effects on cloud droplet number concentration and cloud albedo of major significance.

Table 3.1: Initial aerosol size distributions and chemical composition used for the simulations in Figure 3.3

Median r (nm)	σ_g	N (cm^{-3})	Soluble fraction
30	1.35	600	0.05
30	1.35	400	0.3
100	1.60	150	0.05
100	1.60	350	0.3

3.8 References and notes

1. Reference [76]
2. Aristotle, "Meteorologica" (ca. 340 B.C.) reviewed and excerpted in [44].
3. Reference [9]
4. References [86, 87]
5. Reference [108]
6. Reference [142]
7. References [90, 93]
8. Reference [145]
9. Reference [36]
10. Reference [109]
11. References [77, 117]
12. Reference [143]
13. Reference [164]
14. Reference [16]

15. Reference [89]

16. References [50, 51, 32]

17. Additional solute derived from the gas phase may also result from aqueous-phase chemical reactions involving species absorbed by the droplets. [109] show that in the presence of SO_2, H_2O_2, O_3, and NH_3, at SO_2 levels of 20 to 40 ppb, the sulfate mass in the droplets may be increased tens to hundreds of percents at relative humidities of 95 to 99%.

18. Reference [64]

19. References [141, 165, 35, 129]

20. Reference [30]

21. Reference [34]

22. The molecular structure of polycarboxylic acids identified in aerosol and cloud water appears related to that of humic substances. Surface tension depressions caused by fulvic acid in solution [20] agree with those observed in ambient cloud/fog water samples (Figure 3.2).

23. Reference [100]

24. The enhancement of droplet concentration in the presence of HNO_3 occurs by a more traditional route in clouds formed at higher cooling rates. In that case the ambient S exhibits a clear maximum, and the droplets are activated. The presence of HNO_3 leads to enhanced droplet concentrations because smaller droplets acquire higher HNO_3 concentrations than do larger droplets in the limited time before activation takes place.

25. Reference [104]

26. Reference [41]

27. Reference [4]

28. Cloud optical properties depend on cloud thickness, cooling rate, volatile gas concentration, and aerosol size distribution. In convective clouds, cloud thickness affects both optical depth and the vertical transit time of air parcels; we consider values ranging from 10 to 1000 m. Updraft velocity influences both the transit time and the maximum S in a cloud updraft; we consider updraft velocities of 0.1, 0.3, 1, and 3 m s^{-1}. For stratus cloud simulations we consider cooling rates of –8.6 and –86.4 K d^{-1}. Simulations are carried out until the cloud liquid water content reaches the typical value of 0.1 g m^{-3}. We consider the marine (pristine) and urban tri-modal lognormal aerosol size distributions of [160]. The inorganic fraction is composed of $(NH_4)_2SO_4$, while the organic fraction is assumed to be composed of 18% (by mass) levoglucosan ($C_6H_{10}O_5$, molar mass = 0.162 kg mol^{-1}, density = 1600 kg m^{-3}, van't Hoff factor = 1), 41% (by mass) succinic acid ($C_6O_4H_6$, molar mass = 0.118 kg mol^{-1}, density = 1572 kg m^{-3}, van't Hoff factor = 3), and 41% (by mass) fulvic acid [158] ($C_{33}H_{32}O_{19}$, molar mass = 0.732 kg mol^{-1}, density = 1500 kg m^{-3}, van't Hoff factor = 5). Surface tension is given by the "Po Valley 2" data in Figure 3.2. Pressure and temperature are initially set at 800 mbar and 273 K, respectively.

29. Cloud albedo is calculated based on the two-stream approximation of a non-absorbing, horizontally homogeneous cloud [94]: $R = \tau/(7.7 + \tau)$, τ = cloud optical depth,

$$\tau = \int_0^H \frac{3\rho_a w_L(z)}{2\rho_w r_{\text{eff}}(z)} dz$$

where $w_L(z)$ = liquid water mixing ratio at height $z$in the cloud column, ρ_w and ρ_a are water and air densities, and $r_{eff}(z)$ is the cloud droplet distribution effective radius.

30. Reference [88]

31. Reference [92]

32. Reference [133]

Chapter 4

Can chemical effects on cloud droplet number rival the first indirect effect?

Note: This chapter appeared as reference [114].

4.1 Abstract

An increase in cloud droplet number concentration resulting from an increase in ambient aerosol (and subsequent albedo increase) is typically identified as the first indirect (or "Twomey") climatic effect of aerosols [156]. A key question is whether chemical effects (dissolution of soluble gases and slightly soluble substances, surface tension depression by organic substances and accommodation coefficient changes) could potentially rival changes in droplet number from changes in aerosol number concentration. We assess the sensitivity of cloud droplet number concentration to such chemical factors, using a cloud parcel model. We find that numerous conditions exist, for which chemical influences on cloud droplet activation can indeed rival the Twomey effect.

4.2 Introduction

Anthropogenic influences on cloud properties, better known as indirect climatic effect of aerosols, could constitute a major climate forcing [76]. A major challenge is to predict global cloud droplet number, N_d, from the precursor aerosol. While it is commonly assumed that the most important aerosol parameter influencing N_d is aerosol number concentration,

N_a, we present cases for which (unaccounted) chemical factors resulting from anthropogenic activities, can produce variations in N_d comparable to those of the Twomey effect; if neglected, additional uncertainty can be introduced to current estimates of the aerosol indirect effect.

4.3 Chemical effects considered in this study

The chemical factors examined are the dissolution of soluble gases [90] and partially soluble solutes in the growing droplet [145], surface tension (σ) depression by dissolved organic substances [145, 36] and accommodation coefficient changes from the formation of organic films at the droplet surface [37]. Of all the water soluble gas-phase species, probably the most important is nitric acid (HNO_3), since it is ubiquitous and can be found in relatively large concentrations (e.g., [50]).

A water-soluble trace gas can provide enough solute to interstitial (or unactivated) cloud condensation nuclei (CCN) so that they transform into activated droplets. Partially soluble species can also contribute solute, but, compared to soluble salts, are usually less efficient; this tends to increase the critical supersaturation, S_c, and also may lead to complex equilibrium curves [145]. The highest S_c is seen when the species becomes effectively insoluble. Both insoluble and soluble substances can form films (in which the chemical composition differs from the bulk phase) so that the droplet σ, and thus S_c, decreases. We refer to these compounds as "surfactants" (although the usage of the term, in terms of the solubility, varies in the literature). Atmospheric compounds that exhibit significant surfactant behavior are usually water-soluble organic compounds (WSOC) [145]. Changes in the osmotic coefficient (often assumed to be 1.0) from dissolved species can also affect S_c, but is not addressed in this study. Finally, a change in the water vapor accommodation (or condensation) coefficient, α, will not necessarily affect droplet S_c, but can still strongly influence N_d by modifying the parcel maximum supersaturation, S_{max}.

As this study focuses on the aerosol-cloud droplet formation sensitivity, it is assumed that Köhler theory can be used to predict the CCN properties of the aerosol. Although this has been confirmed to within a reasonable degree for laboratory aerosol (e.g., [16, 17]), measurements of ambient aerosol can exhibit significant discrepancy between predicted and measured CCN concentrations, with a tendency towards overprediction for polluted

conditions [23, 17]. It is still unclear, however, how much of this discrepancy is a result of incomplete theory or instrumental biases.

4.4 Description of simulations

To examine the potential importance of chemical effects on N_d, we simulate N_d (using an adiabatic cloud parcel model with explicit aerosol microphysics, [117]) relative to a baseline case. The "Twomey effect" is assessed by calculating the change in N_d for a doubling of the baseline N_a. We then compare the Twomey effect to the change in N_d seen with no changes in size distribution (only chemistry).

N_d depends on updraft velocity (or cooling rate), U, soluble gas concentration, and aerosol size distribution and chemical characteristics. U varies between 0.1 and 3 m s^{-1}. To assess cloud droplet concentration, we employ the criterion used in [117], which is to find the CCN of highest S_c that strictly activates (i.e., exceeds its critical diameter); anything larger than this CCN is counted as a drop. Note that this definition accounts for mass transfer limitations: large CCN that have not attained their critical diameter are considered as droplets, but not those that deactivate and become interstitial aerosol. Droplet concentration is evaluated at 250 m above cloud base. The parcel pressure, temperature, and relative humidity are initially set at 800 mbar, 273 K, and 98%, respectively.

The aerosol is assumed to be an internal mixture of $(NH_4)_2SO_4$, organic, and an insoluble substance. The osmotic coefficient is assumed to be 1.0. The aerosol organic component is a simplification of chemical composition observed in the Po Valley fogs and is assumed to be composed of 18% (by mass) levoglucosan ($C_6H_{10}O_5$, density = 1600 kg m^{-3}, van't Hoff factor = 1), 41% (by mass) succinic acid ($C_6O_4H_6$, density = 1572 kg m^{-3}, van't Hoff factor = 3), and 41% (by mass) fulvic acid [158], ($C_{33}H_{32}O_{19}$, density = 1500 kg m^{-3}, van't Hoff factor = 5). As samples from completely different environments tend to exhibit similar behavior [19] we used the curve reported in [36] to describe the σ depression for all types of aerosol that contain WSOC. The organic mixture is assumed to be either completely soluble, or with solubility, Γ, varying between 10^{-4} and 10^{-1} M. When present, the film forming compound (FFC) follows the behavior proposed by [37], in which α has a low value when an film exists, and then attains a large value once the film breaks. The FFC is part of the insoluble fraction, and has a density of 1760 kg m^{-3}. Furthermore, α=10^{-5} when

the film exists, and 0.043, after the film breaks. The film exists when its thickness is larger than 0.5 nm. The insoluble fraction has a density of 1760 kg m^{-3}. [37] found that when the FFC is distributed according to the surface area of single mode lognormal aerosol, N_d is suppressed. This is still expected to hold for ambient aerosol, as the growth of CCN with high S_c are mostly affected in this configuration. [37] also presented simulations assuming that the FFC mass fraction is constant throughout the size distribution, and found that N_d is effectively unchanged. Given that their simulations do not contain many large CCN, we perform simulations with a constant mass fraction of FFC, for multimodal aerosol, to examine whether the inhibition of the growth of larger CCN would lead to an increase of droplet number.

At this point, we would like to clarify that the definition of film as used in [37] differs from the film that forms in any surfactant system; the former reflects the water vapor permeability, while the latter reflects a region adjacent to the surface with composition different from the bulk. Furthermore, in this work and the [37] study, it is assumed that the film is unconditionally stable, so that all of the FFC mass remains in the film. This configuration reflects the maximum possible influence of FFCs on droplet growth. Insoluble surfactants, which are candidate FFC, tend to form micelles in the aqueous phase (or precipitate) when present in quantities larger than that to form a few monolayers [113]. In this case, the film, depleted from FFC, would break and the CCN would resume rapid growth sooner. The actual fate of the FFC, and how that would influence the droplet thermodynamics and water vapor condensation kinetics are issues that need to be addressed in future studies.

The baseline case selected depends on the chemical effect examined. For α effects, the baseline is assumed to be 10% by mass insoluble for marine and 50% for urban aerosol; the remainder of the aerosol is assumed to be $(NH_4)_2SO_4$. For all other chemical effects, the baseline aerosol is assumed to be pure $(NH_4)_2SO_4$.

We consider the marine and urban tri-modal lognormal aerosol size distributions of [160] to represent pristine and polluted aerosol, respectively. The marine distribution mode diameters are 0.01, 0.071, 0.62 μm, their corresponding dispersions are 1.6, 2.0, 2.7 and the number concentrations are 340, 60, 3.1 cm^{-3}. The urban distribution mode diameters are 0.014, 0.054, 0.86 μm, their corresponding dispersions are 1.8, 2.16, 2.21 and the number concentrations are 106000, 32000, 5.4 cm^{-3}.

4.5 Sensitivity of cloud properties to chemical effects

Figures 4.1 and 4.2 show N_d normalized to the baseline N_d, as a function of U, for the pristine and polluted aerosol, respectively. The "Twomey" simulation is same as the pure $(NH_4)_2SO_4$ baseline, but with aerosol concentrations doubled. "HNO_3" is same as the baseline simulation, with 5 ppb HNO_3 in the gas phase, which is within measured values in plumes advected off the northeast United States (G.Huey, personal communication). The "Surface tension" corresponds to an aerosol composed of (by mass) 75% $(NH_4)_2SO_4$, and 25% organic. The organic is completely soluble, acts as a surfactant, and α=1.0. "Organic" is same as "Surface tension" simulation, without σ effects included. "Insoluble" corresponds to an aerosol composed 75% (by mass) $(NH_4)_2SO_4$, and 25% insoluble, and α=1.0. Finally, "Accommodation coefficient" assumes the aerosol contains 10% by mass FFC; an additional 40% by mass insoluble is assumed to exist in the polluted aerosol. The remaining mass is $(NH_4)_2SO_4$.

Between 7% (U=0.1 m s^{-1}) and 18% (U=3 m s^{-1}) of the aerosol activates in the pure $(NH_4)_2SO_4$ baseline case. The presence of insoluble material in the aerosol tends to increase the S_c of the particles, which results in a reduction of the water vapor condensation in the initial stages of cloud formation. As a result, the parcel tends to attain a higher S_{max} to compensate for any loss in droplets by activating CCN of higher S_c. The simulations for marine conditions show no change in N_d for weak updrafts, and a small decrease at stronger updrafts. Under urban conditions, the insoluble substance does not substantially change N_d regardless of U (for higher values of insoluble fraction, the change in cloud droplet concentration does becomes significant).

The presence of HNO_3 dissolving in the droplets can substantially increase N_d. The effect is most pronounced for weak updrafts because HNO_3 is partitioned amongst fewer droplets, and more time is allowed for the soluble gas to dissolve in the droplets. This results in a larger amount of HNO_3 dissolved per droplet, and large reductions in S_c. That the soluble gas effect is strongest for weak as opposed to strong updrafts is an important distinction from other chemical effects. Under urban conditions, the effect of HNO_3 on N_d is negligible because the amount of solute partitioned in each particle, and its subsequent effect on S_c, is small. One cannot conclude, however, that polluted clouds are never affected by soluble gas dissolution; important HNO_3 effects can be seen for moderately polluted aerosol

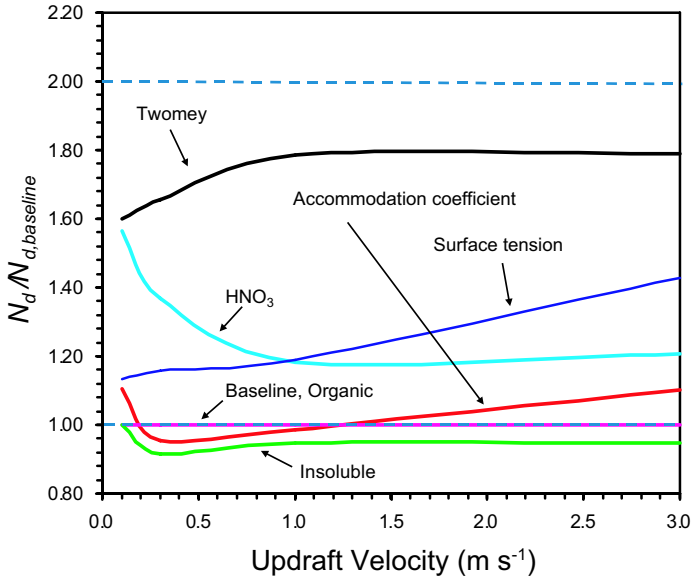

Figure 4.1: Droplet number concentration normalized to the baseline N_d, as a function of updraft velocity, for marine aerosol size distributions.

[88].

The presence of a WSOC, even if it does not act as a surfactant, alters the activation behavior of the aerosol by changing the moles of dissolved solute in each droplet. The organic mixture activation behavior is not substantially different from $(NH_4)_2SO_4$ and therefore the "Organic" simulation behaves identically to the baseline (for both marine and urban conditions). Once σ changes are introduced, N_d increases regardless of U. σ effects can be important for both marine and urban aerosol. For the marine distribution, the strongest effects are seen at high U, and for the urban, at low U. For the marine aerosol, the σ effect can become as much as 50% of the Twomey effect, while for the urban, σ effects can exceed the Twomey effect.

In Figures 4.1 and 4.2, we have assumed that the WSOC is completely soluble. Although the parameterization of WSOC concentration and σ corresponds to a highly complex mixture, it is possible that substances, not represented in the measurements, can decrease the WSOC solubility; this can potentially affect its ability to change droplet number and needs to be examined. This is done in Figure 4.3, which shows the fractional change in N_d with respect to the organic mass fraction, ε_o, and Γ. In these simulations, α is assumed to be unity, and the dissolved organic is assumed to decrease droplet σ.

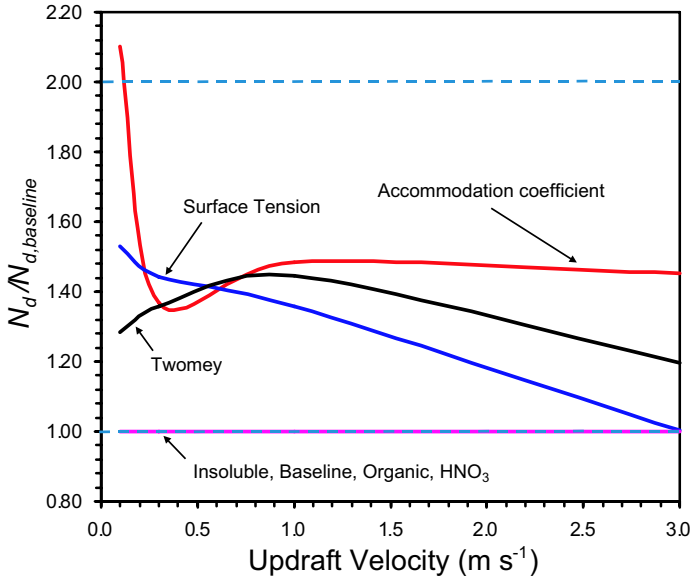

Figure 4.2: Same as Figure 4.1, but for the urban size distribution.

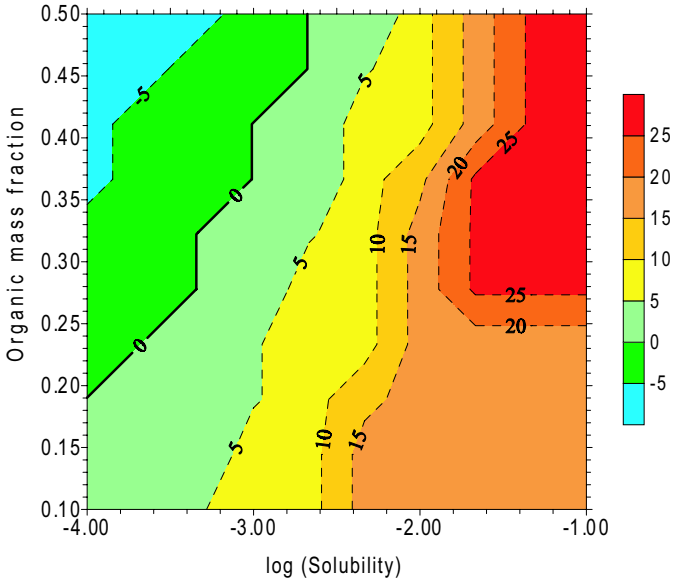

Figure 4.3: Isopleth contours of cloud droplet number concentration change (%) relative to the baseline simulation, with respect to the logarithm of solubility (moles L^{-1}) and organic mass fraction of aerosol. The σ effects are as described in the text. Marine conditions and an updraft velocity equal to 1 m s^{-1} are assumed in these calculations.

At the $\Delta N/N = 0$ contour, the effects from decreased inorganic solute and σ exactly compensate for each other, and the aerosol behaves (on average) as if it were composed entirely of $(NH_4)_2SO_4$. To the left of the $\Delta N/N = 0$ contour (Figure 4.3), dissolved organics do not compensate for the decrease in inorganic solute. Comparing the "Insoluble" simulation of Figure 4.1 with Figure 4.3, we can see that for $\Gamma < 10^{-4}$ M, the organic behaves as if it were insoluble. To the right of the line, overcompensation occurs. Depending on ε_o, larger values of Γ can notably increase N_d. The largest decrease in σ occurs when the volume of water in the droplet is precisely that needed to completely dissolve the organic; further solubility will not affect droplet formation. Indeed, by comparing "Surface tension" simulation from Figure 4.1 and 4.3, we see that $\Gamma > 5{\times}10^{-2}$ M displays the same effect on N_d. Thus, a significant decrease in the Γ will not significantly hinder the ability of WSOC to enhance droplet formation.

When α decreases, the rate of water absorption in the cloud decreases in the initial stages of its formation (since droplets do not grow as rapidly); this leads to a higher S_{max}. If α remained constant for all CCN (meaning that the film never breaks), the resulting effect would always be an increase in N_d, since all CCN are equally delayed in their activation (simulations indicate that for urban distributions, N_d can increase threefold from $\alpha = 1.0$ to 0.01, and tenfold from $\alpha = 0.01$ to 0.001, for U=1.0 m s^{-1}). However, when a threshold transition between a low and a high α is assumed, N_d can either increase or decrease, depending on how the film-forming substance is distributed throughout the size distribution. For the simulations carried out in this study, we can see that α effects are rather small for the marine aerosol. This conclusion is consistent with the simulations of [37], as the larger CCN are too few to have a significant impact on N_d. For the urban aerosol, on the other hand, the aerosol number is enhanced substantially, as the inhibition of the larger CCN growth significantly increases S_{max} and allows water vapor to condense on smaller particles.

4.6 Conclusions

Numerous conditions are found for which chemical effects on droplet activation can be significant when compared to the Twomey effect; in some cases, chemical effects can be even larger. All effects exhibit strong dependence on the magnitude of U. For WSOC, the lowering of σ is predicted to have a stronger effect on activation than its contribution to the

Raoult effect; thus, even though both effects need to be considered, uncertainties in the σ behavior of the aerosol may be more influential than uncertainties in the solute contribution alone.

The dissolution of a soluble gas during droplet formation can also have a large impact on N_d. In contrast to other chemical effects, higher U (and, as a consequence, higher N_d) diminish the impact of a soluble gas, as increased N_d and shorter dissolution times lead to less solute introduced per droplet.

If both surfactants and condensable gases are present, they can act synergistically to increase N_d, i.e., for dynamical conditions where one effect is negligible, the other can become influential. This is an important point: given that large variability in updrafts occurs in real clouds, it is quite possible that marine clouds affected by polltion can experience an even larger enhancement in N_d than previously thought. The influence of WSOC can be even larger if they are distributed according to the CCN surface area, since a larger mass of WSOC will be found on CCN with high S_c. Finally, if the aerosol contains a FFC, the resulting effect can have a substantial effect on N_d, either positive or negative.

4.7 Acknowledgments

A. Nenes and J.H. Seinfeld were supported by U.S. Office of Naval Research grant N00014-96-1-0119. We would also like to thank P.Y.Chuang and J.Snider for their important comments during the review process. Finally, we would like to acknowledge M. Mircea for helpful suggestions during the preparation of the manuscript.

Chapter 5

Impact of biomass burning on cloud properties in the Amazon Basin

Note: This chapter appeared as reference [135].

5.1 Abstract

We used a 1-D cloud parcel model to assess the impact of biomass-burning aerosol on cloud properties in the Amazon Basin and to identify the physical and chemical properties of the aerosol that influence droplet growth. Cloud condensation nuclei (CCN) measurements were performed between 0.15 and 1.5% supersaturation at ground-based sites in the states of Amazonas and Rondônia, Brazil, during several field campaigns in 1998 and 1999 as part of the Large Scale Biosphere-Atmosphere Experiment in Amazonia (LBA). CCN concentrations measured during the wet season were low and resembled concentrations more typical of marine conditions than most continental sites. During the dry season, smoke aerosol from biomass burning dramatically increased CCN concentrations. The modification of cloud properties, such as cloud droplet effective radius and maximum supersaturation, is most sensitive at low CCN concentrations. Hence, we could expect larger inter-annual variation of cloud properties during the wet season that the dry season

We found that differences between CCN spectra from forested and deforested regions during the wet season are modest, and result in modifications of cloud properties that are small compared to those between wet and dry seasons. Our study suggests that the differences in surface albedo, rather than cloud albedo, between forested and deforested

regions may dominate the impact of deforestation on the hydrological cycle and convective activity during the wet season. During the dry season, on the other hand, cloud droplet concentrations may increase by up to seven times which leads to a model-predicted decrease in cloud effective radius by a factor of two. This could imply a maximum indirect radiative forcing due to aerosol as high as ca. -27 W m^{-2} for a non-absorbing cloud. Light-absorbing substances in smoke darken the Amazonian clouds and reduce the net radiative forcing, and a comparison of the AVHRR analysis and our modeling studies suggests that absorption of sunlight due to smoke aerosol may compensate for about half of the maximum aerosol effect.

Sensitivity tests show that complete characterization of the aerosol is necessary when kinetic growth limitations become important. Subtle differences in the chemical and physical make-up are shown to be particularly influential in the activation and growth behavior of the aerosol. Knowledge of the CCN spectrum alone is not sufficient to fully capture the climatic influence of biomass burning.

5.2 Introduction

Biomass burning in the Amazon Basin [144] generates a smoke pall of variable density across millions of square kilometers during the dry season between June and December. A complex interaction among water vapor, cloud condensation nuclei (CCN) abundance, light absorption by "black carbon," and atmospheric stability affects the strength of convection and subsequent cloud development and cloud albedo. Measurements during the dry season reveal a stable spatial distribution of water vapor in contrast to the variability of aerosol concentrations [82]. Hence, the cloud optical properties in the Amazon dry season may be less dependent on variations of the meteorological conditions than those of CCN. Smoke aerosol dramatically increases CCN concentrations, which could lend to increased cloud droplet stability and cloud lifetime [10]. The influence of smoke on rain formation was also shown during the Tropical Rainfall Measuring Mission (TRMM) taken near Kalimantan, where a distinct difference in cloud structure and radar reflectance was seen between clouds influenced by biomass burning and those in cleaner areas. Clouds in cleaner areas had warmer and larger drops than the non-precipitating clouds affected by smoke [138].

AVHRR (Advanced Very High Resolution Radiometer) analysis during the 1987 biomass

burning season in the Amazon Basin also demonstrated the direct influence of smoke on cloud properties [79]. Their study showed that smoke particles reduced droplet size from 14 to 9 μm and increased the reflectance of thin to moderately thick clouds from 0.35 to 0.45. In a previous study, remote sensing of smoke and cloud properties over the Amazon Basin showed a similar decrease in effective droplet radius and a decrease in reflectance from 0.71 to 0.68 due to the absorption of sunlight by biomass-burning aerosol [81]. However, only the bright clouds that are strongly affected by biomass-burning aerosol were used in the analysis, thus obscuring the effects of CCN on cloud reflectance.

Effective cloud droplet radii have decreased by 10 to 15% in the Amazon Basin from 1985 to 1995 (AVHRR analysis by T. Nakajima, personal communication, 2000). The reduction in cloud droplet radii has been more significant during the wet season (i.e., 13.6 to 11.8 μm) compared to the dry season (i.e., 9.7 to 9.0 μm) and may be related to the rapid demographic and land-use changes in the Amazon Basin during this period. Recent studies of radar and satellite observations in the Amazon Basin have shed light on the roles of updraft and aerosol in influencing the maritime or continental behavior of clouds [162]; extreme cases were identified in which either the updraft or aerosol dominate cloud development. The aerosol is important because of its effect on droplet size and hence collision/coalescence processes. The updraft velocity is crucial because of its effect on the time available for coalescence, its ability to raise particles above the freezing level and subsequent generation of ice nuclei.

The motivation of our work is to assess the potential impact of human development in the Amazon Basin, and in particular the effect of smoke aerosol on cloud properties. Measured wet-season CCN spectra differ dramatically from dry-season spectra due to the presence of biomass-burning aerosol. In the following sections, we explore cloud droplet formation for measured CCN spectra in the Amazon Basin using a 1-D cloud parcel model with detailed aerosol microphysics. This model incorporates water vapor growth kinetics and is discussed in detail by [117]. Measurement uncertainties and approximations preclude an exact representation of the aerosol population; hence, we examine the dependence of cloud properties on the chemical and physical make-up of the aerosol in the form of a sensitivity analysis. The model calculations are should not be used for prognostic purposes, but to diagnose the sensitivity of droplet nucleation to changes in the CCN population. Expressing changes in droplet concentration in terms of changes in effective radius and albedo, give a

physically based measure of the importance of a, e.g., 1% increase in droplet number.

5.3 Experimental Description

5.3.1 Site Description

The measurements were performed as part of the Large Scale Biosphere-Atmosphere Experiment in Amazônia (LBA) in 1998 and 1999, during the wet and dry seasons. LBA is an international research initiative designed to study the interactions between Amazônia and the Earth system. The Cooperative LBA Airborne Regional Experiment (LBA-CLAIRE) took place during the wet season from 28 March to 15 April 1998, and included measurements at a ground site (Balbina, 1^o 55.5' S, 59^o 24.8' W; 160 m above sea level) located 125 km northeast of Manaus, in the state of Amazonas, Brazil. Backward airmass trajectory calculations indicate that our site was not affected by anthropogenic sources, as surface air masses originated from the northeast to east; hence had traveled a thousand kilometers over the most remote regions of the Amazon rain forest for almost a week before being sampled. Inlets for all instruments were located 6 m above the ground, via individual sampling lines that extended 2 m above the roof of the laboratory.

In 1999, the European Studies on Trace gases and Atmospheric Chemistry experiment (LBA-EUSTACH) extended operations to include wet- and dry-season measurements [12]. Forest and pasture sites near Ji-Paraná in the state of Rondônia were selected to characterize the influence of human settlement and deforestation in the Amazon Basin. The wet-season measurements continued into the beginning of the burning season, when fires began in the neighboring state of Mato Grosso. The dry-season experiment occurred from 15 September to 1 November 1999, encompassing the period from the peak of fire activity (beginning to middle of September) to the onset of the wet season (end of October). The forest site was located in the Jarú Biological Reserve (10^o 05.07' S, 61^o 55.92'; 130 m above sea level) about 90 km north of Ji-Paraná along the Machado River. Measurements took place at 50 m height on a meteorological tower to characterize the composition of the mixed boundary layer. The surrounding forest canopy is approximately 30 m high. During the wet season, anthropogenic contributions to the ambient aerosol were minimal, since the prevailing wind direction was mostly from forested regions to the east. The pasture site was located on the Fazenda Nossa Senhora (10^o 45.78' S, 62^o 21.45' W; 270 m above sea

level) about 50 km to the east of Ji-Paraná. Sampling for each instrument took place 5 m above the ground via individual inlets that were extended 1.5 m above the roof of the laboratory. The deforested region extends for at least 60 km surrounding the pasture site. As a consequence, anthropogenic contributions from local traffic, charcoal factories, and nearby cities (i.e., Ouro Preto d'Oueste and Ji-Paraná) influenced aerosol properties at the site, representing conditions that are fairly typical for deforested parts of the Amazon.

5.3.2 Instrumentation

We measured CCN concentrations, N_{CCN}, at supersaturations, S_v, between 0.15 and 1.5% using a static thermal-gradient chamber. The operation of the instrument is similar to the chamber described by [96]. Instead of the original light-scattering design, our CCN counter was fitted with a photodiode laser and digital camera to measure droplet concentrations. A detailed description of the CCN counter and calibration procedure is found in [134]. A 670 nm wavelength photodiode laser illuminates the activated droplets while the digital camera, normal to the laser beam, registers images every second during the supersaturation cycle. The CCN concentration at a particular supersaturation is determined during post processing. Imaging software automatically determines the number of activated CCN in each image. The CCN concentration is calculated based on the image with the highest number of particles and on the calibrated illuminated volume. The calibration procedure involved generating a quasi-monodisperse aerosol of a known concentration and counting the number of activated droplets in the digital image. An error analysis for calibration measurements indicates that for typical aerosol spectra, the overall measurement error in number concentrations is approximately ±15% at 1.5% S_v and ±30% at 0.15% S_v. These uncertainties are in agreement with theoretical predictions by [115].

CCN number concentrations were determined every 25 s at a series of supersaturations between 0.15 and 1.5 % S_v, yielding a complete CCN spectrum in six to seven minutes. A CCN cycle begins with a seven-second flush at 3 liters min^{-1} to remove the previous sample and draw in air for a new sample. The instrument's inlet valve closes and isolates the chamber, which allows the supersaturation profile to develop between two horizontal parallel wetted plates. The CCN counter operates at a desired supersaturation by controlling the temperature difference between the wetted plates. The diameter of the chamber is 100 mm and the top and bottom plates are separated by 10 mm. These dimensions allow for air in

the chamber to reach an equilibrium supersaturation profile in several seconds. Whatman filter papers on the top and bottom plates are kept wetted by an external capillary system. The top plate temperature is allowed to float with the ambient temperature, which ranged from 20 to 35^{o}C, and the bottom plate is cooled as necessary to achieve the prescribed supersaturation. Temperature fluctuations during measurements are usually within 0.1^{o}C, so the supersaturation is constant within $\pm 0.05\%$ S_v. Activated CCN particles quickly grow to several micrometers in diameter and gravitationally settle out of the chamber.

5.4 Model Description

5.4.1 Cloud Parcel Model

A cloud parcel model [127, 143] is the simplest tool that can be used to simulate the evolution of droplet distributions throughout a non-precipitating cloud column. It also predicts the maximum influence of aerosol on cloud properties because it focuses on the early stages of cloud formation, where droplets are produced through diffusional growth. The cloud parcel model used for this study includes explicit aerosol microphysics [117] and can account for the presence of slightly soluble and surfactant substances. For this study, the parcel is assumed to be adiabatic.

5.4.2 Cloud Optical Properties

Cloud albedo, R_c, is calculated based on the two-stream approximation of a non-absorbing, horizontally homogeneous cloud [94] (e.g., non-precipitating stratocumulus clouds),

$$R_c(z) = \frac{\tau}{7.7 + \tau} \tag{5.1}$$

where τ is the cloud optical depth,

$$\tau = \int_0^H \frac{3\rho_a w_L(z)}{2\rho_w r_{eff}(z)} dz \tag{5.2}$$

and $w_L(z)$ is the liquid water mixing ratio (kg water kg^{-1} air) profile along the cloud column. ρ_w is the water density (kg m^{-3}), ρ_a is the air density (kg m^{-3}), and $r_{eff}(z)$(m) is the cloud droplet distribution effective radius. The difference in cloud albedo at height z is used to assess modifications in cloud properties between the different simulations.

The cloud droplet effective radius was computed by

$$r_{eff} = \frac{\int_0^\infty r^3 n(r) dr}{\int_0^\infty r^2 n(r) dr} \tag{5.3}$$

where $n(r)$ is the droplet size distribution. For the optical depth calculations, we use, by default, the definition of effective radius (equation 5.3). To assess the albedo difference between the equilibrium cloud droplet population and that computed on the basis of dynamic mass transfer of water (see sections 5.3.3 and 5.6.3), we assume a monodisperse droplet population that has a certain amount of available liquid water. For this special case, the expression for $r_{eff}(z)$ is given by

$$r_{eff}(z) = \left(\frac{3\rho_a w_L(z)}{4\pi\rho_w N_d(z)} \right)^{\frac{1}{3}} \tag{5.4}$$

where $N_d(z)$ is the droplet concentration (m^{-3}) and is equal to the number of particles that are larger than the activated particle with the smallest dry diameter. We invoke the monodispersity assumption only when assessing the extent of kinetic limitations when comparing kinetic with thermodynamic albedo. This is done because thermodynamic activation by definition does not prescribe size distribution information, only total droplet number. So, when computing optical properties, in order to avoid systematic biases, we use a consistent base, which for simplicity, is provided by using equation 5.4.

5.4.3 Kinetic Limitations

While it is often assumed that particles are always at equilibrium with the local ambient water vapor concentration, cloud droplets, however, need a finite time to grow. As a result, the assumption of equilibrium can lead to an overestimation in droplet number as a result of mass transfer limitations [117].

The importance of kinetic growth limitations for droplet formation will be measured in terms of both droplet number and cloud albedo. For this purpose, the number concentrations of droplets, N_{eq} and N_{kn}, based on equilibrium and kinetic approaches, respectively, are required. N_{eq} is based on the assumption that particles activate instantaneously and represents the upper limit to the number of droplets that can be formed. N_{kn} is the droplet concentration from the 1-D dynamic parcel model [117]. Based on the variation of N_{kn} and

N_{eq} with cloud depth, z, one can define another useful quantity, the total droplet ratio, $\alpha(z)$,

$$\alpha(z) = \frac{N_{kn}(z)}{N_{eq}(z)} \tag{5.5}$$

which expresses the ratio of actual droplets formed to the maximum droplets attainable at a certain cloud depth. Vertical profiles of the activation ratios can provide insight regarding the importance of kinetic limitation mechanisms [117].

5.5 CCN Spectra Measurements

CCN spectra measurements for all the field campaigns are summarized in Figure 5.1. CCN number concentrations during wet-season field campaigns were low and resulted in a spectrum typical of oceanic environments [136]. The LBA-CLAIRE and LBA-EUSTACH experiments took place in 1998 and 1999, respectively, at sites nearly 1,000 km apart; yet, the wet-season CCN spectra were nearly identical regardless of the sampling location and the year. The uniformity of physical and chemical aerosol properties suggests a common biogenic source of the aerosol throughout the Amazon Basin. Hence, we consider the forest site wet-season CCN spectrum as representative of the natural background Amazonian CCN spectrum and as a reference to which a change in cloud properties may be compared.

The pasture site wet-season CCN spectrum was similar to that of the wet-season forest site. However, there is a slight shift to higher CCN concentrations at larger supersaturations due to local anthropogenic aerosol sources. The significance of this enhancement in the CCN spectra will be characterized in later sections and yields useful information regarding the potential changes due to human development in the Amazon Basin.

At the end of the wet season (e.g., middle of May 1999), biomass burning began in the neighboring state of Mato Grosso. Isentropic backward airmass trajectories [119] indicate that the surface air masses originated from the east; hence had traveled several hundred kilometers over the Amazon rain forest for a couple of days before being sampled. We observed a strong diel cycle in CCN concentrations that varied by nearly a factor of two, which suggests evidence of coupling aerosol transport to the development of the boundary layer. Obvious changes to the CCN spectra were observed as the fire activity increased during the transition period. CCN concentrations increased and the shape of the spectra changed,

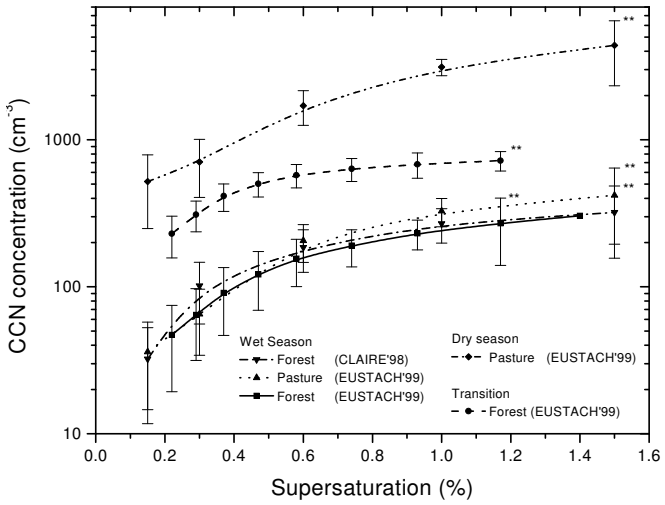

Figure 5.1: Summary of cumulative CCN spectra measured for wet, transition and dry seasons in the Amazon Basin. The error bars indicate one sigma variation in the CCN spectra normalized to its highest supersaturation, except for the error bars at the highest supersaturation of each spectrum. ** These error bars represent one sigma variation in the CCN number concentration for the selected sample period.

as well. The enhanced "curvature" of the transition period CCN spectrum (Figure 5.1) probably occurs because of a shift to a larger median diameter of the number distribution of aged smoke aerosol [132].

During the dry season, N_{CCN} were highly variable depending on the proximity of the burning and averaged about an order of magnitude higher than during the wet season. The spectra were similar to measurements at mid-latitudes near urban centers [68, 73] and oil-fire plumes in Kuwait [72]. The sources of the biomass-burning aerosol included local fires and aged smoke that had been transported from other regions in Brazil.

5.6 Simulation Parameters

To investigate the relationship between the CCN spectra and the development of convective cloud formation in the boundary layer, we used a 1-D parcel model. With this model, we explored the sensitivity of effective cloud radius, albedo, and maximum parcel supersaturation on physical and chemical properties of the aerosol population. Size distributions of lognormal form were used to represent the aerosol for which CCN spectra had

been measured,

$$\frac{dN_i}{d\ln d_p} = \frac{N_i}{\sqrt{2\pi}\ln\sigma_{g,i}} \exp\left[\frac{-(\ln d_p - \ln d_{pg,i})^2}{2\ln^2\sigma_{g,i}}\right] \tag{5.6}$$

where N_i is the aerosol number concentration, $d_{pg,i}$ is the geometric median diameter, and $\sigma_{g,i}$ is the geometric standard deviation for mode i. We assume an aerosol distribution assumed to be composed of either one (i= 1 only) or three (i= 1,2,3) such modes, which is specified in Table 5.1.

Table 5.1: Size distribution parameters for CCN spectra

Season[a]	ID	number distribution			NH_4HSO_4	OC
		N, cm^{-3}	D_{pg},μm	σ_g	mass fraction	mol C liter^{-1}
Wet season	WA	458.7	0.083	1.83	0.055	0
	WB	458.7	0.083	1.83	0.0611	0
	WCST	458.7	0.083	1.83	0.035	0.01
	WMST[b]	338.8	0.072	1.541	0.055	0
		92.37	0.163	1.307	0.15	0
		19.05	0.900	1.419	0.02	0.01
Pasture site	PA	550	0.086	1.83	0.055	0
	PB	500	0.100	1.83	0.055	0
Transition	TA	770	0.150	1.706	0.055	0
	TB	830	0.140	1.738	0.055	0
Dry season	DA	5200	0.090	1.896	0.056	0
	DB	5200	0.120	1.801	0.019	0
	DC	5200	0.150	1.706	0.007	0
	DDST	5200	0.090	1.896	0.02	0.035
	DEST	6000	0.090	1.896	0.02	0.01

[a] Each case was run at constant updraft velocities of 0.1, 0.3, 1.0 and 3.0 m s^{-1}. For all cases except WMST, the insoluble core density was 1.55 g cm^{-3}.

[b] WMST is a tri-modal distribution that also contained an insoluble core of 2.5 g cm^{-3}in the 0.900 μm mode (mass fraction = 0.13). The remainder of the mass fraction was organic carbon (OC).

Values for N (sum of N_i), d_{pg}, and σ_g that best represent the measured CCN spectra are given in Table 5.1. A particle's critical supersaturation, S_c, is determined for a two-component aerosol based on measured literature values for the amount of NH_4HSO_4 [132, 137] and water-soluble organic compounds (WSOCs) [110]. WSOC content was divided into neutral, mono/diacids, and polycarboxylic acids whose mass ratios and molecular weights

are described in Table 5.2. Although this is not a unique representation, it is quite realistic as reflected by the recent work of [49]. WSOCs enhance CCN activity by adding soluble material and reducing the surface tension of liquid cloud droplets. [36] determined the relationship between dissolved WSOC concentrations and the reduction in surface tension for ambient atmospheric cloud water samples, which was applied here to estimate potential influences of surfactants on CCN spectra and subsequent cloud properties.

Table 5.2: Properties of important components used in Köhler theory to estimate CCN activity.

Material	Density ($g\ cm^{-3}$)	Molecular weight ($g\ mol^{-1}$)	Solubility (mole $liter^{-1} H_2O$)	Van't Hoff factor
NH_4HSO_4	1.780	115.11[a]	6.55[a]	2.0
WSOC	1.55[b]	194.3[b]	0.01 (carbon)[c]	2.79
Insoluble inorganic	2.5[d]	NA	0.0	0.0
Insoluble organic	1.55[b]	NA	0.0	0.0

[a] CRC Handbook [98]

[b] Facchini (person communication); neutral compounds (18% by mass of WSOC) can be modeled as levoglucosan (162 g mol^{-1}, 1.6 g cm^{-3}, van't Hoff factor (vH) = 1); mono/di-acids (41% by mass of WSOC) can be modeled as succinic acid (118 g mol^{-1}, 1.572 g cm^{-3}, vH = 3); Poly-carboxylic acids (41% by mass of WSOC) can be modeled as fulvic acid (732 g mol^{-1}, 1.5 g cm^{-3}, vH = 5)

[c] [36]

[d] average crustal material [107]

The properties of all the aerosol components are shown in Table 5.2. The size distribution and relative mass fraction of each component (Table 5.1) were chosen to accurately describe measured CCN spectra (Figures 5.1 and 5.2). Parameters were either measured or constrained based on previous experiments. The number distribution was first determined, and chemical composition was adjusted to yield a CCN spectrum that matched the measured spectrum. The error bars in the figures represent the resulting one-sigma variations between the simulations for a particular season.

The wet-season number distribution was directly measured during the CLAIRE experiment [167] and fitted to a single or tri-modal lognormal distribution (Table 5.1). By varying the chemical properties of the single mode distributions, we assessed the effect of WSOCs. A tri-modal distribution with a composition similar to the average chemical composition reported in [137] serves as a "realistic" wet-season aerosol distribution. The principal difference is the addition of a large mode at 0.90 μm, which illustrates the effects of the "giant"

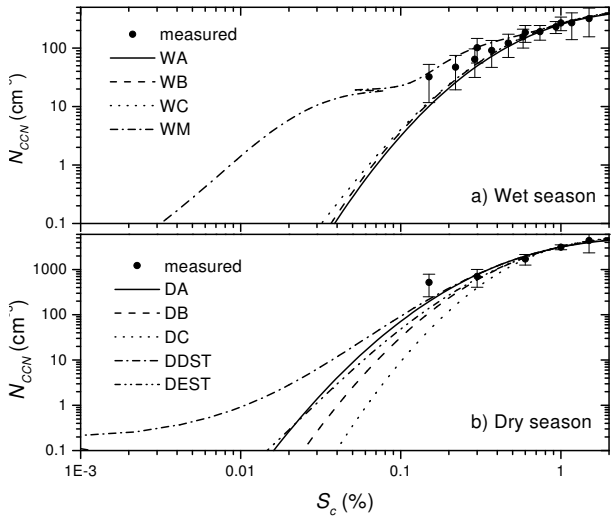

Figure 5.2: Modelled and measured CCN spectra for the wet and dry season. The simulations (WA, WB, etc.) are defined in Table 5.1.

CCN (GCCN).

Wet-season pasture site CCN spectra were nearly identical to the forest data except for a slight increase in N_{CCN} at higher supersaturations, which can be accounted for in the model by increasing N and/or d_{pg} of the wet-season number distribution. Anthropogenic inputs, such as exhaust from diesel automobiles or nearby factories, increase aerosol concentrations and may contribute to a larger median diameter in the size distribution [85]. Two alternative number distributions were investigated for the pasture site CCN spectrum by varying d_{pg} and N of the wet-season forest size aerosol distribution (Table 5.1).

Number distribution measurements for the transition and dry-season spectra were not available; as a result, approximations were made based on literature values. Since both the transition and dry-season CCN spectra involved biomass smoke aerosol, d_{pg} and σ_g were constrained by a linear relationship reported by [132],

$$\sigma_g = \lambda_1 d_{pg} + \lambda_2$$

where λ_1 =-3.16 μm^{-1}, λ_2= 2.18 and $0.09 < d_{pg} < 0.28$ μm is the maximum range allowed based on measurements during the SCAR-B (Smoke, Clouds and Radiation-Brazil experiment) [80]. These constraints on the geometric median diameter limit the range of the geometric standard deviation to $1.3 < \sigma_g < 1.9$. Smoke particles evolve rapidly after

emission, and their physical and chemical properties are related to their age. Young smoke exhibits a smaller median diameter than aged smoke and could be reflected by the difference in CCN spectra between the dry and transition periods. The more pronounced "curvature" in the transition period CCN spectra is indicative of aged, larger smoke aerosol, which was transported for several days over the rain forest.

Since a large fraction of the biomass-burning aerosol consists of water-soluble and humic-like substances [110], solubility and surface tension effects of this aerosol may play an important role in increasing the CCN activity during the dry season. [132] also report average sulfate composition for biomass-burning smoke aerosol to be several percent of the total aerosol mass (i.e., 1-2% for young aerosol and $< 7.6\%$ for aged aerosol). Hence, the physical and chemical properties of the dry-season aerosol were selected based on literature values and constrained to fit the measured CCN spectra between 0.15 and 1.5% S_v. As the mode diameter or surface tension effects increase, the amount of soluble material (i.e., NH_4HSO_4) must be reduced (see Table 5.1) to maintain agreement between modeled and observed CCN spectra. Such chemical and physical differences in aerosol properties will affect cloud droplet growth and result in a range of cloud properties. The effect of GCCN was not studied for the biomass-burning aerosol; however, the presence of GCCN can enhance the development of precipitation in mixed-phase convective clouds in regions with high aerosol concentrations [163].

The sensitivity of cloud properties was also calculated as a function of increasing aerosol number concentration using the size distributions obtained during the wet season at the forest site. The median diameter, median standard deviation, and chemical composition of simulation WA (Table 5.1) were kept constant, while the number concentration was varied from 10^2 to 10^4 cm^{-3}. The wet-season forest site spectrum provides a reference to assess the effects of increasing aerosol concentration on cloud properties in the Amazon Basin due to the input of anthropogenic aerosol.

5.7 Cloud properties of average aerosol distributions

The effects of biomass burning and the sensitivity of wet-season cloud properties are considered for the measured CCN spectra in the Amazon Basin (Figure 5.1). This section presents the cloud properties based on an ensemble average for each season (e.g., the mean

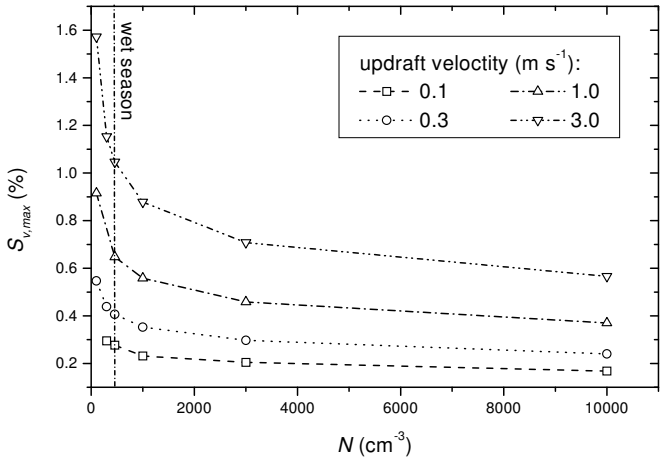

Figure 5.3: Cloud parcel maximum supersaturation as a function of increasing aerosol concentrations using the wet-season forest site CCN number distribution (WA). Each curve represents a different updraft velocity.

droplet number for the dry season was based on the average droplet number of the five dry-season simulations). Error analysis reflects the inter-seasonal variance of the ensemble average for each season.

Wet-season CCN spectra allowed for maximum supersaturations that were nearly two times higher than for the dry-season spectra (Table 5.3). Maximum parcel supersaturation attained in the cloud increased with updraft velocity due to the higher rates of adiabatic cooling and decreased with increasing N (and N_d) because of the competition for water vapor by more particles. The reduction in maximum parcel supersaturation is a nonlinear function of N_{CCN} and is most sensitive at low concentrations (Figure 5.3), such as those observed during the wet season.

5.7.1 Cloud droplet number

The cloud droplet number is a key parameter in regulating cloud properties. As evapotranspiration maintains a relatively uniform spatial distribution of water vapor above the forest canopy, cloud droplet number is primarily dependent on updraft velocity and the CCN spectra. The fraction of aerosol that serves as CCN, $f_{CCN/CN}$, for each of the simulated size distributions is shown in Figure 5.4. In spite of the lower parcel supersaturations for the transition period (Table 5.3), the larger mode diameter allows for higher $f_{CCN/CN}$ than during the wet season. For the dry-season spectra, on the other hand, $f_{CCN/CN}$ are

Table 5.3: Simulated maximum supersaturations as a function of updraft velocity for different periods in the Amazon Basin.

	Maximum supersaturation, $S_{v,max}$ (%)			
Updraft vel. (m s^{-1})	Wet season[a] (forest)	Wet season (pasture)	Transition period	Dry season
0.1	0.270 ± 0.007	0.253 ± 0.013	0.191 ± 0.001	0.179 ± 0.027
0.3	0.399 ± 0.007	0.375 ± 0.016	0.285 ± 0.002	0.262 ± 0.027
1.0	0.639 ± 0.008	0.569 ± 0.067	0.462 ± 0.003	0.404 ± 0.028
3.0	1.034 ± 0.012	0.972 ± 0.023	0.756 ± 0.003	0.619 ± 0.027

[a] The averages in the table do not include the tri-modal wet-season simulation. The maximum supersaturation values for the tri-modal simulations are as follows: 0.199, 0.325, 0.578, and 1.007 for updraft velocities of 0.1, 0.3, 1.0, and 3.0 m s^{-1}, respectively.

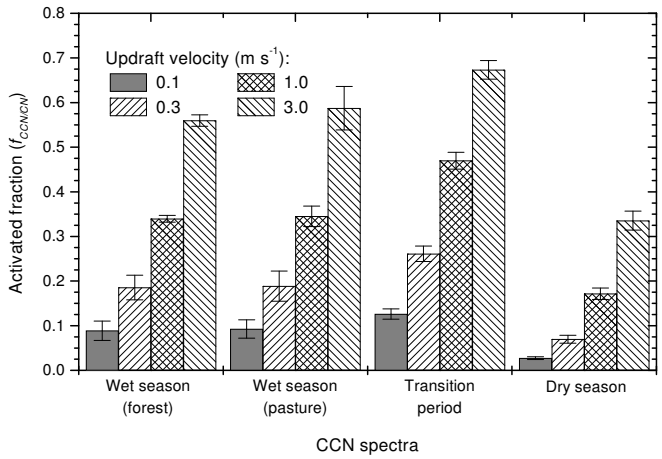

Figure 5.4: Fraction of aerosol that serves as CCN, $f_{CCN/CN}$, for the measured CCN spectra in the Amazon Basin. The error bars in this and the following figures represent one-sigma variations for a particular season using the simulations from Table 5.1.

less than for the wet season due to the order of magnitude increase in number concentrations and the enhanced kinetic growth effects.

The fractional increase in cloud droplet number concentration compared to the wet-season (forest) reference spectrum is shown in Figure 5.5. The differences in droplet concentrations between the wet-season forest and pasture sites are minimal. This similarity in droplet concentration is expected since the maximum parcel supersaturation is 0.82% (at 3.0 m s^{-1} updraft velocity; Table 5.3), and the CCN spectra for the forest and pasture sites are nearly identical for $S_c < 0.82\%$. The initial conditions and dynamic forcing for these simulations are the same in order to isolate the effect of the aerosol properties on clouds.

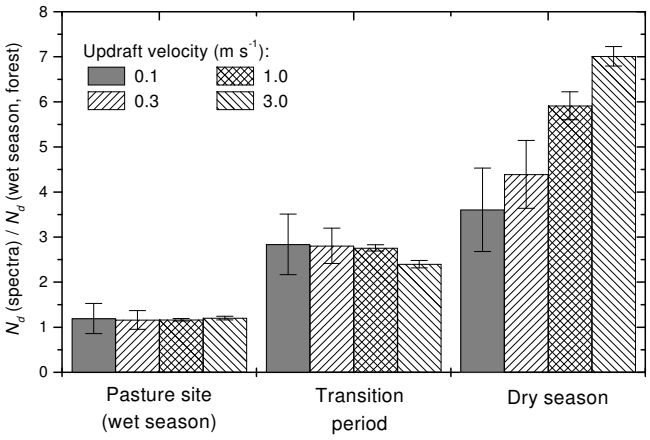

Figure 5.5: Ratio of cloud droplet concentration between the measured CCN spectra in the Amazon Basin and the wet season. The wet-season forest site CCN spectrum was used as a reference.

Significant differences in the water vapor content and surface heating rates resulting from the different land-cover could, however, induce dramatic changes in convective activity.

Biomass burning yields up to a sevenfold increase in droplet concentrations (Figure 5.5), even though the maximum parcel supersaturation decreased (Table 5.3). The largest increase in droplet number occurred for the dry season because of the order of magnitude increase in aerosol concentration. In spite of only a 40% increase in N from the wet season to the transition period, the cloud droplet concentration increased by at least a factor of two. The large mode diameter in the transition period size distribution allows for more particles to activate at lower supersaturations. This increase in droplet concentration also induces a significant reduction in maximum parcel supersaturation (Table 5.3). Small changes in parcel supersaturation while activating aerosol near the mode diameter (i.e., transition period) have a greater effect than activating aerosol at the shoulder of the distribution (i.e., dry season); hence the difference in trends with respect to updraft velocity in Figures 5.5 and 5.6.

During the initial stages of cloud development, water vapor transport to the growing droplets may not be sufficiently rapid for small particles near their critical size to activate. Consequently, they can re-evaporate and become interstitial aerosol particles, which exert a negligible effect on the cloud optical properties and precipitation processes. These simulations reveal that kinetic limitations are important regardless of updraft velocity and cloud

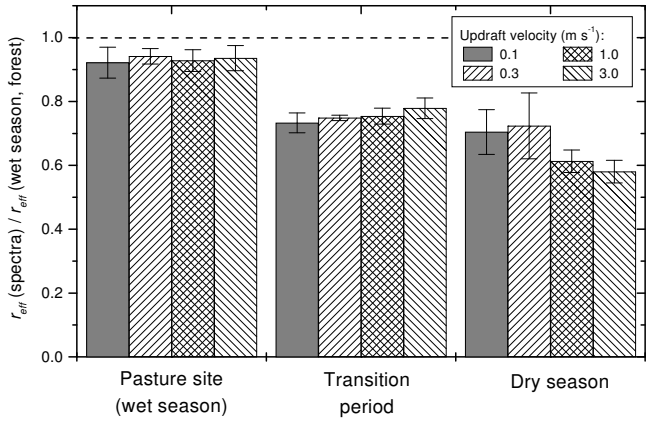

Figure 5.6: Ratio of effective cloud radius between the measured CCN spectra in the Amazon Basin and the wet season. The wet-season forest site CCN spectrum was used as a reference.

height for all measured Amazonian CCN spectra. Such results are not unexpected since kinetic effects have been shown to be present for number concentrations greater than 100 cm^{-3} [117]. We calculate asymptotic values for $\alpha(z)$, and the results are summarized in Table 5.4. Kinetic effects become more apparent as updraft velocity decreases (e.g., smaller water vapor flux) and droplet concentrations increase (e.g., dry season). The use of an equilibrium activation assumption could lead to an overprediction of cloud droplet number by 20% and 35% for low updraft velocities of 0.1 m s^{-1} during the wet and dry seasons, respectively (Table 5.4).

Table 5.4: Simulated asymptotic alpha ratios (N_{kn}/N_{th}) as a function of updraft velocity attained in the cloud parcel model for different periods in the Amazon Basin.

	Maximum droplet ratio, $\alpha(z)$ (N_{kn}/N_{th})			
Updraft vel. (m s^{-1})	Wet season (forest)	Wet season (pasture)	Transition period	Dry season
0.1	0.800 ± 0.033	0.825 ± 0.019	0.765 ± 0.011	0.674 ± 0.033
0.3	0.869 ± 0.014	0.859 ± 0.008	0.853 ± 0.002	0.736 ± 0.019
1.0	0.890 ± 0.018	0.910 ± 0.023	0.913 ± 0.010	0.824 ± 0.017
3.0	0.936 ± 0.020	0.945 ± 0.007	0.958 ± 0.001	0.886 ± 0.010

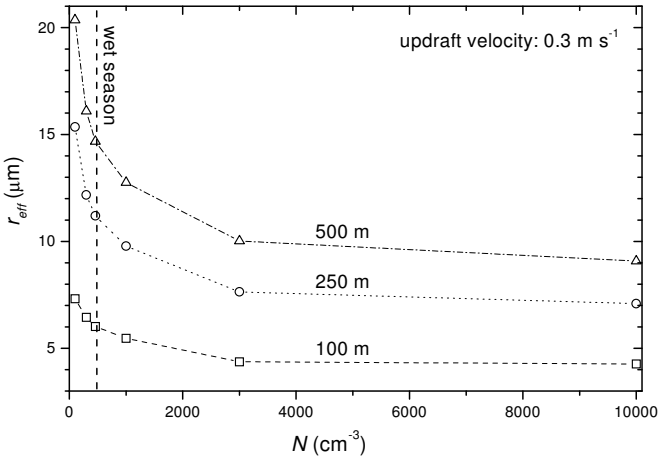

Figure 5.7: Predicted effective cloud radius as a function of increasing aerosol concentrations for a variety of cloud depths. The wet-season forest site CCN spectrum was used with an updraft velocity of 0.3 m s^{-1}. The cloud depth is indicated on each line.

5.7.2 Cloud droplet effective radius

The higher aerosol number concentrations and larger mode diameters during the transition period and dry season reduce the effective radius by nearly a factor of two compared to the wet season (Figure 5.6). These results are not surprising given that the liquid water content is assumed to be the same. Indeed, it can be shown that for constant liquid water content, $r_{eff} \propto N_d^{-1/3}$ [157]; an increase in N_d by a factor of 2.5 (5.5) for the transition period (dry season) results in a 30% (45%) reduction in effective cloud radius. A constant liquid water content and geometric standard deviation of the droplet distribution would merit a perfect $r_{eff} \sim N_d^{-1/3}$ dependence. However, even in a world of variations, this dependence still holds well [157], given the narrow spread of droplet populations when growing via the diffusional mechanism. A more general relationship is $r_{eff} \sim k^{-1/3} N_d^{-1/3}$, where $k = (r_v/r_{eff})^3$ and r_v is the volumetric average radius of the distribution [18]. *In situ* observations have shown that k varies from 0.67 in continental air masses to 0.80 in marine ones [106], meaning that in these drastically different air masses, $r_{eff} \sim 1.142 N_d^{-1/3}$ in the former and $r_{eff} \sim 1.077 N_d^{-1/3}$ in the latter.

As one would expect, the trends in r_{eff} with respect to updraft velocity reflect the N_d^{-3} dependence, which is reported in the previous section. These results are supported by satellite images taken over the Amazon Basin, which show that the presence of dense

smoke can reduce the remotely sensed drop radius of continental cloud drops from 14 to 9 μm [79].

Although collision and coalescence are not included in the simulation, the large reduction in r_{eff} reduces the probability for collision with other droplets [127], and thus the chance of rain formation by liquid phase processes. Although the differences between the forest and pasture site CCN spectra lead to only modest changes in cloud properties, sensitivity of r_{eff} is greatest at low aerosol concentrations (Figure 5.7), such as those found during the wet season. Hence, a slight increase in N_d (Figure 5.5) due to anthropogenic sources could support AVHRR analysis, which shows a larger reduction in r_{eff} during the wet season compared to the dry season (T. Nakajima, personal communication, 2000). Other mechanisms, such as changes in direct and indirect forcing and subsequent effects on convection and clouds, are beyond the scope of this paper, but should also be investigated.

5.7.3 Cloud albedo

A change in cloud albedo larger than ca. 0.005 can be considered climatically important; this albedo change can potentially exert a diurnally averaged radiative forcing of nearly –1 W m^{-2} [33]. Since we have used a 1-D model, the albedo and maximum albedo differences are a parameterization to measure the maximum aerosol effect within a cloud layer. Since we express everything in terms of maximum cloud albedo difference, cloud height becomes a free parameter in our calculations, and thus, can be interchanged with cloud thickness. The maximum aerosol effect on indirect radiative forcing has been estimated by comparing integrated cloud albedos for a given height of different simulations. Initially, the differences are small because the clouds are optically thin; whereas albedo converges to unity for optically thick non-absorbing clouds. Hence, albedo difference is a function of cloud depth and usually reaches a maximum within the first 300 m of the cloud. Figure 5.8 shows the maximum difference in cloud albedo for simulations using the measured Amazonian CCN spectra for non-absorbing clouds. The differences are positive due to the increasing droplet concentrations at the pasture site, and during the transition period and dry season. The wet-season forest site provides a reference for assessing the change in albedo.

The difference in cloud albedo between the forest and pasture site (Figure 5.8) does not appear to be significant because the number of activated droplets (Figure 5.3) is almost the same. This implies that during the wet season, the dominant driving force in climate change

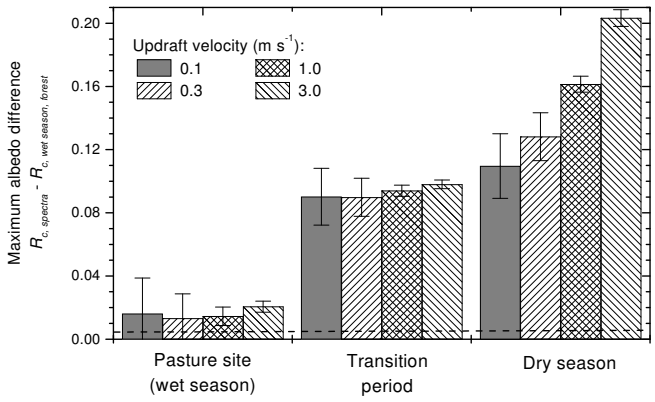

Figure 5.8: Predicted maximum albedo differences among measured CCN spectra in the Amazon Basin for different updraft velocities. The aerosol distributions in Table 1 are used and the wet-season forest case is used as a reference. The dashed lines represents a climatically significant radiative forcing of 1 W m^{-2} or a change in cloud albedo of 0.005.

may result from the surface albedo change due to forest/pasture conversion. The surface albedo of the Amazon rain forest is between 0.11 and 0.13 [52]. Following deforestation, there will almost always be an increase in surface albedo. In Rondônia, the forest is often replaced by short grass for cattle grazing, which can result in surface albedos up to 0.25 [52]. Deforestation will thus result in a reduction in the amount of radiative energy that is absorbed by the Earth's surface, resulting in less evaporation and a smaller driving force for convective activity [52]. A reduction in convective activity could inhibit precipitation; however, an inhomogeneous region of forest and pastures generates areas of local instability, which could actually increase the incidence of convective activity [13].

Significant enhancements in cloud albedo are calculated to result from the addition of smoke aerosol (Figure 5.8). The maximum change in albedo between the wet and dry seasons (assuming non-absorbing clouds) is 0.20, which corresponds to an interseasonal indirect aerosol forcing up to ca. –27 W m^{-2}. These simulated values for indirect forcing are comparable to the direct forcing from biomass-burning aerosol reported by [139]. Albedo difference is primarily dependent on droplet concentration; hence, changes in albedo difference, shown in Figure 5.8, follow similar trends as droplet concentration (Figure 5.5). The results from our modeling studies represent the upper limit of the aerosol effect, since we did not include the effect of the absorption of incoming solar radiation due to the absorbing components of the smoke aerosol. A comparison of the AVHRR analysis and our modeling

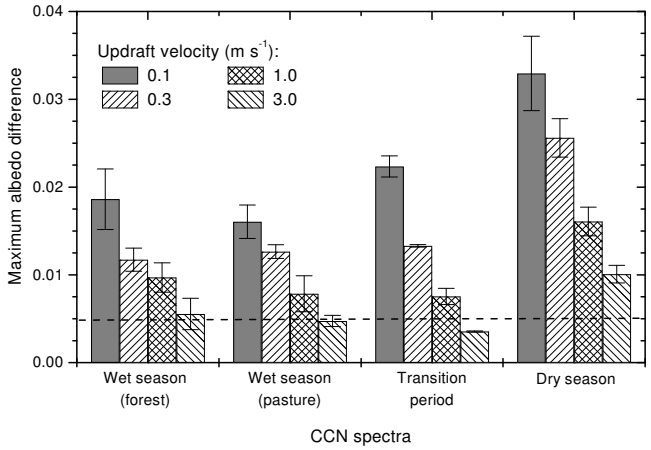

Figure 5.9: Maximum differences between thermodynamically and kinetically predicted cloud albedo for different updraft velocities. The aerosol distributions in Table 5.1 are used. The dashed lines represent a climatically significant radiative forcing of 1 W m^{-2} or a change in cloud albedo of 0.005.

studies suggests that absorption of sunlight due to smoke aerosol may compensate for about half of the maximum aerosol effect shown in Figure 5.8.

The quantity used for assessing the importance of kinetic effects on cloud activation, in terms of cloud albedo, is the difference between thermodynamic and kinetic albedo. The discrepancy in albedo comes from the difference in simulated cloud droplet number concentration between the two approaches to predicting cloud droplet activation and growth. The thermodynamic albedo tends to be higher than the kinetic albedo, because the same amount of liquid cloud water is shared among a larger number of cloud droplets. The height at which the maximum difference occurs decreases with increasing updraft velocity and number concentration. The dry-season distribution exhibits the largest albedo difference, shown in Figure 5.9, due to enhanced kinetic effects. Wet season (i.e., pasture and forest sites) and transition period conditions result in comparable differences (Figure 5.9). The differences in albedo from kinetic effects, however, are small compared to the increase in albedo resulting from enhanced aerosol concentrations during biomass burning.

5.8 Effect of aerosol chemical composition on cloud properties

Sensitivity tests using the wet- and dry-season CCN spectra have been performed to determine the influence of the physical and chemical characteristics of an aerosol popu-

lation on CCN activity and their subsequent growth into cloud droplets. Variations in CCN populations change the maximum in-cloud supersaturation, because particles that activate into cloud droplets at low supersaturations effectively scavenge the available water vapor. Therefore the CCN spectra that extend into lower supersaturations (i.e., WM and DDST; Figure 5.2) exhibit the lowest attained in-cloud supersaturations compared to other simulations of the respective season. WC and DC, whose CCN spectra are shifted to higher supersaturations, exhibit the highest in-cloud supersaturations, implying that surface-tension effects and the presence of GCCN could play an important role in droplet growth.

Because of the nonlinear feedback of the changing aerosol growth histories (from changes in chemical composition) into supersaturation profiles, the effect of chemistry on cloud droplet number, effective radius, and cloud albedo is not intuitive. We will take a closer look at the differences between the wet- and dry-season spectra in the following sections.

5.8.1 Wet-season CCN spectra

CCN spectra resulting from the modeled size distributions presented in Table 5.1 closely resemble the measured wet-season spectra between 0.15 and 1.5 % S_v (Figure 5.2a). Activation and growth of the cloud droplets were similar between the single mode distributions in spite of the differences in assumed chemical composition, as shown in Figure 5.10a. Hence, differences in cloud albedo are suspected to be less influenced by aerosol chemistry during the wet season. The larger effective radius resulting from the tri-modal distribution, however, can have a significant impact on indirect radiative forcing. For example, [53] found that a decrease in global mean cloud effective radius by 4.3% exerted an indirect forcing of nearly -1 W m^{-2}.

The tri-modal distribution exhibited larger droplets due to the activation of the 0.90 μm mode. This large mode is a source of GCCN, which could be important for initiating precipitation processes [163]. Although collision and coalescence were not included in the simulation, strong kinetic effects may enhance the precipitation process, because the driving force for droplet growth (i.e., the difference between the saturation ratio at the droplet surface and that of the surrounding air) is greater for larger droplets. Hence larger droplets, which are necessary to initiate collision and coalescence, could effectively draw water vapor away from the smaller droplets. The competition for water vapor by GCCN will likely be

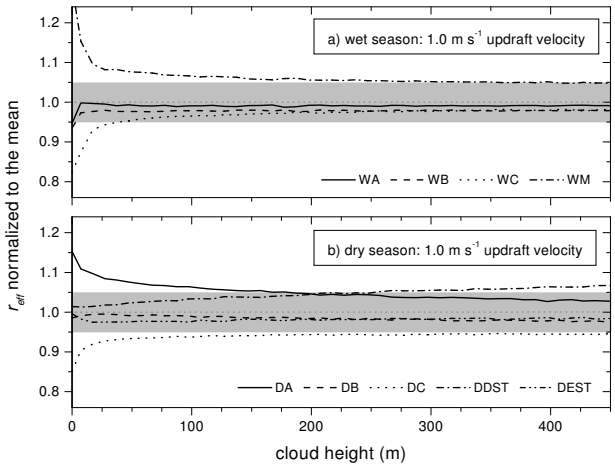

Figure 5.10: Effective radius for each distribution normalized to the mean. Wet- and dry-season profiles from Table 5.1 are shown for an updraft velocity of 1.0 m s^{-1}. The shaded area indicates the region of reff within 5% of the mean. The simulations (WA, WB, etc.) are defined in Table 5.1.

enhanced at higher aerosol concentrations when kinetic limitations are more pronounced. A strong kinetic effect, however, could also decrease the precipitation efficiency because the overall droplet population becomes smaller due to evaporative and deactivation mechanisms shown in [117]. This question should be addressed in future studies.

5.8.2 Dry-season CCN spectra

In spite of the similarity of the modeled dry-season CCN spectra to the measured results between 0.15 and 1.5% S_v (Figure 5.2b), variations in number distribution and chemical composition can yield climatically significant differences in cloud properties. The non-converging behavior of the effective cloud radii for the dry-season simulations, shown in Figure 5.10b, illustrates the differences in activation and growth of the cloud droplets. Relative differences in cloud effective radius between simulations can exceed 10%, which could yield differences in indirect forcing as high as 2 W m^{-2} [140]. These results suggest that changes in cloud albedo are more influenced by chemical and physical properties in cases of high aerosol concentrations, such as those found during the biomass-burning season.

The importance of chemical composition and the influence of kinetic effects for the dry-season CCN spectra are highlighted by DDST and DEST (Table 5.1; Figure 5.10b), where the slower initial rate of droplet activation allows a few particles to grow into cloud droplets

before kinetic limitations become significant at larger droplet concentrations. The enhanced CCN activity of larger particles (i.e., smaller critical supersaturation; Figure 5.2b) due to surface tension effects of DDST appears to effectively compete for water vapor as r_{eff} continues to increase relative to the mean droplet size. The surface tension effect essentially serves the same role as GCCN, and the kinetic limitations at high droplet concentrations appear to amplify this effect.

Although the CCN spectra of DA and DEST are nearly identical, even at smaller supersaturations than measured, Figure 5.10b illustrates significant differences in the activation and growth of the droplets. The difference in cloud effective radii for the two simulations is ca. 4.5%, which is of climatic significance [53], and could be related to surface tension effects. Surface tension effects not only reduce the droplet's critical supersaturation, but also influence the shape of the Köhler curve, which can alter the growth behavior of a droplet. Therefore, knowledge of the CCN spectra alone may not be adequate in fully assessing the climatic effects of aerosol.

5.9 Conclusions

We have investigated the change in cloud properties based on measured CCN spectra between 0.15 and 1.5% S_v during the wet and dry seasons in the Amazon Basin. CCN concentrations rise by nearly an order of magnitude from wet to dry seasons, which increase droplet concentrations up to a factor of seven at high updraft velocities. Throughout the text, we have compared the changes in cloud properties relative to wet-season forest CCN spectra. Although the differences between the forest and pasture site CCN spectra lead to only modest changes in cloud properties, the resulting modifications in cloud properties are most sensitive at low number concentrations, such as those that are found in wet-season conditions.

Our results indicate that knowledge of the CCN spectra alone is insufficient to fully capture the climatic influence of biomass burning. The activation and growth behavior of CCN are shown to be influenced by subtle variations in the size distribution and chemical composition, which are not well constrained by our measurements. Kinetic limitations to droplet activation and growth reduce droplet concentrations by up to 20% in the wet season and 35% in the dry season as compared with simulations based on equilibrium Köhler theory.

Kinetic effects are, however, small compared to the predicted changes in cloud properties induced by biomass-burning aerosol.

Human activity, such as industrial emissions and biomass burning, modifies physical and chemical properties of the aerosol population –components that dictate CCN activity– and could lead to important changes in cloud properties that govern the energy and water cycle within the Amazon Basin. The response of cloud droplet concentration to changes in CCN concentrations is the basis for the modification of precipitation, cloud fraction, and indirect forcing. However, changes in surface albedo have not been included in this study and are an important driving force in the hydrological cycle and convective activity. Light-absorbing substances in smoke darken the Amazonian clouds, and our modeling studies suggest that absorption of sunlight due to smoke aerosol may compensate for about half of the maximum aerosol effect. An increase in aerosol concentrations during the wet season will likely have a greater effect on the rain forest climate than further intensification of biomass burning during the dry season, due to the higher sensitivity at the low ambient aerosol concentrations.

5.10 Acknowledgments

We thank G. Lala and P. Guyon for support with building the CCN instruments. These experiments would not be possible without support from the following Brazilian institutions: INPE, CPTEC, IBAMA, INCRA, and UNIR. This project was supported by the Max Planck Gesellschaft and by the European Commission (Project EUSTACH-LBA). G.R. was funded by the Max Planck Institute for Chemistry and by Environment Now at the California Institute of Technology. This work was also supported by Office of Naval Research grant N00014-96-0119.

Chapter 6

Black carbon radiative heating effects on cloud microphysics and implications for aerosol indirect forcing: 1. Extended Köhler theory

Note: This chapter appeared as reference [28].

6.1 Abstract

Black carbon (BC) aerosol absorbs sunlight that might have otherwise been reflected to space and changes the radiative heating of the atmosphere and surface. These effects may alter the dynamical and hydrological processes governing cloud formation. A new, *microphysical*, effect of BC on climate is identified here, in which solar heating within BC-containing cloud condensation nuclei (CCN) slows or prevents the activation of these CCN into cloud drops. Solar-heated BC-containing droplets are elevated in temperature by fractions of a degree above the ambient, thus raising the droplet vapor pressure, and inhibiting activation of the most absorptive CCN. This paper develops the theory describing the alteration of the Köhler curve (i.e., the equilibrium vapor pressure over a droplet as a function of water uptake) as a function of CCN size and chemical composition (BC fraction, in particular). The effect is most significant in those CCN that contain volumes of BC larger than a 500 nm diameter sphere. For an aerosol population with 10% BC mass fraction per particle, solar heating can cause a 10% reduction in the CCN concentration at 0.01% critical supersaturation. On the other hand, the effect of heating by BC absorption on CCN activation above about 0.1% critical supersaturation is negligible.

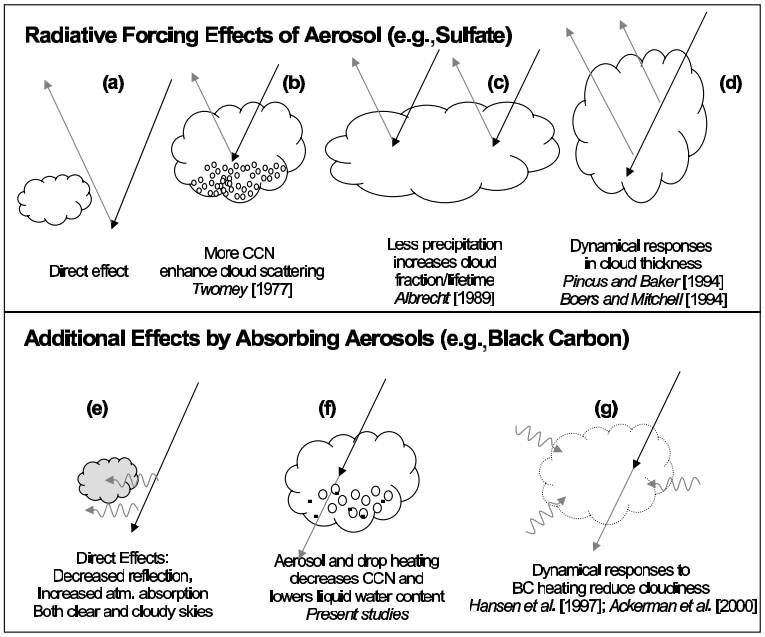

Figure 6.1: Direct and indirect radiative effects of aerosol, divided into those effects unrelated to aerosol absorption **(a)-(d)**, and those related to aerosol absorption **(e)-(g)**.

6.2 Introduction

Atmospheric aerosols reduce the solar radiation absorbed by the Earth through direct and indirect mechanisms (Figures 6.1a-d). In the direct effect, aerosols scatter radiation to space that would have otherwise heated the surface or atmosphere (Figure 6.1a). In the indirect effect, increased concentrations of cloud condensation nuclei (CCN) alter the microphysical properties of clouds, enhancing cloud reflectivity (Figure 6.1b). Additional indirect effects on clouds have been proposed that involve aerosol-induced changes in precipitation, radiative heating, and atmospheric dynamics (Figures 6.1c-d). In contrast, absorptive particles, black carbon (e.g., soot) in particular, exert a positive (warming) climate forcing (Figures 6.1e-g). Uncertainties in the distribution of natural and anthropogenic aerosols, their chemical speciation, and the aerosol-cloud-climate interactions they induce presently constitute the largest source of uncertainty in climate models that attempt to predict the role of anthropogenic emissions on climate.

Carbonaceous particles are an important class of primary aerosol emitted into the atmosphere. These particles tend to be a complex mixture of graphitic material and organic

compounds. The graphitic component, called soot or black carbon, is characterized by significant absorption of solar radiation. Freshly emitted black carbon particles tend to be hydrophobic; as they age in the atmosphere they tend to acquire a hydrophilic coating. As black carbon becomes sufficiently hydrophilic, it is able to form cloud droplets upon activation in a supersaturated environment. Black carbon can play a role in indirect aerosol radiative forcing in two ways: (6.1) BC particles absorb solar radiation, changing the vertical and horizontal thermal structure of the atmosphere and surface, changes that can have an impact on dynamical processes governing cloud formation and evaporation; (6.2) Those particles that act as CCN and become incorporated in cloud droplets absorb solar radiation and heat the droplets and the air around them, processes that can potentially alter cloud activation itself. Effect (6.1) was identified in the INDOEX campaign through observation and modeling of absorptive species [6, 97]. Effect (6.2) is the subject of this and a companion paper [116].

6.3 Theoretical development

Köhler theory [86, 143] predicts the equilibrium water vapor pressure of an aqueous droplet containing solute given its physical and chemical properties, and hence can be used to predict the exchange of water vapor between the droplet and the ambient atmosphere during cloud formation. The Köhler equations are most often implemented under the assumption that radiative heating of the droplet is negligible [45]. Absorption and emission of solar and infrared radiation by liquid water have since been found to play an important role in the evolution of the drop size distribution near cloud top ([62], and references therein). However, these studies treat the droplet absorption spectrum as that of pure water and do not address the presence of black carbon in the seed aerosol.

This study examines how radiative heating by black carbon within a particle affects equilibrium Köhler theory. Effects of non-BC absorption (e.g., H_2O and H_2SO_4 absorption in the near infrared) and long-wave radiative effects are neglected to isolate the perturbation by BC. The effect of this perturbation on the time-dependent (non-equilibrium) cloud activation problem is treated in a companion paper [116] using a cloud parcel model with explicit microphysics that includes the effect of BC heating on parcel thermodynamics.

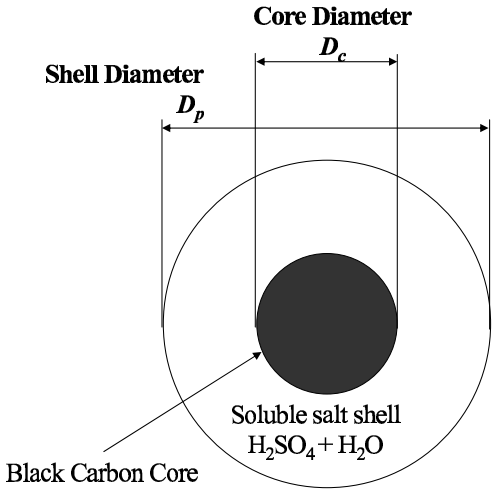

Figure 6.2: Concentric shell geometry assumed for the calculation of droplet heating.

6.3.1 Heating by black carbon

Black carbon (BC) is the most efficient aerosol species at absorbing solar radiation. Aged anthropogenic aerosol often contains 5% to 20% black carbon by mass [122, 120, 67]. Aged atmospheric BC particles are rarely pure, externally mixed, species, but are most often found to be coated with water soluble compounds such as sulfate and organic carbon [126]. BC is produced by incomplete combustion in the form of 10–50 nm diameter spherules that agglomerate into chains [112]. In well-aged aerosol, the bulk of the BC mass is contained in particle sizes from 300 to 700 nm diameter through coagulation, coalescence in evaporated cloud drops, and addition of secondary aerosol mass [78]. Because this size range encompasses that of particles most likely to serve as CCN, we investigate the impact of droplet solar heating on the properties of BC-containing CCN.

To compute the droplet heating for BC-containing aerosols, we represent the internally mixed BC aerosol as a layered sphere with a black carbon core of diameter D_c coated by a hydrophilic sulfate shell of diameter D_p (Figure 6.2). The heating rate for each particle, Φ (W), is obtained from

$$\Phi = \int_{0.2\mu m}^{5\mu m} I(\lambda)\sigma_a(\lambda)d\lambda \tag{6.1}$$

where $I(\lambda)$ is the spectral actinic flux (spherically integrated spectral intensity) having units W m^{-2} nm^{-1}, and $\sigma_a(\lambda)$ is the particle absorption cross section (m^2), and solar wavelength, λ, is assumed to range from 0.2 to 5 μm. For the purposes of this study, $I(\lambda)$ is predicted by a 38-band multispectral Monte Carlo radiative transfer model [125], which assumes a sub-tropical marine atmosphere over ocean, an aerosol optical depth of 0.3 (at 0.5 μm), and no clouds; the model described by [125] has been slightly modified here to predict actinic flux instead of irradiance. To test the sensitivity of actinic flux to these assumptions, Figures 6.3 a, b illustrate the variation of actinic flux with surface type and the presence of clouds. Figure 6.3a illustrates that actinic flux varies by about a factor of two from cloud base to cloud top, with peak fluxes occurring at cloud top. Figure 6.3a considers only ocean, whereas Figure 6.3b shows that cloud base and cloud top actinic flux are also sensitive to surface albedo. Together, Figures 6.3a and 6.33b show that the actinic flux of 1000 W m^{-2} assumed in the remainder of this paper (except where stated otherwise) is appropriate for clear-sky cases and thin clouds, will be a slight overestimate for the base of moderately well–established clouds over ocean or land, and will be a slight underestimate for cases at or above cloud top or over bright surfaces.

The particle absorption cross section, $\sigma_a(\lambda)$, is computed for each particle as a function of D_p and D_c using a 2-layer radiative parameter model based on Mie theory [152]. [48] show that the concentric geometry assumed here overestimates absorption by at most 15% compared to a randomly placed encapsulated inclusion, and that the treatment of the carbon as a single sphere instead of an agglomeration of spherules underestimates the absorption by at most 30%. BC located near the edge of the droplet could enhance the heating an order of magnitude beyond that considered here [25]. Indices of refraction for BC, sulfate, and water are obtained from [65]. The imaginary index of refraction for BC used here (0.45 at 0.55 μm) is on the lower end of observed values [48, 105]. Shell index of refraction is a function of aerosol hydration, and is determined based on the molar ratios and indices of refraction for sulfate and water, following [151].

6.3.2 Droplet equilibrium temperature

The equilibrium temperature of an (static) aerosol particle of diameter D_p is governed by the balance between net radiative heat absorbed by the particle, Φ, and the sensible heat flux conducted away from the particle, F(W m^{-2}),

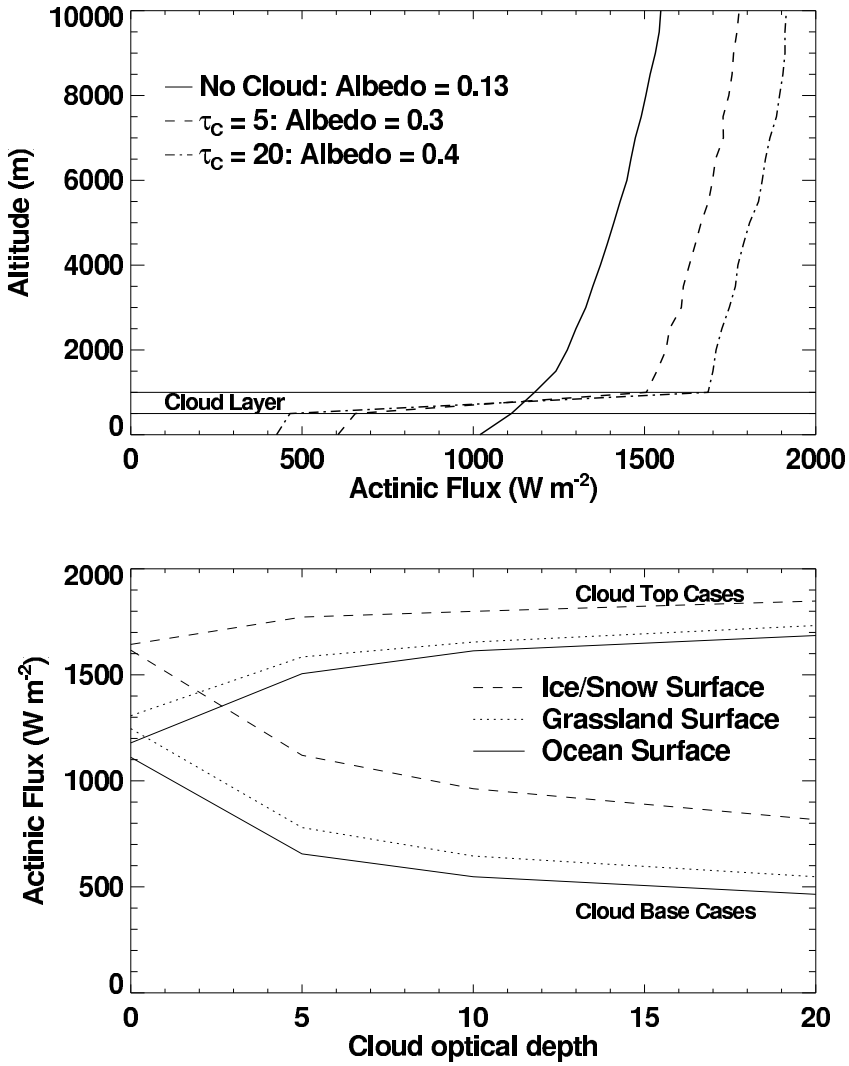

Figure 6.3: Actinic flux under varying conditions of cloudiness and surface albedo. **(a)** Vertical profile of actinic flux calculated for 3 cases: no cloud, cloud with optical thickness $\tau_c = 5$, and cloud with $\tau_c = 20$. Each case considers a solar zenith angle of 60^o, ocean surface reflection (albedo $\sim$0.07 for no cloud case), and clouds are horizontally homogeneous. **(b)** Actinic flux for cloud base and cloud top as a function of cloud optical depths ranging from 0 (no cloud) to 20. Three cases of surface albedo are considered: ocean reflection (explicitly accounting for both Fresnel and bulk reflection), (b) grassland (isotropic albedo of 0.26), and (c) snow/ice (isotropic albedo of 0.6).

$$\Phi = \pi D_p^2 F \tag{6.2}$$

Through scaling arguments it can be shown that the temperature profiles both within the droplet and in the surrounding gas phase, for typical atmospheric conditions, are in steady state. As a result, F depends on ΔT, the difference between the particle surface temperature, T_p, and the ambient temperature, T_a, far from the particle as follows,

$$F = 2k_{air}^{'} \frac{\Delta T}{D_p} \tag{6.3}$$

where $k_{air}^{'}$ is the thermal conductivity of air corrected for the noncontinuum effect. (The noncontinuum effect reduces thermal conductivity for submicron or high-altitude particles.)

Combining (6.2) and (6.3) yields the dependence of equilibrium particle surface temperature perturbation on radiative heating,

$$\Delta T = \frac{\Phi}{2\pi D_p k_{air}^{'}} \tag{6.4}$$

6.3.3 Modification to the Köhler equation

The temperature perturbation by radiative heating raises the vapor pressure over the surface of the particle; the resulting modification to Köhler theory has been discussed elsewhere [5, 62]. The Köhler equation expresses the equilibrium vapor pressure over an aerosol surface, $p_w(T_p, D_p)$, in reference to $p^{\circ}(T_p)$, the vapor pressure over a flat surface of pure water at the same temperature T_p [143],

$$\ln\left(\frac{p_w\left(T_p, D_p\right)}{p^{\circ}(T_p)}\right) = \frac{4M_w\sigma}{RT_p\rho_w D_p} - \frac{6n_s M_w}{\pi\rho_w\left(D_p^3 - D_c^3\right)} \tag{6.5}$$

where M_w is the molecular weight of water, σ is the surface tension of the droplet, ρ_w is the density of water, R is the ideal gas constant, and n_s is the number of moles of solute in the shell. D_c is the geometric diameter of any insoluble core, and D_p varies due to condensation and evaporation of water. The first term on the right side of (6.5) describes the tendency for the vapor pressure to increase over a curved surface (Kelvin effect), and the second term expresses the vapor pressure depression caused by the solute mole fraction (Raoult effect).

Particle saturation, S_p, is defined as the ratio of particle surface vapor pressure to vapor

pressure of water over a surface at ambient temperature, $p^{\circ}(T_a)$,

$$\ln S_p = \ln\left(\frac{p_w\left(T_p, D_p\right)}{p^{\circ}(T_a)}\right) \tag{6.6}$$

Without radiative heating, $T_a = T_p$, (6.5) and (6.6) are equivalent, and (6.5) can be used to obtain the particle saturation. In the presence of heating, the relationship between $p^{\circ}(T_a)$ and $p^{\circ}(T_p)$ must be accounted for using the Clausius-Clapeyron relation [143],

$$\ln\left(\frac{p^{\circ}(T_p)}{p^{\circ}(T_a)}\right) = \frac{\Delta H M_w}{R T_a^2}\Delta T \tag{6.7}$$

where ΔH is the latent heat of condensation and $\Delta T \ll T_a$. Combining (6.4)-(6.7) yields the modified Köhler equation in the presence of radiative heating,

$$\ln S_p = \frac{4 M_w \sigma}{R T_p \rho_w D_p} - \frac{6 n_s M_w}{\pi \rho_w \left(D_p^3 - D_c^3\right)} + \frac{\Delta H M_w}{R T_a^2}\frac{\Phi}{2\pi k_{air}^{'} D_p} \tag{6.8}$$

Table 6.1: Sensitivity of Köhler curve to elevated droplet temperature. (When required, a 10 μm droplet diameter is assumed.)

Temperature Sensitive parameter	$d \ln S_p / d\Delta T$	Sensitivity (K^{-1})
Clausius-Clapeyron effect	$\frac{\Delta H M_w}{R T_a^2}$	6.2×10^{-2}
Gas-phase temperature gradient effects	$<$ order $\left(\frac{1}{T_a}\right)$	$< 3.4\times10^{-3}$
Water density	$-\left(\frac{A}{D_p} - \frac{B}{D_p^3 - d_p^3}\right)\frac{d\ln\rho_w}{dT_a}$	$2.4 \times 10^{-4} \ln S_p$ $< 10^{-6}$ for $\ln S_p < .4\%$
Temperature sensitivity of Kelvin effect	$-\frac{A}{D_p T_a}$	-7.5×10^{-7}
Water-air surface tension	$\frac{A}{D_p}\frac{d\ln\sigma_w}{dT_a}$	-4×10^{-7}

The last term in (6.8) is the solar heating term. Equation (6.7) provides the dominant source of sensitivity of equilibrium particle saturation to elevated droplet temperature. For comparison, Table 6.1 lists the magnitude of other, minor effects that arise from either variations in droplet properties with temperature or from simplifications made deriving equilibrium saturation (6.8). These minor effects will be neglected in the remainder of this study.

Because of its inverse dependence on D_p, we can express the heating effect as a modification to the Kelvin effect term in the Köhler equation,

$$\ln S_p = \frac{4M_w\sigma}{RT\rho_w D_p}(1+\gamma_a) - \frac{6n_s M_w}{\pi\rho_w\left(D_p^3 - D_c^3\right)} \tag{6.9}$$

where we define the aerosol *heating parameter*, γ_a, as,

$$\gamma_a \equiv \frac{\Delta H \rho_w \Phi}{8\pi k'_{air} T_a \sigma} \tag{6.10}$$

In the limit that $\Phi \rightarrow 0$, $\gamma_a \rightarrow 0$ and (6.9) reduces to the traditional Köhler equation (6.5).

It is convenient at this point to consider the absorption efficiency, Q_{abs}, defined as the ratio of the absorption cross section to the physical cross section,

$$Q_{abs} = \frac{4}{\pi}\frac{\sigma_a}{D_p^2} \tag{6.11}$$

which generally can range from 0 to order unity, tending asymptotically to 1 for large, perfectly absorptive particles. In Figure 6.4, the heating parameter is shown as a function of dry particle diameter, d_p, and absorption efficiency. For the purpose of calculating the Kelvin effect, the surface tension of the droplet is assumed to be that of water. Also shown in Figure 6.4 is the absorption efficiency calculated for aerosols of mixed BC and sulfate (H_2SO_4) composition; two cases are shown, one with 50% BC by mass, the with 10% BC by mass. The purpose of these calculations is to illustrate reasonable heating parameters expected for a given dry particle diameter, and hence define the conditions in which the effect is most likely to be important. When γ_a =1, the heating effect is equal in magnitude to the Kelvin effect. For the conditions described above, γ_a =1 for a 3.5 μm (dry) particle that is 10% BC by mass. The heating parameter presented in Figure 6.4, which is computed for dry aerosol, will generally be lower than that for an activated particle due to the enhancement of BC heating when included within a droplet. This amplification is predicted by the model described in Section 2.1. and will be included when calculating droplet heating.

6.3.4 Effect of black carbon radiative heating on critical supersaturation

Figure 6.5 illustrates the effect of droplet heating on the Köhler curves for dry particle diameters of 0.5 μm and 1.0 μm and γ_a values of 0.1 and 0.2. These curves correspond to particles with the hygroscopic properties of pure sulfate. Droplet heating has the effect

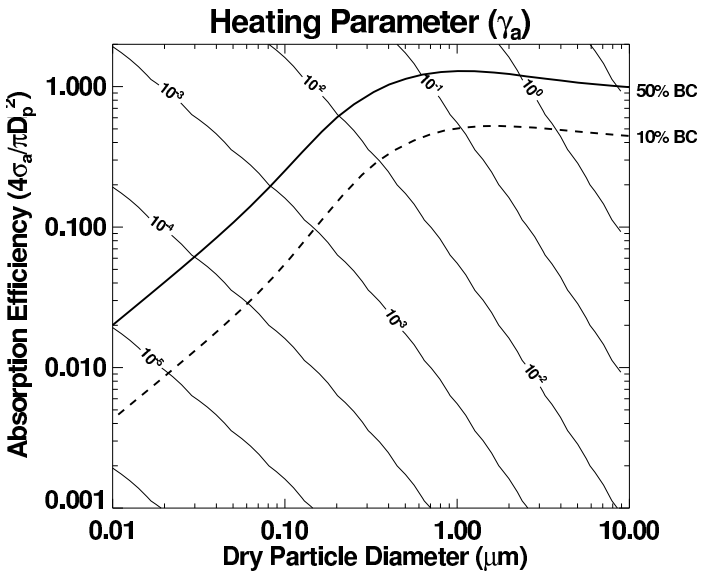

Figure 6.4: Heating parameter, γ_a, for dry particles (contour lines) as a function of dry particle diameter, d_p, and spectrally averaged absorption efficiency, Q_{abs}. The heavy solid and dashed lines represent the relationship between Q_{abs} and d_p for dry aerosols composed of 50% BC by mass and 10% BC, respectively.

of increasing the maximum equilibrium saturation of the droplet (i.e., critical saturation, S_c), above which the droplet is unstable to condensational growth. Thus the effect of the heating is to delay activation of the aerosol into a cloud drop. Note, however, that for these large droplet sizes, the unactivated aerosol is already comparable in size to cloud drops, and should be treated as such for radiative purposes [117].

A value for γ_a above which heating can become important can be quantified in terms of the change in particle critical saturation in the presence of heating. If the critical diameter is much larger than the diameter of the insoluble core, then the particle critical saturation ratio without the heating source, S_c^{wo}, can be computed by classical Köhler theory,

$$\ln S_c^{wo} = \left(\frac{4A^3}{27B}\right)^{1/2} \tag{6.12}$$

where $A = 4M_w\sigma/RT\rho_w$, and $B = 6n_sM_w/\pi\rho_w$. Similarly, in the presence of the internal heat source, the critical saturation ratio, S_c^w, is given by (6.12) with A multiplied by the factor $(1+\gamma_a)$,

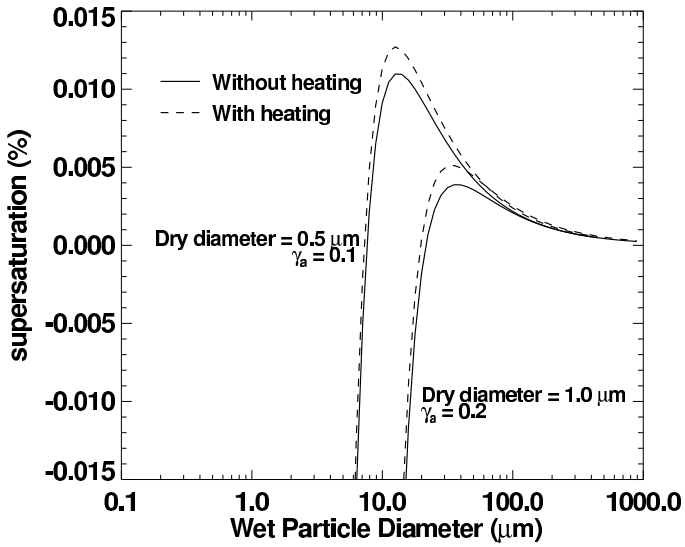

Figure 6.5: Effect of droplet heating on the Köhler curves of particles of 0.5 μm and 1.0 μm dry diameter. Heating parameters of 0.1 and 0.2 are chosen for the two droplet sizes, respectively. The solid curve represents the no-heating case, the dashed curve represents the heating case. Particles are assumed to have the hygroscopic properties of sulfate.

$$\frac{\ln S_c^w}{\ln S_c^{wo}} = (1+\gamma_a)^{3/2} \tag{6.13}$$

By expanding $\ln S = \ln(1+s) \approx s$, where s is the supersaturation, the ratio of particle critical supersaturation with and without heating is given by

$$\frac{s_c^w}{s_c^{wo}} = (1+\gamma_a)^{3/2} \tag{6.14}$$

In a similar fashion, it can be shown that the ratio of critical diameter with heating, D_{pc}^w, to that without heating, D_{pc}^{wo}, is given by

$$\frac{D_{pc}^w}{D_{pc}^{wo}} = (1+\gamma_a)^{-1/2} \tag{6.15}$$

Figures 6.6a and 6.6b show the critical supersaturation and critical diameter as functions of dry particle diameter, d_p, for two cases: (6.1) 10% BC and 90% sulfate; and (6.2) 50% BC, 50% sulfate. For each case, the results are shown both with and without the effect of heating (i.e., daytime and nighttime cases, respectively). The first effect of the BC

inclusion is to reduce the mass of solute, hence increasing critical supersaturation with increasing BC fraction irrespective of the heating. This is identified in Figure 6.6a as the "solute effect," seen as the difference in supersaturation between the two cases where heating is not introduced. The difference between the daytime and nighttime cases, identified as the "heating effect," is greatest for the largest particles for which heating parameter is greatest (Figure 6.4). The heating effect is further isolated by considering particles of fixed composition under conditions of varying solar irradiance. Figures 6.7a and 6.7b illustrate the sensitivity of critical supersaturation to actinic fluxes varying from 0 W m^{-2} (nighttime) to 1500 W m^{-2}, for the 50% BC and 10% BC cases, respectively. For these cases actinic flux is scaled uniformly across the solar spectrum.

One interesting result seen in Figures 6.6a and 6.7 is the local minimum in the dependence of s_c on d_p. This minimum, s_{low}, occurs for particles of dry diameter d_{low}. This is a result of the assumption of fixed BC mass fraction in the dry particle. In unheated particles, the critical supersaturation monotonically decreases with increasing d_p. However, BC heating increases approximately with d_p^2 for supermicron particles, and eventually dominates over the Raoult term, leading to an increase in s_c with d_p for the largest sizes. We can obtain some insight by including the heating effect into (6.12) and differentiating with respect to dry particle diameter,

$$\frac{\partial \ln s_c}{\partial d_p} = \frac{\partial}{\partial d_p}\left[\frac{3}{2}\ln A + \frac{3}{2}\ln\left(1+\gamma_a\right) - \frac{1}{2}\ln B\right] \tag{6.16}$$

Note that A, the Kelvin effect term, is insensitive to dry particle diameter if we ignore surface active species; B, the Raoult term, increases with d_p^3 due to increased moles of solute; and, γ_a increases with d_p^2, for the supermicron particles considered here. It can be shown from (6.16) and the above assumptions that d_{low} occurs where $\gamma_a = 1$, and thus (6.16) yields two regimes for the dependence of s_c on d_p based on γ_a.

$$\begin{aligned} \tfrac{\partial \ln s_c}{\partial d_p} &= -\tfrac{1}{2}d_p; \quad \gamma_a \ll 1 \quad and \quad d_p \ll d_{low} \\ \tfrac{\partial \ln s_c}{\partial d_p} &= \tfrac{3}{2}d_p; \quad \gamma_a \gg 1 \quad and \quad d_p \gg d_{low} \end{aligned} \tag{6.17}$$

For $\gamma_a \ll 1$, the change in supersaturation with dry diameter is dominated by the Raoult term, and s_c decreases with increasing d_p, as expected from the classical solution. However, for $\gamma_a \gg 1$, the heating term dominates over the Raoult term, and s_c increases with dry

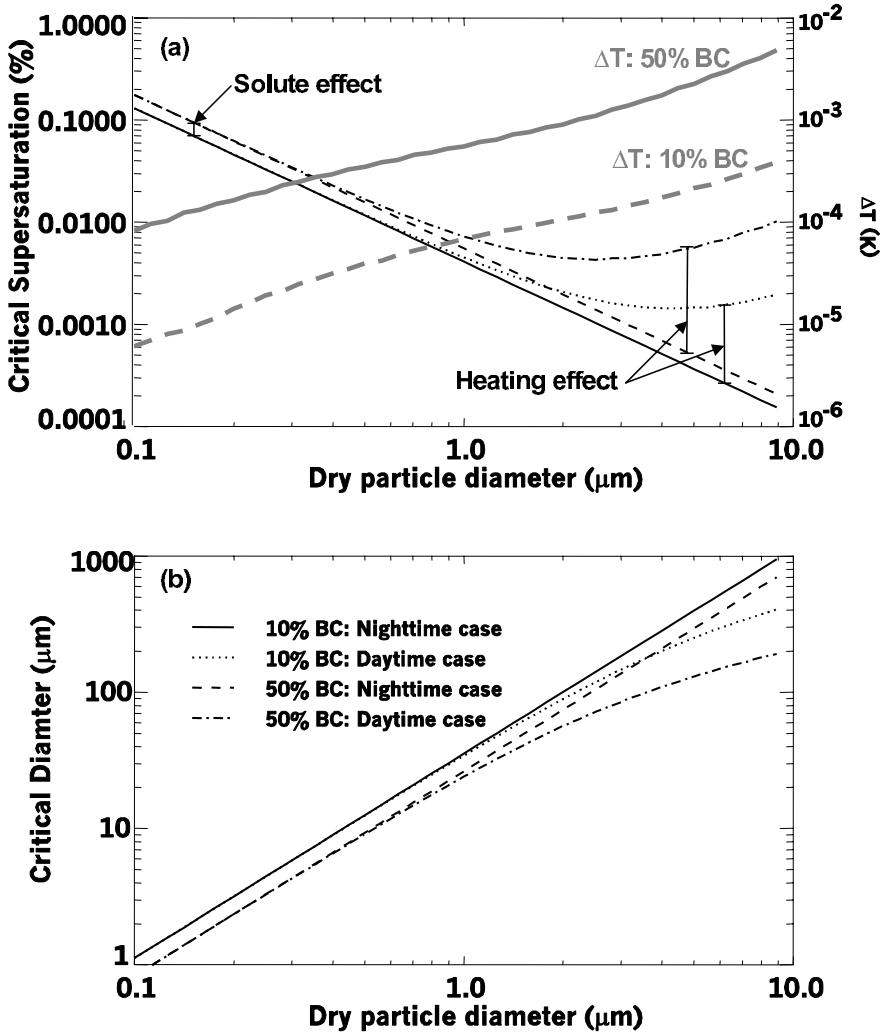

Figure 6.6: Effect of BC on **(a)** critical supersaturation, and **(b)** critical diameter. Four cases are considered: (6.1) 10% BC by mass and no heating; (6.2) 10% BC and heating by a 1000 Wm^{-2} actinic flux; (6.3) and (6.4) same as (6.1) and (6.2) but for 50% BC by mass. The difference between the no heating cases (6.1) and (6.3) is caused by the reduced sulfate mass in the 50% BC case compared to the 10% BC case. The heating effect is apparent as a divergence between the heating and no heating cases towards large particle sizes. The perturbation in droplet temperature at critical diameter is shown as the thick, gray lines in (a). The legend in (b) applies to both (a) and (b).

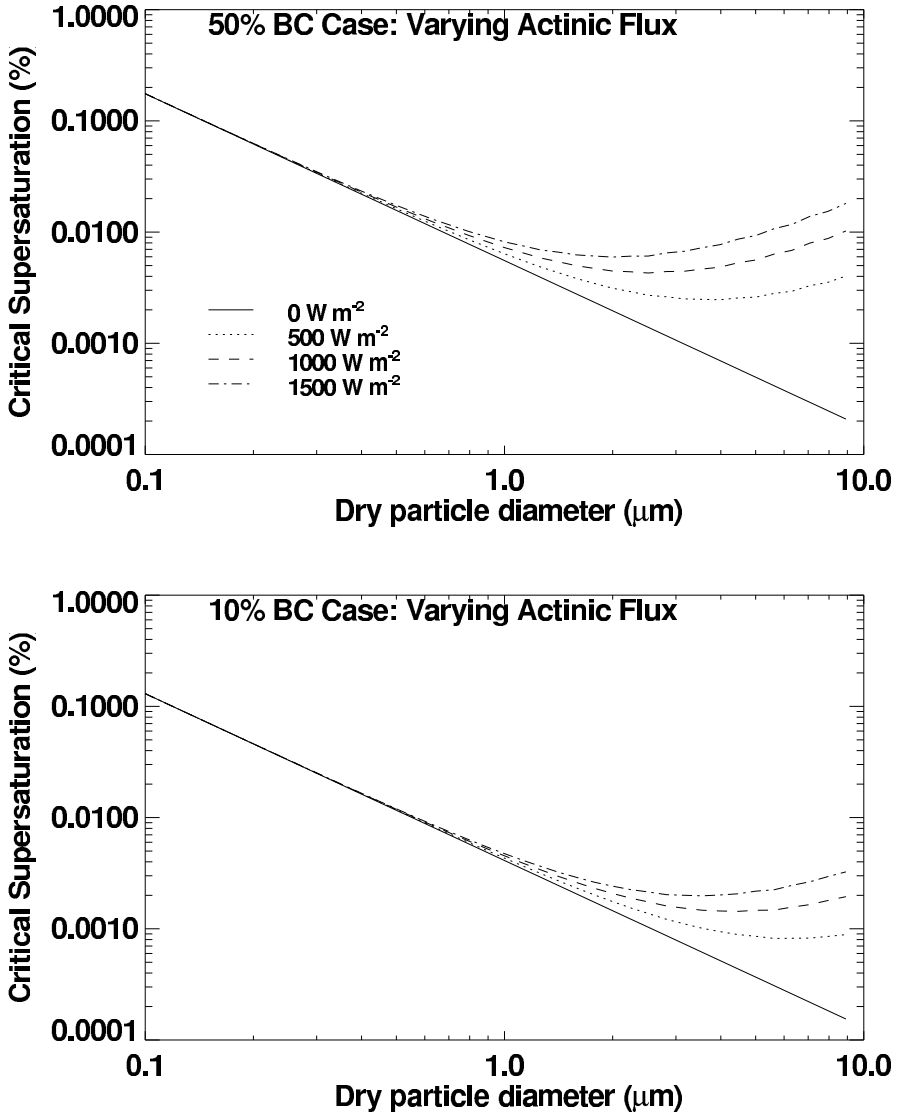

Figure 6.7: Illustration of the impact of actinic flux on critical supersaturation for **(a)** 50% BC by mass, and **(b)** 10% BC by mass. The effect of increasing actinic flux is to increase the lowest possible critical supersaturation, s_{low}, for particles of a given composition and to decrease the dry particle diameter, d_{low}, at which this minimum occurs.

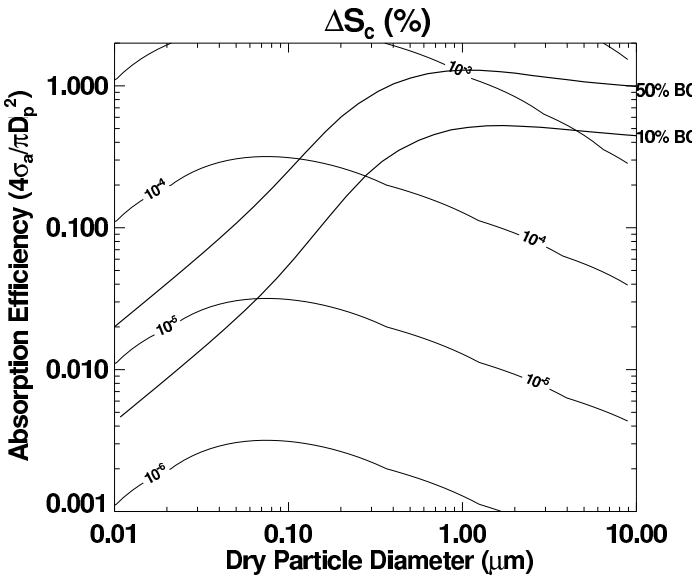

Figure 6.8: Change in critical supersaturation computed for dry particles as a function of particle diameter and absorption efficiency, Q_{abs}. Contours delineate values of Δs_c. The solid and dashed lines represent the relationship between Q_{abs} and d_p for dry aerosols composed of 100% BC and 10% BC, respectively. The calculation of Δs_c includes the enhancement of heating caused by the encapsulation of the soot core in the droplet.

diameter. For the case of 10% BC mass fraction, $d_{low} \cong 4\mu$m, meaning dry particles at 4 μm have the lowest s_c relative to larger and smaller particles. For clouds with slow cooling rates, this suppression of the activation of the largest CCN may impact the rate at which the larger particles uptake liquid water, with potentially important effects on the water mass balance during cloud formation.

The magnitude of the change in critical supersaturation is shown in Figure 6.8 as a function of the dry particle diameter and absorption efficiency. The relationship between dry diameter and absorption efficiency for the two cases of 50% BC and 10% BC is repeated in Figure 6.8. The magnitude of critical supersaturation increase for 10% BC aerosol ranges from 10^{-4}% to about 2×10^{-3}% as aerosol dry diameter ranges from 0.3 μm to 10 μm. The maximum impact of heating shown here is to elevate the critical supersaturation of 10 μm 50% BC particles by 0.01 percentage units, which can be compared to the 0.02%–0.25% median critical supersaturation associated with marine cumulus cloud drops [153].

6.4 Effect of black carbon radiative heating on CCN spectra

To understand the implications of droplet heating for cloud activation, we consider the change in the CCN supersaturation spectrum for three aerosol distributions. The CCN supersaturation spectrum $N_{CCN}(s_c)$ is that property of an aerosol population defined as the number of particles (cm^{-3}) that have critical supersaturations less than s_c. $N_{CCN}(s_c)$ is a monotonically increasing function of s_c, and approaches the total aerosol concentration as $s_c \rightarrow \infty$. The three cases considered here are based on modeled and observed size distributions and varying assumptions about BC heating. The first two cases comprise three-mode lognormal size distributions from the observations of [160] that were chosen to represent urban and clean continental aerosols.

The third case uses size distributions of North Indian Ocean aerosol observed from ship during the Indian Ocean Experiment (INDOEX) [130]. Extensive observations of aerosol size distribution, composition, and mixing state were made, affording a detailed analysis of the BC heating effect in this region where BC ranged from 10%–15% of the dry aerosol mass [120, 97]. Size distribution measurements are taken from the tandem differential mobility analyzer and aerodynamic particle size measurements of [14]. Each aerosol particle is assumed to be an internal mixture of BC and sulfate, based on findings using time-of-flight aerosol mass spectrometry that each BC particle was coated with sulfate and/or organics, and few anthropogenic particles were found without soot inclusions [97]. (This treatment neglects the presence of pure seasalt aerosol, which may have been more prevalent than anthropogenic particles at the largest sizes.)

Figure 6.9 a-c illustrates the supersaturation spectrum, $N_{CCN}(s_c)$, calculated for pure sulfate, 10% BC, and 50% BC for each of the size distributions described above. Some of the differences seen between the three compositional cases can be explained by the solute effect that was illustrated in Figure 6.6, and some of the differences are due to the heating effect. For each case that includes the radiative heating, $N_{CCN}(s_c)$ remains 0 until s_c exceeds the threshold critical supersaturation s_{low}. The effect of BC radiative heating on the supersaturation spectrum is isolated from solubility effects in Figures 6.9 d–f by illustrating the percent change in supersaturation spectrum from the nighttime case (no heating) to the daytime case (actinic flux of $\sim$1000 W m^{-2}). Despite the variations in the aerosol size distributions considered here, we consistently see that the 10% BC case

predicts a 1% reduction in CCN for $s_c = 0.03\%$ supersaturation, and that the 50% BC case predicts a 7%-10% reduction in CCN at this supersaturation. For all cases, the change in supersaturation spectrum is less than 1% for values of s_c exceeding 0.08%.

6.5 Effect of radiative heating on time-dependent droplet activation

This study has addressed the equilibrium Köhler theory that is the foundation for theory and models of cloud and droplet activation. The following discussion demonstrates the applicability of the equilibrium theory described above to the non-equilibrium equations underpinning cloud activation theory.

Droplet activation theory is expressed by the equations relating energy and mass flux between the droplet and the ambient atmosphere. The time-rate of change of temperature is given by the energy balance,

$$m_p c_w \frac{dT_p}{dt} = \Phi - 2\pi k'_{air} D_p \left(T_p - T_a\right) + \Delta H \frac{dm_p}{dt} \tag{6.18}$$

The term on the left is the rate of change of internal particle energy, where m_p is the particle mass and c_w is the heat capacity of water (J kg^{-1} K^{-1}). The terms on the right side of (6.18) are, respectively, the radiative heating from equation (6.1), the conductive heat loss from equations (6.2) and (6.3), and the condensational heat gain, where changes in mass are assumed to be solely due to condensation/evaporation. Note that in steady state, m_p and T_p are constant in time, and equation (6.18) reduces to (6.4). Scaling arguments can be used to show that the heat content term plays a minor role in the energy balance. Thus the temperature difference $\Delta T = T_p - T_a$ can be obtained in terms of the equilibrium temperature difference from (6.4), (hereafter ΔT_{eq}) plus the effect of condensational heating, ΔT_{con},

$$\Delta T = \frac{\Phi + \Delta H \frac{dm_p}{dt}}{2\pi D_p k'_{air}} = \Delta T_{eq} + \Delta T_{con} \tag{6.19}$$

The time rate of change of particle mass is governed by diffusion of water vapor to/from the droplet surface, which is conventionally expressed as proportional to the difference in water vapor concentration between the droplet and the ambient [143]. Thus, the mass flux

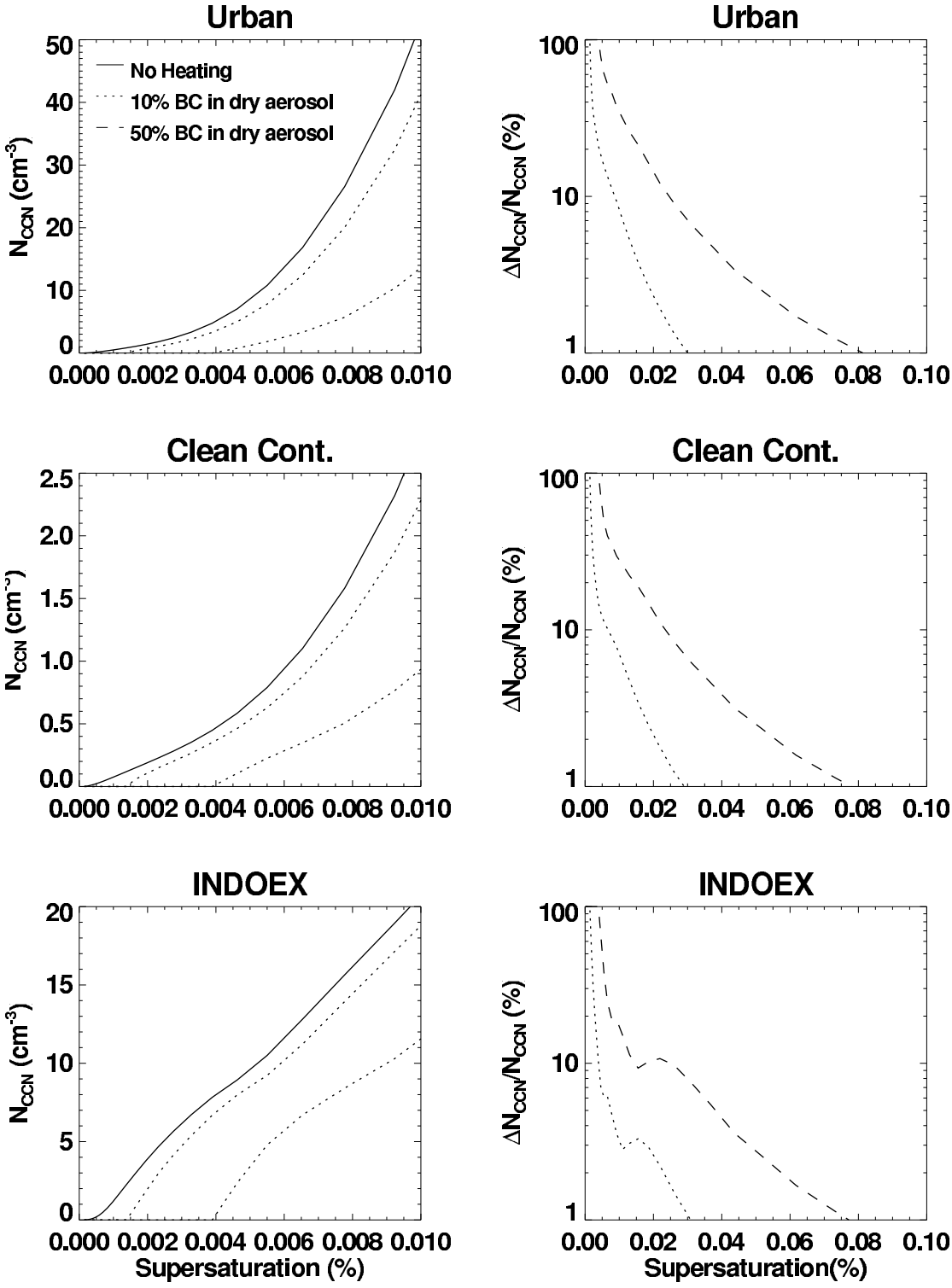

Figure 6.9: **(a)-(c)** CCN spectrum calculated from size distributions assuming each particle is either pure sulfate, 10% BC by dry mass, or 50% BC. Cases (a)-(b) are calculated from [160] size distributions, case (c) from INDOEX. Effects of BC seen in (a)-(c) are partially due to the solute effect (see Figure 6.6.) **(d)-(f)** BC heating effect on CCN spectrum. The percent perturbation in CCN spectrum between nighttime (no heating) and daytime (heating) corresponding to (a)-(c), respectively, are shown as a function of supersaturation for both the 10% BC and 50% BC cases.

in the presence of a small temperature gradient is

$$\frac{dm_p}{dt} = \rho_w \frac{\pi}{2} D_p^2 \frac{dD_p}{dt} = 2\pi D_p \frac{D_v^{'}}{RT_a} \left[p_{w,a} - \frac{T_a}{T_p} p_w(T_p, D_p) \right] \tag{6.20}$$

where $p_{w,a}$ is the ambient vapor pressure, and $D_v^{'}$ is the diffusivity of water vapor in air corrected for noncontinuum effects and the mass accommodation coefficient. For the steady-state case, (6.20) prescribes zero net vapor concentration gradient. The equations for the equilibrium Köhler curve in the presence of radiative heating, (6.6)-(6.8), when combined with (6.20) yield,

$$D_p \frac{dD_p}{dt} = \frac{4 M_w D_v^{'}}{\rho_w} \frac{p^{\circ}(T_a)}{RT_a} \left[S_a - S_p \frac{T_a \exp\left(\frac{\Delta H M_w}{RT_a^2} \Delta T_{con}\right)}{T_a + \Delta T_{con}} \right] \tag{6.21}$$

where S_a is the ambient saturation and S_p is the particle equilibrium saturation. The term to the right of S_p is due to modification of particle saturation due to condensational heating. Because ΔT_{con} is proportional to droplet growth rate (6.19) and $\Delta T_{con} \ll T_a$, we have (after some algebra),

$$D_p \frac{dD_p}{dt} = \frac{S_a - S_p}{\frac{\rho_w R T_a}{4 p^{\circ}(T_a) D_v^{'} M_w} + \frac{\Delta H \rho_w}{4 k_a^{'} T_a} \left(\frac{\Delta H M_w}{RT_a} - 1 \right)} \tag{6.22}$$

Equation (6.22) is identical to the growth equation in the absence of radiative heating [143]. The radiative effect is contained within the modified equilibrium particle saturation, S_p, defined in (6.8), subject to the simplifications quantified in Table 6.1. Thus, the effects of radiative heating on droplet growth rate can be implemented using the modified Köhler curve, obviating the need to explicitly calculate the time-dependent droplet temperature perturbation.

6.6 Conclusion

In this study we have examined the effect of the radiative heating of black carbon (BC) on the critical supersaturation spectrum of internally mixed aerosol. Radiative heating raises the critical supersaturation of BC-containing CCN, thus reducing the number of particles available for activation at a given maximum supersaturation. The effect is found to be strongest for large aerosol particles with high BC mass fractions. For a 10% BC dry

mass fraction at all aerosol sizes, over several aerosol size distributions considered, only about a 1% reduction in CCN is predicted at 0.03% critical supersaturation. At a critical supersaturation of 0.01%, the reduction in CCN can be nearly 10%. This equilibrium heating effect is expected to be most important for clouds formed at low cooling rates (e.g., stratus clouds and radiative fogs). Although we did not consider the case of contrails or high altitude stratiform clouds here, we can speculate that the heating effect may be important in their formation due to high observed BC fractions [126], low thermal diffusivity, and high actinic fluxes. Perturbations to the supersaturation spectrum are known to have highly nonlinear effects on the resulting cloud drop concentration, and hence indirect radiative forcing [121]. To assess the impact of black carbon radiative heating on cloud albedo, [116] incorporate radiative heating into a detailed cloud parcel model that explicitly accounts for the complex processes linking cloud albedo to the aerosol on which the cloud forms.

6.7 Acknowledgments

This work was supported by Office of Naval Research grant N00014-96-1-0119.

Chapter 7

Black carbon radiative heating effects on cloud microphysics and implications for aerosol indirect forcing: 2. Cloud microphysics

Note: This chapter appeared as reference [116].

7.1 Abstract

This work examines the effect of black carbon (BC) radiative heating on cloud droplet formation. Changes in cloud droplet concentration and cloud albedo due to the presence of black carbon are computed for different cases of aerosol size distributions, meteorological conditions, BC mixing state, and aerosol composition. We examine the effect of three new mechanisms (that result from BC heating) that can affect cloud droplet number and lifetime. Two of these mechanisms act to *increase* cloud droplet number or lifetime: *i*) the ability of BC to decrease the collection efficiency of giant CCN, and, *ii*) the delayed growth of low S_c CCN that allow higher S_c CCN to form droplets. These two mechanisms complement each other in terms of increasing cloud droplet number, since it is shown that the former is most efficient at strong updrafts, and the latter at low updraft velocities. A third mechanism identified, gas-phase heating (which is different from the so-called "semi-direct effect") in our simulations acts to decrease LWC, and thus albedo; however the droplet number concentration does not change significantly due to dynamic readjustments in cloud supersaturation. The simulations indicate that the mixing state of BC with the CCN population can have an important influence on the effect of BC heating on the droplet

population. Although additional work is necessary to fully assess the effects of BC heating on cloud microphysics and climate, this work shows that these effects are more complex than currently thought.

7.2 Introduction

Black carbon (BC) has important effects on climate, owing to its ability to absorb incoming shortwave radiation. Heating of air masses containing BC is predicted to lead to changes in large-scale atmospheric circulation [61]. On smaller scales, heated air masses can also exhibit increased static stability, reducing convective activity and cloud coverage [6]. [102] studied the competition between BC warming and sulfate indirect aerosol cooling and concluded that sulfate cooling prevails globally. The authors note that their simulations likely underestimate BC effects, since they neglected the enhancement of BC absorption when included within cloud droplets [25, 48].

Heat released by BC included within the CCN populations can also hinder their ability to activate; the energy absorbed acts to increase the droplet temperature and the critical supersaturation ([28], hereafter referred to as"Part 1"). The change in cloud condensation nucleus (CCN) activation spectrum from this heating was studied in Part 1; a reduction in CCN concentration between 1 and 10% (depending on the cloud parcel maximum supersaturation and the CCN BC mass fraction) is seen when compared to the same CCN without heating present.

For typical atmospheric conditions, the reduction in CCN from BC heating is expected to be on the order of a few percent. Although these changes are minor, numerous microphysical (and previously unaccounted) mechanisms arise that can magnify the effect on the droplet population. One of the reasons for this is that BC heating selectively affects CCN with a low critical supersaturation, S_c. Although these particles would eventually form droplets in typical cloud updrafts, their transformation is delayed compared to the rest of the CCN population; this delay allows water vapor, which would otherwise condense on these larger CCN, to condense on aerosol of higher S_c. Second, the energy released from the radiative heating will conduct into the gas phase, affecting parcel temperature and supersaturation. Finally, additional dynamical adjustments in the cloud supersaturation (because of the change in droplet number and cooling rate) can further change the supersaturation profile

that develops in the cloud. Depending on the dominant mechanism, BC heating can either decrease or increase the droplet concentration throughout the cloud column.

Droplet number concentration can also be affected by another mechanism previously unaccounted for: by decreasing the efficiency of Giant Cloud Condensation Nuclei (GCCN, here defined as particles that have a diameter larger than 5 μm) in initiating the formation of drizzle. It is well known that GCCN can form haze drops that are large enough to initiate drizzle formation. Usually, the size needed to be attained to initiate drizzle is about 38-40 μm diameter [38]. When BC is present in these particles, their growth can be slowed down enough to decrease their size and ability to form drizzle. If this happens, the cloud droplet number concentration would increase (when compared to a non-heated cloud, where drizzle has formed), potentially leading to a more reflective and persistent cloud.

If all these aerosol-cloud interactions are important, then knowledge of the total BC heating rate (an approach used in previous studies) is not sufficient to fully characterize BC effects on climate; additional information regarding the size distribution and mixing state of BC (within the CCN population) and the influence on cloud droplet concentration is necessary.

We estimate here the potential climatic significance of the BC-cloud microphysical mechanisms previously identified. A cloud parcel model with explicit microphysics, modified to account for the effects of radiative absorption on the gas-phase and droplet energy balance, is used to simulate the growth of CCN to form cloud droplets. Simulations are carried out for a suite of conditions representative of regions with varying degrees of anthropogenic influence and aerosol mixing state so that the importance of each mechanism (including those that tend to increase cloud drop number and albedo) is explored. In assessing the effect of radiative heating on the ability of giant CCN to initiate precipitation we also use a parcel model coupled with Lagrangian trajectories derived from an LES simulation of a stratocumulus cloud.

7.3 Effects of BC heating on cloud microphysics

Here we discuss in depth the various mechanisms that were briefly touched upon in the introduction. Since all the mechanisms studied in this work result from BC warming, the term "positive feedback," is used to characterize a mechanism that tends to further warm

the climate system (usually because of a decrease in cloud droplet number), while "negative feedback" is used for characterizing cooling mechanisms (usually because of an increase in cloud droplet number).

7.3.1 Extended Köhler theory

It has been shown (Part 1) that in addition to providing insoluble material, BC can heat up a droplet sufficiently to change its CCN activation characteristics. This effect can be expressed in terms of a modified Köhler equation for the equilibrium saturation ratio, S_{eq},

$$S_{eq} = \exp\left[\frac{A\,(1+\gamma_a)}{D_p} - \frac{B}{D_p^3 - d_u^3}\right] \tag{7.1}$$

$\gamma_a = \frac{\rho_w \Delta H_v \Phi}{8\sigma\pi k_a' T}$ is the "heating parameter," where ΔH_v latent heat of condensation of water, Φ is the heating rate per particle, ρ_w density of water, σ water surface tension, T is the droplet temperature and k_a' is the thermal conductivity of air. Furthermore, D_p is the wet diameter, d_u is the diameter of the insoluble core, and $A = \frac{4M_w\sigma}{RT\rho_w}$, $B = \frac{6n_s M_w}{\pi\rho_w}$, are standard Köhler theory parameters, with M_w being the molecular weight of water, R is the universal gas constant, and n_s is the number of moles of ions in solution. Φ is sensitive to the radiation field, the mass of black carbon in the droplet, and the diameter of the droplet. Generally Φ increases with increased BC mass, although the rate of increase is a complex function of the size and geometry of the BC inclusion and the droplet. Part 1 provides a detailed discussion of this dependence for the simple case of a spherical BC inclusion at the center of the droplet under cloud-free skies. The uncertainty in Φ associated with these simplifications is generally within 50%.

Radiative heating changes the Köhler curve by multiplying the Kelvin term A/D_p with a factor of $(1+\gamma_a)$. This tends to increase the critical supersaturation, S_c, of CCN (because $\gamma_a > 0$) and implies that fewer CCN will tend to activate (under constant ambient supersaturation) than in the absence of heating. Thus, this effect represents a positive feedback since the decreased droplet concentration would lead to less reflective clouds and diminish their cooling effect. This implicitly assumes that supersaturation and liquid water profiles within a cloud do not change, whether radiative heating is present or not. Dynamical adjustments and gas-phase heating can change parcel supersaturation profiles between heated

and non-heated CCN; these effects have to be considered for a comprehensive assessment of BC on droplet number.

7.3.2 Dynamical adjustments in cloud supersaturation

Dynamical adjustments are seen in cloud supersaturation whenever the CCN population changes. In the case of BC heating, the lower critical supersaturation portion of the "CCN spectrum" (defined as the number of CCN that can activate as a function of supersaturation) shifts towards higher S_c; this physically means that the rate of water absorption in the early stages of cloud formation is decreased (since fewer particles activate). As a result, the parcel S_{max} increases accordingly, until enough droplets form to consume the available water vapor. This response in parcel supersaturation acts to restore the original cloud droplet number.

Dynamical adjustments in parcel supersaturation can lead to non-monotonic activation behavior. For example, when seasalt and sulfate compete as CCN, under certain conditions the presence of additional CCN can lead to a decrease (as opposed to an increase) in droplet number [57, 147]. In the case of radiative heating, the opposite may happen: by selectively inhibiting low S_c particles from scavenging water vapor (which has been shown in Part 1 to be the main effect of BC heating on droplet thermodynamics), particles of higher S_c, which are less susceptible to kinetic limitations [117] and more numerous, may compensate for the initial loss in droplets.

7.3.3 Gas-phase heating

Heat released from the particles to the gas phase has an influence on parcel supersaturation, because the effective parcel cooling rate is decreased. This tends to decrease the cloud maximum supersaturation, S_{max}, and fewer CCN will tend to activate. The result is lower droplet concentrations and liquid water, and with it, decreased cloud optical depth and albedo. This means that gas-phase heating can have a positive climate feedback, i.e., additional warming, from decreased cloud coverage and albedo. This type of feedback is different from the "semi-direct" mechanism proposed by [61], because it reflects the effect of gas-phase warming on parcel supersaturation and cloud droplet number, not on static stability and the consequences thereof.

It should be noted that the previous discussion assumes the CCN spectrum between heated and non-heated parcels remains the same. This is not true if the BC is contained

within the CCN; in this case, the nonlinear interplay between droplet number, cloud supersaturation and liquid water need to be considered. The knowledge of ambient meteorological conditions and CCN spectrum may not be sufficient to fully describe droplet formation. It is possible that two identical CCN spectra, one corresponding to pure salt and one composed of a mixture of salt and BC, still produce different droplet concentrations for identical meteorology (because gas-phase heating in the second population lowers the S_{max} compared to the first aerosol). This is an important point; traditional thinking holds that identical CCN spectra yield the same droplet concentrations for given ambient conditions.

Gas-phase heating effects can be important even for negligible changes in the CCN spectrum. Cases where this will happen are: *i*) if the absorptive species are located primarily in the smaller CCN (so that γ_a for each droplet becomes negligible), *ii*) if the absorptive species are externally mixed in the CCN population, or, *iii*) if the parcel S_{max} is outside the region of influence of radiative absorption on the CCN (i.e., is not on the "lower end" of the spectrum), but the BC heating rate is comparable to the parcel cooling rate.

Heating of the gas phase can be important without appreciable changes in the CCN spectrum, but the reverse is not seen; important gas-phase heating is always present when the number of CCN are influenced by BC inclusions. This can be illustrated by the following order of magnitude calculation. It was shown in Part 1 that a heating parameter $\gamma_a \approx 0.1$, or a heating rate of order 10^{-9} W per particle, is required for a droplet to experience appreciable changes in its S_c. Assuming $\gamma_a = 0.1$ and that radiative heating affects 10 drops cm^{-3} (which is a few percent of the total droplet concentration for polluted conditions) and that BC is contained only in these 10 drops, a total heating rate of 10^{-5} K s^{-1} is computed (assuming $c_{p,air} = 10^3$ J kg^{-1} K^{-1}, and $\rho_{air} = 1$ kg m^{-3}). An updraft of 10^{-2} m s^{-1}, following a moist adiabat of -5.8×10^{-3} K m^{-1} (which corresponds to 1000 mbar and 273 K), produces a cooling rate of -5.8×10^{-5}K s^{-1}. We observe that the BC heating rate and the updraft cooling rates are of the same order, meaning that the parcel (in this example) experiences a nontrivial decrease in cooling rate. As a result, parcel supersaturation, being a strong function of cooling rate, will also drop. Thus, even for conditions where gas-phase heating is minimum and droplet number is maximum, gas-phase heating cannot be neglected. In reality, particles containing BC can reside in the interstitial aerosol, further increasing the heating rate.

An important issue is the resulting effect of gas-phase heating on the cloud dynamics.

An immediate effect of the released heat is to increase the buoyancy of the cloud parcel; this would tend to accelerate the cloud parcel, and effectively lead to additional activation of cloud droplets. The former effect is another negative feedback, since the additional activated CCN can enhance cloud albedo. This is an effect relevant for activation timescales ($\sim$ 1 min), as for longer timescales, radiative heating tends to destabilize the stratocumulus cloud layer by decreasing the efficiency of radiative cooling at the top of the cloud layer [6, 7]. All these effects can be adequately addressed only with a full cloud resolving model, so, for the purposes of this study, we decouple the feedback of BC heating on parcel dynamics with the intent of addressing these issues in the future.

7.3.4 Effect of aerosol mixing state and composition on heating effects

A consequence of the gas phase-droplet energy coupling is that the mixing state of the BC within the CCN population may play an important role in the overall effects of BC heating on cloud microphysics. This is embodied in the following question: "If the BC is assumed to heat only the gas phase, without perturbing the CCN spectrum (i.e., an externally mixed BC population), how would the resulting cloud compare, in terms of droplet number and aerosol optical properties, to that when the BC is internally mixed in the CCN population?" In lieu of the feedback mechanisms, it becomes unclear which mixing state would produce fewer drops and liquid water content (LWC).

7.3.5 Effect of heating on GCCN

While black carbon is normally associated with particles of submicron size, an interesting, and unrecognized, effect of BC absorption on the growth of GCCN arises if absorbing material is present in such particles: by changing the behavior of giant CCN (GCCN), defined as particles with a dry diameter larger than 5 μm. Numerous studies (e.g., [38]) have investigated the catalytic role of GCCN in initiating precipitation. For situations in which absorbing material is present in large enough quantities, radiative heating can delay their growth; if this happens, the number of collector drops will decrease, and the probability for drizzle formation is reduced. In contrast to the radiative heating effects on the gas phase and CCN spectrum, the effect on giant CCN constitutes a (counter-intuitive) negative climate feedback, i.e., this mechanism of BC heating would tend to *increase* the lifetime of clouds, and thus enhance their cooling effect.

7.4 Effects of BC heating on cloud droplet number

7.4.1 Cloud parcel and albedo models

To address all of the heating effects quantitatively, we simulate cloud albedo and droplet number concentration using an adiabatic cloud parcel model with explicit aerosol microphysics. The model of [117] is used, with two modifications. First, Equation (7.1) is used for computing S_{eq} in the droplet growth rates, and second, the energy released by BC absorption is included in the gas-phase (parcel) energy balance. γ_a is computed online, from the BC content and droplet diameter.

Cloud albedo, R_c, is estimated based on the two-stream approximation of a non-absorbing, horizontally homogeneous cloud [94],

$$R_c = \frac{\tau}{\tau + 7.7} \tag{7.2}$$

where τ is the optical depth, computed from the liquid water and effective radius profiles in the cloud. The effective radius is computed as the ratio of the third over the second moment of the droplet size distribution. Equation (7.2) neglects the reduction in single-scattering albedo from the presence of BC in the cloud, so that albedo changes are only a result of changes in effective radius and liquid water content.

The optical depth and albedo calculations we present here are not intended to be used for prognostic purposes, but only to diagnose the sensitivity of droplet nucleation and condensational growth to changes in the CCN population from the radiative heating. For this purpose, the use of Equation (7.2) should suffice. Expressing changes in terms of changes in effective radius and albedo gives a physically based measure of the importance of heating effects. This is important because albedo is sensitive not only to droplet concentrations, but also to changes in the LWC (which is important when the gas phase is heated). An analysis using effective radii and droplet concentrations cannot capture this dimension.

7.4.2 Aerosol distributions and simulation scenarios considered

It was shown in Part 1 that the CCN spectrum for pristine conditions is not significantly affected by heating; therefore, we focus primarily on aerosol representative of polluted air masses. The urban aerosol size distribution of [160] is used (Table 7.1), with an aerosol

assumed to be composed of BC (or insoluble material) and $(NH_4)_2SO_4$. Updraft velocities of 0.10, 0.25, and 0.50 m s^{-1} are examined. An emphasis is given to low values, since the BC heating effects are most prominent at low updraft (or cooling) rates. The initial parcel temperature, pressure, and relative humidity are 298K, 800 mbar, and 96% respectively. BC warming is assumed to begin from cloud base, i.e., the parcel does not experience heating until it reaches saturation. In reality, the parcel containing BC will experience heating even before it becomes saturated, and thus, will differ from the non-heated parcel. We chose to neglect this in order to have consistent LWC fields, and initial aerosol sizes at cloud base. We do not consider the vertical variation of actinic flux with cloud height. The heating rates Φ are computed using the procedure presented in Part 1.

Table 7.1: Aerosol distribution parameters (geometric radius $r_{g,i}$ in μm, number concentration N_i in cm^{-3}) [160]

Aerosol type	Nuclei Mode			Accumulation Mode			Coarse Mode		
	$r_{g,1}$	σ_1	N_1	$r_{g,2}$	σ_2	N_2	$r_{g,3}$	σ_3	N_3
Marine	0.005	1.6	340	0.035	2.0	60	0.31	2.7	3.1
Urban	0.007	1.8	106000	0.027	2.16	32000	0.43	2.21	5.4

Four heating "scenarios" are considered in the parcel simulations. The first is a simulation in the absence of radiative heating altogether ("NoHeat" scenario). In this case, the black carbon core acts solely as an insoluble inclusion. The second scenario assumes radiative heating to be present, but allows only for changes in the droplet thermodynamics ("Drop" scenario); that is, the droplet attains the steady state temperature profile and heats up, but no conduction of energy occurs into the gas phase. This scenario extends the analysis of Part 1 to find the effect of BC droplet heating on cloud activation. The third scenario represents a situation in which BC radiative heating influences only the gas phase. This scenario, referred to as "External," corresponds physically to a CCN population that contains a non-BC insoluble core externally mixed with a BC population that produces a total heating rate equal to that of the "Drop" scenario. Finally, a fourth scenario, named "Internal," represents the opposite situation where the black carbon is contained within the CCN, and the heat generated from the radiative absorption is allowed to affect both the gas-phase energy balance and the droplet thermodynamics. The four scenarios are illustrated in Figure 7.1.

Evaluating these four scenarios gives a comprehensive picture of the effect of radiative

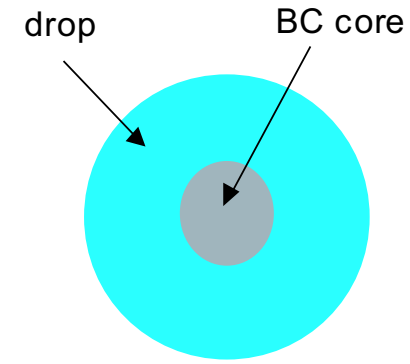

“NoHeat” scenario:

BC acts as an insoluble core

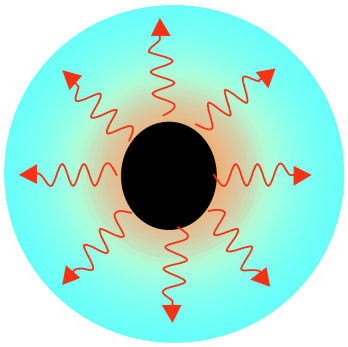

“Drop” scenario:

BC heats drop only

Heat does not affect surrounding gas phase

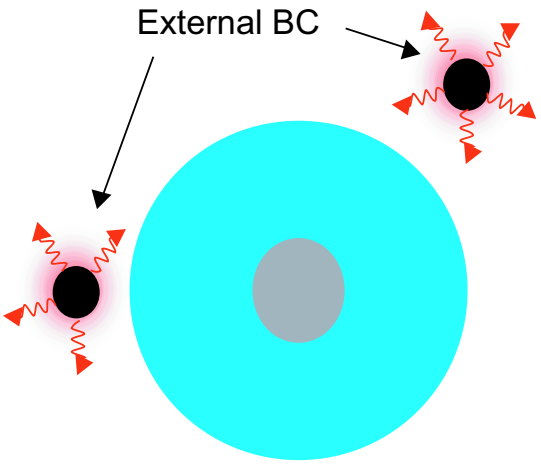

“External” scenario:

BC does not heat droplet

Energy from externally mixed BC affects gas phase

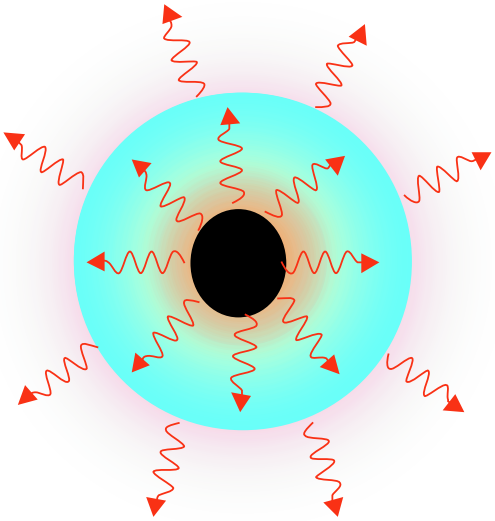

“Internal” scenario:

BC heats droplet

Energy dissipates to surrounding gas phase

Figure 7.1: Illustration of the BC heating scenarios considered in this study.

heating on droplet formation. The total heating rate, when BC is present, is the same among the scenarios, and the critical supersaturation spectra of the aerosol, in the absence of radiative heating, are identical. Thus, differences in cloud droplet number and cloud properties among the scenarios are due solely to the location of the heating and the feedbacks allowed to exist.

7.5 Dynamical simulations

Aerosol heating effects are quantified by comparing cloud albedo and effective radius between any two heating scenarios. The resulting difference, ΔR_c, in cloud albedo for a cloud of the same depth is a direct measure of the change exerted on the optical properties of a cloud.

Figures 7.2, 7.3 present typical parcel supersaturation, liquid water content and cloud droplet profiles for the different heating scenarios. The updraft velocity in these simulations is 0.25 m s^{-1}, while the aerosol is assumed to be 50% BC (the large value of BC fraction was selected so that the effects of heating on the parcel LWC and supersaturation are clearly identified). As expected, the liquid water contents of the "NoHeat" and "Drop" scenarios are the same (after cloud base is reached). This is because the in-cloud lapse rates are identical, as a result of the gas-phase energy balance being identical in these two cases. Similarly, the liquid water content profiles of the "External" and "Internal" scenarios are similar, but differ from the "NoHeat" scenario. The cloud maximum supersaturation varies by 10% for the different heating scenarios when compared to the "NoHeat" scenario ($S_{max} = 0.0660\%$); supersaturation increases in the "Drop" scenario (S_{max}= 0.0695%), and decreases for the "External" (S_{max}= 0.0630%) and "Internal" (S_{max}= 0.065%) scenarios. These supersaturations are within the range of reported values for polluted stratocumulus clouds and fogs [69, 70]. The changes in S_{max} may appear small, but are sufficient to reflect important changes in particle growth kinetics between the scenarios (Figure 7.3); the "Drop" scenario responds the quickest to form droplets, due to the accelerated response of higher S_c CCN. The "NoHeat" scenario responds almost as fast, while the "Internal" and "External" scenarios take longer to form droplets. The "Internal" scenario, for the same reasons as "Drop" forms droplets more quickly than "External," which even at 125 m cloud depth has not formed all of its droplets. The S_{max} values for these simulations correlate

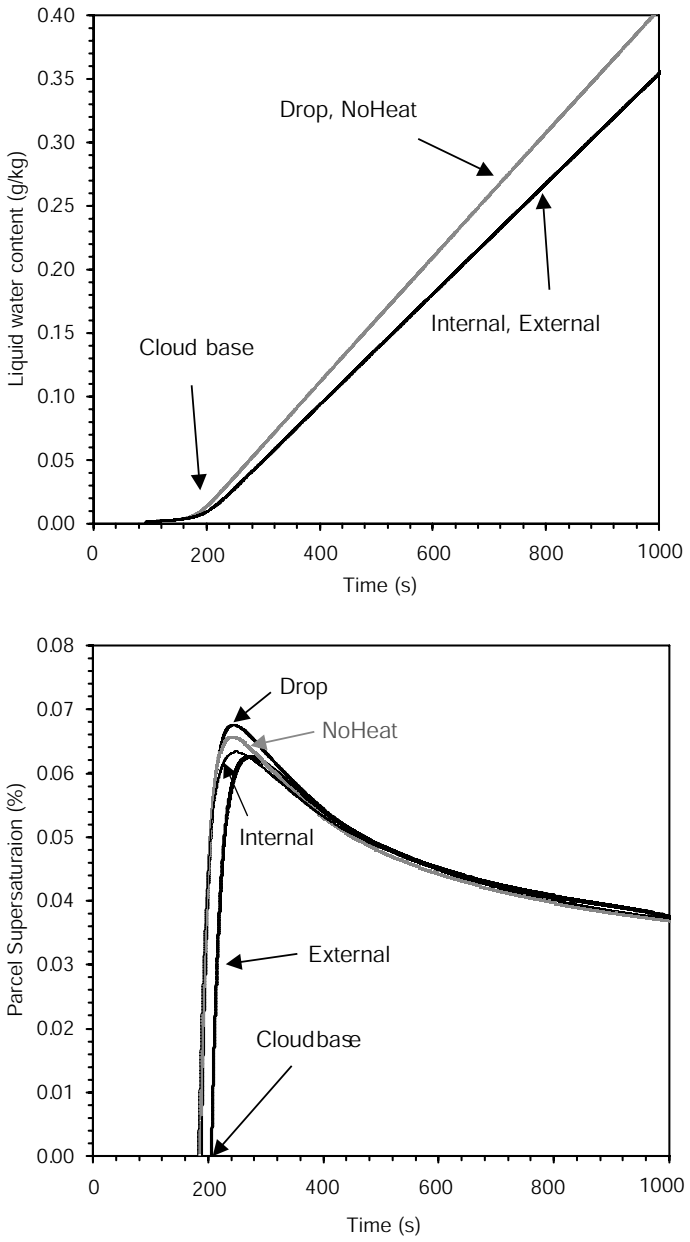

Figure 7.2: Parcel liquid water content (a) and supersaturation (b) profiles for four different radiative heating scenarios. Updraft velocity is 0.25 m s^{-1} and BC content is 50%.

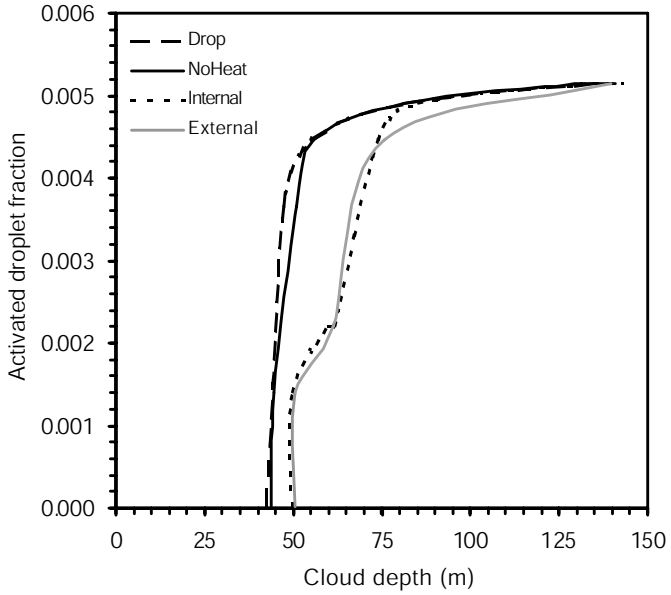

Figure 7.3: Parcel droplet activation ratio for the simulations of Figure 7.2.

well with the droplet activation behavior shown in Figure 7.3.

Table 7.2: Effective radius (at 140 m cloud depth) and maximum supersaturation (%) for the parcel simulations in Figures 7.4 and 7.5

Simulation	r_{eff}, 10% BC	r_{eff}, 20% BC	S_{max}, 10% BC	S_{max}, 20% BC
External	5.17	5.20	3.00×10^{-2}	3.12×10^{-2}
Internal	5.15	5.26	3.05×10^{-2}	3.17×10^{-2}
Drop	5.21	5.33	3.12×10^{-2}	3.35×10^{-2}
NoHeat	5.24	5.36	3.08×10^{-2}	3.27×10^{-2}

We now examine lower BC fractions, which are within atmospheric observations. Figures 7.4 and 7.5 show the liquid water content, and the albedo difference between heating scenarios, as a function of cloud depth. The BC mass fraction is 0.1 and 0.2, and the updraft velocity is assumed to be 0.1 m s^{-1}. The presence of radiative heating has an important effect on cloud properties. This can be seen in the values of effective radius and S_{max} (Table 7.2). The "Drop" effective radius is slightly smaller than for "NoHeat" in the initial stages of the cloud; dynamic adjustment mechanism in cloud supersaturation, which tends to form slightly more droplets in the "Drop" scenario. As a result, the "Drop" scenario leads to slightly higher optical depths and albedo. The situation is quite different for the "External" scenario, where differences in albedo with "NoHeat" can be explained from the

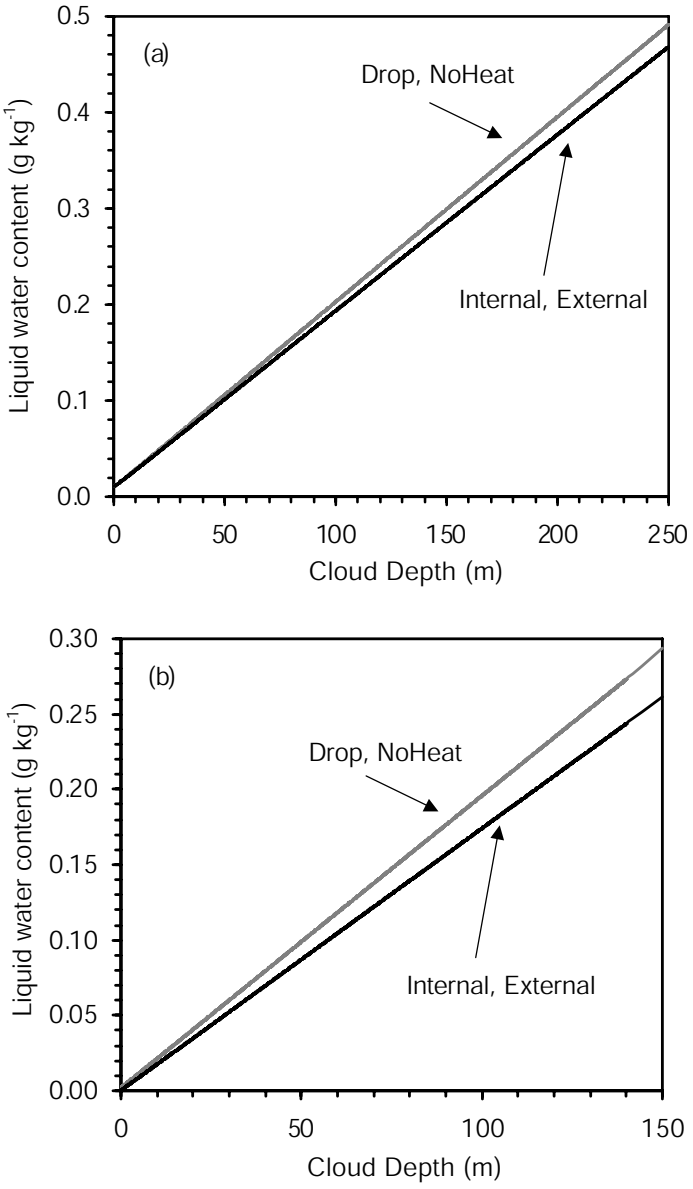

Figure 7.4: Liquid water content between heating scenarios as a function of cloud depth. The BC mass fraction is (a) 0.1, and (b) 0.2. The updraft velocity is assumed to be 0.1 m s^{-1}.

reduced parcel LWC in the former scenario (even though the effective radius is smaller than in the "NoHeat" scenario). The maximum albedo difference between the two scenarios is 0.009 for 10% BC and 0.024 for 10% BC, at a cloud depth of 150 m. The albedo difference for the "Internal" and "External" scenarios looks similar. The "Internal" scenario however exhibits the smallest albedo difference; given their identical LWC, the difference arises from changes in effective radius (which is a result of the different timescales of droplet formation). S_{max} varies between 4 and 5%, while effective radius varies between 2 and 4 %.

Simulations for other updrafts indicate that, whenever the heating rate is non-negligible (compared to the adiabatic cooling rate), an effect is seen on cloud properties. The magnitudes of each feedback of course vary, but both positive and negative feedbacks are seen. What also can be seen in the Figure 7.5 is that the mixing state of the black carbon can have an important effect on the cloud optical properties. As the LWC between the "Internal" and "External" scenarios are the same, this difference is due to the dynamical readjustments in parcel supersaturation. Furthermore, the simulations indicate that the assumption of externally mixed BC with the CCN population would tend to maximize the effects of BC heating. We should note that we have assumed the same gas-phase heating rate from the BC, regardless of its mixing state within the CCN population. In reality, externally mixed BC would heat the parcel less efficiently [25, 48]; the difference between mixing states may therefore be smaller, but qualitatively unchanged.

7.6 Radiative heating and giant CCN

It can be shown that, based on its effect on critical supersaturations, BC does not increase the S_c of GCCN enough to inhibit their strict activation for supersaturation typically found in clouds. However, the critical radius of GCCN is too large (hundreds of μm or larger) to be attained in clouds through the mechanism of diffusional growth, and GCCN can effectively initiate precipitation at much smaller sizes that its critical diameter. Therefore, it is necessary to study the kinetics of GCCN growth in order to get a more comprehensive picture of the sizes these particles attain in clouds.

Two approaches are used in order to study the growth of GCCN. In the first approach, we use simple adiabatic cloud parcel theory to assess the time needed for GCCN to grow to a large enough size to effectively initiate drizzle formation. This approach allows us to

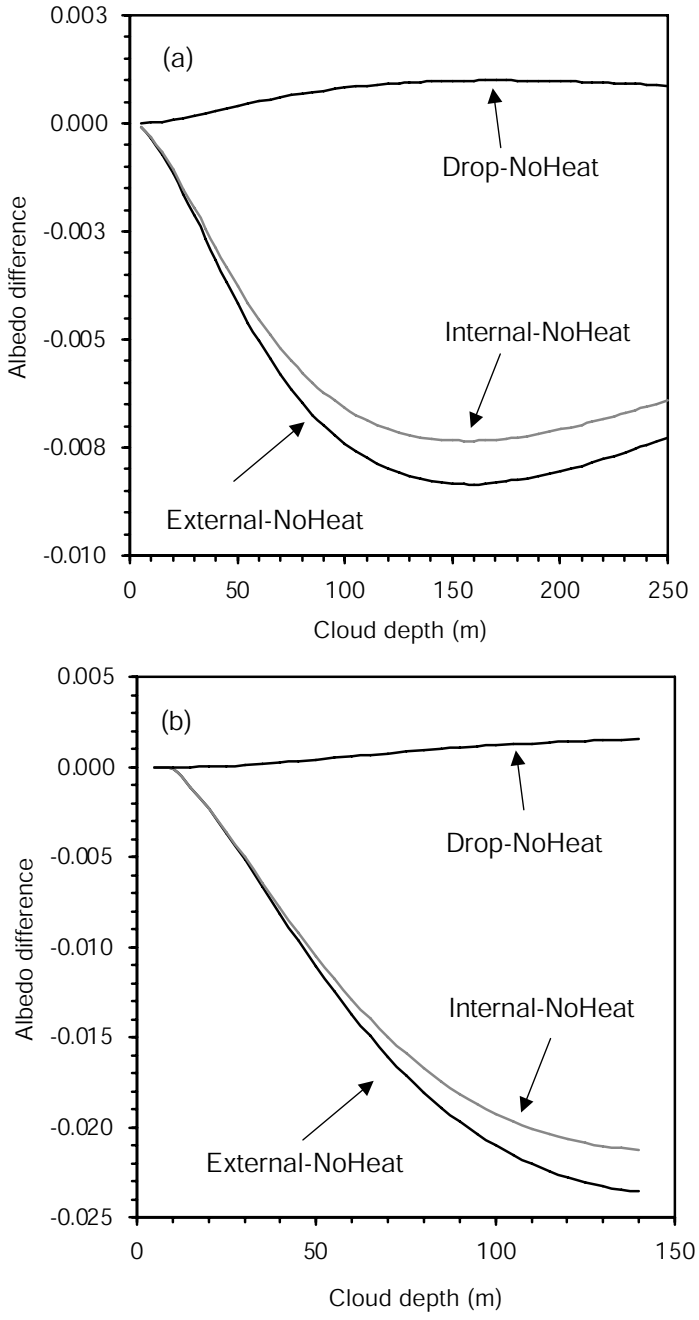

Figure 7.5: Albedo difference between the curves of Figure 7.4, as a function of cloud depth.

systematically explore parametric space and determine the conditions of updraft velocity and particle size for which BC heating effects are expected to become important. The simulations are carried on by exposing a BC-containing particle to supersaturation profiles computed with the adiabatic cloud parcel model. The lognormal distributions by [160], which are used in our simulations, include nucleation, accumulation, and coarse modes. The presence of a coarse mode ensures that we include the effect of GCCN on parcel supersaturation, which can be important [57]. BC is included only in one particle, while the rest of the CCN are assumed to be composed of $(NH_4)_2SO_4$. The BC-containing particle is initially assumed to be dry and then allowed to grow as the supersaturation profile develops; the GCCN is assumed to follow the parcel without dropping out. The portion of cloud for which these GCCN are smaller than the threshold size of 40 μm diameter (larger particles have a high collection efficiency and for ambient concentrations can initiate precipitation) are examined with and without radiative heating. Collision and coalescence processes are not considered in these simulations. Furthermore, we assume that ventilation effects are not important, so that the transfer of heat from the droplet to the gas phase is primarily from conduction. This assumption holds reasonably well up to 50 μm in diameter [148].

Although useful, the adiabatic parcel simulations reflect idealized cloud parcels. A second approach is therefore necessary, to verify that the insight obtained from simple parcel theory can also be applied to a more realistic description of GCCN growth in clouds. This is realized by adopting the Trajectory Ensemble Model (TEM) of [150], in which a set of 500 trajectories derived from a Large Eddy Simulation (LES) of a non-precipitating marine stratocumulus deck is used to "drive" a non-adiabatic parcel model and compute supersaturation profiles. GCCN are exposed to the supersaturation profiles (using the same procedure as in the adiabatic parcel profile simulations) and are allowed to grow with and without radiative heating present. Horizontal and temporal (one-hour) ensemble averages are then computed for the GCCN size throughout the cloud column. The portion of cloud for which GCCN are smaller than the threshold size (40 μm wet diameter) is examined with and without radiative heating.

A typical stratocumulus cloud was selected for the TEM. This cloud has an average liquid water content of about 0.3 g kg^{-1}, while the average vertical velocity (updrafts and downdrafts), average and maximum updraft velocity of the stratocumulus cloud are shown in Figure 7.6, as a function of height. This cloud selected is both well developed and

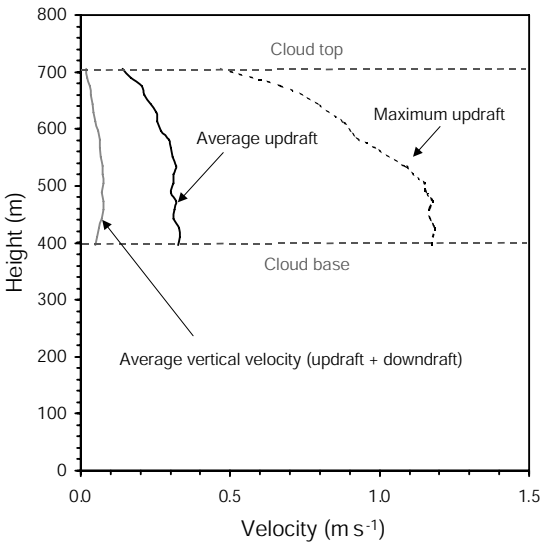

Figure 7.6: Vertical profiles of average vertical velocity (updrafts and downdrafts), average and maximum updraft velocity for the stratocumulus cloud trajectories used in this study.

energetic enough to ensure that the GCCN will remain in the cloud. Two types of CCN are used to compute the supersaturation trajectories: one representing pristine (marine size distribution of [160]) and one representing polluted conditions (urban size distribution of [160]). The aerosol is assumed to be composed of $(NH_4)_2SO_4$.

Figure 7.7 shows the growth of GCCN throughout an adiabatic cloud column that experiences an updraft of 0.25 m s^{-1} (the "NoHeat" scenario of the previous section is used to generate the supersaturation profile). The composition of the BC-containing GCCN is assumed to be 10% $(NH_4)_2SO_4$, 0-20% BC, the remaining mass being insoluble material. The rest of the CCN are composed of pure $(NH_4)_2SO_4$. The particle dry diameter is allowed to vary between 5 and 10 μm. GCCN that contain BC are assumed to experience radiative heating, so that a particle with 0% BC has the same amount of insoluble material as one with 10% BC, but experiences no heating. By examination of the growth curves we can see that the GCCN that contain BC and have a dry size of 5 μm practically never grow beyond 40 μm in size; without BC, the same particles would easily exceed 40 μm. As expected, a larger BC content tends to decrease the growth rate of the droplet. Therefore, particles of 5 μm dry diameter containing BC are effectively inhibited from reaching a size that is generally considered necessary for initiating precipitation. Even for particles that have a dry diameter of 10 μm, the presence of BC can substantially reduce their ultimate size

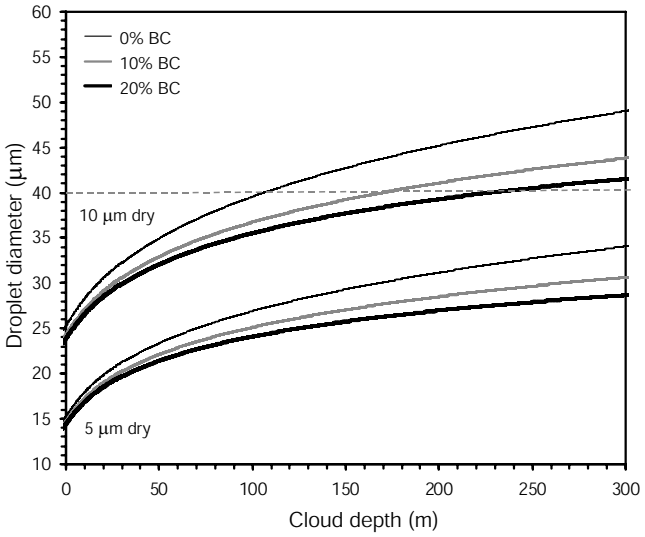

Figure 7.7: Growth of GCCN throughout a cloud column that experiences an updraft of 0.25 m s^{-1} (the "NoHeat" scenario of the previous section is used to generate the supersaturation profile). The composition of these particles is assumed to be 10% $(NH_4)_2SO_4$, 0-20% BC (the rest is dust). Curves are shown for particles with dry diameter of 5 and 10 μm. The dashed line represents the threshold size above which the collection efficiency of the droplets is assumed to become large.

(43-46 μm with BC vs. 50 μm without BC), although still large enough to act as collector drops.

The behavior seen in Figure 7.7 is also seen for larger updraft velocities. Figure 7.8 shows the growth of GCCN throughout a cloud column that experiences an updraft of 0.5 m s^{-1} (the "NoHeat" scenario of the previous section is used to generate the supersaturation profile), with the same GCCN as in Figure 7.7. Compared to Figure 7.7, particles grow to smaller sizes. This is because in stronger updrafts, droplets have less time for condensational growth. Therefore, the presence of BC is even more effective in prohibiting drizzle formation, since less BC per particle is necessary to keep the droplet below the threshold size. Given these results, one would expect to see that a further increase in updraft velocity would render GCCN even more susceptible to BC inclusions. Indeed, simulations performed for updrafts velocities of 0.5 and 1.0 m s^{-1} (not shown) confirm this.

An interesting feature of the GCCN growth curves is illustrated in Figure 7.9, which shows the normalized droplet sizes of the heated GCCN with respect to their unheated size, for the curves in Figure 7.8. The figure suggests that the size difference between a heated and non-heated GCCN increases as the particle traverses the cloud column. This is

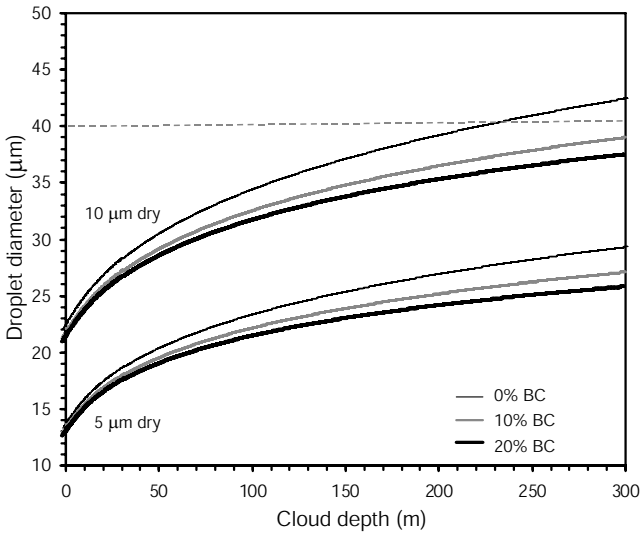

Figure 7.8: Same as Figure 7.7, but for an updraft velocity of 0.5 m s^{-1}.

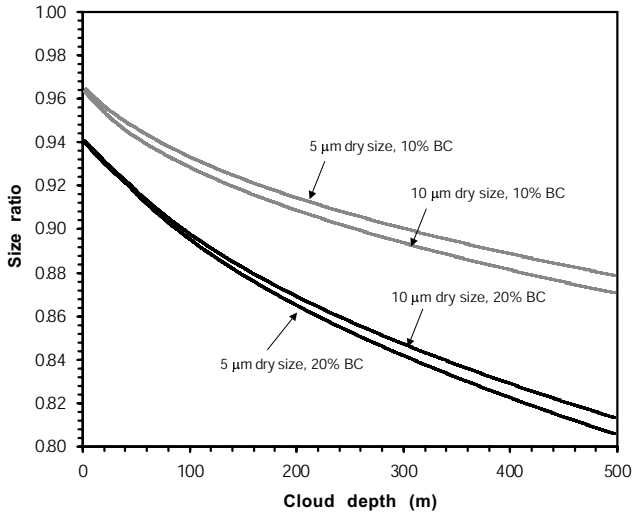

Figure 7.9: Normalized droplet sizes of the heated GCCN with respect to their unheated size, for the curves in Figure 7.7

an important feature; this means that heated drops will *always* be smaller than unheated drops, and that this size difference will become *larger* with time. As the updraft velocity increases, the normalized ratio decreases, which means that the size difference becomes larger. Another striking feature is that the normalized droplet size curves of the same BC content seem to collapse onto each other. This implies that particles, regardless of their dry size (and critical supersaturation), experience approximately the same (relative) decrease in their size.

One might suspect that the behavior illustrated in Figure 7.9 is a consequence of the supersaturation profile (and hence the driving force for particle growth) that decreases as the cloud drops rise further up in the cloud column. This is not true. We will demonstrate this behavior is not unique to adiabatic parcels with smooth supersaturation profiles, but can be expected for any randomly fluctuating positive supersaturation environment (such as that existing in real clouds). Starting from Equation 7.1, we can relate the equilibrium saturation ratio of a GCCN that experiences radiative heating, S_{eq}^{w}, to the equilibrium saturation ratio of a GCCN that does not experience radiative heating, S_{eq}^{wo}:

$$S_{eq}^{w} = S_{eq}^{wo} + \frac{A\gamma_a}{D_p} \tag{7.3}$$

The rate of growth for the GCCN particle with radiative heating is [117] :

$$\frac{dD_{p,w}^2}{dt} = 2G(S - S_{eq}^{w}) \tag{7.4}$$

where G is a function of T,P and S is the parcel saturation ratio. Substituting Equation 7.3 into 7.4, and given that the rate of growth of the GCCN in the absence of radiative heating, $\frac{dD_{p,wo}^2}{dt} = 2G(S - S_{eq}^{wo})$, we obtain

$$\frac{dD_{p,w}^2}{dt} = \frac{dD_{p,wo}^2}{dt} - \frac{2GA\gamma_a}{D_{p,w}} \tag{7.5}$$

Assuming that $(D_{p,w} + D_{p,wo}) \approx 2D_{p,w}$ and defining the quantity $\Delta D_p = D_{p,w} - D_{p,wo}$, Equation 7.5 becomes

$$\frac{d\Delta D_p}{dt} = -\left(\frac{2GA\gamma_a + 2Gs\Delta D_p}{D_{p,w}^2}\right) \tag{7.6}$$

where s is the parcel supersaturation, $S - 1$. Given that $S_{eq}^{w} \approx 1$, then $S - S_{eq}^{w} \approx s$, and

Equation 7.4 can be integrated over the supersaturation history to give the GCCN diameter at any time:

$$D_p^2 = d_p^2 + 2G \int_0^t s(\tau) d\tau \tag{7.7}$$

where d_p is the dry diameter of the GCCN (we assume the particle to be dry at t=0). Substituting Equation 7.7 into 7.6 gives

$$\frac{d\Delta D_p}{dt} = -\left(\frac{A\gamma_a + s\Delta D_p}{\frac{d_p^2}{2G} + \int_0^t s(\tau) d\tau} \right) \tag{7.8}$$

Equation 7.8 expresses the rate of change of ΔD_p (which is the difference in size of a GCCN for when it experiences radiative heating and when it does not, for identical supersaturation history), as a function of the supersaturation history, γ_a and the dry diameter. Under the condition of a supersaturated environment, the right-hand side of the equation is always negative. This means that a GCCN that experiences heating will always be smaller than if it were not heated. Furthermore, the magnitude of ΔD_p will grow continuously with time, with a rate that depends on the specific cloud supersaturation history. Equation 7.8 also explains the weak dependence of the size ratio in Figure 7.9 on the GCCN dry diameter: for small exposure times, the absolute value of ΔD_p is small, while for long exposure times, $\frac{d_p^2}{2G} \ll \int_0^t s(\tau) d\tau$, and so the denominator of the right-hand side will lose its dependence on d_p. Equation 7.8 also shows that γ_a (or % BC content) has a strong influence on the magnitude of ΔD_p, which is also seen in Figure 7.9.

The TEM simulations confirm what was seen in the adiabatic parcel calculations, despite the substantial differences between the two cloud models. Figure 7.10 shows the average size of 5 μm (dry diameter) GCCN as predicted by the TEM for (a) pristine cloud conditions and (b) polluted cloud conditions. The black dashed line indicates cloud base, while the grey dashed line indicates the size beyond which a GCCN can effectively initiate drizzle formation. One can observe the characteristic increase of the GCCN size for increasing cloud depth, indicative of the larger residence times experienced by parcels that reach deep into the cloud. The effect of radiative heating is significant: in the presence of BC, the size of the GCCN is always smaller than 40 μm. Particularly interesting is that without the presence of radiative heating, GCCN will exceed the threshold of 40 μm for the pristine

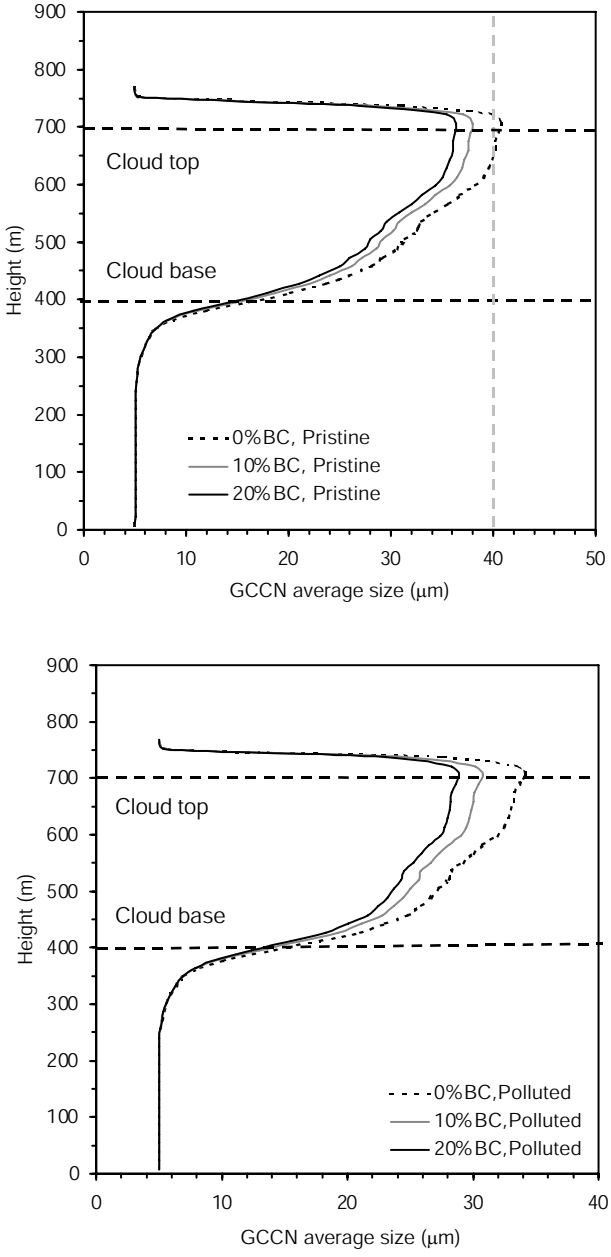

Figure 7.10: Average size of GCCN as predicted by TEM for (a) pristine cloud conditions and (b) polluted cloud conditions. The dry diameter of the GCCN is assumed to be 5 μm. The black dashed line indicates cloud base, while the grey dashed line indicates the size beyond which the GCCN is assumed to effectively initiate drizzle formation.

cloud; this does not happen once BC is present in the particles. Another interesting feature is that throughout the cloud column, the size ratios of GCCN with 10% BC to those with 0% BC is around 0.9, and the size ratio for particles with 20% to those with 0% BC is around 0.85. The fact that these ratios remain almost constant throughout the cloud can be explained from Equation 7.8: given that the supersaturation profiles do not change between curves (because the same trajectories are used for GCCN of different BC content), the ΔD_p will depend primarily on BC content.

When larger GCCN are used in the trajectories, similar behavior to Figure 7.10 is obtained. This is illustrated in Figure 7.11, which is same as Figure 7.10, but for a GCCN dry diameter of 10 μm. The effect of radiative heating is significant, although the decrease in size is insufficient in pristine clouds to make the GCCN smaller than 40 μm. Another interesting feature is that throughout the cloud column, the size ratios of GCCN with 10% BC to 0% BC is between 0.88-0.9, and the size ratio for particles with 20% to 0% BC is around 0.85. The stability of the size ratios throughout the cloud can be explained, just like before, from Equation 7.8. What is surprising is that the size ratios remain relatively constant between the pristine and polluted clouds. Furthermore, the size ratios are consistent with those ratios obtained from adiabatic parcel theory for a 0.25 m s^{-1} updraft (Figure 7.9), which is the average vertical velocity for the updrafts (Figure 7.6). This suggests that perhaps BC content primarily controls the size reduction of GCCN from BC heating, and to a lesser degree, supersaturation history statistics.

7.7 Conclusions

The effect of radiative heating on cloud droplet number concentration and cloud optical properties can be important for conditions characteristic of polluted, aged aerosol with a significant fraction of black carbon (BC). The sign of the climatic feedback from BC effects on cloud microphysics can be either positive or negative, rendering the overall BC influence on climate even more complex than previously thought. Two effects of BC radiative heating can increase cloud droplet concentration: *i*) the effect of BC on the ability to decrease the collection efficiency of giant CCN, and, *ii*) the delayed growth of low S_c CCN that permits CCN of higher S_c to form drops. These two mechanisms complement each other in terms of increasing the cooling effect of clouds, since the former is most efficient at strong

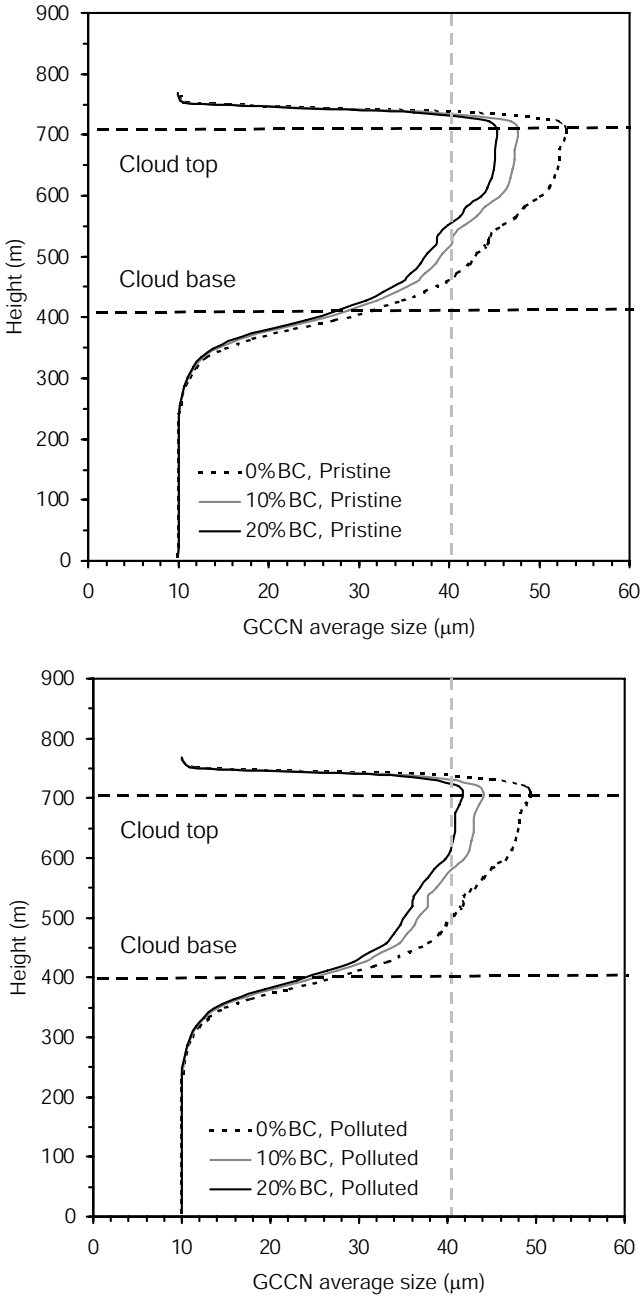

Figure 7.11: Same as Figure 7.10, but for a GCCN dry diameter of 10 μm.

updrafts, and the latter at lower updraft velocities. The latter mechanism does not seem to substantially increase cloud albedo on its own, but in conjunction with gas-phase heating, can decrease the effects of heating. This means that the mixing state of the BC, i.e., whether it is located in the interstitial aerosol, or included within the cloud droplets, can influence the resulting cloud droplet population and optical properties. For the conditions studied here, the change in cloud albedo relative to a cloud without radiative heating can be as large as 0.025. The presence of radiative heating seems to decrease cloud albedo; the simulations indicate that this is an effect of decreased LWC; droplet concentrations either remain the same or increase.

The effect of gas-phase heating on the cloud dynamics still remains to be addressed. An immediate effect of the released heat is to increase the buoyancy of the cloud parcel; this would tend to accelerate the cloud parcel, and possibly lead to additional activation of cloud droplets. The former effect is a negative feedback, since the additional activated CCN can enhance cloud albedo. This is an effect relevant for activation timescales ($\sim$ 1 min); for longer timescales however, radiative heating tends to destabilize the stratocumulus cloud layer by decreasing the efficiency of radiative cooling at the top of the cloud layer [6, 7]. An appropriate tool for addressing the importance of such feedbacks, is an LES cloud simulation. The importance of these feedbacks on droplet number remains an open question.

The effect of radiative heating on the ability of Giant Cloud Condensation Nuclei (GCCN) to reach sizes that are generally considered necessary to initiate precipitation is examined by assessing the effect of droplet growth kinetics on the size of GCCN using: *i*) adiabatic parcel theory, and, *ii*) trajectories derived from a large eddy simulation of a marine stratocumulus deck. It is shown through theoretical arguments and simulations that radiative heating consistently decreases the size of GCCN, regardless of the GCCN dry size and type of supersaturation profile to which the particle was exposed to. The simulations also suggest that this size reduction can effectively reduce the probability of drizzle formation for both polluted and pristine cloud conditions.

Incorporating the effect of BC on droplet activation in a global model is possible; one needs to account for the gas-phase heating and changes in the CCN spectrum from BC inclusions in a coupled manner. The former can be addressed using an "effective vertical velocity" approach, such as that proposed in [56]; while the latter can be treated by

appropriate modifications to a droplet activation parameterization (illustrated in Part 1). However, this approach, apart from any inherent uncertainties, neglects any subsequent effects on cloud dynamics that arise from the BC heating.

Assessing the global impact of BC on GCCN is not currently possible, although this works suggests that the controlling factors that determine the relative size reduction from BC heating are the BC content and average updraft velocity. The simulations further indicate that simple adiabatic parcel theory can be used to assess the size reduction for the average vertical velocity of the updrafts, although this is subject to further evaluation.

The simulations presented in this study comprehensively define the effects of BC absorption on cloud formation; however, more work is needed to provide a conclusive assessment. This work does show, however, that effects of BC forcing on climate are more complex than currently thought.

7.8 Acknowledgments

This work was supported by Office of Naval Research grant N00014-96-1-0119. The authors would like to thank Dr. Graham Feingold for providing the LES trajectories used in this work, and an anonymous reviewer for helpful comments.

Chapter 8

Parameterization of cloud droplet formation in global climate models

Note: This chapter has been submitted to *J.Geoph.Res.*

8.1 Abstract

An aerosol activation parameterization has been developed, based on a generalized representation of aerosol size and composition within the framework of an ascending adiabatic parcel; this allows for parameterizing the activation of chemically complex aerosol with arbitrary size distribution and mixing state. The new parameterization introduces the concept of "population splitting", in which the CCN that form droplets are treated as two separate populations: those which have a size close to their critical diameter, and those that do not. Explicit consideration of kinetic limitations on droplet growth is introduced. Our treatment of the activation process unravels much of its complexity. As a result of this, a substantial number of conditions of droplet formation can be treated completely free of empirical information or correlations; there are, however, some conditions of droplet activation for which an empirically derived correlation is utilized. Predictions of the parameterization are compared against extensive cloud parcel model simulations, for a variety of aerosol activation conditions that cover a wide range of chemical variability and CCN concentrations. The parameterization tracks the parcel model simulations closely and robustly. The parameterization presented here is intended to allow for a comprehensive assessment of the aerosol indirect effect in GCMs.

8.2 Introduction

The most uncertain of all climate forcings is the aerosol indirect effect [76]. There are two reasons for this. The first originates from the wide range of length scales involved in cloud-aerosol interactions: from hundreds of kilometers (that of the largest cloud systems) down to tens of meters (that of individual updrafts responsible for production of new drops). Sizes of typical General Circulation Model (GCM) grid cells range from $4^o \times 5^o$ to $2^o \times 2^o$. Such grid sizes can resolve only the largest cloud systems. To estimate how aerosol perturbations affect cloud properties from first principles, one needs to explicitly resolve processes that take place down to the smallest scales of new droplet formation. Cloud-resolving large eddy simulations can potentially address these smaller length scales, but the computational burden associated with such simulations prohibits their use in climate models. The second reason lies in the sheer complexity of aerosol-cloud interactions themselves.

The first attempts to relate cloud properties to aerosols in GCMs (e.g. [15, 84]) empirically linked cloud droplet number concentration to a property available in a global aerosol model, such as total aerosol sulfate mass (e.g. [15]), or total aerosol number (e.g. [60]). The empirical relationship itself is subject to substantial uncertainty; aerosol-cloud interactions are highly complex and cannot be represented by a simple correlation based on a single aerosol property. This is illustrated by the [83] study, in which several different empirical relationships yield estimates of the global annual average indirect forcing ranging between -0.40 W m^{-2} and -1.78 W m^{-2}. To address the deficiencies of purely empirical correlations, first-principle approaches to predicting cloud droplet number have emerged (e.g., [58, 103]).

Calculation of cloud droplet number from first principles entails setting up a cloud droplet number balance in each GCM grid cell,

$$\frac{dN_d}{dt} = Q_{activation} - Q_{evaporation} - Q_{collision} + Q_{advection} + ... \tag{8.1}$$

where N_d is the droplet number concentration, $Q_{activation}$ is the droplet source from droplet activation, $Q_{evaporation}$ is the loss from droplet evaporation, $Q_{collision}$ is the loss from collision-coalescence processes, and $Q_{advection}$ is the net source of droplets advected from adjacent grid cells (other processes can be present, particularly if the cloud contains ice or is precipitating). Cloud droplet activation is a key process for the indirect effect, since it is the direct microphysical aerosol-cloud link. Explicitly resolving each of these processes from

first principles necessitate resolution on scales of tens of meters, since this is the smallest scale for which aerosol droplet activation, and hence cloud formation, can take place. Such resolutions are far beyond anything computationally feasible for GCMs. As a consequence, a prognostic GCM estimate of the aerosol indirect effect must rely on parameterizations of all such sub-grid processes. Implementation of explicit aerosol activation within a GCM presupposes that the dynamics of cloud formation (particularly the probability distribution of updraft velocity or cooling rate below cloud), and the aerosol characteristics below cloud are known. Such dynamical information is not readily available from a GCM, so it must be obtained from a parameterization. The basic theory of aerosol activation is well established, and many numerical models describing it have appeared in the literature (e.g., [77, 40, 127, 143, 117]); inclusion of numerical activation models is in itself computationally challenging, so the activation process needs to be parameterized. Parameterization of the subgrid cloud dynamics is not addressed in the current study.

In parameterizations of aerosol activation that have appeared in the literature over the years, treatments of the aerosol size distribution and activation process differ. The first parameterization appeared four decades ago (e.g. [154, 149]). Although providing elegant solutions and simple expressions for the number of nucleated droplets, these approaches rely on both simple aerosol size distributions (power law) and idealized expressions for droplet condensation rate. As a result, systematic errors arise in their predictions, such as prediction of droplet number that exceeds the total condensation nuclei. Other subsequent approaches have adopted a functional relationship between number of CCN that activate at a given supersaturation level (otherwise known as the "CCN spectrum"). [39] adopted a power law to describe the CCN spectrum, although their approach can be extended to any functional form. [26, 27] in their treatment assumed a generalized sigmoidal function. The abstraction and detachment from assumptions regarding size distribution and chemical homogeneity theoretically can allow any size distribution to be described through the generalized CCN spectrum. Other parameterizations have used log-normal representations of aerosol size distributions, and used Köhler theory to compute the CCN spectrum (e.g., [56, 55, 3, 1]). [2] propose an algorithm for use of their multiple log-normal population parameterization [1] in sectional aerosol models. Their approach is to use an empirically prescribed value of geometric dispersion, and treat each section as a separate mode. [21] parameterized sulfate transfer to and production in preexisting particles by condensation of gas-phase sulfuric acid

and aqueous oxidation of sulfur dioxide. The most sophisticated current aerosol activation parameterizations still rely principally on empirical information obtained from detailed numerical parcel simulations. To compute the number of activated droplets, [39] compute the cloud maximum supersaturation from a nonlinear equation, which contains a parameter evaluated through multivariate regression of numerical adiabatic parcel calculations. [3] and [1] calculate the maximum parcel supersaturation explicitly, by using a correlation derived from regression of numerical parcel calculations. [91] assume a power law aerosol size distribution to develop an analytical expression linking CCN number concentration to parameters that are related to aerosol growth under subsaturated conditions.

To summarize, previous aerosol activation parameterizations assume one (or more) of the following: i) specified aerosol size distributions (power law, log-normal), or prescribed activation spectrum; ii) uniform chemical composition over particle size composed of only a completely soluble and insoluble fraction; iii) a single aerosol population (that is, an internally mixed aerosol); and iv) instantaneous activation of CCN (absence of kinetic effects). Any of these assumptions, under certain conditions, may not be satisfied, so application of the parameterization may lead to bias. The aerosol may be chemically complex, the composition of which can vary considerably with size and may be externally mixed. Certain aerosol chemical components can alter the activation behavior, in a manner which is not easily introduced in parameterizations. For example, the presence of surface active species, i.e., those that tend to lower the droplet surface tension, facilitate the activation of CCN [36]. The amount of surface tension depression depends on the concentration of the dissolved organic (e.g. [145, 19]); since the concentration of dissolved species at the point of activation varies considerably with CCN dry size, one cannot assume a uniform or average change in surface tension throughout the CCN population. The resulting modified Köhler equation for such CCN cannot be solved explicitly for their critical supersaturation, s_c. As most extant parameterizations rely on an explicit link between s_c and dry CCN diameter, it is difficult to incorporate the implicit link surface-active species impose between s_c (or D_c) and the CCN dry size. Similar difficulties arise from the presence of slightly soluble species [93], which can also exhibit surface-active behavior. Such "chemical" effects cannot be neglected, as they can potentially constitute a large component of the aerosol indirect effect [19, 114]. Also, with the emergence of global aerosol models that allow completely general distributions of both size and composition [8], the stipulation of a prescribed dis-

tribution may be overly constraining. For example, the constraint that the aerosol has to follow a log-normal distribution has been shown to lead to discrepancies in droplet number when applied in a 1-D climate model [166]. The generalized CCN spectrum approach of [26, 27], when used in conjunction with a GCM simulation of global aerosols, necessitates an undesirable on-line curve-fitting procedure.

Although utilizing empirical information can be a powerful tool, it is desirable, for sake of generality and robustness, to minimize the amount of such information contained within a parameterization. It is not clear when a parameterization, which is based on empirical fits, will exhibit biases in the prediction. For example, [2] show that the sectional version of their activation parameterization follows a full numerical activation model for high updraft velocities, but the performance deteriorates as the updraft velocity decreases. For log-normal aerosol, the parcel model results are generally reproduced well when 10-90 % of the aerosol becomes activated [1, 3].

The present work develops a new aerosol activation parameterization, intended for use in GCMs, which is based on a generalized representation of aerosol size and composition within the framework of an adiabatic cloud parcel. Explicit treatment of mass transfer (kinetic) limitations in droplet growth is included. We focus on minimizing the amount of empirical information included within the parameterization. In the sections that follow, we present the derivation of the activation parameterization and then outline its use. We compare the new parameterization with that of [1]; the two are compared to the predictions of a cloud parcel model with detailed growth kinetics for a variety of cloud condensation nucleus (CCN) activation conditions.

8.3 Definition of size distributions

Although any size distribution (such as a power law or lognormal) can be used in the new parameterization, we select a sectional representation to allow the most general possible representation of aerosol size and composition. In this representation, we divide the aerosol into an arbitrary number of size sections, each of which has its own chemical composition. Each section m is characterized by its lower and upper diameters, $D_{p,m-1}$ and $D_{p,m}$, and the total number concentration of particles in the section, N_m (Figure 8.1a). The aerosol chemical composition within each section is assumed to be uniform, and independent of

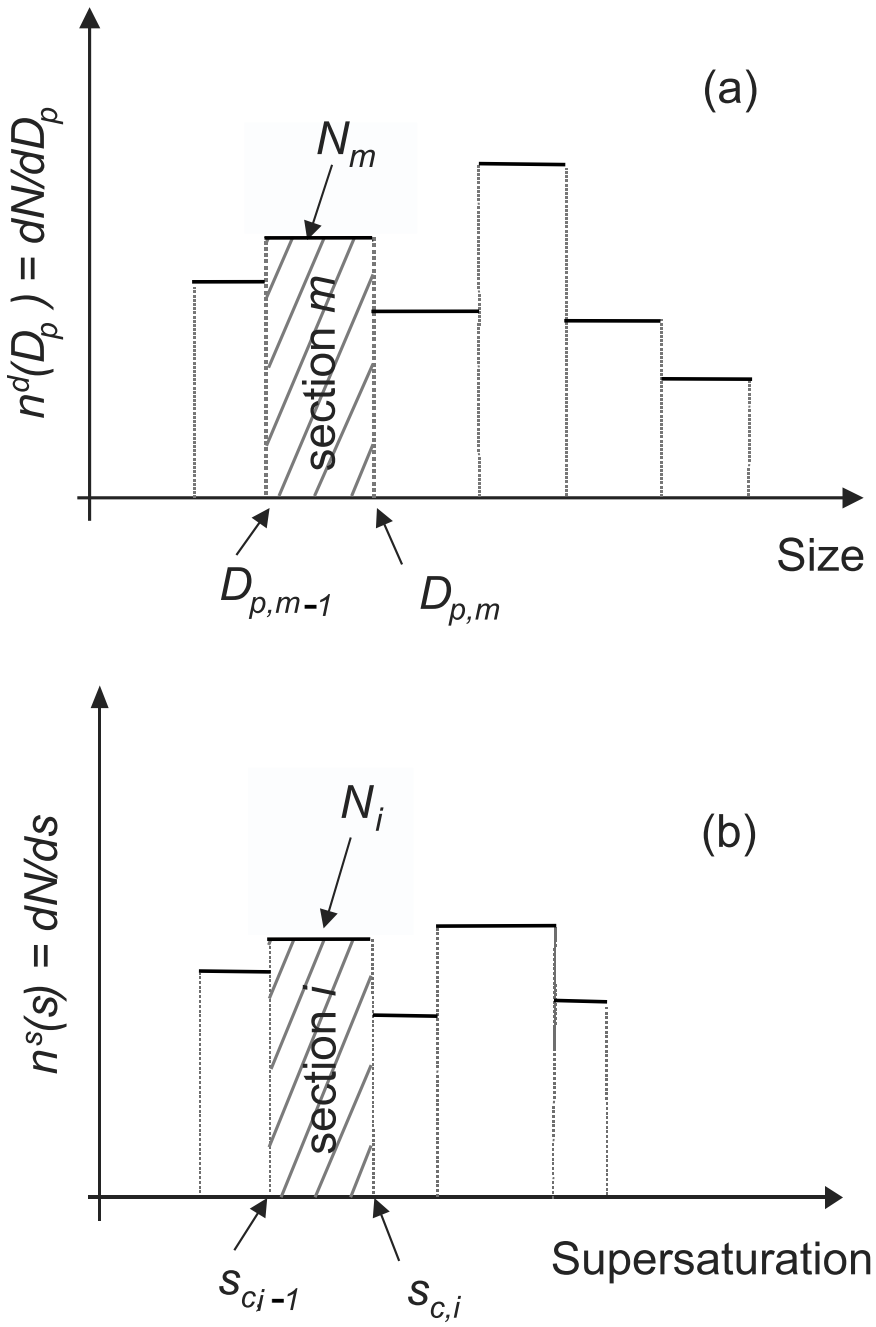

Figure 8.1: Illustration of the sectional representation of (a) aerosol number distribution, $n^d(D_p)$, and (b) supersaturation distribution, $n^s(D_p)$.

those in other sections. A linear profile (which is a common assumption for sectional implementations of aerosol microphysics) of aerosol number concentration across a section is assumed. With these assumptions, the size distribution, $n^d(D_p) = dN/dD_p$, over $D_{p,m-1} \leq D_p < D_{p,m}$, is given by,

$$n^d(D_p) = \frac{dN}{dD_p} = \frac{N_m}{D_{p,m} - D_{p,m-1}} \tag{8.2}$$

and the cumulative size distribution (total number of particles with diameter smaller than D_p), $F^d(D_p)$, is given by,

$$F^d(D_p) = \int_0^{D_p} n^d\left(D'_p\right) dD'_p = \sum_{j=1}^{m-1} N_j + N_m \left(\frac{D_p - D_{p,m-1}}{D_{p,m} - D_{p,m-1}}\right) \tag{8.3}$$

where m is the section that contains D_p.

The above treatment assumes a single aerosol population. Multiple aerosol populations can exist (externally mixed aerosol); in this case, a separate size distribution, $n_k^d(D_p)$, is defined for each population, k. Then the cumulative size distribution is given by summing over all the populations,

$$F^d(D_p) = \sum_{l=1}^{k} \int_0^{D_p} n_l^d\left(D'_p\right) dD'_p = \sum_{l=1}^{k} \left\{ \sum_{j=1}^{m(l)-1} N_{j,l} + N_{m(l),l} \left(\frac{D_p - D^l_{p,m(l)-1}}{D^l_{p,m(l)} - D^l_{p,m(l)-1}}\right) \right\} \tag{8.4}$$

where $D^l_{p,m(l)-1}$, $D^l_{p,m(l)}$ are the boundaries of section i that contain D_p and population l. $m(l)$ is used to indicate that each population l has its own section boundaries.

8.4 Definition of CCN spectrum

After the size distributions are defined for each of the aerosol populations, $n^d(D_p)$ is then mapped to supersaturation space (Figure 8.1b), and the critical supersaturation distribution, $n^s(s)$, is obtained,

$$n^s(s) = \frac{dN}{ds} = \frac{N_i}{s_{c,i} - s_{c,i-1}}, \quad s_{c,i-1} \leq s < s_{c,i} \tag{8.5}$$

where $s_{c,i-1}$ and $s_{c,i}$ are the critical supersaturations corresponding to the boundaries of section i. For simplicity, we assumed that $n^s(s)$ is piecewise linear. We change the index

used for representing a section from m to i, to reflect the change in the ordering of the sections as they are mapped onto (monotonically increasing) supersaturation space.

The critical supersaturation corresponding to the section boundaries can be calculated using Köhler theory (i.e. the critical supersaturation corresponding to the diameter of each section boundary is calculated). We will not present a procedure for calculating the critical supersaturation of the sectional boundaries, as it is a standard procedure that can be found throughout the literature (e.g., [143]). We would like to note however, that we do not need an explicit link between aerosol dry size and critical supersaturation, a restraint which is necessary in most parameterizations. Relaxing this restraint allows for addressing the activation of highly complex activation curves, such as that seen for slightly soluble and surface active compounds [145].

The sectional representation of the CCN spectrum (total number of particles with critical supersaturation smaller than s), $F^s(s)$, is given by,

$$F^s\left(s\right) = \int_0^s n^s\left(s'\right) ds' = \sum_{j=1}^{i-1} N_j + N_i \left(\frac{s - s_{c,i-1}}{s_{c,i} - s_{c,i-1}} \right) \tag{8.6}$$

where i is the section that contains s, and $s_{c,0} = 0$.

When k populations exist, the CCN spectrum is obtained by summing over all the aerosol populations,

$$F^s\left(s\right) = \sum_{l=1}^{k} \int_0^s n_l^s\left(s'\right) ds' = \sum_{l=1}^{k} \left\{ \sum_{j=1}^{i(l)-1} N_{j,l} + N_{i(l),l} \left(\frac{s - s^l_{c,i(l)-1}}{s^l_{c,i(l)} - s^l_{c,i(l)-1}} \right) \right\} \tag{8.7}$$

where $s^l_{c,i(l)-1}$, $s^l_{c,i(l)}$ are the critical supersaturations for the boundaries of section i and population l that bound s. $i(l)$ is used to indicate that each population l has its own section boundaries.

Equation 8.7 represents the CCN spectrum of the aerosol; once the maximum parcel supersaturation, s_{max}, is known, the number of CCN that will activate into drops, N_d, is given by,

$$N_d = F^s(s_{max}) \tag{8.8}$$

8.5 Formulation of the Aerosol Activation Parameterization

The aerosol activation parameterization is developed in two steps. The first involves the representation of the aerosol number and chemical composition distribution with respect to size, and calculation of the number concentration of droplets that can potentially form at a certain level of supersaturation (the cloud condensation nucleus, CCN, spectrum). Modified Köhler theory, which embodies effects of surfactant and slightly soluble species, is used to compute the supersaturation needed for a CCN to activate [145, 93]. In the second step, the CCN spectrum is included within the framework of an adiabatic cloud parcel model, with specified updraft velocity (or cooling rate), to compute the maximum supersaturation, s_{max}, of the cloud parcel. The number concentration of nucleated drops is calculated from Equation 8.8.

Considerable attention has been given to the approximation used in estimating the droplet size, at the point of parcel maximum supersaturation (which is a key parameter, as it controls the condensation rate). A common assumption taken is that the CCN grows instantaneously to its critical diameter, when the parcel supersaturation becomes equal to the CCN's critical supersaturation, i.e. the activation process is not kinetically limited. When this condition is not satisfied, it can be a source of significant error in prediction of the number of activated droplets [117]; this is one of the issues addressed in the new parameterization. We would like to note that the previously described kinetic limitation mechanism has long been known (e.g., [77, 22]); this was called "inertial" kinetic limitation by [117]. (In addition to the "inertial" mechanism, [117] also identified two other kinetic limitation mechanisms, the "de-activation" and "evaporation" mechanisms. In this study, we only consider the "inertial" mechanism, as that can have a substantial effect on the condensation rate and thus s_{max}).

8.5.1 Computation of parcel maximum supersaturation

In an adiabatic parcel, the rate of change of the supersaturation, s, for a cloud parcel that ascends with a constant vertical velocity, V is [127, 143]:

$$\frac{ds}{dt} = \alpha V - \gamma \frac{dW}{dt} \tag{8.9}$$

where

$$\alpha = \frac{gM_w\Delta H_v}{c_pRT^2} - \frac{gM_a}{RT}, \quad \gamma = \frac{pM_a}{p^sM_w} + \frac{M_w\Delta H_v^2}{c_pRT^2} \tag{8.10}$$

and where ΔH_v is the latent heat of condensation of water, T is the parcel temperature, M_w is the molecular weight of water, g is the acceleration of gravity, M_a is the molecular weight of air, c_p is the heat capacity of air, p^s is the water saturation vapor pressure, p is the ambient pressure, dW/dt is the rate of condensation of liquid water onto the drops, and R is the universal gas constant.

The first term on the right hand side of Equation 8.9 expresses the tendency of supersaturation to increase from the cooling of the parcel, while the second term expresses the tendency of supersaturation to decrease because of depletion of water vapor by the activated droplets.

The rate of water condensation on the droplet population can be expressed as,

$$\frac{dW}{dt} = \frac{\pi}{2}\rho_w \int_0^s D_p^2 \frac{dD_p}{dt} n^s(s')ds' \tag{8.11}$$

where ρ_w is the density of water. By substituting Equation 8.11 into 8.9, we obtain,

$$\frac{ds}{dt} = \alpha V - \gamma\frac{\pi}{2}\rho_w \int_0^s D_p^2 \frac{dD_p}{dt} n^s(s')ds' \tag{8.12}$$

The parcel supersaturation reaches a maximum when water vapor availability from parcel cooling becomes equal to the depletion rate from the activated drops; this is expressed by setting ds/dt in Equation 8.12 equal to zero:

$$\alpha V - \gamma\frac{\pi}{2}\rho_w \int_0^{s_{max}} D_p^2 \frac{dD_p}{dt} n^s(s')ds' = 0 \tag{8.13}$$

The rate of growth of a drop of diameter D_p is determined from [143],

$$\frac{dD_p}{dt} = \frac{G}{D_p}\left(s - s_{eq}\right) \tag{8.14}$$

$$G = \frac{4}{\frac{\rho_w RT}{p_v^* D_v M_w} + \frac{\Delta H_v \rho_w}{k_a T\left(\frac{\Delta H_v M_w}{RT} - 1\right)}} \tag{8.15}$$

and k_a is the thermal conductivity of air, D_v is the water vapor diffusivity, and s_{eq} is the

equilibrium supersaturation of the droplet.

With the assumption that beyond the point of activation, the growth rates are not significantly influenced by droplet curvature and solute effects, $s_{eq} = 0$, Equation 8.14 becomes [154],

$$\frac{dD_p}{dt} = \frac{G}{D_p} s \tag{8.16}$$

One can integrate Equation 8.16 from time τ, when the parcel supersaturation is equal to the CCN critical supersaturation, to the time of maximum supersaturation, t_{max}, to give the droplet diameter at the time of s_{max},

$${D_p}^2 = D_p^2(\tau) + 2\int_{\tau}^{t_{max}} Gsdt \tag{8.17}$$

By substituting Equations 8.17 and 8.16 into Equation 8.13, we obtain,

$$\frac{2\alpha V}{\pi\gamma\rho_w} - Gs_{max} \int_0^{s_{max}} \left(D_p^2(\tau) + 2G\int_{\tau}^{t_{max}} sdt \right)^{1/2} n^s(s')ds' = 0 \tag{8.18}$$

Before proceeding further, we need to evaluate the integral in Equation 8.18, referred to herein after as $I(0, s_{max})$,

$$I(0, s_{max}) = Gs_{max} \int_0^{s_{max}} \left(D_p^2(\tau) + 2G\int_{\tau}^{t_{max}} sdt \right)^{1/2} n^s(s')ds' \tag{8.19}$$

where the parameters in the parenthesis indicate the limits of integration. If $I(0, s_{max})$ is evaluated and substituted in Equation 8.18, the parcel maximum supersaturation can then be calculated, and subsequent substitution into 8.8 would yield cloud droplet number concentration.

8.5.2 Calculation of integral I.

An analytical expression for I is not possible, but I has two asymptotic limits. The first limit, I_1, is obtained when

$$D_p^2(\tau) << 2G\int_{\tau}^{t_{max}} sdt \tag{8.20}$$

In this limit, the CCN experience significant growth beyond the point where they are

exposed to $s > s_c$. Note that the above approximation is used to derive the parameterization of [154]. The supersaturation integral in Equation 8.19 can be evaluated using the lower bound of [154],

$$\int_{\tau}^{t_{max}} s dt \approx \frac{1}{2\alpha V}(s_{max}^2 - s(\tau)^2) \tag{8.21}$$

where $s(\tau)$ is the parcel supersaturation at time τ. Substituting Equations 8.20, 8.21 and 8.5 into 8.19, we eventually obtain,

$$I_1(0, s_{max}) = \frac{s_{max} G^{3/2}}{(aV)^{1/2}} \sum_{j=1}^{i} \frac{N_j}{s_c^j - s_c^{j-1}} \left[\frac{x}{2} \left(s_{max}^2 - x^2 \right)^{1/2} + \frac{s_{max}^2}{2} Arc \sin \frac{x}{s_{max}} \right]_{x=s_c^{j-1}}^{x=s_c^j} \tag{8.22}$$

where the bracket signifies the difference between evaluation at $x = s_c^j$ and $x = s_c^{j-1}$, and, i is the section that contains s_{max} (i.e., $s_c^{i-1} \leq s_{max} \leq s_c^i$).

The second limit, I_2, of I is obtained when

$$D_p^2(\tau) >> 2G \int_{\tau}^{t} s dt \tag{8.23}$$

which physically means that the CCN do not experience significant growth beyond the point where they are exposed to $s > s_c$. A common assumption (used in the parameterization of [56]) is that $D_p(\tau)$ is equal to the critical diameter, $D_c = 2A/3s_c$, when the parcel s becomes equal to the particle s_c ($A = 4M_w\sigma/RT\rho_w$, and σ is the droplet surface tension at its critical diameter). This can be assumed when the timescale of particle growth is small compared to the rate at which supersaturation changes in the parcel [22]; this implies that the CCN is in equilibrium with the parcel supersaturation until the point of activation, hence will instantaneously grow to D_c when exposed to its critical supersaturation. (We will elaborate on the implications of this assumption subsequently.) Substitution of Equation 8.23 into Equation 8.19 (with the assumption $D_p(\tau) = D_c$) and evaluation of the integral yields,

$$I_2(s_c^1, s_{max}) = \frac{2Gs_{max}}{3} \left[\sum_{j=2}^{i-1} \left(\frac{N_j A_j}{s_c^j - s_c^{j-1}} \right) \ln \frac{s_c^j}{s_c^{j-1}} + \left(\frac{N_i A_i}{s_c^i - s_c^{i-1}} \right) \ln \frac{s_{max}}{s_c^{j-1}} \right] \tag{8.24}$$

where A_j is an average A over section j. Note that j starts from 2, otherwise $I_2 \to \infty$ as $s_c^0 \to 0$. This asymptotic limit will not be a problem for the parameterization, as I_2 will always be used with a nonzero lower bound. In equation 8.24, i is the section that contains s_{max} (i.e., $s_c^{i-1} \leq s_{max} \leq s_c^i$).

8.5.3 The concept of "population splitting".

While neither of Equations 8.22 or 8.24 alone is expected to describe the behavior of all the CCN during their activation, it is reasonable to divide the CCN into two groups: those that would follow Equation 8.22, and others that would follow 8.24. This classification of CCN, which we call *population splitting*, will be used to approximate I,

$$I = I_1(0, s_{part}) + I_2(s_{part}, s_{max}) \tag{8.25}$$

The ordering of the two integrals is deliberate; I_1 is used for low s_c CCN, while I_2 is used for the remaining CCN. This ordering will be justified subsequently (in section 4.4). The upper bound of I_1 and the lower bound of I_2 in Equation 8.25 is termed the *partitioning critical supersaturation*, s_{part} (Figure 8.2). Physically, this supersaturation defines two populations of droplets: one for which $D_p \approx D_c$, and one for which either $D_p \gg D_c$ or $D_p \ll D_c$ (but still large enough to be considered a droplet). Note that Equation 8.25 assumes that for a given population, there is only one s_{part}. If s_{part} is known, the integral I can be evaluated and substituted into Equation 8.18; s_{max}, and N_d can then be calculated. The following sections develop the procedure used for calculating s_{part}.

8.5.4 Implementation of population splitting.

Numerical simulations with a cloud parcel model [117] reveal that s_{part} depends on s_{max}, V, and the CCN spectrum characteristics. We will now attempt to derive theoretical expressions for s_{part}. An obvious candidate for s_{part} is the critical supersaturation of the CCN population for which $D_p^2(\tau) = 2G\int_\tau^{t_{max}} s dt$. From Equation 8.21 and substituting $D_p(\tau) = 2A/3s_{part}$, we obtain,

$$\frac{4A^2}{9s_{part}^2} = \frac{G}{\alpha V}(s_{max}^2 - s_{part}^2) \tag{8.26}$$

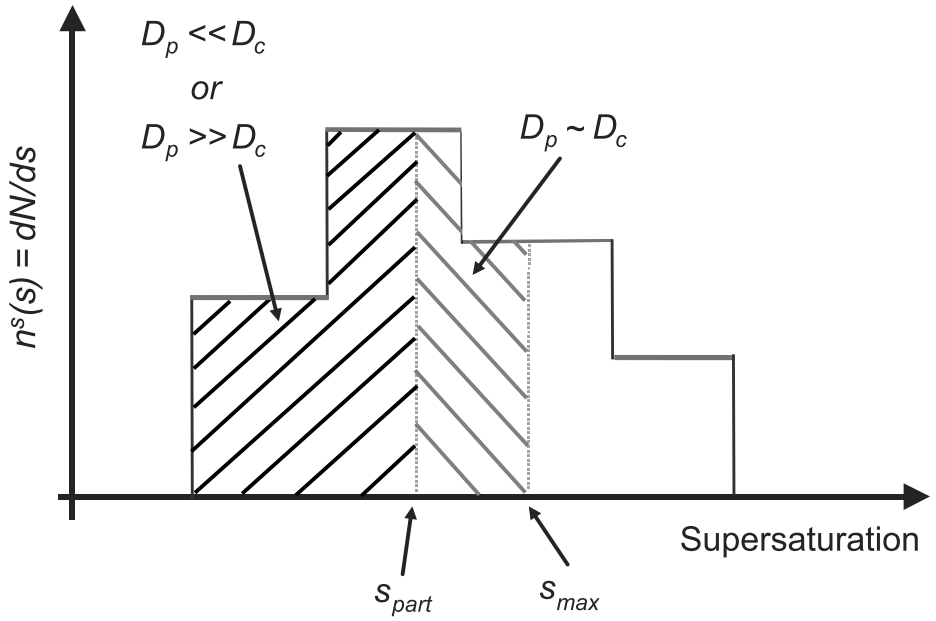

Figure 8.2: Illustration of the two sub-populations used in developing the parameterization.

where $A = 4M_w\sigma_w/RT\rho_w$, and σ_w is the surface tension of water. After some algebra, Equation 8.26 leads to the quartic equation,

$$p(s_{part}) = s_{part}^4 - s_{max}^2 s_{part}^2 + \frac{4A^2\alpha V}{9G} = 0 \tag{8.27}$$

If the descriminant, $\Delta = s_{max}^4 - \frac{16A^2\alpha V}{9G}$, of $p(s_{part})$ is non-negative, then Equation 8.27 has two real roots with respect to s_{part}:

$$\begin{aligned}\left(\frac{s_{part,1}}{s_{max}}\right)^2 &= \frac{1}{2}\left[1 - \left(1 - \frac{16A^2\alpha V}{9s_{max}^4 G}\right)^{1/2}\right] \\ \left(\frac{s_{part,2}}{s_{max}}\right)^2 &= \frac{1}{2}\left[1 + \left(1 - \frac{16A^2\alpha V}{9s_{max}^4 G}\right)^{1/2}\right]\end{aligned} \tag{8.28}$$

Each of the two roots, $s_{part1,2}$, expresses the s_c of those CCN for which their subsequent growth beyond activation is equal to D_c. These two characteristic s_c divide the CCN population into three groups: those with $s_c < s_{part,1}$, those with $s_{part,2} < s_c < s_{part,1}$, and those with $s_{part,2} < s_c$. If a CCN has an s_c between $s_{part,1}$ and $s_{part,2}$, then $p(s_c) < 0$, which means that the CCN experiences significant growth after it attains its critical diameter.

For other values of s_c, $p(s_c) > 0$, which means that the growth experienced by the CCN is smaller than its critical diameter. Note the latter does *not* mean that when $p(s_c) > 0$, the CCN size can be approximated by its critical size; further knowledge of droplet growth kinetics is needed for deciding whether this approximation can be used.

Of all the CCN that form droplets, those with the highest s_c have sizes close to their D_c. This is because i) high s_c CCN are less influenced by kinetic limitations and thus would be in equilibrium with parcel supersaturation until the point of activation, and ii) because they have the least time to grow beyond activation [117]. This condition is valid for particles which $s_c > s_{part,2}$. However, as s_c decreases, the time available for growth increases, and at some point, the droplet growth becomes large enough to substantially exceed the CCN critical diameter. This happens for the particles for which $s_{part,1} < s_c < s_{part,2}$. Apart from having the benefit of increased exposure time, a decrease in s_c also leads to a larger D_c; at the value of $s_c = s_{part,1}$, the subsequent growth beyond activation becomes equal to D_c; for lower s_c, D_c is larger than the growth experienced by the particle. Therefore, CCN for which $s_c < s_{part,1}$ are kinetically limited and do not attain their critical diameter; Equation 8.20 cannot be used to estimate the CCN size, as it never approaches its critical diameter (this is confirmed from simulations with a detailed adiabatic cloud model [117]). Therefore, approximating I with I_2 for the kinetically-limited CCN can lead to large biases because their droplet size would be systematically overestimated by assuming $D(\tau) = D_c$.

Since those CCN, the growth of which is kinetically limited, have a small s_c, it is reasonable to approximate their driving force for droplet growth (Equation 8.14), $s - s_{eq}$, with s, even before they activate (this is because, $s_{eq} \leq s_c \approx 0$). The growth of such a particle can then be expressed as,

$$D_p^2 \approx 2G \int_{\tau}^{t_{max}} s dt \tag{8.29}$$

which is equivalent to Equation 8.20. Thus, I_1 is used to approximate I for CCN with $s_c < s_{part,1}$. On this basis, $s_{part} = s_{part,2}$ and the following can be said,

$$\begin{aligned} \left(\frac{s_c}{s_{max}}\right) \leq \left(\frac{s_{part}}{s_{max}}\right) &\Rightarrow D_p^2(\tau) << 2G \int_{\tau}^{t_{max}} s dt \Rightarrow I \approx I_1 \\ \left(\frac{s_c}{s_{max}}\right) > \left(\frac{s_{part}}{s_{max}}\right) &\Rightarrow D_p^2(\tau) >> 2G \int_{\tau}^{t_{max}} s dt \Rightarrow I \approx I_2 \end{aligned} \tag{8.30}$$

The descriminant Δ expresses the extent of kinetic limitations throughout the droplet formation, and depends on s_{max} (which depends primarily on V and CCN characteristics), V, and the timescale of water vapor diffusion (embodied in G). $\Delta = 0$ marks a boundary between two growth regimes: one where most CCN are free from kinetic limitations ($\Delta > 0$) and one in which kinetic limitations are dominant ($\Delta < 0$). As Δ increases, $s_{part,1} \rightarrow 0$ and $s_{part,2} \rightarrow s_{max}$, so that more of the CCN attain sizes larger than their critical diameter; this means that fewer CCN are subject to kinetic limitation. (This is consistent with the analysis of [117], as increasing parcel s_{max} and V leads to rapid particle growth and therefore to a decrease in kinetic limitations.) The rules in Equation 8.30 indicate that for a non-negative Δ, $\left(\frac{s_{part}}{s_{max}}\right) \geq \sqrt{0.5}$. In this regime, s_{part} decreases with decreasing s_{max}.

When $\Delta < 0$, Equation 8.27 is without real roots; under these conditions, kinetic limitations in droplet growth are strong throughout the entire CCN population. Of all the CCN, those with the highest s_c would tend to have size of order D_c, since: i) the timescale of activation decreases with particle size (or with increasing s_c) [22], and, ii) $p(s_c)$ is closest to zero as $s_c \rightarrow s_{max}$. Therefore, for CCN of high s_c, I_2 can be used to approximate I. The lower s_c particles can be considerably smaller than their critical size, but with small s_c, their growth, as before, can be represented by Equation 8.29; I_1 will therefore be used to approximate I. Consequently, Equations 8.30 will still be used to approximate I, even if $\Delta < 0$. Based on the previous discussion we anticipate that fewer CCN can attain their critical diameter as the parcel maximum supersaturation decreases; numerical simulations support this expectation. s_{part} increases with decreasing s_{max} and is calculated from the following correlation, derived from regression of a large set of empirical s_{part} that reproduce the predictions of a detailed microphysics model,

$$\frac{s_{part}}{s_{max}} = min\left\{0.666 \times 10^7 A s_{max}^{-0.3824}, 1.0\right\} \tag{8.31}$$

The simulations on which Equation 8.31 is based were chosen so that $\Delta < 0$. In generating numerical values for Equation 8.31, the mass accommodation coefficient of water vapor on aqueous drops is equal to 1.0, and $T = 283$ K. Equation 8.31 indicates that as $s_{max} \rightarrow 0$, $s_{part}/s_{max} \rightarrow 1$, meaning that as the s_{max} decreases, fewer and fewer of the CCN can attain their critical diameter. All the rest are kinetically-limited.

Combination of the two expressions for calculating s_{part} (Equation 8.31 for $\Delta < 0$ and

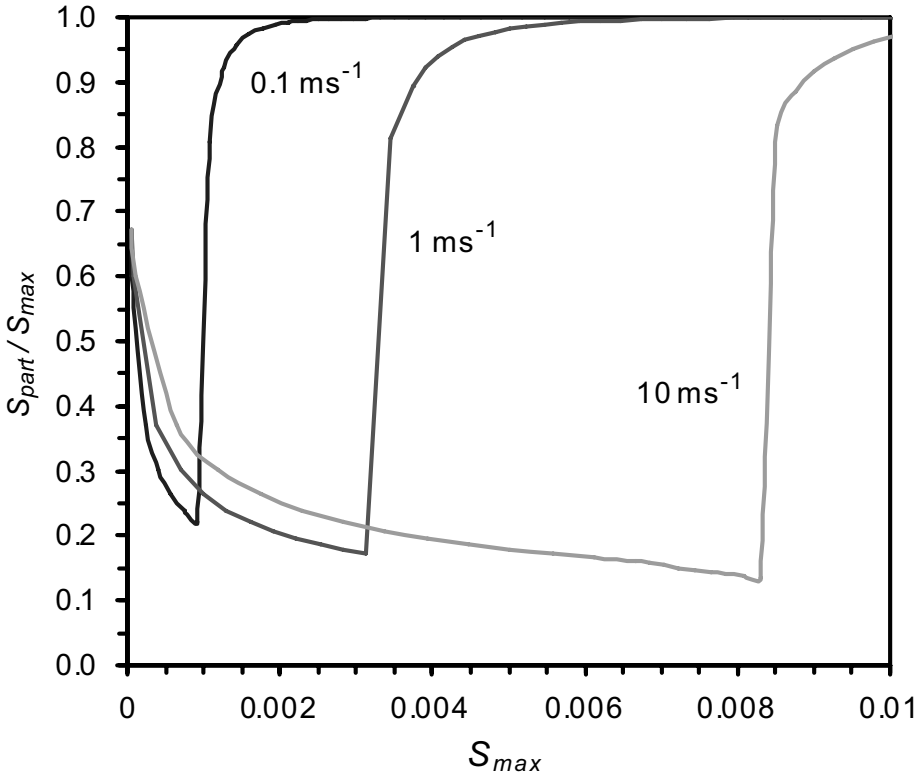

Figure 8.3: s_{part}/s_{max} as a function of s_{max}. Each curve corresponds to a constant updraft velocity.

$s_{part} = s_{part,2}$ for $\Delta > 0$) displays physically expected behavior. Figure 8.3 shows s_{part}/s_{max} as a function of s_{max}. Each line corresponds to a different value of updraft velocity, V. Given that each curve in Figure 8.3 is for constant updraft velocity V, s_{max} varies only because of changes in aerosol concentration; Figure 8.3 thus displays the Twomey effect on s_{part}. Note that there are regions for which s_{part} is insensitive to changes in s_{max}; we would expect that simple parameterizations perform well in these regions, as they do not exhibit implicit dependence on s_{max}. At large values of s_{max}, $s_{part}/s_{max} \rightarrow 1$, indicating that the vast majority of the CCN are not subject to kinetic limitations. For lower values of s_{max}, s_{part}/s_{max} reaches a minimum; a further decrease in s_{max}, however, reverses the trend for s_{part}/s_{max}, as explained above. An activation parameterization is severely tested in regions where s_{part} changes rapidly.

It is also important to examine the behavior of s_{part}, for constant aerosol concentration and variable updraft velocity. To do so, we need information regarding the relationship between aerosol concentration, V and s_{max}. This is accomplished by using a numerical

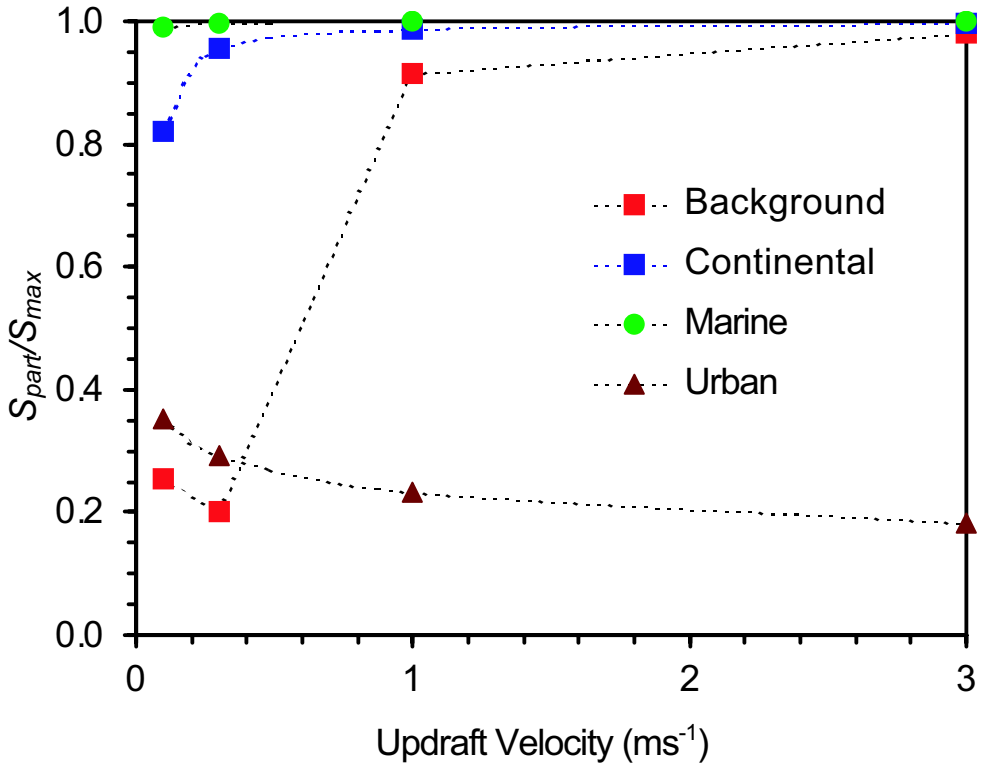

Figure 8.4: s_{part}/s_{max} as a function of updraft velocity. Each curve corresponds to one of the aerosol types in Table 8.2. s_{max} is computed using the numerical parcel model of [117].

parcel activation model for the four aerosol types shown in Table 8.2. The results are shown in Figure 8.4. Clearly we can see that for marine-type aerosols, s_{part} is close to unity (meaning that the vast majority of the droplets attain sizes larger than their critical diameter) for all updraft velocities; the other extreme is the urban aerosol, which always experiences significant kinetic limitations. For the distribution used here, between 20% to 40% of the particles do not reach critical size at any updraft velocity. These percentages agree well with the numerical results of [117] for the same aerosol size distributions; this is verification that the procedure used for calculating s_{part} is realistic. (Note that the correlation was derived from many simulations).

8.5.5 Final form of aerosol activation parameterization

After evaluation of Equation 8.25, and substitution into Equation 8.18, we obtain the final form of the parameterization, which is a nonlinear algebraic equation for the maximum supersaturation of the cloud parcel,

$$\frac{\pi}{2}\frac{\gamma\rho_w G s_{max}}{aV}\left\{\int_0^{s_{part}} D_p n^s(s')ds' + \int_{s_{part}}^{s_{max}} D_p n^s(s')ds'\right\} - 1 = 0 \tag{8.32}$$

where,

$$\int_0^{s_{part}} D_p n^s(s')ds' = \left(\frac{G}{aV}\right)^{1/2} \sum_{j=1}^{i_{part}} \frac{N_j}{s_c^j - s_c^{j-1}} \left[\frac{x}{2}\left(s_{max}^2 - x^2\right)^{1/2} + \frac{s_{max}^2}{2} Arc\sin\frac{x}{s_{max}}\right]_{x=s_c^{j-1}}^{x=s_c^j}$$

$$\int_{s_{part}}^{s_{max}} D_p n^s(s')ds' = \frac{2}{3}\left[\sum_{j=i_{part}}^{i_{max}-1}\left(\frac{N_j A_j}{s_c^j - s_c^{j-1}}\right)\ln\frac{s_c^j}{s_c^{j-1}} + \left(\frac{N_{i_{max}} A_{i_{max}}}{s_c^{i_{max}} - s_c^{i_{max}-1}}\right)\ln\frac{s_{max}}{s_c^{i_{max}-1}}\right]$$

where i_{part} is the section boundary closest to s_{part} (implementation of population splitting within an aerosol section is straightforward), and, i_{max} is the boundary closest to s_{max} with $s_{max} \leq s_{i_{max}}$ (Figure 8.2). The calculation of s_{part} is carried out using either Equation 8.28 (when $\Delta \geq 0$) or Equation 8.31 (when $\Delta < 0$).

The procedure for using the parameterization is illustrated in Figure 8.5. Equation 8.32 is solved for s_{max} using the bisection method. All physical properties are evaluated at cloud base conditions. The number of droplets is computed from Equation 8.8.

We would like to point out that the complexity of the integrals in equation 8.32 arises from using a sectional representation for the CCN spectrum (equation 8.6), and not from the procedure used to develop the parameterization (i.e., the concept of populations splitting, and calculation of s_{split}). The formulation for other size distributions (e.g., lognormal) can be much simpler than equation 8.6, but is beyond the scope of this paper.

8.6 Evaluation of new parameterization

8.6.1 Activation conditions considered.

The performance of the new parameterization will be evaluated by comparing the predicted cloud droplet number concentrations with those of a full numerical activation adiabatic cloud parcel model [117]. The parameterization is tested for a large number of aerosol size distributions and updraft velocities (about 200 cases total), which encompass the wide variety of tropospheric aerosols. For convenience, size distributions are taken to be of the

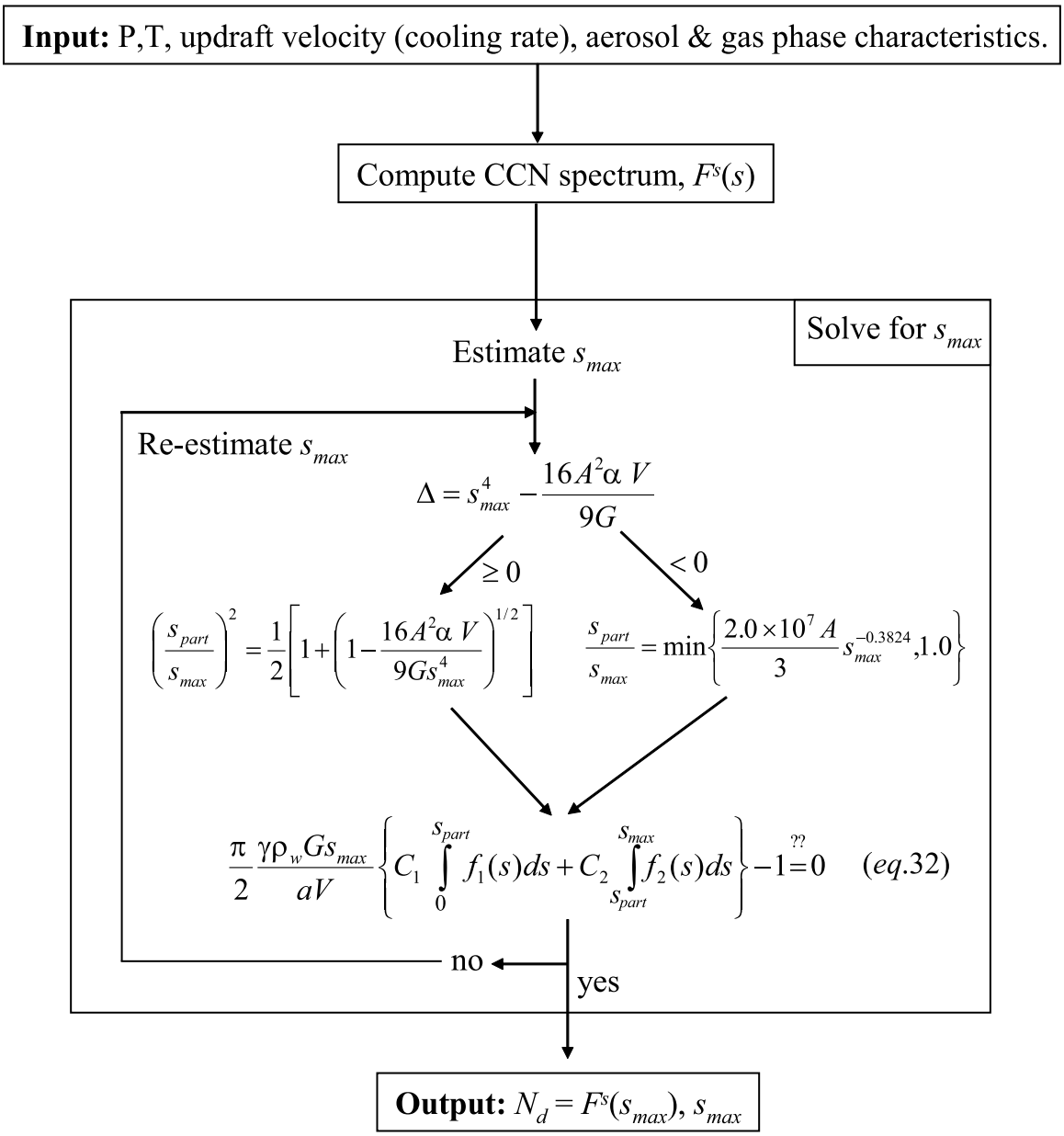

Figure 8.5: Parameterization algorithm.

single or multiple log-normal form,

$$\frac{dn\left(D_p\right)}{d\ln D_p} = \sum_{i=1}^{n_m} \frac{N_i}{\sqrt{2\pi}\ln\sigma_i} \exp\left[-\frac{\ln^2\left(D_p/D_{g,i}\right)}{2\ln^2\sigma_i}\right] \tag{8.33}$$

where N_i is the aerosol number concentration, $D_{g,i}$ the number mode diameter, σ_i is the geometric standard deviation for mode i, and n_m is the number of modes in the distribution.

For single mode aerosol, we consider a wide range in number concentration, mode diameter, and dispersions. The range in mode diameter and number concentration is appropriate for accumulation mode particles, which comprise most CCN. Table 8.1 summarizes the characteristics of the mode radii, number concentrations, and updrafts examined.

For multiple mode aerosol, we have selected four of the [160] trimodal representations, namely the marine, clean continental, average background, and urban aerosol (Table 8.2). The size distributions refer to dry size, while the chemical composition of the aerosol is assumed to be pure ammonium sulfate. To evaluate the ability of the new parameterization to capture the effect of surface-active organics, we also perform simulations for an aerosol that has the [160] marine aerosol size distribution, which is assumed to be composed of 80% by mass $(NH_4)_2SO_4$ and 20% organic that displays surface active behavior. The aerosol organic component is a reconstruction of chemical composition observed in Po Valley fogs and is assumed to be composed of 18% (by mass) levoglucosan ($C_6H_{10}O_5$, density = 1600 kg m^{-3}, van't Hoff factor = 1), 41% (by mass) succinic acid ($C_6O_4H_6$, density = 1572 kg m^{-3}, van't Hoff factor = 3), and 41% (by mass) fulvic acid [158], ($C_{33}H_{32}O_{19}$, density = 1500 kg m^{-3}, van't Hoff factor = 5 [114]). The surface tension behavior of this organic is assumed to follow the correlation of [36]. Finally, to test the performance of the parameterizations under conditions of strong kinetic limitations, we examine the same size distributions with the concentrations doubled. The characteristics of the simulations are summarized in Table 8.3.

In the numerical parcel simulations, particles are assumed initially to be in equilibrium at a relative humidity of 98%, and P,T as specified in Tables 8.1 and 8.3. For both the new parameterization and numerical parcel model, we consider 200 size bins spaced equally in log diameter. Using a size range between $D_{p,g}/10\sigma$ and $10\sigma D_{p,g}$ covers total particle number to within 10^{-7}%. The simulations exhibit little sensitivity with respect to initial relative humidity and use of a denser grid. Using 200 bins for both the parameterization

Table 8.1: Characteristics of single log-normal aerosol distribution runs. Pressure is 800 mbar, and temperature is 283 K.

Simulation set	$D_{g,i}$ (μm)	N_i (cm^{-3})	σ_i	V (m s^{-1})	# of points[a]
SM1[b]	0.02	200	2.5	0.1 - 10.0	18
SM2	0.02	1000	2.5	0.1 - 10.0	18
SM3	0.02	1000	1.5	0.1 - 10.0	18
SM4	0.2	200	2.5	0.1 - 10.0	18
SM5	0.02	10000	2.5	0.1 - 10.0	18
SM6	0.04-0.20	100 - 1000	2.0	0.1 - 3.0	72

[a] i.e. number of simulations considered for the specified range of parameters.

[b] "SM" denotes Single Mode.

Table 8.2: Aerosol distribution parameters ($D_{g,i}$ in μm, N_i in cm^{-3}) [160]

Aerosol type	Nuclei Mode			Accumulation Mode			Coarse Mode		
	$D_{g,1}$	σ_1	N_1	$D_{g,2}$	σ_2	N_2	$D_{g,3}$	σ_3	N_3
Marine	0.010	1.6	340	0.070	2.0	60	0.62	2.7	3.1
Clean Continental	0.016	1.6	1000	0.068	2.1	800	0.92	2.2	0.72
Average Background	0.016	1.7	6400	0.076	2.0	2300	1.02	2.16	3.2
Urban	0.014	1.8	106000	0.054	2.16	32000	0.86	2.21	5.4

Table 8.3: Characteristics of multiple log-normal aerosol distribution simulations. The range in updraft velocity examined is 0.1 - 3.0 m s^{-1}. Pressure is 900 mbar, and temperature is 273 K.

Simulation set	Aerosol type	# of points[a]	Description.
TM1[b]-M[c]	Marine	4	Distribution from Table 8.2
TM1-C	Clean Continental	4	Distribution from Table 8.2
TM1-B	Average Background	4	Distribution from Table 8.2
TM1-U	Urban	4	Distribution from Table 8.2
TM2-M	Marine	4	TM1-M concentration doubled
TM2-C	Clean Continental	4	TM1-C concentration doubled
TM2-B	Average Background	4	TM1-B concentration doubled
TM2-U	Urban	4	TM1-U concentration doubled
TM3	Marine	4	TM1-M concentrations; surfactant present

[a] i.e. number of simulations considered for the specified range of parameters.

[b] "TM" stands for Tri-Modal.

[c] "M" for Marine, "C" for Continental, "B" for Background, and "U" for Urban aerosol.

and the parcel model ensures that differences in droplet number between the two is not due to discretization error.

When using the parameterization, the droplet number is calculated from Equation 8.8. When using the parcel model, the droplet concentration is calculated using the criterion of [117], which is to find the CCN of highest s_c that strictly activates (i.e. exceeds its critical diameter); anything larger than this CCN is counted as a drop. Note that this definition accounts for kinetic limitations; large CCN that have not attained their critical diameter are considered as droplets, but not those that deactivate and become interstitial aerosol. Droplet concentration is evaluated at 250 m above cloud base.

8.6.2 Comparison of new parameterization with parcel model.

Figure 8.6 displays the fraction of aerosol that becomes droplets (termed as "activation ratio"), as predicted by the new parameterization and the parcel model. For the wide variety of aerosol and updraft velocities considered, the activation ratio ranges between 10^{-3} to 1.0. Most of the predicted values are very close to the 1:1 line, and do not display significant systematic biases over the range of activation ratios; this shows that the parameterization performs well regardless of the steepness of the CCN spectrum (at low activation ratios, the spectrum is steep, while at high activation ratios, the spectrum is not). This also indicates that the parameterization is capable of treating highly complex and "irregular" CCN spectra, which deviate substantially from the smoothness of CCN spectra that correspond to log-normal size distributions. We do note however, that although there is scatter about the 1:1 line, more frequently the activated fraction tends to be underestimated. This is because the maximum supersaturation for these cases is slightly underpredicted, and leads to a corresponding underprediction in droplet number. s_{max} is underpredicted, because the condensation rate is slightly overpredicted.

Figure 8.7 displays the droplet number concentration as predicted by the new parameterization and the parcel model. The range of droplet concentrations covers the entire range observed in clouds (e.g. [15, 60]). The predicted droplet number follows the 1:1 line closely. There are no regions with a variable systematic bias in the predictions, indicating that the parameterization performs well, regardless of the extent of kinetic limitations throughout the droplet population. Confirmation of this can be attained by evaluating the performance of the parameterization for the two Δ regimes. This is shown in Figure 8.8, which is the

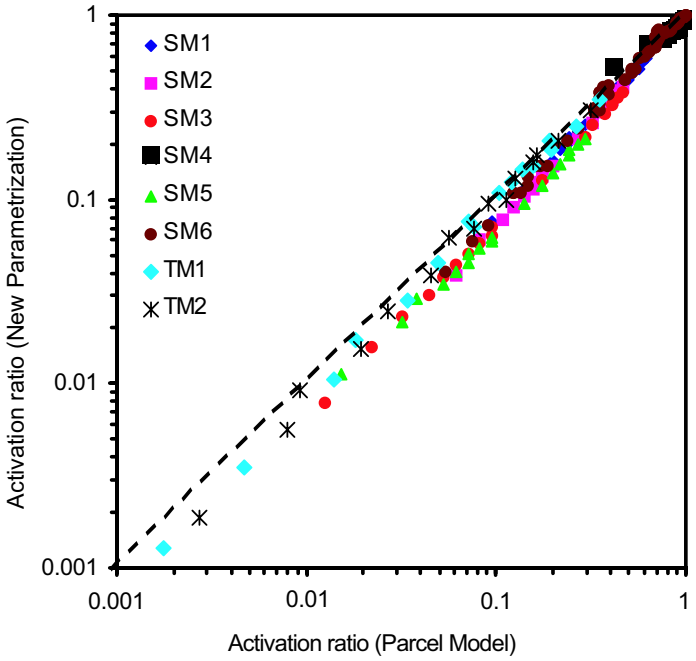

Figure 8.6: Fraction of aerosol that become droplets, as predicted by the new parameterization and the cloud parcel model.

same as Figure 8.7, but with the points colored according to the value of Δ. Most of the points examined are for $\Delta \geq 0$, but clearly the two regimes exhibit equivalent scatter around the 1:1 line; this is a strong indication that the parameterization is insensitive to the extent of kinetic limitations.

It is important to evaluate the performance of the parameterization in predicting the parcel s_{max} (Figure 8.9). The range of maximum parcel supersaturations covers that predicted for most clouds; for most cases, the parcel supersaturation is well captured. It is notable that the parameterization captures even the urban and background aerosols, which are subject to strong kinetic limitations (which account for roughly half of the multimodal cases examined). Particularly challenging are the TM2-U simulations. The s_{max} in these cases is very small (on the order of 0.01%), and errors in this quantity can lead to large biases in predicted N_d; the parameterization nonetheless reproduces the parcel simulations very well. It should be noted however that the parameterization (for these conditions) tends to slightly underestimate s_{max}.

Figures 8.6 to 8.9 display some scatter around the 1:1 line. It is important to examine

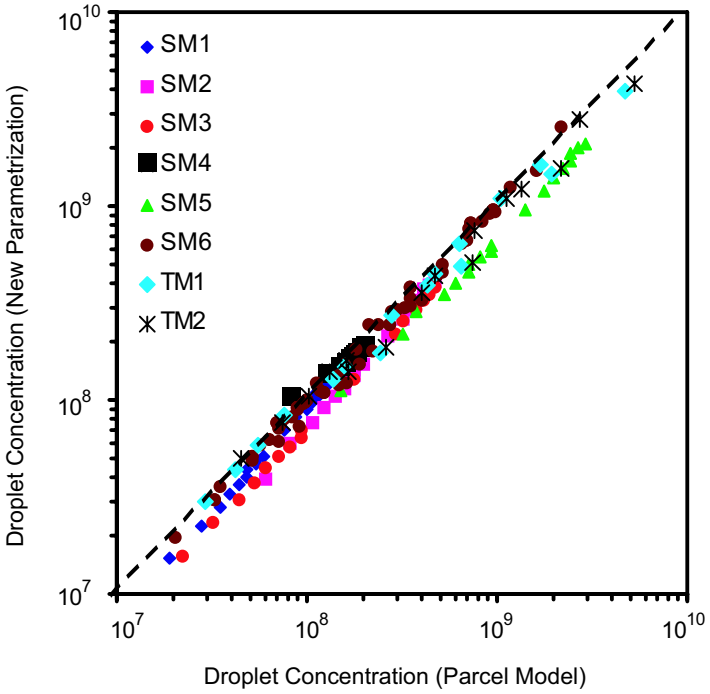

Figure 8.7: Droplet number concentration, as predicted by the new parameterization and the cloud parcel model.

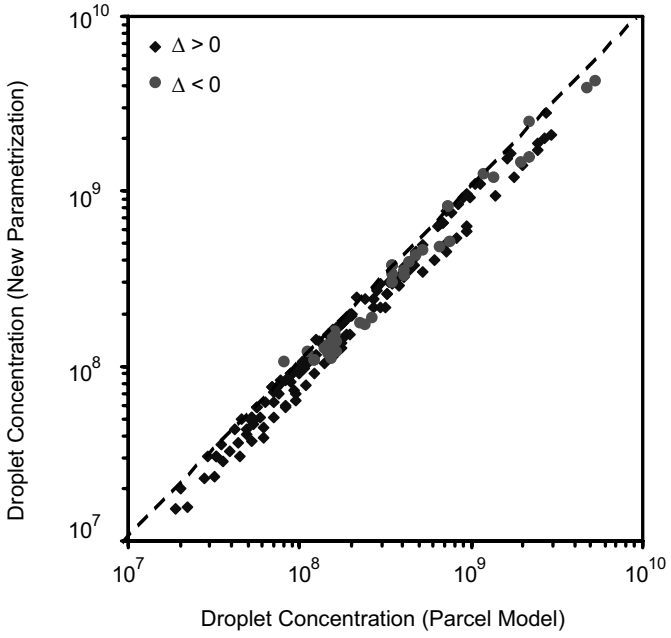

Figure 8.8: Droplet number concentration, as predicted by the new parameterization and the cloud parcel model. The points are colored according to the value of Δ.

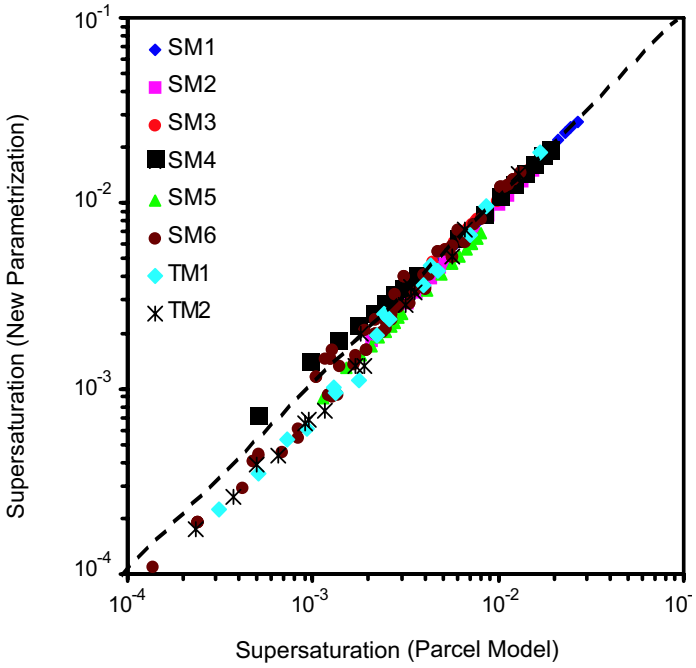

Figure 8.9: Maximum parcel supersaturation, as predicted by the new parameterization and the cloud parcel model.

how significant this scatter is, on average and on a per-case basis, as we can gain further insight into possible systematic biases. Table 8.4 displays the statistics of the ratio of parameterized N_d to the N_d calculated from the parcel model; if the parameterization perfectly captured the parcel simulations, this ratio would be 1.0. The overall average ratio is about 0.95, with a standard deviation of 0.1. Grouping the results according to aerosol case and Δ regime, we note that the performance is excellent for all the multimodal aerosols (TM1, TM2), despite the fact that about half of the cases involve significant kinetic limitations. Some of the single mode cases perform less optimally, but still are quite close to the cloud parcel predictions. The statistics for the two Δ regimes are about the same; the fact that $\Delta < 0$ has double the standard deviation of $\Delta \geq 0$ is likely a result of the smaller statistical sample. In any case, the standard deviation for all of the statistics is small, which indicates the robustness of the parameterization.

Finally, we address the performance of the new parameterization for an aerosol containing an organic species. Capturing the activation behavior of these CCN is more difficult than those containing only soluble salt and insoluble substances, as the presence of an or-

Table 8.4: Statistics of the ratio of N_d calculated from new parameterization to N_d calculated from parcel model.

Simulation Set	Average Ratio	Minimum Ratio	Maximum Ratio	Standard Deviation	# of points (% with $\Delta < 0$)
TM1(all)	0.9332	0.7242	1.0838	0.1137	16 (44)
TM2(all)	0.9159	0.6864	1.0907	0.1284	16 (56)
SM1	0.8819	0.7983	0.9634	0.0530	18 (0)
SM2	0.7923	0.6356	0.9112	0.0722	18 (0)
SM3	0.7333	0.6298	0.8115	0.0494	18 (0)
SM4	1.0204	0.9720	1.2954	0.0782	18 (5)
SM5	0.6955	0.6222	0.7673	0.0406	18 (5)
SM6	0.9780	0.7481	1.1587	0.0854	72 (26)
$\Delta < 0$	0.9082	0.6864	1.2954	0.1461	37 (100)
$\Delta \geq 0$	0.9838	0.7975	1.1530	0.0704	161 (0)
Total	0.9582	0.6864	1.2954	0.1080	198 (19)

ganic species within CCN can affect the activation behavior in many ways: the organic can contribute soluble material (e.g. [145]), can alter the droplet surface tension (e.g., [145, 36], and potentially affect the droplet growth kinetics (e.g., [37, 114]). Here we will focus on the solute and surface tension effects. Given that organics which can substantially affect surface tension can also be highly soluble (e.g., humic-like substances), we will assume that the organic is completely soluble (the overall effect on activation, at least for the conditions examined here, do not change appreciably even if the solubility changes considerably [114]). Under these conditions, the challenge for the organic-containing CCN is to calculate the surface tension at the point of activation (which varies with aerosol size and composition). This difficulty is overcome by the sectional representation of the aerosol, as the effect of the surface-active species can be included in the calculation of the s_c of each CCN section. We simulate the activation of an aerosol assumed to follow the [160] marine aerosol size distribution (Table 8.2), composed of 80% by mass $(NH_4)_2SO_4$ and 20% by mass organic surfactant (with a composition as given before). Figure 8.10 displays the activation ratio as a function of updraft velocity, as predicted by the parameterization and the parcel model. The parameterization captures well the activation behavior of the aerosol. Excluding the effects on surface tension results in the expected decrease in droplet number.

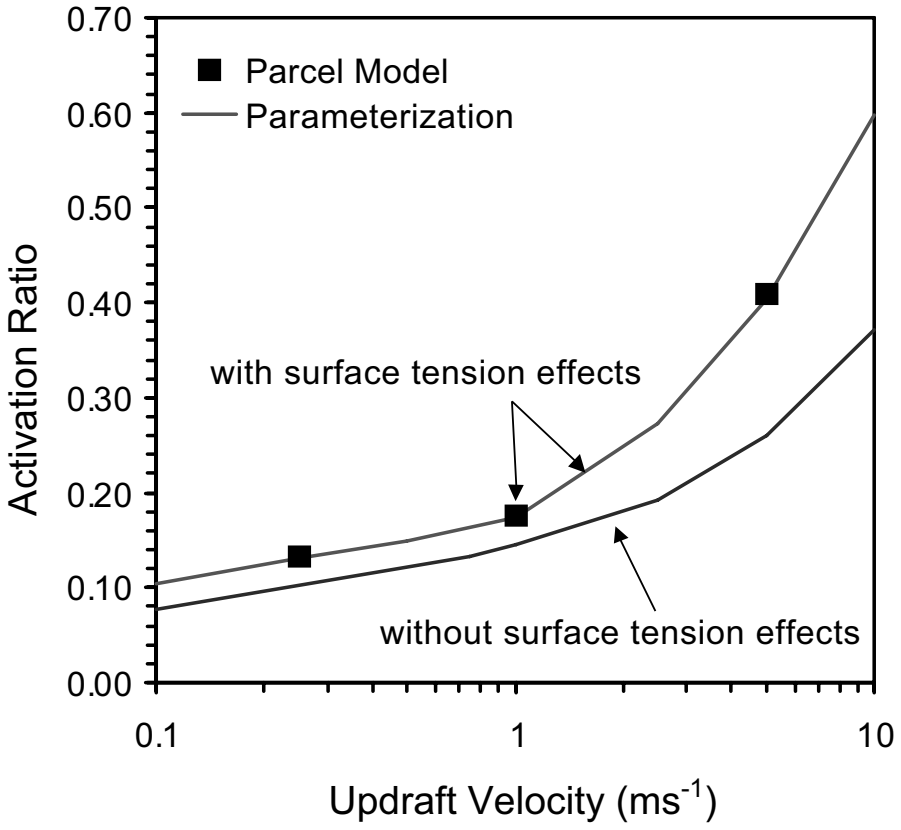

Figure 8.10: Activated droplet ratio, as a function of updraft velocity. Both the cloud parcel model and parameterization results (with and without the effect of the organic from changes in surface tension) are shown. The parcel model simulations include surface tension effects from the dissolved organic. Marine aerosol composed of 80% $(NH_4)_2SO_4$ and 20% organic surfactant is used. The organic surfactant behavior is described in the text.

8.6.3 Comparison with other parameterizations.

The new parameterization is tested against the performance of the [1] parameterization in reproducing the results of the parcel model. These parameterizations were chosen for comparison as they are the most comprehensive formulations available in the literature. We would like to point out that the new and the [3] and [1] parameterizations are fundamentally different in their representation of the CCN spectrum. The former uses a sectional representation, and the latter two, a modal representation (i.e., an exact analytical integration over a lognormal size distribution). We ensured that the differences in droplet number between the parameterizations are only from their treatment of the activation process by using 200 size bins for the new parameterization (and parcel model). This way, when approximating the lognormal distribution with a series of size sections, the discretization error is very small (less than 1% in droplet number).

Figure 8.11 displays the fraction of aerosol that becomes droplets, as predicted by the [1] parameterization and the parcel model. For most cases, these parameterizations perform well, but numerous cases deviate considerably from the 1:1 line. This behavior is also seen in the parameterized s_{max} (not shown). For a given size distribution, the deviations seem to become larger as the activation ratio decreases, that is the steep-slope region of the CCN activation spectrum. Figure 8.12 displays the droplet number for the same conditions as in Figure 8.11. The deviations from the 1:1 line do not seem to follow any systematic behavior, so they are less likely to be controlled by kinetic limitations (this is understandable, as the parameterization is fitted to numerical parcel simulations, thus implicitly accounting for kinetic limitations). Actually, the opposite is occurring: the predictions for the marine aerosols deviate notably from the parcel simulations. [1] report that errors are expected from the parameterization when the modal diameters differ by about an order of magnitude. The nuclei and accumulation modes in the marine and continental aerosol runs vary by a factor of 7, and for the urban and background aerosol, by a factor of 5; therefore, errors are expected. The deviations do not seem to be focused in any particular region of droplet number concentration, but rather for certain combinations of mode dispersion and updraft velocity. This behavior indicates that the biases most likely originate from the correlation used in the parameterization.

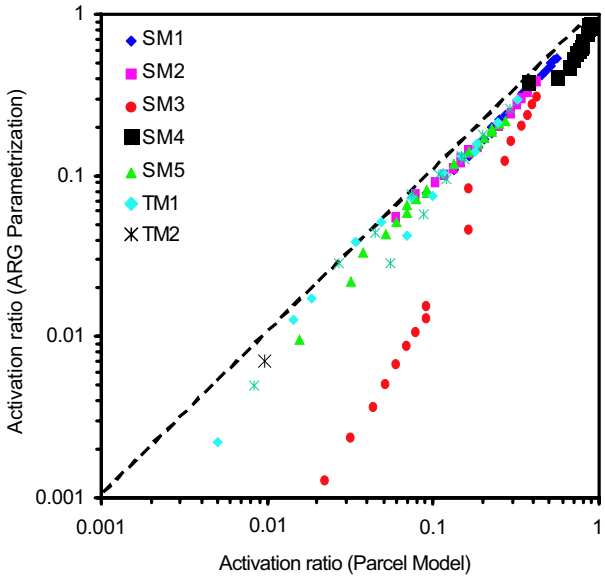

Figure 8.11: Fraction of aerosol that become droplets, as predicted by the [1] parameterization and the cloud parcel model.

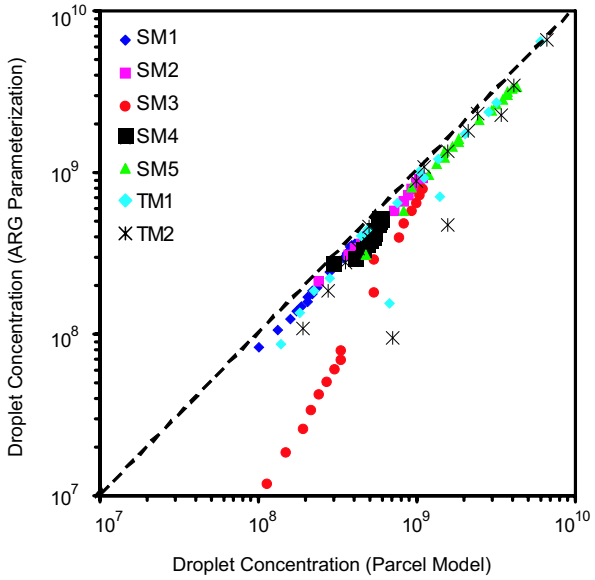

Figure 8.12: Droplet number concentration, as predicted by the [1] parameterization and the cloud parcel model.

8.7 Conclusions

A new aerosol activation parameterization has been developed, based on a generalized sectional representation of aerosol size and composition. The maximum supersaturation needs to be determined first by numerically solving an algebraic equation, and then the droplet number concentration is computed from the supersaturation spectrum. The flexibility of the parameterization and comprehensive treatment of the droplet activation justify the additional computational effort.

We introduce the concept of "population splitting", in which the CCN that form droplets are divided into two separate populations: those which have a size close to their critical diameter, and those that do not. We also explicitly introduce kinetic limitations on droplet growth. For a wide range of CCN activation conditions, the parameterization is free from any empirical information or correlations derived from detailed numerical simulations. There are certain conditions for which an empirically derived correlation is utilized; this is required whenever most of the activated CCN are kinetically limited. Whether the empirical information is needed or not is determined by a parameter that indicates the extent of kinetic limitations (defined as the "descriminant criterion", Δ).

Predictions of the parameterization are extensively compared against those of a detailed cloud parcel activation model, for a variety of aerosol activation conditions that cover a wide range of chemical variability and CCN concentrations. The parameterization closely tracks the parcel model simulations, while the computational burden of the parameterization is more than three orders of magnitude less than that of the parcel model itself. The new parameterization displays superior performance, in both accuracy and robustness, when compared to existing parameterizations. Decreased reliance on empirical information does not diminish the performance of the parameterization; on the contrary, it seems to enhance its robustness.

The new parameterization, in the formulation presented in this paper, can treat all types of aerosol that follow Köhler theory; as no restriction of an explicit link between dry size and critical supersaturation is needed, the parameterization can treat internally or externally mixed aerosol, with size varying composition, including the effects of surface active species (organics), insoluble species and slightly soluble species. The current formulation can even treat recently identified effects, such as the heating of CCN from the presence of black

carbon [28, 116]. The possibilities do not stop here. The structure of the parameterization allows for further extension, such as explicit treatment of condensable gases and organic species that exhibit slow growth kinetics, and including entrainment in the parcel (non-adiabatic activation). Although much is still unknown about the effect of organic species on droplet activation, the ability to parameterize their possible effects is highly desirable, as it establishes the framework for a comprehensive assessment of the aerosol indirect effect in global climate models.

8.8 Acknowledgments

This work was supported by the NASA Earth Observing System-Interdiciplinary Science program (NASA EOS-IDS) and the Office of Naval Research grant N00014-96-1-0119. We would also like to thank T. Rissman for assistance with some of the ARG parameterization calculations.

Chapter 9

A theoretical analysis of cloud condensation nucleus (CCN) instruments

Note: This chapter appeared as reference [117].

9.1 Abstract

The behavior and performance of four cloud condensation nucleus (CCN) instruments are theoretically analyzed. These include the static diffusion cloud chamber (SDCC), the Fukuta continuous flow spectrometer (FCNS), the Hudson continuous flow spectrometer (HCNS) and the Caltech continuous flow spectrometer (CCNS). A numerical model of each instrument is constructed based on a general fluid dynamics code coupled to an aerosol growth/activation model. Instrument performance is explored by simulating instrument response when sampling a monodisperse ammonium sulfate aerosol. The uncertainty in the wall temperature boundary condition is estimated for all the instruments, and is found to be appreciable only for the CCNS. The CCNS and HCNS models reasonably reproduced experimental data, while reported limits were also verified by the FCNS model. Regarding the performance of each instrument, simulations show that the SDCC produces droplets that are monodisperse to within 10% of the particle diameter (for particles of a constant critical supersaturation). The FCNS can potentially activate particles over a wide range of critical supersaturations, but the prevailing design exhibits low sensitivity to particles with critical supersaturations below 0.1% as a result of the short time available for droplet growth under low supersaturations. The resolution capability of both HCNS and CCNS with respect

to critical supersaturation is shown to be particularly sensitive to operational parameters. This is a consequence of the strongly nonlinear nature of droplet growth; droplet size cannot always be used to distinguish particles with different critical supersaturation because of growing droplets trend toward monodispersity. Of the two instruments, the HCNS generally displays higher resolution capability. This is attributed to the smoother and monotonic supersaturation profiles established in the HCNS. While different design parameters or operating conditions may lead to modest shifts in the performance from that predicted here for any of the four instruments, the essential features described in this paper are inherent to their designs.

9.2 Introduction

In theory, the cloud droplet activation spectrum of atmospheric aerosols can be inferred based on composition. Measuring the complete chemical composition of atmospheric aerosol as a function of particle size in real time, however, is not yet possible. Therefore, a direct measurement of the particles that activate to form droplets under supersaturations typical of atmospheric clouds is the accepted way to experimentally measure cloud condensation nuclei (CCN). Existing instruments to determine the CCN distribution expose an aerosol sample to a controlled environment with known water supersaturation profiles; the activation spectrum is then obtained by measuring the number (or size distribution) of particles that activate.

This study analyzes the performance of four existing CCN instrument designs. The main focus of this work is to determine the capability of each instrument (or more precisely, of the methodology embodied by each instrument) to resolve a CCN activation spectrum. The resolution computed is solely a result of the process of CCN activation and growth within each instrument; uncertainty introduced by the droplet detection system is not considered. Furthermore, the models constructed here represent idealized instruments. This abstraction allows one to calculate the best possible (theoretical limit) resolution for an actual instrument; secondary effects not considered in these models will further degrade the resolution.

In addition to assuming idealized instruments, it is also assumed that a perfectly monodisperse aerosol is introduced, composed of pure $(NH_4)_2SO_4$. In reality, atmospheric aerosol

is polydisperse and with a nonuniform composition. As a consequence, particles with the same potential for activation need different times for growth; this should have a deleterious effect on the instrument performance, but will not be addressed in the current study.

An important uncertainty arises from the water film temperatures that are used to generate supersaturation in each instrument. Typically, CCN instruments measure and control temperatures by using thermocouples (or thermistors) that are embedded in the chamber wall rather than at the gas-wet surface interface. The actual temperature difference between the cold and hot water films is lower than the measured value due to the thermal resistances of the plate and films, leading to a lower supersaturation than intended. As a result, the inferred activation spectrum is biased towards smaller sizes.

In the sections that follow, the CCN instruments are described, then the mathematical models used to simulate them are presented. An estimate of uncertainty in the water film temperature boundary conditions then follows. The response to a monodisperse aerosol input is simulated for each instrument. Finally, the performance of each (idealized) instrument is assessed based on these simulations.

9.3 Description of CCN instruments

Of the CCN instruments currently available, we will focus upon four: a) the static diffusion cloud chamber (SDCC), b) the continuous flow parallel plate chamber, specifically the design of [46] (FCNS), c) the CCN spectrometer of [71], (HCNS) and, d) the Caltech CCN spectrometer [CCNS; [24]. Other instruments, for example, isothermal haze chambers [95] (IHC) have been used to measure CCN but will not be discussed here. IHC instruments do not actually activate the particles into droplets, but rather measure the diameters of particles in equilibrium with an ambient relative humidity of 100%, from which the critical supersaturation, S_c, can be inferred. In theory, this is not a limitation if the particles are composed of inorganic salts, but ambiguity could arise if slightly soluble compounds or surfactants are present in the particles [11, 145].

9.3.1 Static thermal diffusion cloud chamber

These instruments are amongst the oldest for measuring CCN concentrations. The original static thermal diffusion chamber design [155] consists of two parallel metal plates,held at

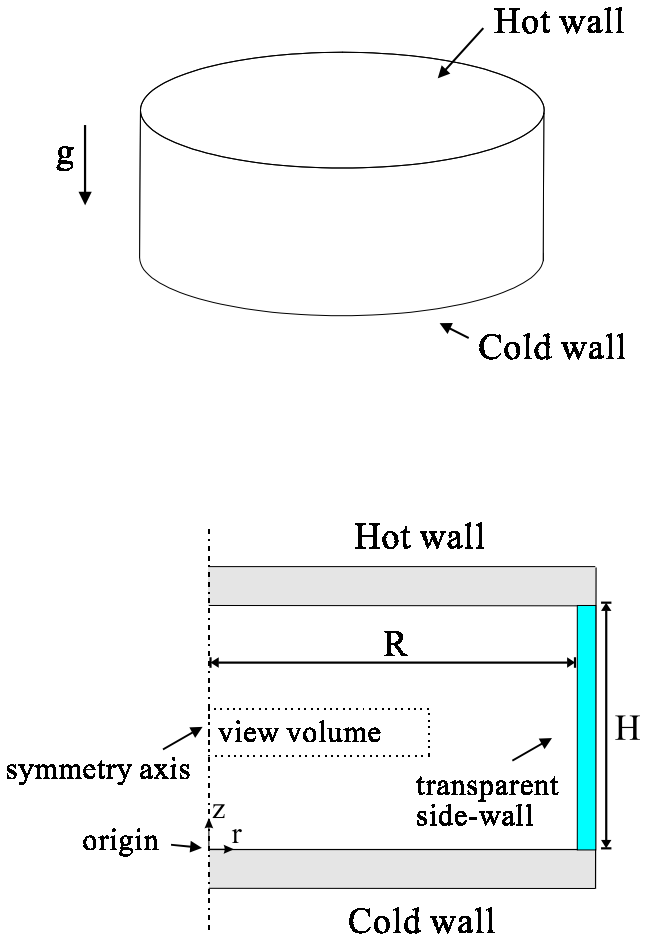

Figure 9.1: The static diffusion cloud chamber (SDCC).

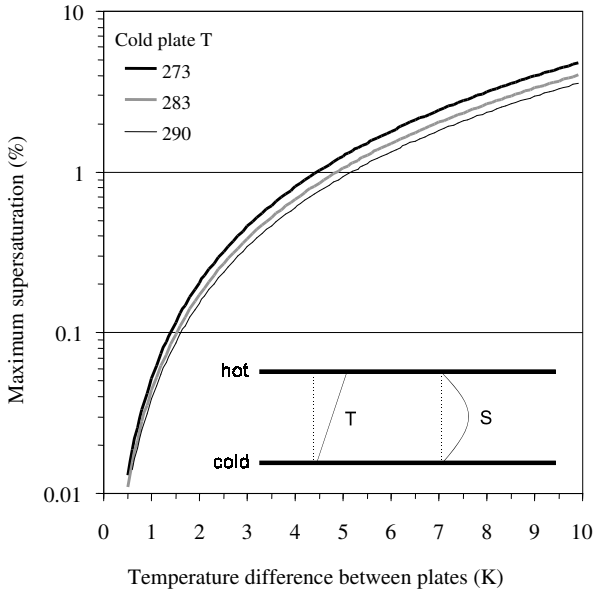

Figure 9.2: Maximum supersaturation (%) in the SDCC as a function of hot and cold plate temperatures. A linear temperature profile is assumed. Water vapor pressure is calculated from a correlation given by [143].

different temperatures, with their facing surfaces wetted (Fig. 9.1). Assuming quiescent conditions throughout the chamber, linear temperature and nearly parabolic supersaturation profiles develop between the plates, with the maximum supersaturation located midway. Figure 9.2 shows the maximum supersaturation generated in the SDCC for a variety of hot and cold plate temperatures. The CCN that are able to activate at the prescribed maximum supersaturation grow to become large droplets and in this way are distinguished from those that do not activate. The concentration of CCN that activate at this prescribed supersaturation is determined by measuring the droplet number concentration. In order to obtain the CCN spectrum, the number of activated droplets must be measured at several supersaturations, which is achieved by changing the temperature difference between the plates. This process typically requires several minutes per spectrum [96]. The lowest critical supersaturation that can be measured in the SDCC is around 0.2% [146].

One of the primary challenges regarding SDCC measurements involves the method used for counting the particles that activate within the region close to the maximum supersaturation. Initially, direct counting of the activated droplets was used, but has been abandoned due to the difficulty associated with such measurements. Photometric estimation is now the

method of choice; concentration is inferred from the light scattered off the growing droplets contained within a view volume in the proximity of the instrument's center. Regardless of the scattering metric used (such as peak intensity, rate of signal growth, etc), each introduces uncertainties that affect the resolution that can be obtained with SDCC's, because light scattering, is a strong function of concentration and particle size (both of which vary considerably during the measurement).

One could make the simplifying assumption that all activating particles, regardless of their critical supersaturation, have approximately the same growth behavior. This approximation is reasonable when the critical supersaturation, S_c, is much smaller than the maximum supersaturation, S_{max} (because then the driving force for growth then is approximately equal to the supersaturation). For S_c close to S_{max}, particles with different critical supersaturations need different times to grow up to a given size. Furthermore, the parabolic supersaturation profile within the instrument exposes particles to different supersaturations within the view volume, so droplets with same critical supersaturation do not grow uniformly throughout the view volume. The combination of a non uniform supersaturation profile and different growth rates among the activating particles generates a droplet distribution within the view volume that contributes to the uncertainty in the aerosol measurement. As mentioned in the introduction, additional uncertainty arises from the difference between the imposed and effective temperature differences.

9.3.2 Continuous flow parallel plate diffusion chamber

The continuous flow parallel plate thermal diffusion chamber (CFDC) [146] was developed to overcome some of the limitations of the SDCC. Because the sample flow is continuous, the instrument operates at steady state, eliminating transients that complicate data analysis. Furthermore, useful data can be obtained continuously, rather than in the sampling intervals of batch cycle operation. When the sample is confined to the region close to the centerline of the instrument, all CCN are exposed to essentially the same supersaturation. CFDC measurements are limited to supersaturations larger than about 0.1%, due to the long growth time required at low supersaturations. When the two plates are oriented horizontally, gravitational sedimentation limits the time during which droplets experience a uniform supersaturation and can cause significant particle loss within the instrument. For vertically oriented plates, the maximum temperature difference that can be imposed is

limited by buoyancy-induced flows. Of the two configurations however, the vertical seems to be more effective and is normally used.

An improvement of the CFDC was proposed by [46] (FCNS). In this design, a gradient in temperature is imposed perpendicular to the flow direction, so that particles with the same residence time experience different supersaturations along different streamlines (Fig. 9.3). This instrument can be regarded as a series of CFDC instruments operating at different temperature differences. Figure 9.4 shows calculated temperature and supersaturation profiles perpendicular to the flow, for fully developed laminar flow (neglecting side wall and buoyancy effects). The profiles are similar to those attained in the SDCC at steady state, so diagrams such as Figure 9.2 can be used for predicting S_{max} at different positions in the instrument. It should be noted that S_{max} is attained towards the exit of the instrument, after the concentration and temperature fields develop. A significant portion of the instrument is used to "precondition" the aerosol flow, by developing the velocity and temperature profiles before exposing the flow to the wetted hot wall. If this is not done, incoming air that mixes with saturated hot air in the entrance region of the instrument can generate much higher supersaturations than intended. This may bias the measurement by activating aerosol corresponding to a different supersaturation than prescribed. Strictly speaking, the FCNS is a particle counter, since each streamline is exposed to only one supersaturation (after the flow completely develops). If all streamlines can be probed, a CCN spectrum can be obtained in real time.

9.3.3 Dynamic CCN spectrometers

The underlying idea behind these instruments is to expose an aerosol sample to a variable supersaturation field, and infer the CCN spectrum from the outlet droplet size distribution. CCN with low S_c are expected to activate near the entrance of the instrument, so they have more time to grow than do particles with higher S_c; the latter activate farther down the instrument. Therefore, the outlet droplet size is expected to decrease with increasing critical supersaturation. Thus the particles start growing with a bias in size that enhances the spread of the outlet size distribution. Furthermore the equilibrium size of the particles entering the instrument decreases with increasing critical supersaturation, thus enhancing the size differences between particles of different critical supersaturation, S_c. The sensitivity of the instrument depends critically on how the outlet droplet size varies with initial size,

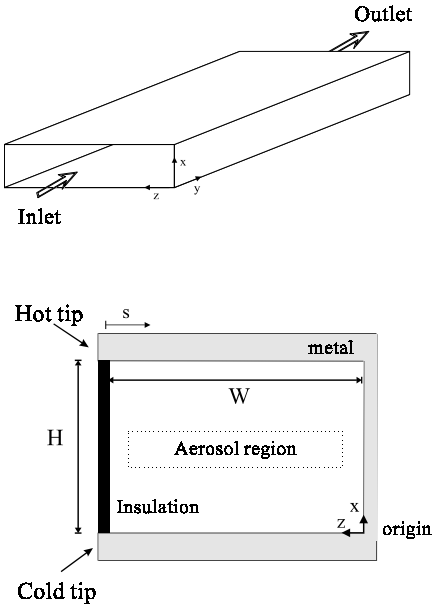

Figure 9.3: The Fukuta continuous flow spectrometer (FCNS).

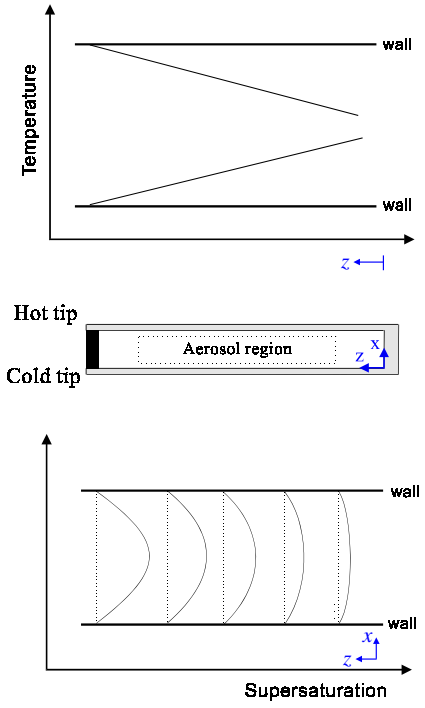

Figure 9.4: Typical temperature and supersaturation (%) profiles for the FCNS along a flow section, for developed inlet conditions.

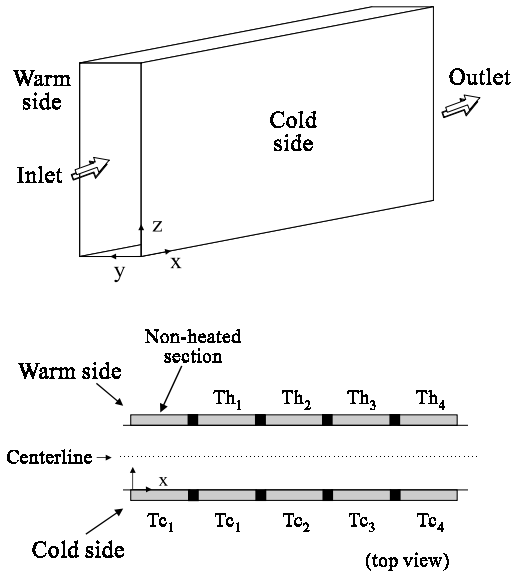

Figure 9.5: The Hudson continuous flow spectrometer (HCNS).

and hence S_c. Because the rate of change of size varies inversely with particle diameter, the droplet size distribution narrows as particles grow, implying that a very precise size measurement may be needed at the outlet of the instrument. Compared to SDCCs and CFDCs, dynamic spectrometers utilize a completely different concept in instrument design, in both the activation and size measurement components.

[71] developed a dynamic spectrometer by modifying a continuous flow thermal diffusion chamber (HCNS) (Fig. 9.5). This instrument exposes the sample air to a supersaturation profile that increases in the streamwise direction, as shown in Figure 9.6. The flow field is preconditioned before a supersaturation is imposed, in a similar fashion to the FCNS. Because the HCNS design measures particles over a large range of S_c simultaneously, CCN spectra can potentially be determined rapidly. The reported range of measurable critical supersaturations in the HCNS is considerably larger than that for thermal diffusion chambers, 0.01 to 1%, covering much of the range of interest for climatically important warm clouds. The supersaturation range is extended because low Sc particles are exposed to much higher supersaturations than needed for their activation, thus considerably accelerating their growth. Because of the speed and wide range of supersaturations that can be covered, this instrument has been used frequently on airborne measurements [111].

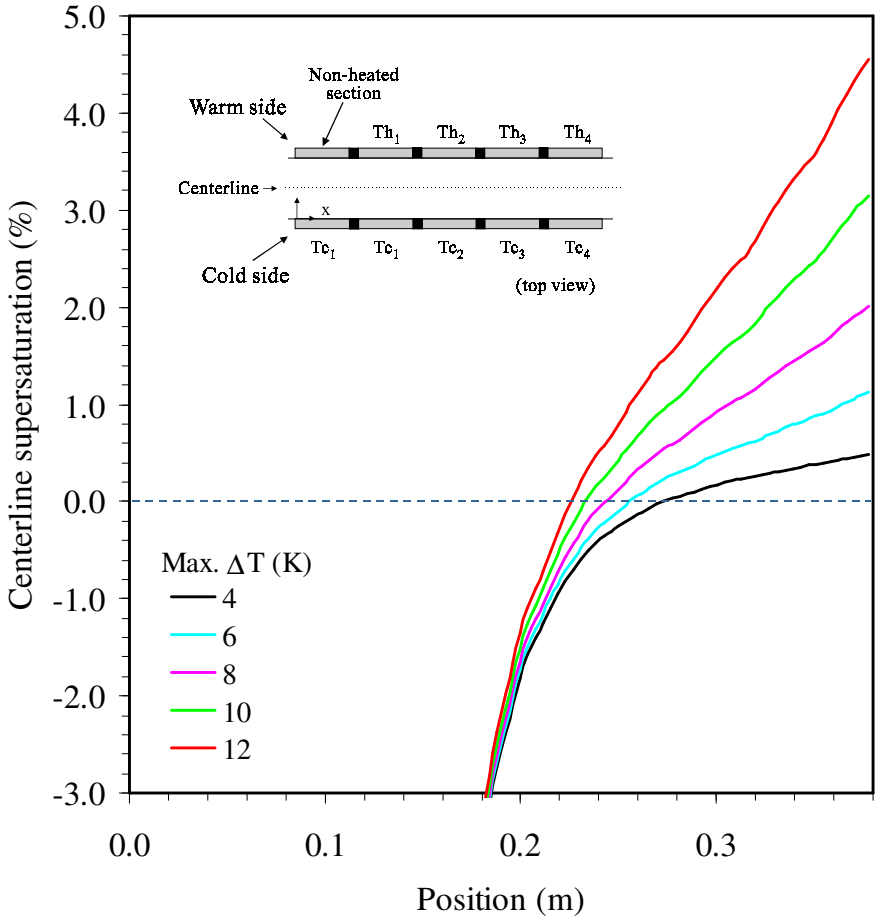

Figure 9.6: Typical supersaturation (%) profiles for the HCNS along a flow section, for various maximum temperature differences, ΔT_{max} (the ΔT at the last segment). The temperature difference between each segment is assumed to increase with a constant step ("linear ramp") on both cold and warm sides. The profiles are computed using the HCNS numerical model in this paper.

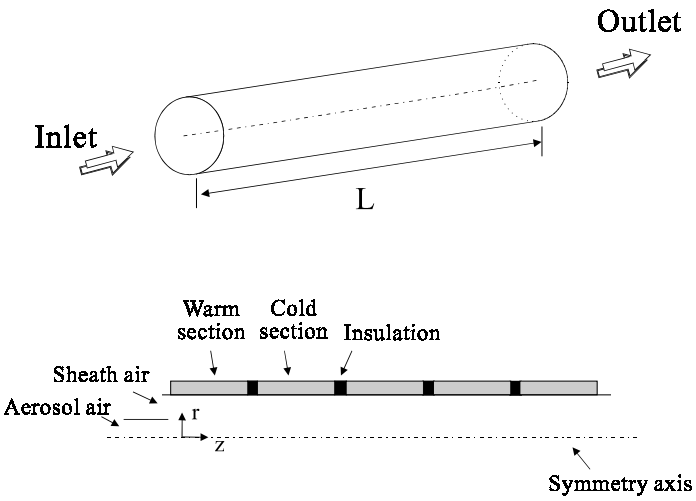

Figure 9.7: The Caltech continuous flow spectrometer (CCNS).

The Caltech CCN spectrometer (CCNS; [24]) (Fig. 9.7) implements Hudson's streamwise gradient method in tube flow. A method originally developed by *Hoppel et al.* [1979] is employed to produce supersaturation in the flow in a wet-walled cylindrical tube; the tube is divided along its length into sections that are alternately heated or cooled. As the air flows through the tube, it is saturated in the warm sections and then cooled to produce supersaturation near the center of the tube. The supersaturation profile that develops depends on the geometry of the segments, the flow rates, the temperature difference, and the operating pressure. The supersaturation is increased along the length of the tube by increasing the temperature difference between successive tube segments, leading to the centerline supersaturation profiles shown in Figure 9.8. The first section can be used to precondition the inlet flow.

Another important issue is to estimate the uncertainty that would arise, when calibration curves produced using pure salt aerosol are used to infer ambient CCN spectra. Both spectrometers operate on the assumption that particles with the same S_c (but different composition) will have the same growth behavior when exposed to an identical supersaturation field. In reality, an even stricter constraint must be satisfied: the Köhler curves need to be similar, which is not the case for aerosol containing surfactant and slightly soluble material. Furthermore, the inlet air may also contain condensable gases that can also have a large

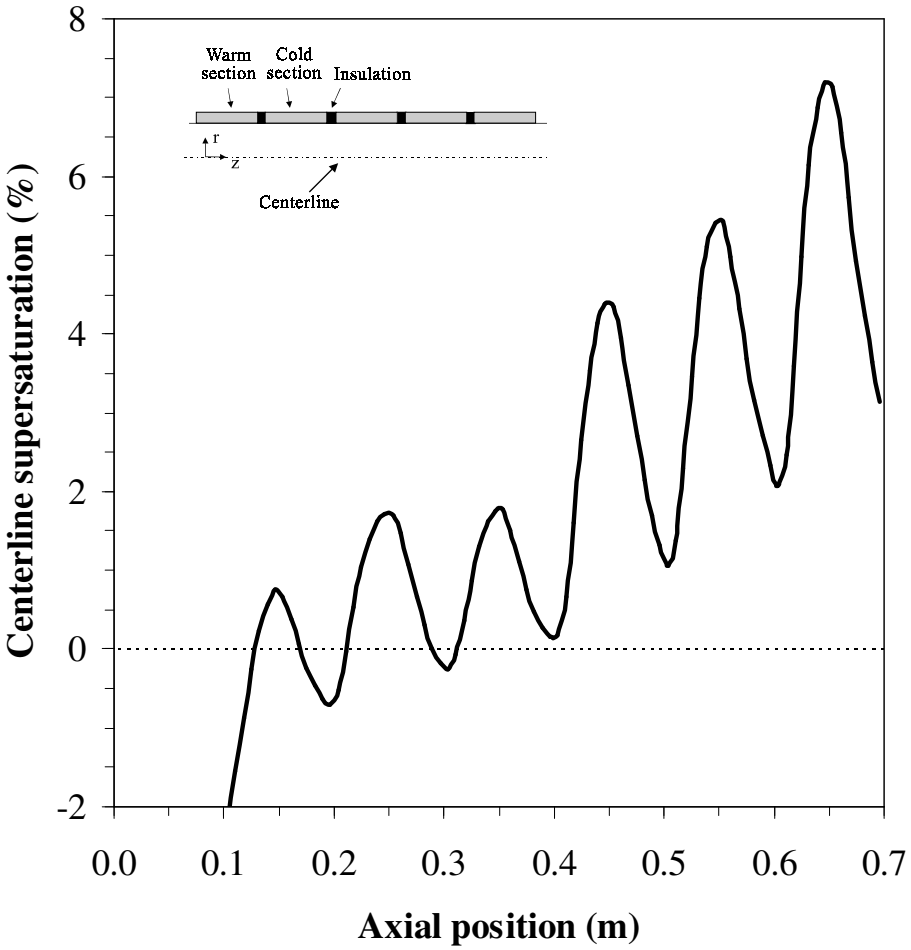

Figure 9.8: Indicative supersaturation (%) profiles for the CCNS along a flow section, for various maximum temperature differences. The volumetric flow rate is 0.7 l min^{-1}. The profiles are computed using the CCNS numerical model of this paper.

impact on the activation properties of the aerosol; this may not be correctly accounted for in the instrument. These issues are to be addressed in future studies.

9.4 Mathematical models of CCN instruments

To evaluate the performance of the different CCN instruments, flow, heat, and mass transfer have been numerically modeled within each instrument to determine the temperature, water vapor, and supersaturation distributions as a function of position and, for unsteady instrument operation, time. Particle activation and growth are simultaneously simulated by tracking individual particles as they flow through the instrument. The equations used to describe aerosol particle growth are first given in the next section, followed by the general form of the gas-phase equations used for all the instruments. Finally, the appropriate boundary conditions and instrument-specific relations for each instrument are given.

9.4.1 Aerosol growth

The rate of change of droplet size for each of the particles is calculated from the diffusional growth equation [143]:

$$D_p \frac{dD_p}{dt} = \frac{S_v - S_v^{eq}}{\frac{\rho_w RT}{4p^* D_v' M_w} + \frac{\Delta H_{vap} \rho_w}{4k_a' T}\left(\frac{\Delta H_{vap} M_w}{TR} - 1\right)} \tag{9.1}$$

where D_p is the particle diameter, p^* is the saturation vapor pressure at the local temperature T, $S_v = p_v/p^* - 1$ is the local supersaturation, S_v^{eq} is the equilibrium supersaturation of the droplet, ρ_w is the water density, ΔH_{vap} is the enthalpy of vaporization of water, M_w is the molar mass of water and R is the universal gas constant. D_v' is the diffusivity of water vapor in air modified for noncontinuum effects [47],

$$D_v' = \frac{D_v}{1 + \frac{2D_v}{a_c D_p}\sqrt{\frac{2\pi M_w}{RT}}}$$

where D_v is the diffusivity of water vapor in air, a_c is the condensation coefficient, k_a' is the thermal conductivity of air modified for noncontinuum effects,

$$k_a' = \frac{k_a}{1 + \frac{2k_a}{a_T D_p \rho c_p}\sqrt{\frac{2\pi M_a}{RT}}}$$

where M_a is the mean molar mass of air, k_a is the thermal conductivity of air, ρ is the air density, c_p is the heat capacity of air, and a_T is the thermal accommodation coefficient. The equilibrium supersaturation of the droplet, S_v^{eq} is given by the Köhler equation,

$$S_v^{eq} = \exp\left(\frac{4M_w\sigma_w}{RT\rho_w D_p} - \frac{6n_s M_w}{\pi\rho_w\left(D_p^3 - d_p^3\right)}\right) - 1$$

where σ_w is water surface tension, n_s is the number of moles of solute per particle and d_p is the dry diameter of the particle.

9.4.2 Gas-phase equations

Differential momentum, energy and mass conservation balances are written for the gas phase, assuming a two-dimensional Cartesian, or axisymmetric, coordinate system. This results in a system of differential equations, each of which is of the general form,

$$\frac{\partial}{\partial t}\left(x_2^a \rho\phi\right) + \frac{\partial}{\partial x_1}\left(x_2^a \rho u\phi\right) + \frac{\partial}{\partial x_2}\left(x_2^a \rho v\phi\right) - \frac{\partial}{\partial x_1}\left(x_2^a \Gamma_\phi \frac{\partial\phi}{\partial x_1}\right) - \frac{\partial}{\partial x_2}\left(x_2^a \Gamma_\phi \frac{\partial\phi}{\partial x_2}\right) = S_\phi \quad (9.2)$$

where x_1, x_2 are the spatial coordinates, ϕ is the dependent variable (e.g., T). S_ϕ is a source term, and Γ_ϕ is a transport coefficient, both of which depend on the form of ϕ. Table 9.1 lists the expressions of S_ϕ, Γ_ϕ for each type of ϕ. For Cartesian geometry, the exponent $a = 0$ and the coordinates x_1, x_2 can be replaced with the more conventional x, y. For axisymmetric geometry, $a = 1$ and the coordinates x_1, x_2 can be replaced with the more conventional z, r.

The rate of condensation of liquid water (in moles per volume of air per second) on the aerosol particles, J_{cond}, is needed in the water vapor and energy conservation equations. This quantity is given by

$$J_{cond} = \frac{1}{M_w}\frac{dw_L}{dt}$$

Table 9.1: Transfer coefficients and source terms for the gas-phase equations.

Conservation Law	ϕ	Γ_ϕ	S_ϕ
Continuity	1	0	0
x_1- momentum	u	μ	$-x_2^a \frac{\partial P}{\partial x_1} + x_2^a \frac{\partial}{\partial x_1}\left(\mu \frac{\partial u}{\partial x_1}\right) + \frac{\partial}{\partial x_2}\left(x_2^a \mu \frac{\partial v}{\partial x_1}\right) + J_{buoy}$
x_2- momentum	v	μ	$-x_2^a \frac{\partial P}{\partial x_2} + x_2^a \frac{\partial}{\partial x_1}\left(\mu \frac{\partial u}{\partial x_2}\right) + \frac{\partial}{\partial x_2}\left(x_2^a \mu \frac{\partial v}{\partial x_2}\right) - \frac{a\mu v}{x_2}$
Heat	T	$\frac{k_a}{c_p}$	$\frac{\Delta H_{vap}}{c_p} J_{cond}$
Water vapor	C	ρD_v	$-\rho J_{cond}$

where w_L is the local liquid water content (kg m^{-3} air). For a population of water droplets consisting of N_i droplets of diameter D_{pi} per volume of air, $w_L \approx \rho_w \frac{\pi}{6} \sum_{i=1}^{n} N_i D_{pi}^3$, where n is the number of droplet sizes found in the distribution, and ρ_w is the density of water. Based on this definition of w_L, the rate of change of liquid water content of the particles is

$$\frac{dw_L}{dt} = \frac{d}{dt}\left\{\rho_w \frac{\pi}{6} \sum_{i=1}^{n} N_i D_{pi}^3\right\} = \rho_w \frac{\pi}{2} \sum_{i=1}^{n} N_i D_{pi}^2 \frac{dD_{pi}}{dt} \tag{9.3}$$

where dD_{pi}/dt is calculated from the aerosol growth equations. By substituting equation (9.3) into the definition for J_{cond} gives

$$J_{cond} = \frac{\pi}{2} \frac{\rho_w}{M_w} \sum_{i=1}^{n} N_i D_{pi}^2 \frac{dD_{pi}}{dt} \tag{9.4}$$

Furthermore, a source term in the momentum equations, J_{buoy}, represents the momentum generated from thermal buoyancy effects. For ideal gases it is given by

$$J_{buoy} = -\rho g_{x_2} \left(\frac{T - T_{bulk}(x_2)}{T_{bulk}(x_2)}\right) \tag{9.5}$$

where T is the temperature and g_{x_2} is the component of gravity in the x_2-direction. $T_{bulk}(x_2)$ is the x_1-average temperature at position x_2, and is computed differently for each instrument. Finally, ρ is gas phase density, calculated at $T_{bulk}(x_2)$.

9.4.3 Static diffusion cloud chamber (SDCC)

The geometry and characteristic parameters of the SDCC are shown in Figure 9.1. The following assumptions are made to simulate the instrument: a) a two-dimensional axisymmetric chamber geometry, b) the air is quiescent, c) particles fall by gravitational sedimentation and attain terminal velocity instantaneously as they grow, d) coagulation and

Brownian diffusion of particles are neglected, and e) wet walls act as a perfect sink/source of water vapor, i.e., the air is saturated with water vapor at the walls.

At the top and bottom walls, a constant temperature boundary condition is imposed, while at the symmetry axis, $\frac{\partial T}{\partial r} = 0$. At the side wall, a composite heat conduction-natural convection heat flux boundary condition is used,

$$\dot{q} = U\left(T_{amb} - T_f\right) \tag{9.6}$$

where $\dot{q}$ is the heat flux per unit area, T_{amb} is the ambient temperature outside of the cell, T_f is air temperature of the computational cell adjacent to the side wall, and U is the appropriate heat transfer coefficient between the outside ambient and chamber fluid,

$$\frac{1}{U} = \frac{C_p}{h} + \frac{C_p}{k_{wall}} \ln\left(1 + \frac{\Delta r}{R}\right) \tag{9.7}$$

where C_p is the wall heat capacity, k_{wall} is the side wall thermal conductivity, and h is the natural convection heat transfer coefficient, which is calculated by the following correlation [75]:

$$\frac{hL}{k_a} = Nu_L = 0.68 + \frac{0.670 Ra_L^{1/4}}{\left[1 + (0.492/\mathrm{Pr})^{9/16}\right]^{4/9}} \tag{9.8}$$

where $Ra = \frac{c_p \rho^2 g L^3}{\mu k_a} \frac{\left(\bar{T}_w - T_{amb}\right)}{T_{amb}}$ is the Rayleigh number for an ideal gas, $\mathrm{Pr} = \frac{\mu}{\rho k_a}$ is the Prandl number, $\bar{T}_w$ is the average temperature of the SDCC plexiglass wall and T_{amb} is the ambient temperature. The first term on the right-hand side of equation (9.7) is the heat conduction resistance between the outer side wall and the environment, and the second term is the resistance within the side wall. At the side wall and the symmetry axis, $\frac{\partial C}{\partial r} = 0$. Particles are assumed initially to occupy the entire chamber, with a uniform concentration and size distribution throughout.

The droplet sedimentation velocity is given by the Stokes equation [143],

$$u_t = \frac{1}{18} \frac{D_p^2 \rho_p g C_c}{\mu} \tag{9.9}$$

where $C_c = 1 + \frac{2\lambda}{D_p}\left[1.257 + 0.4 \exp\left(-\frac{1.1 D_p}{\lambda}\right)\right]$ is the slip correction factor, ρ_p is the particle density, μ is the air viscosity, g is the gravity constant, and λ is the mean free path of air.

9.4.4 Fukuta continuous flow spectrometer (FCNS)

Using scaling arguments, it can be shown that side wall effects in the velocity field become significant when the distance from the side walls is of order H. The FCNS geometry examined has an aspect ratio of $W/H = 20$, so more than 90% of the total width of the instrument remains unaffected by the presence of walls. Thus, the FCNS (Fig. 9.3) can be reasonably simulated by solving a series of two-dimensional problems, each of which is for a fixed value of the z-coordinate. A vertical flow configuration is assumed. In addition, the following assumptions are made: a) steady state conditions, b) aerosol particles follow the air flow streamlines, at the same velocity as the surrounding air, c) sedimentation, coagulation and Brownian diffusion of particles are neglected, d) walls act as a perfect sink/source of water vapor, and e) the temperature profile along the wall (in the z-direction) is linear.

Two types of inlet velocity conditions are considered, fully developed (i.e., parabolic) or plug flow. The other variables (T, C) are assumed to have a uniform profile at the inlet. At the walls, a no-slip boundary condition is assumed, $u = v = 0$, and for the outlet, $\frac{\partial u}{\partial x} = 0$; $v = 0$. At the outlet, $\frac{\partial T}{\partial x} = 0$. A constant temperature condition is used for the walls; this is a function of the z-position of the section examined, and is computed using assumption (e). Given that the temperatures at the two tips T_h (for any x, $y = H$ and $z = W$), and T_c (for any x, $y = 0$ and $z = W$) are known, the temperatures at the top wall T_t and the bottom wall T_b at a given coordinate z are

$$T_t(z) = T_h - \left(\frac{dT}{ds}\right)(W - z) \quad ; \quad T_b(z) = T_c + \left(\frac{dT}{ds}\right)(W - z)$$

where s is a coordinate that runs along the heated wall, with its origin located at the hot tip (Fig. 9.3) and ends at the cold tip. $\left(\frac{dT}{ds}\right) = \frac{T_h - T_c}{2W + H}$ is the temperature gradient along the s-coordinate. At the walls, the air is assumed to be saturated with water vapor at the local temperature. At the outlet, $\frac{\partial C}{\partial x} = 0$. Based on the sheath/aerosol flow ratio, the section of the flow field occupied by the aerosol is calculated from a mass balance. Finally, the mean temperature $T_{bulk}(y) = \frac{\int_0^H T(x,y)dx}{\int_0^H dx}$ is used in calculating the buoyancy term in the $u-$momentum equation.

9.4.5 Hudson continuous flow spectrometer (HCNS)

In simulating the HCNS (Fig. 9.5), the following assumptions are invoked: a) steady state conditions, b) two-dimensional Cartesian geometry, c) aerosol particles follow the air flow streamlines with the same velocity as the surrounding air, d) sedimentation, coagulation, and Brownian diffusion of particles are neglected, e) walls act as a perfect sink/source of water vapor, i.e., the air is saturated with water vapor right adjacent to the walls, and f) buoyancy is neglected. The two-dimensional assumption neglects top and bottom wall effects. This can be shown through scaling arguments to be a good approximation when the aspect ratio H/W is large and breaks down only when the distance from the side walls is of order W. In addition to the constant temperature condition posed at the controlled temperature sections, a zero-heat flux condition is assumed at the insulated areas.

9.4.6 Caltech continuous flow spectrometer (CCNS)

In formulating the conservation equations for the CCNS, the same assumptions as for the HCNS are made, except that an axisymmetric coordinate system is used. Although buoyancy is not expected to be significant, it is included in the model for completeness. $T_{bulk}(z)$ in this case is the radial-average temperature at axial position z: $T_{bulk}(z) = \frac{\int_0^R 2\pi r T(r,z) dr}{\int_0^R 2\pi r dr}$. Boundary inlet conditions used are similar to those of Section 9.7.4. In addition to those, $\frac{\partial u}{\partial r} = \frac{\partial v}{\partial r} = \frac{\partial C}{\partial r} = \frac{\partial T}{\partial r} = 0$ at the symmetry axis.

9.5 Numerical solution of conservation equations

The conservation equations for the four devices cannot be solved analytically, so a numerical solution is obtained by the finite volume method [124]. A hybrid upwind-central differencing scheme is used for calculating the convective-diffusive fluxes over the finite control volumes. The scheme used employs a staggered grid, in which each velocity grid node lies between two scalar volumes, ensuring that the numerical solution is consistent with respect to pressure. The Semi-Implicit Method for Pressure-Linked Equations (SIMPLE) iterative solution method [124] is used to solve the hydrodynamic cycle of the finite volume equations, while the particle growth equations are solved numerically using the LSODE

solver of [66]. The computer code used for the numerical simulations was based on a modified version of the TEACH-2E code [59] coupled together with an aerosol growth code. The computational grid and time step used ensure that the numerical solution is within a few percent of the asymptotic (with respect to grid density) limit. The numerical solution was obtained using 100 cells for each spatial coordinate. For the unsteady state simulations of the SDCC, a time step of 0.025s is taken for the gas phase equations, for a total integration time of 30s. The aerosol growth equations use a variable time step, which is scaled depending on the instrument simulated. For the SDCC simulations, it is scaled on the gas-phase integration step, while the others use the transit time through a computational cell.

9.6 Uncertainty analysis for wall temperature of CCN instruments

Before proceeding with the numerical simulation of the instruments, it is instructive to perform an analysis of the uncertainty in one of the most critical parameters of CCN instruments, namely the temperature boundary condition for the instrument wall. When operating the instruments, one controls the temperature of the metal supporting wall (or plates), whereas the boundary condition that actually governs the performance of the instrument is the temperature of the inner face of the water film on the wall. Differences between these two temperatures would bias the predictions since the supersaturation is a strong function of temperature difference. One could include heat transfer through the walls and film in the simulations, but the analysis of constant wall temperature is adequate for the purpose of estimating the relative magnitude of the uncertainty arising from a temperature difference. Furthermore, such an analysis is useful in that it is independent of any specific geometry or configuration.

When estimating the wall temperature uncertainty, one must consider all the factors that contribute to the temperature drop between the controlled temperature side and the water film. Apart from the metal walls and the water film, there is also a material that helps keep the walls wet. The material conventionally used for the SDCC, FCNS, and CCNS is filter paper, while the HCNS uses a steel matrix. The material will be shown to have a larger impact on the wall temperature uncertainty in the continuous flow instruments than on the SDCC. The results for the SDCC may be considered intuitive, but the analysis is

included for completeness.

In order to assess the effect of wall temperature uncertainty, simple heat transfer models will be constructed for all of the instruments. In these models, the inner water film temperature, T_f, is estimated from the heat flux through the walls. The temperature difference between T_f and the controlled wall temperature, T_w, is then computed and expressed as a fraction of the "nominal" difference, $T_h - T_c$, for various values of water film thickness, filter paper thickness, and flow rates. Realistic values for both paper and water film thickness is 10^{-3}m; the wall is assumed to be of order 10^{-2}m.

9.6.1 SDCC uncertainty analysis

With respect to wall heat transfer in the SDCC, the following can be assumed: a) steady state conditions, and b) one-dimensional conductive heat transfer (stagnant flow field) along the axial direction of the instrument (see Fig. 9.9a). With these assumptions, the heat flux between points 1 and 2, Q_{12}, is equal to the heat flux between the top and bottom wall, Q_{tb}. Expressing these fluxes as a function of the temperature differences, $T_h - T_c$ and $T_1 - T_2$, we have $Q_{12} = Q_{tb}$, which leads to

$$U_{1,2}\,(T_1 - T_2) = U_{t,b}\,(T_h - T_c) \tag{9.10}$$

where $U_{1,2}$, and $U_{t,b}$are the total heat transfer coefficients between points 1,2 and t,b, respectively. These heat transfer coefficients can be evaluated by the resistance method [75] to lead to

$$\frac{1}{U_{1,2}} = \frac{L - (l_1 + l_2) - (\delta_1 + \delta_2)}{k_a} \tag{9.11}$$

$$\frac{1}{U_{t,b}} = \frac{(w_1 + w_2)}{k_{st.steel}} + \frac{L - (l_1 + l_2) - (\delta_1 + \delta_2)}{k_a} + R_{s1} + R_{s2} \tag{9.12}$$

where $k_{st.steel} = 15$, $k_{water} = 0.58$ and $k_{paper} = 0.1$ are the thermal conductivities (in W m^{-1} K^{-1}) of stainless steel, water, and filter paper, respectively. Also, w_i, l_i, δ_i are the thickness of the wall, filter paper and water film, respectively (i=1 corresponds to the hot plate, while i=2 refers to the cold plate). In equation (9.12), the resistances of the wall, soaked filter paper and air are assumed to be in series. The resistance of the soaked filter

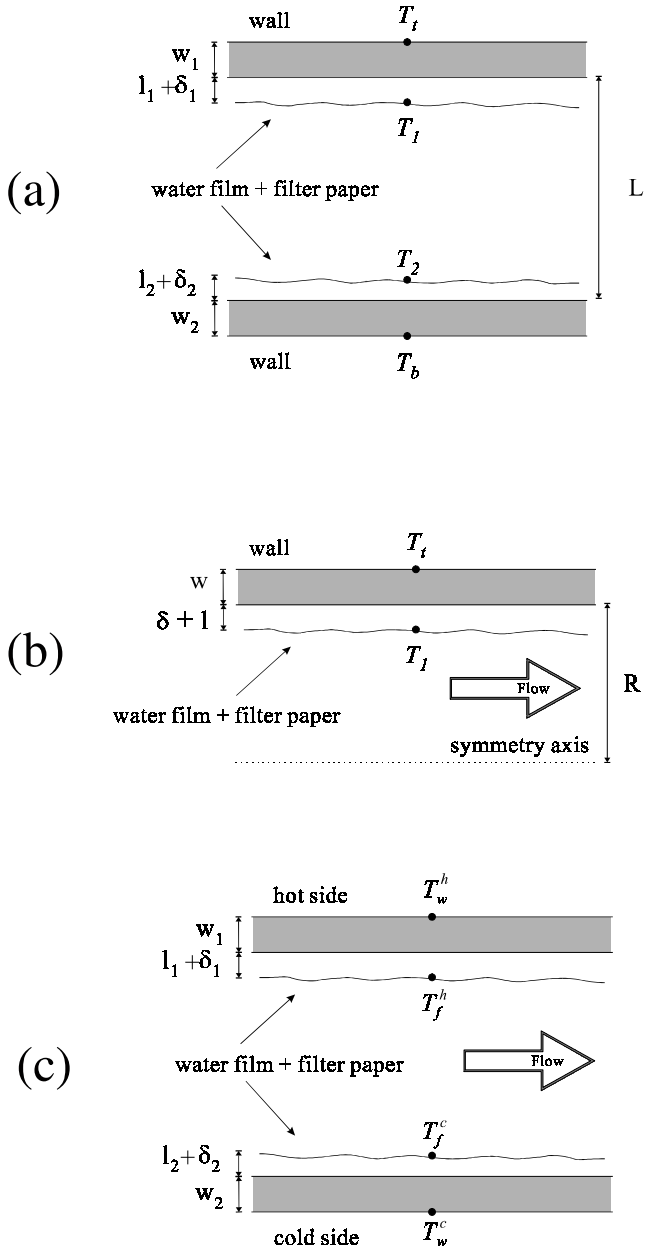

Figure 9.9: The geometries used in the simple models developed for determining the uncertainty in the temperature boundary conditions for a) the SDCC, b) the CCNS, and c) the HCNS.

paper, R_{si}, is

$$R_{si} = \frac{1}{\frac{k_{water}}{\min(\delta_i,l_i)} + \frac{k_{paper}}{\min(\delta_i,l_i)}} + \frac{\delta_i - \min(\delta_i,l_i)}{k_{water}} + \frac{l_i - \min(\delta_i,l_i)}{k_{paper}} \tag{9.13}$$

The first term in the above equation assumes that an equal segment of water and filter paper are combined in parallel (which corresponds to the well-soaked portion of the filter paper), and the remaining paper (or water) is connected in series. Allowing for the excess of filter paper and water considers situations where the filter paper is partially dry, or when too much water is provided on the filter paper. The sensitivity of the uncertainty to these conditions is an important operating parameter of these instruments.

Substituting equations (9.12), (9.13), and (9.11) into (9.10) and solving for $\frac{T_1-T_2}{T_h-T_c}$ yields

$$\frac{T_1 - T_2}{T_h - T_c} = \left(1 + \frac{(w_1 + w_2)\frac{k_a}{k_{st.steel}} + R_{s1}k_a + R_{s1}k_a}{L - (l_1 + l_2) - (\delta_1 + \delta_2)}\right)^{-1} \tag{9.14}$$

The uncertainty could therefore be defined as $\left(1 - \frac{T_1-T_2}{T_h-T_c}\right) \times 100\%$.

Using equation 9.12, we calculate that for cases where the water and paper thicknesses are equal, the ratio is at most 0.99. This means that the effective temperature difference is practically equal to the nominal. For example, for $T_h - T_c = 2$ K, then, depending on the thickness of the water film, $T_1 - T_2$ is about 1.99 K, thus the uncertainty being at most 0.01 K. This result is not surprising, since the gap between the plates is occupied mostly by air, which has low thermal conductivity compared to those of the other materials. The resistance therefore to heat conduction is mainly due to the air and is relatively insensitive to the presence of water and filter paper. In addition, variations in water film or changes in wall thickness do not have a large impact on the uncertainty. It can be concluded that once the steady-state temperature profile has been achieved, the temperature uncertainty in the instrument is negligible.

9.6.2 CCNS uncertainty analysis

In our presentation of the two spectrometers, usually the HCNS preceds the CCNS. For convenience, however, we shall begin now with the CCNS, for which we assume a) steady state conditions, b) one-dimensional conductive heat transfer along the radial direction and convective heat transfer along the axial direction of the instrument, c) on the entry

to each hot and cold segments, the temperature profile is uniform, and equal to the wall temperature of the previous section, d) the flow field is fully developed and laminar, and e) the latent heat flux from water condensation through the wall is small compared to the sensible heat transfer, which is reasonable for near-atmospheric pressures and small temperature differences. The appropriate geometry is defined in Figure 9.9b. With these assumptions, the problem reduces to a developing temperature profile in the entry region of a pipe, with a fully developed hydrodynamic flow field. The heat flux through the wall for the given segment therefore can be calculated by

$$\dot{q} = hA\Delta T \tag{9.15}$$

where A is the total surface exchange area, ΔT is the temperature change of the bulk fluid between entry and exit of the pipe segment, and h is the mean heat transfer coefficient, which is calculated by the following correlation [75]:

$$\frac{hD}{k} = Nu_D = 3.66 + \frac{0.0668Gz}{1 + 0.04Gz^{2/3}} \tag{9.16}$$

where $Gz = \mathrm{RePr}\frac{\mathrm{D}}{\mathrm{L}}$ is the Graetz number, $\mathrm{Re} = \frac{4\rho\dot{V}}{\pi D\mu}$ is the Reynolds number, $\mathrm{Pr} = \frac{\mu}{\rho k_a}$ is the Prandl number, L, D are the length and diameter of the segment, and $\dot{V}$ is the volumetric flow rate through the pipe. Using assumption (c), the bulk temperatures in and out of the section are equal to either T_h or T_c. The temperature difference ΔT then in (9.15) is approximated with $T_h - T_c$.

Furthermore, the heat flux can be expressed as a function of the inner film T_f and the outer wall temperature T_w as

$$\dot{q} = UA\left(T_w - T_f\right) \tag{9.17}$$

where U is the heat transfer coefficient through the combined metal wall, filter paper and water film, and is calculated as

$$\frac{1}{U} = \frac{w}{k_{st.steel}} + R_s \tag{9.18}$$

where as in equation (9.13), $R_s = \frac{1}{\frac{k_{water}}{\min(\delta,l)} + \frac{k_{paper}}{\min(\delta,l)}} + \frac{\delta - \min(\delta,l)}{k_{water}} + \frac{l - \min(\delta,l)}{k_{paper}}$.

Equating equations (9.15) and (9.17) and solving for $\frac{T_w - T_f}{T_h - T_c}$ yields

$$\frac{T_w - T_f}{T_h - T_c} = h\left(\frac{w}{k_{st.steel}} + R_s\right) \tag{9.19}$$

The uncertainty could therefore be defined as $\left(1 - \frac{T_w - T_f}{T_h - T_c}\right) \times 100\%$.

Equation (9.19) depends on the thickness of the materials and also on the Reynolds number. The validity of assumption (c) decreases as Re increases but can be used in our analysis since the instrument is operated usually at low Re, and provides an upper-limit estimate of the uncertainty. The appropriateness of assumption (c) can be assessed from the numerical solutions.

Figure 9.10 shows contours of $\frac{T_w - T_f}{T_h - T_c}$ as a function of water film and paper thickness. The wall thickness is assumed to be 1 cm, and the flow rate is equal to 10 l min^{-1}. As can be seen, the uncertainty is a somewhat strong function of filter paper thickness and has a weaker dependence on water film thickness. Everything else remaining constant, the minimum uncertainty is encountered when the water film and filter paper have the same thickness; under this condition the uncertainty ranges between 4 % and 6%. However, when the water thickness becomes smaller than of the filter paper (i.e., the paper partially dries) the magnitude of the uncertainty increases and can approach 10%, or higher. The reason for this behavior, which differs from the SDCC, lies in the fact that forced convection in the CCNS increases the heat transfer efficiency through the bulk of the fluid, so the resistances in the water film and filter paper have a larger effect on the temperature drop across the wall than in the SDCC. Furthermore, the temperature differences between segments needed to generate supersaturations along the centerline are increased, compared to the SDCC, so the absolute value of the uncertainty increases with it. For example, for $T_h - T_c = 10$ K, then, depending on the thickness of the water film, $T_w - T_f$ can range between 0.5 and 1 K.

Given that heat transfer efficiency increases with the flow rate, one would expect that $\frac{T_w - T_f}{T_h - T_c}$ depends on the flow rate. Indeed this is the case, assuming that wall and paper thickness do not change, a tenfold increase in flow rate adds an additional 10% to the uncertainty; this would translate to a $T_w - T_f$ as high as 2 K if $T_h - T_c = 10$ K. As stated before, assumption (c) is not as appropriate at high flow rates, so the uncertainty may not increase by as much as 10%, but still one would expect an appreciable change in film temperature.

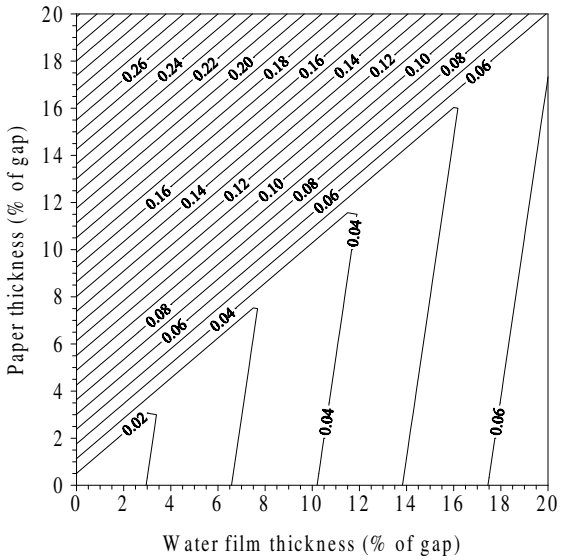

Figure 9.10: $\frac{T_w - T_f}{T_h - T_c}$ contours for the CCNS as a function of paper and water film thickness. The thickness of the metal wall is assumed to be 1 cm.

In any case, especially when condensational heat flux is considered (which further increases the temperature uncertainty), one would expect that the effective temperature in the instrument would be appreciably smaller than that posed on the walls. Therefore, any simulations or experimental calibrations should be adjusted for this difference.

9.6.3 HCNS, FCNS uncertainty analysis

Both the HCNS and FCNS employ laminar flow between parallel plates. The two systems differ in the choice of the porous wetted layer; the FCNS uses filter paper (as in the SDCC and CCNS) while the HCNS uses porous metal. The thermal conductivity of the latter material is much higher than that of the paper, leading to much smaller temperature differences between the measured and surface temperatures. A general model that accounts for the resistance in the porous material will enable evaluation of the uncertainties in both systems.

In the following analysis, we assume a) steady state conditions, b) one-dimensional conductive heat transfer perpendicular to the flow and convective heat transfer along the flow axis, c) the fluid reaches the developed linear temperature profile at the exit of each segment, d) the sectional-average temperature does not vary throughout the instrument

(which is true in the HCNS for a symmetrically cold-hot temperature profile), e) the flow field is fully developed and laminar, and f) the latent heat flux due to water condensation is small compared to the sensible heat transfer, which is reasonable for near-atmospheric pressures and small temperature differences. The geometry is defined in Figure 9.9 c. Resistance through the steel matrix of the HCNS is neglected. With these assumptions, the problem reduces to a developing temperature profile in the entry region of an enclosed plate geometry, with the hydrodynamic flow field fully developed. Assumption (d) ensures that the bulk enthalpy of the fluid does not change as it passes through the instrument; thus, any heat exchange between the plates is perpendicular to the flow. For a given segment, the heat flux through the hot wall, $\dot{q}^h$, can be expressed as a function of the inner film T_f^h and the outer wall temperature T_w^h as

$$\dot{q}^h = U^h A^h \left(T_w^h - T_f^h\right) \tag{9.20}$$

where U^h is the heat transfer coefficient through the combined metal wall, filter paper, and water film (Equation 9.18), and A^h is the exchange surface on the hot-wall side. A similar expression can be written for the cold-plate side:

$$\dot{q}^c = U^c A^c \left(T_w^c - T_f^c\right) \tag{9.21}$$

where T_f^c, T_w^c are the inner film and outer wall temperatures at the cold wall, respectively, and A^c is the exchange surface on the cold-wall side. Furthermore, because the system is in steady state, and the fluid does not experience any overall increase in enthalpy, $\dot{q}_h = \dot{q}_c$, so

$$U^h A^h \left(T_w^h - T_f^h\right) = U^c A^c \left(T_f^c - T_w^c\right) \tag{9.22}$$

Assuming that the surface areas and heat transfer coefficients are also equal, we get that

$$T_w^h - T_f^h = T_f^c - T_w^c \tag{9.23}$$

which means that the temperature drop across the film is the same magnitude for both cold and hot walls. After further manipulations of equation (9.23) we obtain

$$\frac{T_f^h - T_f^c}{T_w^h - T_w^c} = 1 - 2\left(\frac{T_f^c - T_w^c}{T_w^h - T_w^c}\right) \tag{9.24}$$

The heat flux from the fluid to the cold film, $\dot{q}^c$, can also be expressed as

$$\dot{q}^c = hA^c\left(T_{bulk} - T_f^c\right) \tag{9.25}$$

where T_{bulk} is the bulk temperature of the fluid (which is the same along a segment), and h is the mean heat transfer coefficient. Since the system is in steady state, this heat flux is equal to the flux that passes through the cold wall (Equation 9.25). By equating the two fluxes, and solving for T_f^c, we obtain

$$T_f^c = \frac{hT_{bulk} + U^c T_w^c}{h + U^c} \tag{9.26}$$

By substituting equation (9.26) into equation (9.24), we finally get

$$\frac{T_f^h - T_f^c}{T_w^h - T_w^c} = 1 - 2\left(\frac{h}{h+U}\right)\left(\frac{T_{bulk} - T_w^c}{T_w^h - T_w^c}\right) \tag{9.27}$$

The uncertainty could therefore be defined as $\left(1 - \frac{T_f^h - T_f^c}{T_w^h - T_w^c}\right) \times 100\%$. The heat transfer coefficient h is calculated from equation (9.16), using the hydraulic diameter. To incorporate the non-circular section effects, the heat transfer coefficient calculated from (9.16) is then multiplied by a factor of two, which is the limiting factor for an aspect ratio approaching infinity [75]. This approximation is reasonable, given that the HCNS examined here has an aspect ratio $W/H = 20$.

Equation (9.27) depends on the thickness of the materials, and also on the Reynolds number. However, if T_{bulk} remains the same between segments, then the uncertainty remains the same throughout the instrument. Given that heat transfer efficiency increases with the flow rate, one would expect that $\frac{T_f^h - T_f^c}{T_w^h - T_w^c}$ depends on the flow rate. Indeed this is the case, as shown by Figure 9.11. The wall thickness is 1.0 cm, and the paper thickness in this plot is assumed to be zero (therefore this plot shows the uncertainty for the HCNS). As can be seen, for a film thickness that is 5% of the gap, a tenfold increase in the flow rate almost doubles the uncertainty, from 11 to 18% (or a ratio of 0.89 to 0.82). However, for film thicknesses around 1% of the gap (or around 1 mm in our case), the flow rate has little

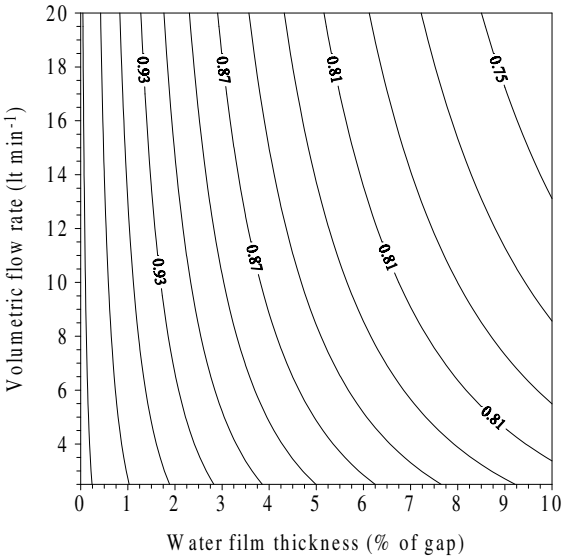

Figure 9.11: $\frac{T_f^h - T_f^c}{T_w^h - T_w^c}$ contours for the HCNS as a function of flow rate and water film thickness. The thickness of the metal wall is assumed to be 1 cm, and no filter paper is used.

effect on the uncertainty, and remains around 3-5% (or a ratio of 0.97 to 0.95). For example, for $T_w^h - T_w^c = 5$ K, depending on the thickness of the water film, $T_f^h - T_f^c$ can range between 4.85 and 4.75 K, or the uncertainty is at most 0.25 K. Thus, the temperature uncertainty is expected to have a minor effect on the instrument performance, and is neglected.

The presence of the filter paper in the FCNS is expected to increase the temperature uncertainty, relative to the HCNS. For a paper thickness of 1 mm, which is well wetted, and wall thickness of 1 cm, the uncertainty is around 5%. A tenfold increase in the flow rate almost doubles the uncertainty, from 5% to 9% (or 0.95 to 0.91 ratio). For example, for $T_w^h - T_w^c = 5$ K, depending on the thickness of the water film, $T_f^h - T_f^c$ can range between 4.75 and 4.55 K, or the uncertainty ranges between 0.25 and 0.45 K. Thus, although the uncertainty is increased with respect to the HCNS, it is still small enough to be neglected.

9.7 Operating conditions

After assessing the uncertainty in the wall temperature boundary condition for each device, the geometric dimensions, operating conditions, and aerosol used for simulating the performance of the instruments need to be specified. The dimensions and operating condi-

tions of each instrument, which are summarized in Tables 9.2 to 9.5, are those reported in the literature. The SDCC dimensions were taken from an existing instrument [Roberts, G., Internal communication, California Institute of Technology, 1999]. The FCNS, HCNS, and CCNS dimensions were based on those given in the literature [46, 74, 71, 24]. The dimensions used for the HCNS simulations [Hudson, J. G., Personal communication, 2000] are different from that those reported by [71] and reflect changes in the instrument that improve its resolution. Flow rates and wall temperatures are allowed to vary, but again reflect reported operating conditions.

To determine the behavior of the instrument, we simulate the response of each instrument as a function of initial particle diameter; the inlet aerosol in all the simulations presented is assumed to be monodisperse and composed of ammonium sulfate. The number concentration in each instrument is assumed to be low, in order to minimize their effect on the supersaturation and temperature fields from the depletion of gas-phase water vapor. This is particularly important for the SDCC, since biases in the supersaturation and temperature fields from the presence of the aerosol complicates growth history.

Table 9.2: Operating conditions and parameters for the SDCC [Roberts, G., Internal communication, California Institute of Technology, 1999]

Parameter	Value/Range
Distance between plates (m)	1×10^{-2}
Radius of plates (m)	0.1
Thickness of view volume (m)	1×10^{-3}
Radius of view volume (m)	1×10^{-3}
Initial pressure (Pa)	1.013×10^{5}
Initial relative humidity	100%
Bottom plate temperature (constant, K)	290
Top plate temperature (variable, K)	292 to 297
Side wall thickness (m)	2×10^{-3}
Thermal conductivity of side wall (W m^{-2} K^{-1})	1.4 (plexiglass)
Ambient temperature (K)	290

Table 9.3: Operating conditions and parameters for the FCNS [46].

Parameter	Value/Range
Length, width, height (m)	0.838, 0.191, 0.018
Orientation	Vertical
Distance from entrance where wall becomes wet on top and bottom plates (m)	0.168, 0.168
Inlet pressure (Pa)	1.013×10^{5}
Inlet relative humidity	100%
Volumetric flow rate (m^3 s^{-1})	1.6667×10^{-4}
Inlet temperature (constant, K)	283
Cold tip temperature (constant, K)	283
Hot tip temperature (variable, K)	284 to 293
Ambient temperature (K)	290

Table 9.4: Operating conditions and parameters for the HCNS [*Hudson et al.*, 1981; *Hudson*, 1989; Hudson, J. G., Personal communication, 2000].

Parameter	Value/Range
Length, width, height (m)	0.38, 0.3, 0.015
Height of aerosol injector	0.0015
Length of wetted wall on hot and cold side (m)	0.28, 0.38
Total number of heated segments	9
Insulator length (m)	0.001
Orientation	Vertical
Sheath/Aerosol volumetric flow ratio	10 to 20
Total volumetric flow rate (m^3 s^{-1})	3.3×10^{-4} to 5.0×10^{-5}
Inlet pressure (Pa)	3.09×10^{4}
Aerosol, sheath flow inlet temperature (constant, K)	295, 295
Aerosol, sheath flow inlet relative humidity	100%, 90%
Minimum cold side temperature (K)	295-289
Maximum hot side temperature (K)	295-301

Table 9.5: Operating conditions and parameters for the CCNS [24].

Parameter	Value/Range
Length, radius of tube (m)	0.7, 9.27×10^{-3}
Radius of aerosol injector	2.29×10^{-3}
Total number of hot-cold pairs	7
Insulator length (m)	0.01
Orientation of instrument	Vertical
Sheath/Aerosol volumetric flow ratio	0.7 to 20.0
Total volumetric flow rate (m^3 s^{-1})	1.166×10^{-5}
Inlet pressure (Pa)	1.013×10^{5}
Inlet relative humidity	100%
Aerosol, sheath flow inlet temperature (constant, K)	295, 295
Aerosol, sheath flow inlet relative humidity	100%, 90%
a_T, a_C	1.0, 1.0 (case 1)
	0.98, 0.041 (cases 2-4)
Wall segment temperature profiles (K)	295,290,295,290,295,290,295, 285,295,285,295,283,295,283 (case 1)
	295,290,295,290,295,290,295, 285,295,285,295,283,295,283 (case 2)
	294,291,294,291,294,291,294, 287,294,287,294,285,297,285 (case 3)
	294,292,294,292,294,292,294, 289,294,289,294,287,297,287 (case 4)

9.8 Simulation of instrument performance

9.8.1 SDCC

First, it is useful to determine the extent of wall effects, the time needed to attain the steady-state profiles, and the concentration below which depletion effects (in the water vapor and temperature fields) are negligible. Simulations reveal that wall effects extend inward on the order of the gap between the plates, which covers roughly one-seventh of the total radius. Thus, wall effects are not expected to influence measurements made near the center of the instrument. The maximum concentration of the aerosol within the instrument, before depletion effects are seen, depends on both S_c and S_{max} ; simulations indicate that concentrations below 1000 cm^{-3} inside the SDCC ensure that the supersaturation field is uninfluenced by the aerosol. When depletion effects are not important, the time needed to achieve steady-state ranges between 3 s (for 7 K difference) to 5 s (for 2 K difference). An interesting feature is that the supersaturation profiles approach the steady state in an non-symmetric fashion, from the bottom plate to the top. Although the direction (from bottom to top or vice versa) could change (depending on the initial conditions in the instrument), the asymmetric approach to a steady-state profile would tend to bias the particles on one side of the view volume towards larger sizes. The strength of this bias depends on the duration of the transients relative to the total growth time.

Figure 9.12a presents the simulated effective radius (defined as the third moment over the second moment of the droplet size distribution) within the view volume as a function of time for different dry aerosol sizes. Figure 9.13a represents the normalized aerosol concentration in the view volume as a function of time. In both plots, the initial aerosol concentration is uniform, and the temperature difference between the plates is kept at 2 K. This temperature difference generates a maximum supersaturation of about 0.15%. Under these conditions, particles with dry diameter larger than 0.1 μm should activate. Indeed, this is what is seen. Simulations for 0.05 and 0.09 μm particles yield constant effective radius and concentration, meaning that the particles grow to their equilibrium size, which is not large enough to experience significant sedimentation on the timescale of the simulations. Larger particles do show variability, and those are the ones that activate. The behavior of particles with a dry diameter 0.50 μm differs from those of the other sizes examined, because sedimentation velocity of such particles is appreciable even for subsaturated conditions. As a result, the

concentration in the view volume increases because aerosol from above falls through it more rapidly than the aerosol within the view volume falls out. Therefore, the effective radius increases faster than for initially smaller aerosol, because both the aerosol size and concentration in the view volume increase during the measurement. The concentration of particles of smaller initial size stays relatively constant, as particles that fall out of the view volume are replaced by those from above. This behavior lasts roughly around 7 s, during which the slope of the effective radius curve is approximately the same for all particle sizes. After most of the aerosol above the view volume has passed through, the aerosol concentration starts dropping.

The behavior of the SDCC depends on the supersaturation profile, which can be characterized by the maximum supersaturation, $S_{\max}$, and the critical supersaturation of the observed particles. Particles with $S_c \approx S_{\max}$ activate only midway between the plates and are observed as they grow and sediment out of that small region. Their growth rate is initially slow, so concentration peaks late. On the other hand, particles with $S_c << S_{\max}$ grow throughout much of the volume of the SDCC and relatively rapidly. Particles that activate well above the view volume grow and reach larger sizes as they sediment toward that level. The peak for 0.05 μm particles occurs as much as 5 s later than that for 0.5 μm particles. This large variation may account for the multiple peaks in scattered light intensity profiles seen when polydisperse aerosols are sampled.

Increasing the temperature difference between the plates increases $S_{\max}$. A larger range of particle sizes satisfies the condition $S_c << S_{\max}$, and the particle size dependence of the effective radius decreases as illustrated in Figures 9.12b and 9.13b, which are the same as Figures 9.12a and 9.13a, but for $\Delta T = 7$ K ($S_{\max} = 1.81\%$). All of the particle sizes considered activate throughout half of the SDCC volume. Both the effective radius and droplet concentration in the view volume display similar time dependence over the 0.05 to 0.5 μm size range.

In determining the precision of the droplet diameter attained in the view volume, we define the *droplet diameter resolution*, $R_{D_p} = \frac{D_p}{\Delta D_p}$, as the ratio of the mean diameter over its variation. A value of $R_{D_p} = 10$ means that the droplet diameter ranges around 10% of its mean value. A high value of this resolution throughout the duration of the measurement ensures that particles with the same critical supersaturation produce droplets that are close to being monodisperse within the view volume. Figure 9.14 displays R_{D_p} as a function

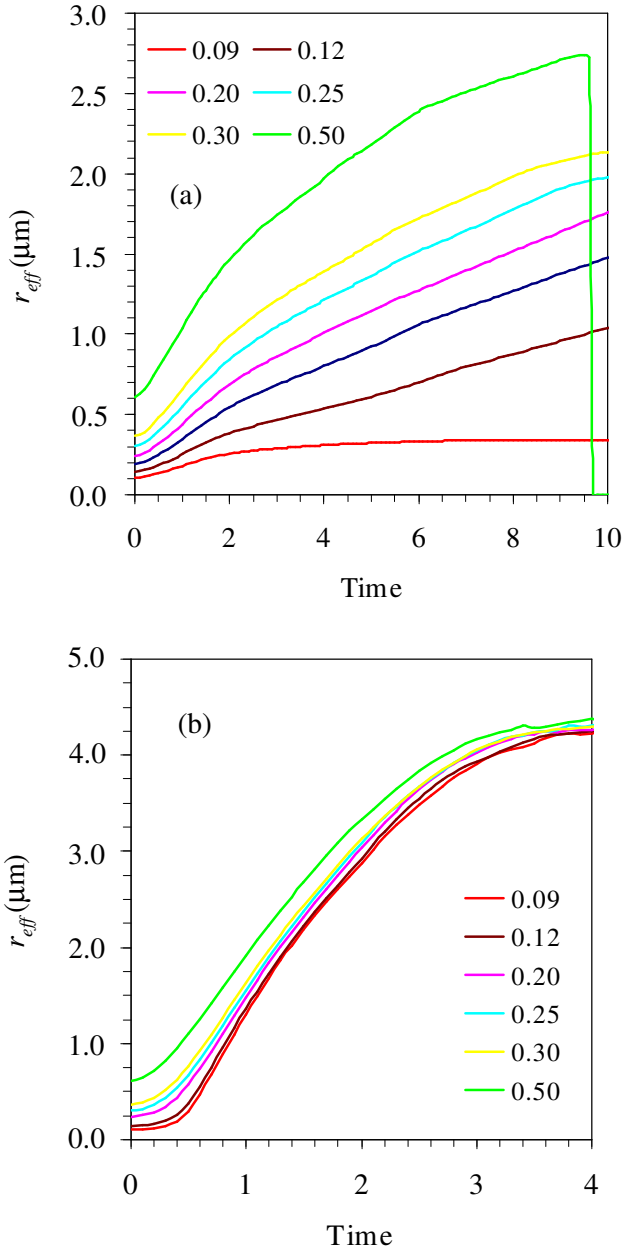

Figure 9.12: Simulated effective radius in the SDCC view window as a function of time for various initial particles sizes (dry diameter, μm). The temperature difference between the two plates is assumed to be (a) 2 K ($S_{\max} = 0.15\%$) and (b)7 K ($S_{\max} = 1.81\%$).

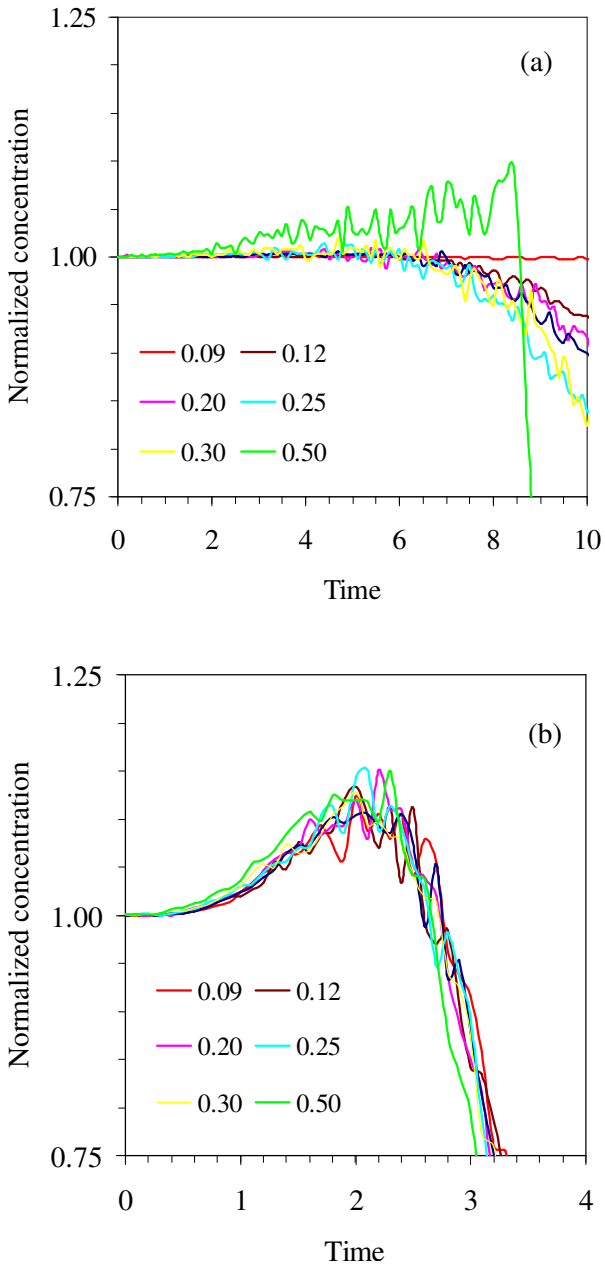

Figure 9.13: Simulated particle concentration in the SDCC view window as a function of time for various initial particles sizes (dry diameter, μm). The temperature difference between the two plates is assumed to be (a) 2 K ($S_{\max} = 0.15\%$) and (b) 7 K ($S_{\max} = 1.81\%$).

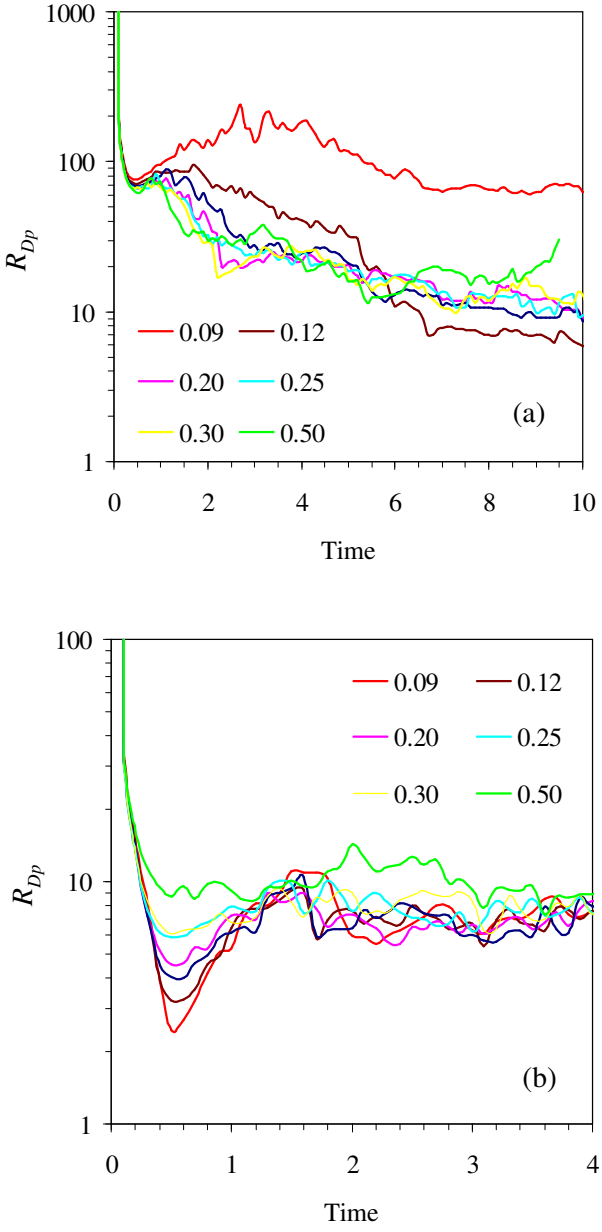

Figure 9.14: Simulated particle size resolution in the SDCC view window as a function of time for various initial particles sizes (dry diameter, μm). The temperature difference between the two plates is assumed to be (a) 2 K ($S_{\max} = 0.15\%$) and (b) 7 K ($S_{\max} = 1.81\%$).

of time, for various particle sizes. Subplot (a) assumes a temperature difference between plates of 2 K, while subplot (b) is for a difference of 7 K. Because initially the aerosol in the SDCC is perfectly monodisperse, the resolution in both plots starts off from infinity. As the supersaturation profiles develop and the particles grow, R_{D_p} drops and fluctuates around the value of 10. So the droplet sizes range within 10% of their mean diameter, regardless of temperature difference or initial particle size.

9.8.2 FCNS

The continuous flow in the FCNS eliminates some of the limitations that arise from the transient nature of SDCC measurements. However, buoyancy forces develop that limit the maximum temperature difference that can be imposed at a given flow rate. Simulations indicate that the maximum temperature difference that can be imposed for the reported flow rate is about 6 K, a value that agrees with the experimentally reported difference [*Fukuta and Saxena*, 1979]. Larger temperature differences lead to flow reversal. The simulations are relatively insensitive to the specific type of inlet velocity profile, so the results presented apply to both inlet velocity types.

The supersaturation fields that develop within the instrument control the growth of aerosol particles. Although the maximum value of the supersaturation can be estimated from the local temperature difference between the hot and cold walls and Figure 9.2, the supersaturation profile has to develop first before this maximum value is attained. Figure 9.15 shows supersaturation profiles for different streamlines along the centerline of the FCNS. As can be seen, half (or more) of the flow path is subsaturated, exposing particles to the maximum supersaturation for only a fraction of their residence time in the instrument. Moreover, the time in the supersaturated region decreases with decreasing $S_{\max}$. Therefore, particles with low S_c may not have sufficient time to activate by the time they reach the outlet. This difficulty is compounded by slow growth once activated at low $S_{\max}$.

Buoyancy effects on the velocity field tend to distort the supersaturation profiles from being symmetric around the centerline; this deviation becomes stronger as the temperature difference between the plates increases. The position of the maximum supersaturation is also shifted slightly. With increasing distance from the tip, the temperature gradient between the walls decreases, buoyancy effects become less important, and symmetric supersaturation (and temperature) profiles are attained. The centerline region however, particularly for the

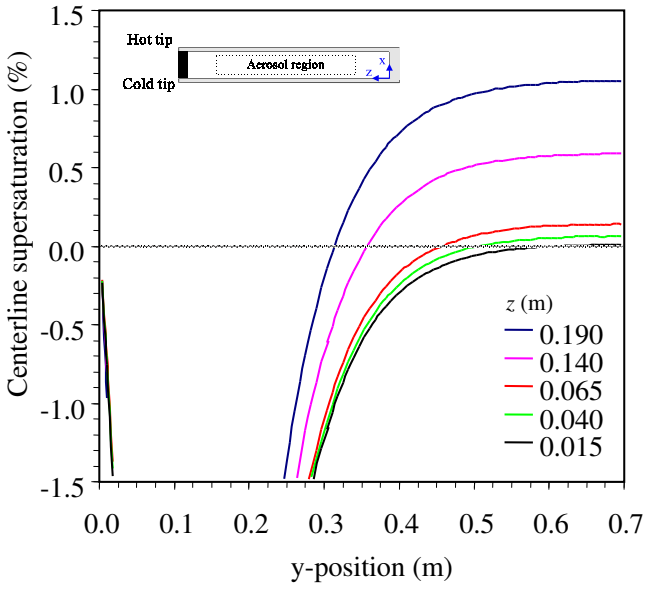

Figure 9.15: Supersaturation (%) profiles for different streamlines along the centerline of the FCNS.

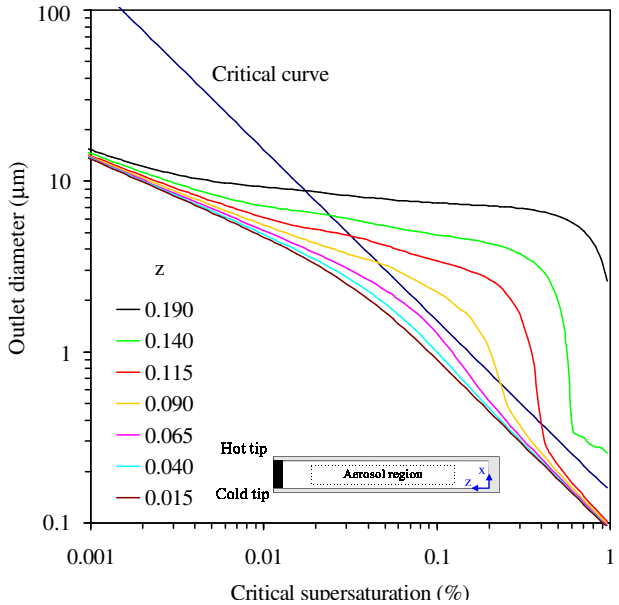

Figure 9.16: Simulated growth curves for various centerline streamlines of the FCNS. The temperature difference between the tips is 5 K, and the volumetric flow rate is 20 l min^{-1}.

low S_c streamlines, is relatively unaffected by buoyancy, for the reasons explained above.

Figure 9.16 shows the simulated response curves for the FCNS. The horizontal axis represents the critical supersaturation of the inlet aerosol, and the vertical axis is the outlet wet diameter of the aerosol. Each curve represents the mean outlet droplet diameter as a function of their critical supersaturation. Also shown is the Köhler theory critical diameter of particles as a function of their critical supersaturation. The particle outlet diameter is relatively insensitive to the inlet aerosol size, for particles for which $S_c < S_{\max}$. Particles of $S_c > S_{\max}$ do not activate, so there is a dramatic decrease in outlet size. The resulting "elbow" in the curve enables detection of particles with $S_c < S_{\max}$ of the specific streamline since there is a clear distinction between particles that activate, and those that do not. The sharper this "elbow" is, the better resolved the CCN concentration is at the given supersaturation. Farther away from the heated tips, the maximum supersaturation decreases, and the position of the "elbow" shifts towards lower critical supersaturations. However, because growth at lower supersaturations is slower, and because the particle exposure to the maximum supersaturation is briefer, droplets do not grow as much (compared to larger supersaturation streamlines). As a consequence, the elbow becomes less pronounced, eventually vanishing completely. The elbow more or less disappears at $S_c = 0.1\%$, in agreement with the value reported by [46]. In its current configuration, the FCNS can probe CCN with S_c between 0.1 and 1.0%.

9.8.3 CCNS

At first glance, this instrument seems to avoid many of the problems encountered in the FCNS. Buoyancy effects are not significant, and most of the instrument is utilized for exposing the particles to supersaturations (Fig. 9.8). The supersaturation profile is, however, considerably more complex, making it more difficult to assess instrument behavior based on the temperature and supersaturation profiles alone. It is, therefore, important to evaluate the sensitivity of the predicted outlet droplet distribution to the parameters that affect particle growth. Two very important parameters affecting the simulations are the film temperature at the wall (which determines the supersaturation), and the mass accommodation coefficient (which affects the particle growth).

Figure 9.22 shows predicted and measured calibration curves for the CCNS. Details about the experimental data can be found in [24]. Curves corresponding to Cases 1 to

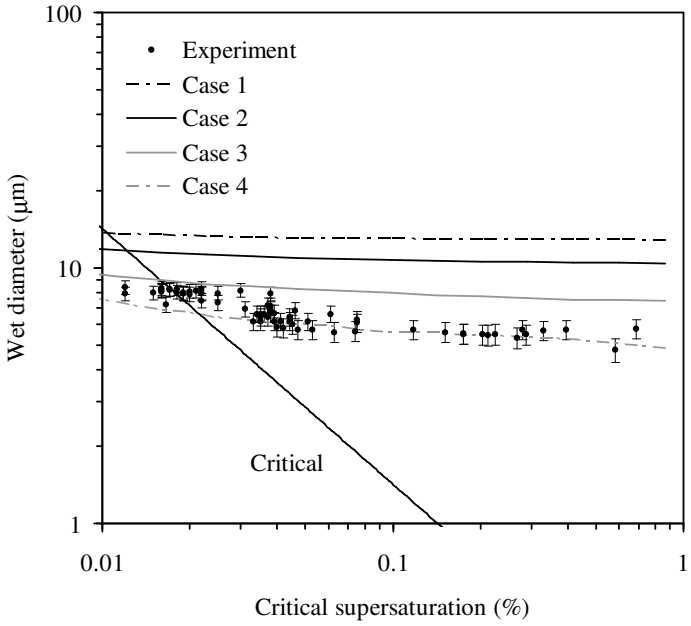

Figure 9.17: Experimental and simulated calibration curves for the CCNS. The different simulation cases correspond to different values of effective wall temperature and accommodation coefficients, the values of which are given in Table 9.5.

4 in Figure 9.17 represent the temperature boundary conditions and accommodation coefficients specified in Table 9.5. Case 1 represents an accommodation coefficient of unity and the nominal wall temperatures as the wall boundary conditions. The predicted size is larger (by about a factor of two) than the measured data. When lowering the temperature boundary condition by around 2-3 K (which according to Section 9.6.2, is a reasonable drop, especially since latent heat flux through the film can further increase the uncertainty), the predicted curves (Case 3, Case 4) lie close to the experimental data. Changing the accommodation coefficient from 1.0 to 0.041 further improves the predictions. In all cases though, the qualitative behavior of the curve does not change: the outlet diameter of droplets is relatively insensitive to critical supersaturation (particularly when the droplets are activated). Thus, the model captures the essential features of the instrument despite the complex growth behavior imposed by the supersaturation profile that develops in the instrument. For subsequent simulations, Case 3 conditions are used.

From both simulations and experimental data, it is clear that the droplet size at the outlet of the CCNS is relatively insensitive to the initial particle size. For a range of critical

supersaturation spanning two orders of magnitude, the outlet diameter changes at most by a factor of two. This low sensitivity arises from the particle growth kinetics. At the late stages of growth, when the particle is in the continuum size region, and solute and surface tension effects are minor, Equation (9.1) can be integrated to yield

$$D_p^2 = D_{po}^2 + \frac{\int_{t_{act}}^{t} S_v dt}{\frac{\rho_w RT}{4p^* D_v M_w} + \frac{\Delta H_{vap}\rho_w}{4k_a T}\left(\frac{\Delta H_{vap} M_w}{TR} - 1\right)} \tag{9.28}$$

The particle size at activation, D_{po}, is relatively small, so at sufficiently long growth time,

$$D_p^2 \approx \frac{\int_{t_{act}}^{t} S_v dt}{\frac{\rho_w RT}{4p^* D_v M_w} + \frac{\Delta H_{vap}\rho_w}{4k_a T}\left(\frac{\Delta H_{vap} M_w}{TR} - 1\right)} \tag{9.29}$$

i.e., all particles approach the same size, regardless of initial size (or S_c). This asymptotic approach of all particles to the same size also explains the uniform response of the SDCC for $S_c << S_{\max}$, and the consistent final particle size of the FCNS over a wide range of supersaturations.

Despite the weak dependence of outlet diameter on particle critical supersaturation, the simulations can be used to compute the resolution in measured droplet diameter necessary for resolving the CCN spectrum. Since the aerosol occupies a finite region of the flow field, not all particles are exposed to the same supersaturation, or have the same residence time. As a consequence, a monodisperse inlet aerosol will produce a droplet distribution with finite spread; this effect may interfere with the ability to resolve a CCN spectrum, since droplets of a given size at the outlet are not unambiguously related to critical supersaturation. This spread at the outlet is a function of the sheath to aerosol flow rate ratio (because that determines the uniformity of the supersaturation field and residence time to which the particles are exposed) and will decrease with increasing ratio.

In determining the precision of the droplet diameter measurement needed, we use the droplet diameter resolution, R_{D_p}, and the critical supersaturation resolution, $R_{S_c} = \frac{S_c}{\Delta S_c}$. Dividing these two quantities, we get the *resolution ratio*, $\frac{R_{S_c}}{R_{D_p}}$, which can then be related to the instrument response:

$$\frac{R_{S_c}}{R_{D_p}} = \frac{S_c}{D_p}\frac{\Delta D_p}{\Delta S_c} \approx \frac{S_c}{D_p}\left[\frac{dD_p}{dS_c}\right]_{cc} \tag{9.30}$$

where $\left[\frac{dD_p}{dS_c}\right]_{cc}$ is the slope of the calibration curve at the given S_c. Figure 9.18 displays the resolution ratio computed for the CCNS for different sheath to aerosol flow rate ratios. Figure 9.18 illustrates that the resolution in critical supersaturation is between 10 and 100 times smaller than the droplet diameter resolution for the volumetric flow rate ratio used in the calibration experiment. This means that if the diameter measurement has an uncertainty of 1% (or, $R_{D_p} = 100$), the uncertainty in critical supersaturation will range between 10% and 100%. Increasing the flow rate ratio increases the resolution notably, but only up to a certain extent; the difference in resolution between ratios of 10 and 20 is quite minimal. This is understandable because the aerosol at such a high flow rate ratio occupies a volume very close to the centerline, so the particles are exposed essentially to a uniform supersaturation profile. The resolution ratio is also a strong function of S_c: it varies almost by a factor of 10 for S_c ranging between 0.01% and 1%. This is a result of the change in the calibration curve slope, which approaches zero as S_c increases; this means that for particles of high S_c, droplet size is more or less insensitive to S_c, or that the asymptotic limit of equation (9.29) has practically been reached. This is not true for activated particles with low S_c; the D_{po} term in equation (9.28) is still not negligible, so particle size still varies with S_c.

To estimate the uncertainty in critical supersaturation from the spread induced by the instrument, we use Equation 9.30, and obtain that

$$\frac{\Delta S_c}{S_c} = \frac{1}{R_{S_c}} \approx \frac{|\Delta D_p|_{inst}}{S_c}\left[\frac{dD_p}{dS_c}\right]^{-1}_{cc} \tag{9.31}$$

where $\frac{\Delta S_c}{S_c}$ is the supersaturation uncertainty and $|\Delta D_p|_{inst}$ is the variation in droplet diameter, calculated from the instrument model. Figure 9.19 displays $\frac{\Delta S_c}{S_c}$ as a function of supersaturation, for the CCNS. The uncertainty was predicted using the curves of Figure 9.18 and the variability of the calculated outlet droplet diameter. As can be seen, the resulting uncertainty is large, ranging from 100 to over 1000 %. This is expected, since the relative variation in droplet diameter at the CCNS outlet is, on average, between 15 and 20% (Table 9.7). Therefore, the aerosol/sheath flow rate ratio used for the operation of this instrument is very influential for obtaining a CCN spectrum. While increasing this ratio to

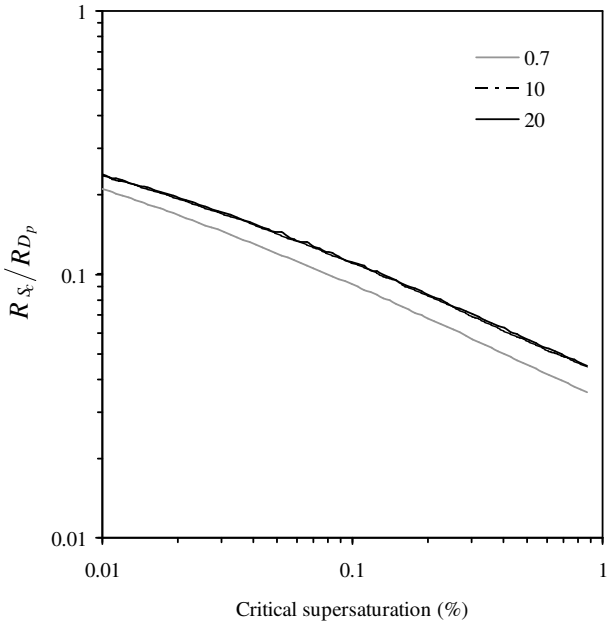

Figure 9.18: Predicted resolution ratio $\frac{R_{S_c}}{R_{D_p}}$ for the CCNS, for different values of $\frac{\dot{V}_{sheath}}{\dot{V}_{aerosol}}$. The Case 3 (Table 9.5) values of effective wall temperature and accommodation coefficients are used.

10 or 20 considerably reduces the uncertainty, the uncertainty still exceeds 50% for $S_c >$ 0.04%. Further increasing the flow ratio might decrease the uncertainty, but obtaining good droplet counting statistics then becomes a problem.

Table 9.6: Summary of SDCC simulations.

ΔT(K)	$S_{\max}$(%)	Dry diameter of smallest $(NH_4)_2SO_4$ particle activated (μm)	$\frac{D_p}{\Delta D_p}$		
			mean	min	max
2	0.15	0.101	14.8	12.6	21.0
3	0.34	0.059	10.0	8.3	13.7
4	0.60	0.040	10.2	5.0	12.7
5	0.93	0.030	8.9	4.0	11.4
6	1.34	0.024	9.3	0.2	13.4
7	1.81	0.019	10.5	8.7	13.0

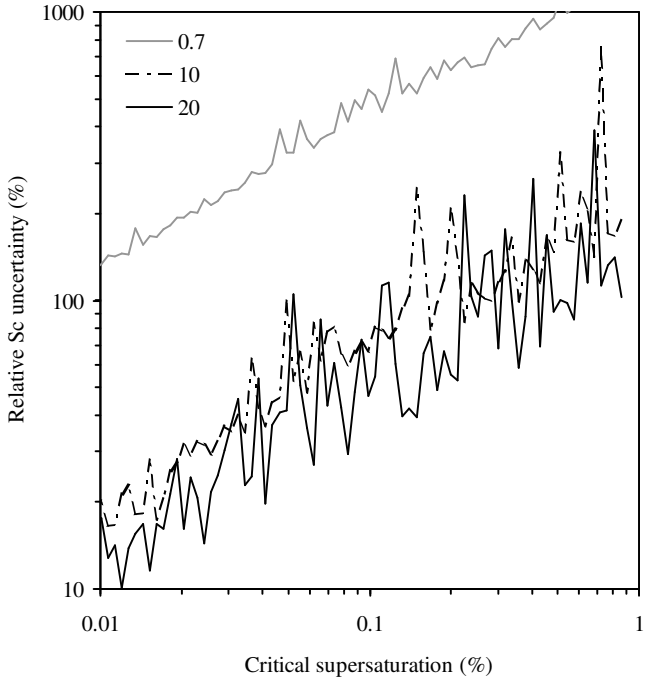

Figure 9.19: Relative critical supersaturation uncertainty as a function of critical supersaturation, for the CCNS. The uncertainty was predicted using the curves of Figure 9.18, and the variability of the outlet droplet diameter (calculated by the model results).

Table 9.7: Predicted outlet droplet diameter variability and resulting critical supersaturation uncertainty for the CCNS.

$\frac{\dot{V}_{sheath}}{\dot{V}_{aerosol}}$	$\frac{\Delta D_p}{D_p}$ (%)			$\frac{\Delta S_c}{S_c}$ (%)		
	mean	min	max	mean	min	max
0.7	28.9	9.7	57.4	303.0	25.1	1326.2
10.0	5.5	1.1	36.5	53.7	2.7	755.3
20.0	4.0	0.6	19.3	38.6	1.5	388.3

Table 9.8: Predicted outlet droplet diameter variability and resulting critical supersaturation uncertainty for the HCNS. $\frac{\dot{V}_{sheath}}{\dot{V}_{aerosol}}$=10.

Max ΔT(K)	$\dot{V}$(l min^{-1})	$\frac{\Delta D_p}{D_p}$(%)			$\frac{\Delta S_c}{S_c}$(%)		
		mean	min	max	mean	min	max
4	6	2.6	0.5	9.0	14.1	1.2	30.9
6	6	2.7	0.6	8.6	35.5	7.5	67.2
8	6	3.2	0.5	9.2	102.5	15.8	393.2
10	6	3.6	0.6	12.8	163.2	16.0	670.2
12	6	3.0	0.4	10.1	203.8	20.2	723.8
4	20	2.4	0.6	10.0	11.4	0.9	26.3
6	20	2.8	0.4	8.8	22.4	7.3	47.9
8	20	3.1	0.4	7.4	31.5	5.6	61.6
10	20	2.6	0.5	7.2	76.7	14.2	259.6
12	20	3.2	0.3	11.6	108.3	7.8	423.4

9.8.4 HCNS

The HCNS exposes particles to supersaturation profiles that vary smoothly and monotonically in the streamwise direction. Simulations were performed for several different temperature profiles at low (6 l min^{-1}) and high (20 l min^{-1}) total volumetric flow rates, Figures 9.20a and 9.20b, respectively. The sheath to aerosol flow ratio was assumed to be 10. These simulations reveal that the droplet growth kinetics, like for the CCNS, lead to a restricted range of final droplet size for particles with a wide range of critical supersaturations. For example, when the maximum plate temperature is set to more than 6 K, the outlet droplet diameter changes by a factor of two for critical supersaturations that span two orders of magnitude (between 0.01% and 1%). This variation does not seem to be strongly influenced by the volumetric flow rate (although the outlet droplet diameter is) but depends strongly on the temperature profile in the instrument. Improvement is seen only when the maximum temperature difference drops to 4 K; in this case, the variation in droplet diameter increases considerably, but has the drawback that particles with $S_c > 0.4\%$ do not activate. As can be seen, the resolution of the instrument increases as the outlet droplet size gets closer to the critical curve; the drawback to this is that the S_c range for which particles are activated becomes more restricted.

Calibration data available in the literature [Hudson, J. G., Personal communication, 2000] do not precisely specify the maximum temperature difference (or the total volumetric

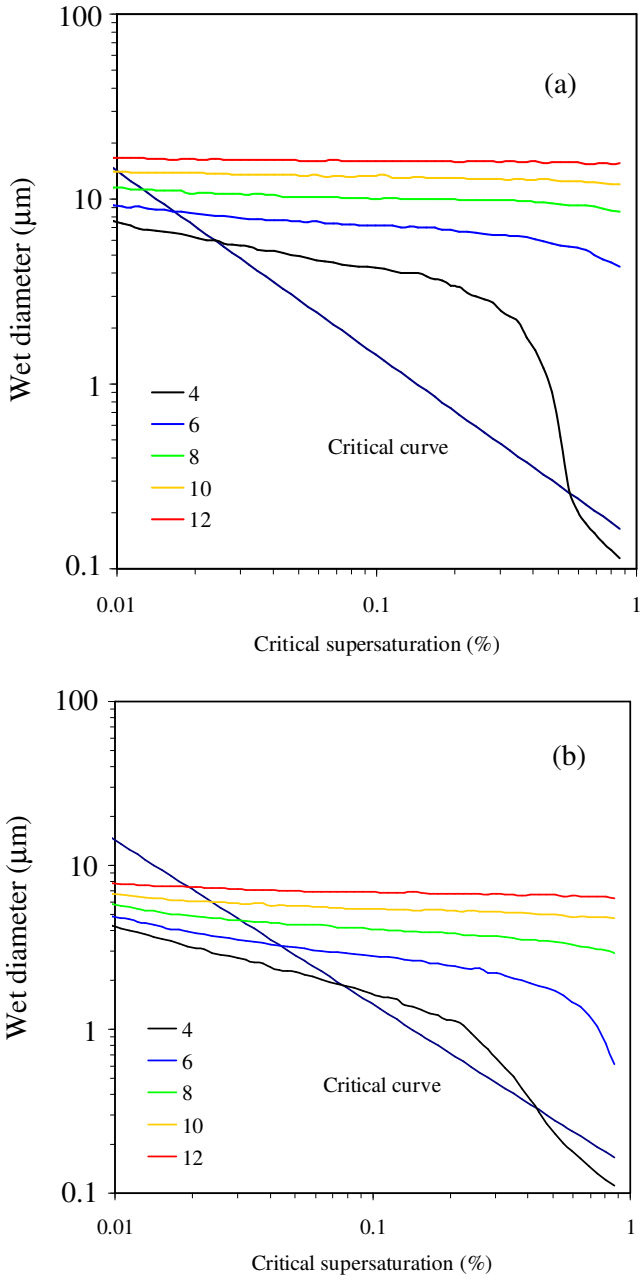

Figure 9.20: Simulated calibration curves for the HCNS, for different temperature profiles, and a volumetric flow rate of (a) 6 l min^{-1}, and (b) 20 l min^{-1}.

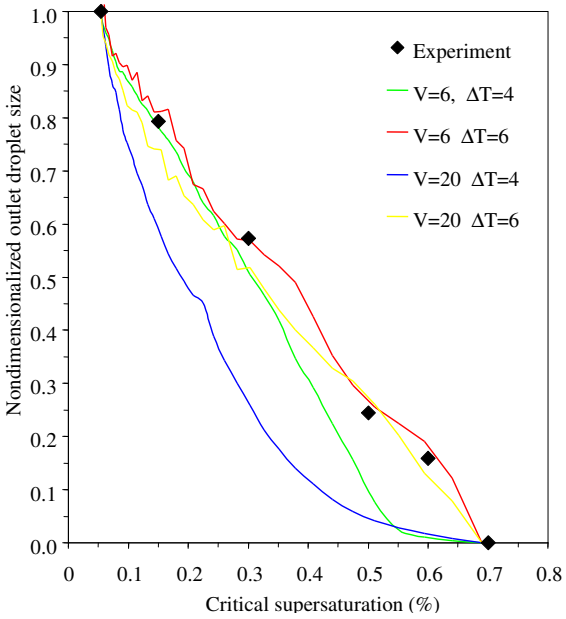

Figure 9.21: Experimental and simulated calibration curves for the HCNS. Non-dimensionalized droplet diameter is plotted as a function of critical supersaturation. V is the total volumetric flow rate, and DT is the maximum temperature difference between the plates. $\frac{\dot{V}_{sheath}}{\dot{V}_{aerosol}} = 10$ in the simulations.

flow rate) used in the HCNS, making it difficult to precisely assess the performance of the HCNS model. In addition, the data provide the mean channel number (as opposed to particle diameter) as a function of critical supersaturation. However, since mean channel number scales linearly with particle size, the non-dimensionalized mean channel number and mean particle diameter are equivalent quantities:

$$\frac{F\left(S_c\right) - F\left(S_{c,high}\right)}{F\left(S_{c,low}\right) - F\left(S_{c,high}\right)} = \frac{D_p\left(S_c\right) - D_p\left(S_{c,high}\right)}{D_p\left(S_{c,low}\right) - D_p\left(S_{c,high}\right)}$$

where F is the mean channel corresponding to critical supersaturation S_c. Using these non-dimensionalized quantities, we compare measurements to the model predictions (Fig. 9.21). As can be seen, the measurements are very close to model predictions for a volumetric flow rate of 20 l min^{-1} and a maximum temperature difference of 6 K. Given that these values of flow rates and maximum temperature difference are within reported operating conditions, we can assume that the model captures the behavior of the HCNS.

Figure 9.22 displays the predicted resolution ratio, $\frac{R_{S_c}}{R_{D_p}}$, for the HCNS, for different temperature profiles, and total volumetric flow rates of (a) 6 l min^{-1}, and (b) 20 l min^{-1}. The sheath to aerosol flow ratio was assumed to be 10. Here the instrument sensitivity is increased relative to that of the CCNS, particularly for low temperature differences and critical supersaturations between 0.1 and 1%. For a maximum temperature difference of 4 K and 6 K, the resolution increases dramatically for $S_c > 0.1\%$. This happens because the supersaturation generated in these cases is not sufficient to activate particles with S_c close to 1%, so an "elbow" similar to those in Figure 9.16 develops. Consequentially, the calibration curve slope becomes much steeper around the region of this "elbow." Because of this effect, and because the sheath to aerosol flow rate ratio is much lower than that of the CCNS, it is expected that the uncertainty in the critical supersaturation is considerably lower than that for the CCNS. Indeed, this is the case, as shown by Figure 9.23. The uncertainty was computed using Equation 28 and the calculated variability of the outlet droplet diameter. Subplot (a) refers to a volumetric flow rate of 6 l min^{-1}, and (b) to 20 l min^{-1} (sheath to aerosol ratio is 10). For these conditions, the relative variation in droplet diameter at the HCNS outlet is on average only between 2 and 3% (Table 9.8). However, this is enough to generate substantial uncertainty in S_c. Minor fluctuations in this variability accounts for the large fluctuations seen in the computed uncertainty. For example, for a maximum temperature difference of 8 K (which is an operational value reported by [71], the S_c uncertainty ranges between 30 and 100%, and can reach as high as 390%. When the maximum temperature difference is around 4 K, the resolution improves by an order of magnitude and averages around 10%. The simulations indicate that a spectrum can be obtained for critical supersaturations between 0.08% and 0.4%. Particles outside of this range do not activate, either because the supersaturation is lower than the critical value, or simply because there are kinetic limitations that inhibit low supersaturation particles from activating.

Compared to the CCNS, the HCNS seems to exhibit less uncertainty; this is attributed to the smoother and monotonic supersaturation profiles generated in the HCNS. The oscillations in the supersaturation seen the for CCNS slow down (or even reverse) particle growth, so less of the instrument is utilized for particle growth. Because of this, particles of different critical supersaturations essentially grow to the same size by the time they reach the outlet of the instrument.

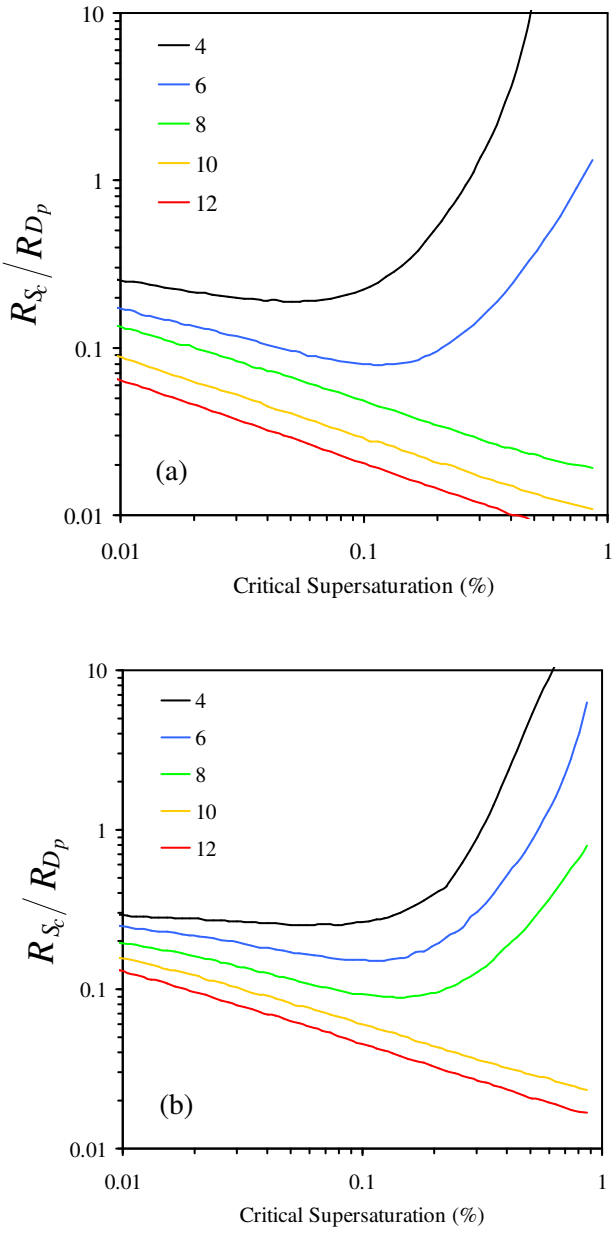

Figure 9.22: Predicted resolution ratio $\frac{R_{Sc}}{R_{Dp}}$ for the HCNS, for different temperature profiles, and a volumetric flow rate of (a) 6 l min^{-1}, and (b) 20 l min^{-1}. $\frac{\dot{V}_{sheath}}{\dot{V}_{aerosol}} = 10$ in these simulations.

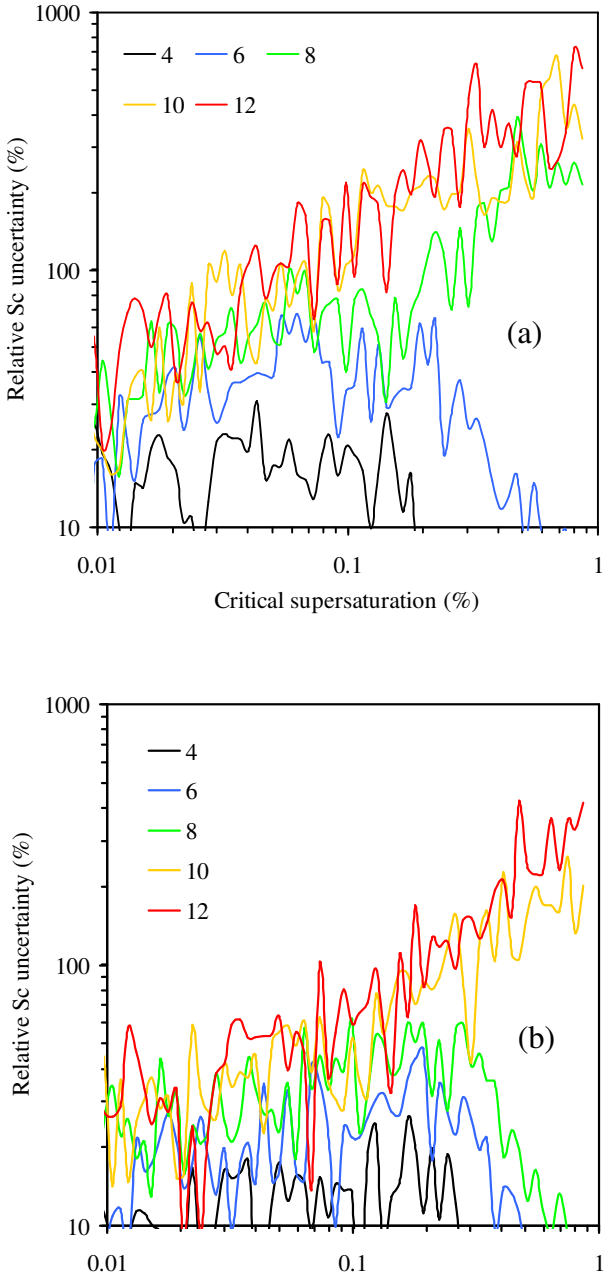

Figure 9.23: Relative critical supersaturation uncertainty as a function of critical supersaturation, for the HCNS. The uncertainty was predicted using the curves of Figure 9.22, and the variability of the outlet droplet diameter (calculated by the model results). Subplot (a) refers to a volumetric flow rate of 6 l min^{-1}, and (b) to 20 l min^{-1}. $\frac{\dot{V}_{sheath}}{\dot{V}_{aerosol}} = 10$ in these simulations.

9.9 Summary and conclusions

The behavior and performance of four cloud condensation nucleus (CCN) instruments are theoretically analyzed. These include the static diffusion cloud chamber (SDCC), the Fukuta continuous flow spectrometer (FCNS), the Hudson continuous flow spectrometer (HCNS), and the Caltech continuous flow spectrometer (CCNS). A numerical model of each instrument based on reported instrument dimensions and operating conditions is constructed based on a general fluid dynamics code coupled to a description of aerosol growth/activation microphysics. Instrument performance is explored by simulating instrument response to a monodisperse ammonium sulfate aerosol. The CCNS and HCNS models were compared to experimental measurements and found to be in good agreement. The FCNS model predictions agreed with instrument limitations reported in the literature.

Uncertainties in the wall temperature boundary condition vary with instrument construction, and arise mainly from the presence of filter paper (used for wetting instrument walls). Using a simple heat transfer model for each instrument, this uncertainty is found to be negligible for the SDCC (of order 0.01 K), and very small for the HCNS and FCNS (ranging between than 0.25 and 0.45 K). It can be appreciable for the CCNS (ranging between 0.5 to 2 K), so the wall boundary condition in the instrument simulations must be adjusted to account for this. The numerical model for the CCNS reproduces experimental measurements, when the wall temperature boundary conditions is adjusted by a factor slightly higher than predicted by this simple uncertainty analysis.

SDCC exhibits the least uncertainty in the wall temperature boundary conditions and produces droplets that are (for a given critical supersaturation) monodisperse to within 10% of the droplet diameter, throughout the duration of the measurement. The FCNS is an instrument that can be used as a CCN spectrometer since different streamlines attain different supersaturations, allowing particles to activate over a range of critical supersaturations. The range of critical supersaturations that can be measured is limited because (i) the temperature difference must be kept small enough to avoid buoyancy-induced flow reversal or secondary flows, and (ii) the instrument loses its sensitivity for particles of critical supersaturation lower than 0.1% because the particles do not have enough time for growth. The first issue is not a serious limitation since the supersaturation on the high temperature difference side is sufficiently high to include all the climatically important

aerosol. The second limitation, however, constrains the ability to probe the climatically critical low supersaturation CCN. Both HCNS and CCNS have inherent limitations in the ability to resolve the distribution of particles with respect to critical supersaturation. The most important parameters affecting the performance of dynamic spectrometers are the maximum temperature difference between the walls, the total volumetric flow rate, and the sheath to aerosol volumetric flow ratio. For the monodisperse ammonium sulfate aerosol considered here, conditions can be found for the HCNS for which an activation spectrum can be resolved for critical supersaturations between 0.08% and 0.4%. Simulations for the HCNS indicate that the calculated uncertainty in critical supersaturation exceeds 100% when the maximum temperature difference exceeds 6 K for 20 l min^{-1} total flow rate or 8 K for 6 l min^{-1} total flow. The same uncertainty can decrease to 10% (on average) when the temperature difference is reduced to 4 K. The uncertainty however, is not uniform and depends strongly on the initial size of the particle. The predicted uncertainty in the critical supersaturation for the CCNS is on average above 50%.

While different design parameters or operating conditions may lead to modest shifts in the performance from that predicted for any of the four instruments, the essential features described in this paper are inherent to their designs.

9.10 Acknowledgments

This work was supported by Office of Naval Research grant N00014-91-0119. We would also like to acknowledge Timothy VanReken for performing part of the CCNS calibration curve experiments.

9.11 Notation

A	heat exchange area
a_c	condensation coefficient
a_T	thermal accommodation coefficient
C	water vapor concentration (moles m^{-3})
C_p	specific heat of controlled-temperature wall.
c_p	specific heat of dry air at constant pressure.
C_c	slip correction factor
d_p	particle dry diameter
D_v	water vapor diffusivity in air
D'_v	water vapor diffusivity in air, corrected for noncontinuum effects
D_p	particle wet diameter
F	mean channel number in particle size measurement of HCNS
g	acceleration of gravity
h	heat transfer coefficient
H	instrument height
J_{cond}	rate of liquid water condensation on aerosol particles
k_a	thermal conductivity of air
k'_a	thermal conductivity of air, corrected for noncontinuum effects
k_{paper}	thermal conductivity of filter paper
$k_{st.steel}$	thermal conductivity of stainless steel
k_{wall}	thermal conductivity of wall
k_{wat}	thermal conductivity of liquid water
l	paper thickness
L	instrument length
M_a	molecular weight of dry air
M_w	molecular weight of water
n	number of size sections in aerosol distribution
n_s	number of moles of solute per particle
N	aerosol number concentration
P	air pressure

Pr	Prandl number
p_v	water vapor pressure
p_v^*	saturation vapor pressure of water
$\dot{q}$	heat flux
r	radial coordinate
R	universal gas constant
Ra	Rayleigh number
R_{Dp}	Droplet diameter resolution, $D_p/\Delta D_p$
Re	Reynolds number
R_{Sc}	Critical supersaturation resolution, $S_c/\Delta S_c$
R_s	Thermal resistance through the soaked filter paper
s	wall coordinate of FCNS instrument
S_c	critical supersaturation for activation, according to Köhler equilibrium theory
$S_{\max}$	maximum supersaturation
S_v	supersaturation
S_v^{eq}	supersaturation in equilibrium with particle size
t	time
$\bar{T}_w$	average temperature of SDCC wall
T	temperature
T_{bulk}	section average (bulk) temperature
$\dot{V}$	volumetric flow rate
u_t	terminal velocity
u	velocity component
U	heat transfer coefficient
v	velocity component
w	wall thickness
W	instrument width
w_L	liquid water content (kg liquid water per volume of air)
x_1, x_2	generalized spatial coordinates
x, y	Cartesian coordinates
z	axial coordinate

ΔH_{vap}	enthalpy of evaporation of water
δ	water film thickness
λ	mean free path of air
μ	air viscosity
ν	number of ions the solute dissociates into in solution
ρ	density of air
ρ_p	density of particle
ρ_w	density of water
σ_w	water surface tension

9.12 Subscripts-superscripts

amb	ambient
f	film
c	cold wall
h	hot wall
w	wall
t	top wall
b	bottom wall

Chapter 10

Summary and conclusions

The motivation of this thesis is to improve our understanding of the aerosol indirect effect. In Chapter 2, we study the dynamics of aerosol activation into cloud droplets, and assess under which conditions mass transfer limitations on the growth of cloud condensation nuclei (CCN) may have a significant impact on the number of droplets that can form in a cloud. The assumption that particles remain in equilibrium until activated may not always be appropriate for aerosol populations existing in the atmosphere. Three mechanisms are identified that lead to kinetic limitations, the effect of which on activated cloud droplet number and cloud albedo is assessed using a one-dimensional cloud parcel model with detailed microphysics for a variety of aerosol size distributions and updraft velocities. Overall, the effect of kinetic limitations on cloud albedo can be considered important when equilibrium activation theory consistently overpredicts droplet number by more than 10%. Kinetic limitations are thus not expected to be climatically significant on a global scale, but can regionally have a large impact on cloud albedo.

In Chapters 3 and 4, the relative importance of traditional Köhler theory extensions (for example, the effect of water soluble gases, substances of partial solubility and surfactants) is assessed with a cloud parcel model. We find that numerous conditions exist, for which chemical influences on cloud droplet activation are significant, to the point where they can even rival the Twomey effect. While it is currently impossible to calculate the global impact of these additional activation effects because of a lack of data on atmospheric composition, sensitivity calculations indicate that realistic conditions representing anthropogenically perturbed environments result in albedo changes that are climatically significant, adding still more uncertainty to the forcing by modification of clouds. More broadly, inclusion of these new factors erases a conceptual boundary between what we call “cloud” and “aerosol” or

"haze," and an "aerosol-cloud continuum" results in which subtle changes in thermodynamic state lead to substantial changes in cloud albedo.

Chapter 5 assesses the impact of biomass-burning aerosol on cloud properties in the Amazon Basin. Cloud condensation nuclei (CCN) measurements were performed at ground-based sites in the states of Amazonas and Rondônia, Brazil, during several field campaigns in 1998 and 1999 as part of the Large Scale Biosphere-Atmosphere Experiment in Amazonia (LBA). CCN concentrations measured during the wet season were low and resembled concentrations more typical of marine conditions than most continental sites. During the dry season, smoke aerosol from biomass burning dramatically increased CCN concentrations. The modification of cloud properties, such as cloud droplet effective radius and maximum supersaturation, is most sensitive at low CCN concentrations. Hence, we could expect larger inter-annual variation of cloud properties during the wet season that the dry season. Differences between CCN spectra from forested and deforested regions during the wet season are modest, and result in modifications of cloud properties that are small compared to those between wet and dry seasons. Our study suggests that the differences in surface albedo, rather than cloud albedo, between forested and deforested regions may dominate the impact of deforestation on the hydrological cycle and convective activity during the wet season. During the dry season, on the other hand, cloud droplet concentrations may increase by up to seven times which leads to a model-predicted decrease in cloud effective radius by a factor of two. Sensitivity tests show that complete characterization of the aerosol is necessary when kinetic growth limitations become important; under strong kinetic limitations, subtle differences in the chemical and physical make-up are shown to be particularly influential in the activation and growth behavior of the aerosol. Knowledge of the CCN spectrum alone is not sufficient to fully capture the climatic influence of biomass burning.

Chapters 6 and 7 study previously unidentified cloud microphysical effects of black carbon inclusions in cloud droplets. Black carbon (BC) aerosol absorbs sunlight that might have otherwise been reflected to space and changes the radiative heating of the atmosphere and underlying surface. These effects may alter the dynamical and hydrological processes governing cloud formation. A new, *microphysical*, effect of BC on climate is identified here, in which solar heating within BC-containing cloud condensation nuclei (CCN) slows or prevents the activation of these CCN into cloud drops. Solar-heated BC-containing droplets are elevated in temperature by fractions of a degree above the ambient, thus raising the

droplet vapor pressure, and inhibiting activation of the most absorptive CCN. As a result, three new mechanisms, that result from BC heating, can affect cloud droplet number and lifetime. Two of these mechanisms act to *increase* cloud droplet number or lifetime: *i*) the ability of BC to decrease the collection efficiency of giant CCN, and, *ii*) the delayed growth of low S_c CCN that allow higher S_c CCN to form droplets. These two mechanisms complement each other in terms of increasing cloud droplet number, since it is shown that the former is most efficient at strong updrafts, and the latter at low updraft velocities. A third mechanism identified, gas-phase heating (which is different from the "semi-direct effect"), in our simulations acts to decrease LWC, and thus albedo; however, the droplet number concentration does not change significantly due to dynamic readjustments in cloud supersaturation. The simulations indicate that the mixing state of BC with the CCN population can have an important influence on the effect of BC heating on the droplet population. Although additional work is necessary to fully assess the effects of BC heating on cloud microphysics and climate, these effects are more complex than currently thought.

Chapter 8 develops an aerosol activation parameterization, based on a generalized representation of aerosol size and composition within the framework of an ascending adiabatic parcel; this allows for parameterizing the activation of chemically complex aerosol with arbitrary size distribution and mixing state. The new parameterization introduces the concept of "population splitting," in which the CCN that form droplets are treated as two separate populations: those which have a size close to their critical diameter, and those that do not. Explicit consideration of kinetic limitations on droplet growth is introduced. Our treatment of the activation process unravels much of its complexity. As a result of this, a substantial number of conditions of droplet formation can be treated completely free of empirical information or correlations; there are, however, some conditions of droplet activation for which an empirically derived correlation is utilized. Predictions of the parameterization are compared against extensive cloud parcel model simulations, for a variety of aerosol activation conditions that cover a wide range of chemical variability and CCN concentrations. The parameterization tracks the parcel model simulations closely and robustly. The parameterization developed is intended to allow for a comprehensive assessment of the aerosol indirect effect in GCMs.

Chapter 9 theoretically analyzes the behavior and performance of four cloud condensation nucleus (CCN) instruments. These include the static diffusion cloud chamber (SDCC),

the Fukuta continuous flow spectrometer (FCNS), the Hudson continuous flow spectrometer (HCNS), and the Caltech continuous flow spectrometer (CCNS). A numerical model of each instrument is constructed based on a general fluid dynamics code coupled to an aerosol growth/activation model. Instrument performance is explored by simulating instrument response when sampling a monodisperse ammonium sulfate aerosol. The uncertainty in the wall temperature boundary condition is estimated for all the instruments, and is found to be appreciable only for the CCNS. The CCNS and HCNS models reasonably reproduced experimental data, while reported limits were also verified by the FCNS model. Regarding the performance of each instrument, simulations show that the SDCC produces droplets that are monodisperse to within 10% of the particle diameter (for particles of a constant critical supersaturation). The FCNS can potentially activate particles over a wide range of critical supersaturations, but the prevailing design exhibits low sensitivity to particles with critical supersaturations below 0.1% as a result of the short time available for droplet growth under low supersaturations. The resolution capability of both HCNS and CCNS with respect to critical supersaturation is shown to be particularly sensitive to operational parameters. This is a consequence of the strongly nonlinear nature of droplet growth; droplet size cannot always be used to distinguish particles with different critical supersaturation because of growing droplets trend toward monodispersity. Of the two instruments, the HCNS generally displays higher resolution capability. This is attributed to the smoother and monotonic supersaturation profiles established in the HCNS. While different design parameters or operating conditions may lead to modest shifts in the performance from that predicted here for any of the four instruments, the essential features described in this paper are inherent to their designs.

By assessing the sensitivity of aerosol droplet formation with respect to a wide variety of parameters, we have consistently seen that aerosol-cloud interactions can be very sensitive to changes in aerosol composition and gas phase composition, particularly in the presence of organic-containing CCN. Measurements of biomass burning aerosol in the Amazon basin support our theoretical studies; depending on the season, variations in aerosol chemical composition may or may not be an important factor that controls the CCN (and resulting droplet) concentrations. This large variability in sensitivity towards chemical composition motivated the development of a general and comprehensive aerosol activation parameterization which will be used within a comprehensive global model for assessing

the aerosol indirect effect. This work also has illustrated our incomplete understanding of the mechanisms of aerosol-cloud interactions. Insoluble aerosol, when it contains enough black carbon, can affect cloud properties in numerous and counterintuitive ways; although a warming mechanism, black carbon heating can actually increase cloud lifetime (and thus, lead to a climatic cooling effect) if it acts to decrease the size of large CCN. Finally, the analysis of current CCN instrumentation clearly illustrates the importance of understanding the strong points and limitations of each measurement methodology. The potential uncertainties of these challenging measurements, which are not necessarily revealed when done with laboratory-generated aerosol, can limit their usefulness, unless the instrument used is carefully characterized and understood. In conclusion, it is fair to state that in any aerosol-cloud-climate interaction study (regardless if it is theoretical or experimental), theory and observations need to be tightly integrated in order to improve our understanding of aerosol indirect forcing; the theoretical and modelling tools developed in this thesis can help achieve this.

Bibliography

[1] H. Abdul-Razzak and S. J. Ghan. A parameterization of aerosol activation 2. Multiple aerosol types. *J. Geophys. Res.*, 105(D5):6837–6844, 2000.

[2] H. Abdul-Razzak and S. J. Ghan. A parameterization of aerosol activation 3. Sectional representation. *J. Geophys. Res.*, 107, 2002.

[3] H. Abdul-Razzak, S. J. Ghan, and C. Rivera-Carpio. A parameterization of aerosol activation. part I: Single aerosol type. *J. Geophys. Res.*, 103:6123–6132, 1998.

[4] A. S. Ackerman, O. B. Toon, and P. V. Hobbs. Dissipation of marine stratiform clouds and collapse of the marine boundary-layer due to the depletion of cloud condensation nuclei by clouds. *Science*, 262:226–229, 1993.

[5] A. S. Ackerman, O. B. Toon, and P. V. Hobbs. A model for particle microphysics, turbulent mixing, and radiative transfer in the stratocumulus-topped marine boundary layer and comparisons with measurements. *J. Atmos. Sci.*, 52:1204–1236, 1995.

[6] A. S. Ackerman, O. B. Toon, D. E. Stevens, A. J. Heymsfield, V. Ramanathan, and E. J. Welton. Reduction of tropical cloudiness by soot. *Science*, 288:1042–1047, 2000.

[7] A. S. Ackerman and O. B. Toon. Unrealistic dessication of marine stratocumulus clouds by enhanced solar absorption. *Nature*, 380:512–515, 1996.

[8] P. J. Adams and J. H. Seinfeld. Predicting global aerosol size distributions in general circulation models. *J. Geophys. Res.*, in press, 2002.

[9] J. Aitken. In E. G. Knott, editor, *Collected Scientific Papers*. Cambridge University Press, Cambridge, 1923.

[10] B. A. Albrecht. Aerosols, cloud microphysics, and fractional cloudiness. *Science*, 245:1227–1230, 1989.

[11] D. J. Alofs. Performance of a dual-range cloud nucleus counter. *J. Appl. Meteorol.*, 17:1286–1297, 1978.

[12] M. Andreae. Biogeochemical cycling of carbon, water, energy, trace gases and aerosols in Amazonia: The LBA-EUSTACH experiments. *Geophys. Res. Lett.*, in press, 2002.

[13] R. Baidya and R. Avissar. Impact of land use/land cover change on regional hydrometeorology in the Amazon. *J. Geophys. Res.*, submitted, 2002.

[14] T. S. Bates, P. K. Quinn, D. J. Coffman, J. E. Johnson, T. L. Miller, D. S. Covert, A. Wiedensohler, S. Leinert, A. Nowak, and C. Neususs. Regional physical and chemical properties of the marine boundary layer aerosol across the atlantic during Aerosols99: An overview. *J. Geophys. Res.*, 106:20767–20782, 2001.

[15] O. Boucher and U. Lohmann. The sulfate-CCN-cloud albedo effect - A sensitivity study with 2 general-circulation models. *Tellus B*, 47(3):281–300, 1995.

[16] F. J. Brechtel and S. M. Kreidenweis. Predicting particle critical supersaturation from hygroscopic growth measurements in the humidified TDMA. Part I: Theory and sensitivity studies. *J. Aerosol Sci.*, 57:1854–1871, 2000.

[17] F. J. Brechtel and S. M. Kreidenweis. Predicting particle critical supersaturation from hygroscopic growth measurements in the humidified TDMA. Part II: Laboratory and ambient studies. *J. Aerosol Sci.*, 57:1872–1887, 2000.

[18] J. Brenguier, Y. Fouquart, and L. Schüller. Radiative properties of boundary layer clouds: Optical thickness and effective radius versus geometrical thickness and droplet concentration. *J. Aerosol Sci.*, 57:803–821, 2000.

[19] R. J. Charlson, J. H. Seinfeld, A. Nenes, M. Kulmala, A. Laaksonen, and M. C. Facchini. Atmospheric science - reshaping the theory of cloud formation. *Science*, 292(5524):2025–2026, 2001.

[20] Y. Chen and M. Schneitzer. *Soil Sci.*, 125:7, 1978.

[21] C. C. Chuang and J. E. Penner. Effects of anthropogenic sulfate on cloud drop nucleation and optical properties. *Tellus B*, 47:566–577, 1995.

[22] P. Y. Chuang, R. J. Charlson, and J. H. Seinfeld. Kinetic limitation on droplet formation in clouds. *Nature*, 390:594–5962, 1997.

[23] P. Y. Chuang, D. R. Collins, H. Pawlowska, J. R. Snider, H. H. Jonsson, J. L. Brenguier, R. C. Flagan, and J. H. Seinfeld. CCN measurements during ACE-2 and their relationship to cloud microphysical properties. *Tellus B*, 52:843–867, 2000.

[24] P. Y. Chuang, A. Nenes, J. N. Smith, R. C. Flagan, and J. H. Seinfeld. Design of a CCN instrument for airborne measurement. *J. Atmos. Ocean. Tech.*, 17(8):1005–1019, 2000.

[25] P. Chýlek, G. B. Lesins, G. Videen, J. G. D. Wong, R. G. Pinnick, D. Ngo, and J. D. Klett. Black carbon and absorption of solar radiation by clouds. *J. Geophys. Res.*, 101(D18):23365–23371, 1996.

[26] J. M. Cohard, J. P. Pinty, and C. Bedos. Extending Twomey's analytical estimate of nucleated cloud droplet concentrations from CCN spectra. *J. Atmos. Sci.*, 55(22):3348–3357, 1998.

[27] J. M. Cohard, J. P. Pinty, and K. Suhre. On the parameterization of activation spectra from cloud condensation nuclei microphysical properties. *J. Geophys. Res.*, 105:11753–11766, 2000.

[28] W. Conant, A. Nenes, and J. H. Seinfeld. Black carbon radiative effect on cloud microphysics and implications for the aerosol indirect effect: 1. Extended Köhler theory. *J. Geophys. Res.*, in press, 2002.

[29] G. Considine and J. A. Curry. Effects of entrainment and droplet sedimentation on the microphysical structure of stratus and stratocumulus clouds. *Q.J.R.Meteorol.Soc.*, 124:123–150, 1998.

[30] S. Decesari, M. C. Facchini, S. Fuzzi, and E. Tagliavini. Characterization of water-soluble organic compounds in atmospheric aerosol: A new approach. *J. Geophys. Res.*, 105:1481–1489, 2000.

[31] P. G. Duynkerke, H. Zhang, and P. J. Jonker. Microphysical and turbulent structure of nocturnal stratocumulus as observed during ASTEX. *J. Aerosol Sci.*, 124:2763–2777, 1995.

[32] W. Elbert, M. R. Hoffmann, M. Kramer, G. Schmitt, and M. O. Andreae. Multiphase chemistry and acidity of clouds at Kleiner-Feldberg. *Atmos. Environ.*, 34:1109–1122, 2000.

[33] E. Eltahir and E. J. Humphries. The role of clouds in the surface energy balance over the Amazon forest. *Int. J. Climatol.*, 18:1575–1591, 1998.

[34] M. C. Facchini, S. Decesari, M. Mircea, S. Fuzzi, and G. Loglio. Surface tension of atmospheric wet aerosol and cloud/fog droplets in relation to their organic carbon content and chemical composition. *Atmos. Environ.*, 34:4853–4857, 2000.

[35] M. C. Facchini, S. Fuzzi, S. Zappoli, A. Andracchio, A. Gelencser, G. Kiss, Z. Krivacsy, E. Meszaros, H. C. Hansson, T. Alsberg, and Y. Zebuhr. Partitioning of the organic aerosol component between fog droplets and interstitial air. *J. Geophys. Res.*, 104:26821–26832, 1999.

[36] M. C. Facchini, M. Mircea, S. Fuzzi, and R. J. Charlson. Cloud albedo enhancement by surface-active organic solutes in growing droplets. *Nature*, 401:257–259, 1999.

[37] G. Feingold and P. Y. Chuang. Analysis of the influence of film-forming compounds on droplet growth: Implications for cloud microphysical processes and climate. *J. Atmos. Sci.*, 59:2006–2018, 2002.

[38] G. Feingold, W. R. Cotton, S. R. Kreidenweis, and J. T. Davis. The impact of giant cloud condensation nuclei on drizzle formation in stratocumulus: Implications for cloud radiative properties. *J. Aerosol Sci.*, 56:4100–4117, 1999.

[39] G. Feingold and A. J. Heymsfield. Parameterizations of condensational growth of droplets for use in general circulation models. *J. Atmos. Sci.*, 49(23):2325–2342, 1992.

[40] A. I. Flossmann, W. D. Hall, and H. R. Pruppacher. A theoretical study of the wet removal of atmospheric pollutants: Part I: The redistribution of aerosol particles capture through nucleation and impaction scavenging by growing cloud drops. *J. Atmos. Sci.*, 42:583–606, 1985.

[41] G. Frank and et.al. *Contr. Atmos. Phys.*, 71:65, 1998.

[42] A. S Frisch, C. W. Fairall, and J. B. Snider. Measurement of stratus cloud and drizzle parameters in ASTEX with a k_α-band doppler radar and a microwave receiver. *J. Aerosol Sci.*, 52:2788–2799, 1995.

[43] A. S Frisch, D. H. Lenschow, C. W. Fairall, W. H. Schubert, and J. S.Gibson. Doppler radar measurements of turbulence in marine stratiform cloud during ASTEX. *J. Aerosol Sci.*, 52:2800–2808, 1995.

[44] H. H. Frisinger. *The History of Meteorology to 1800*. Science History Publications, New York, 1977.

[45] N. A. Fuchs. *Evaporation and Droplet Growth in Gaseous Media*. Pergamon Press, New York, 1959.

[46] N. Fukuta and V. K. Saxena. A horizontal thermal gradient cloud condensation nucleus spectrometer. *J. Appl. Meteorol.*, 18:1352–1362, 1979.

[47] N. Fukuta and L. A. Walter. Kinetics of hydrometer growth from the vapor; spherical model. *J. Aerosol Sci.*, 27:1160–1172, 1970.

[48] K. A. Fuller, W. C. Malm, and S. M. Kreidenweis. Effects of mixing on extinction by carbonaceous particles. *J. Geophys. Res.*, 104(D13):15941–15954, 1999.

[49] S. Fuzzi, S. Decesari, M. Facchini, E. Matta, and M. Mircea. A simplified model of the water soluble organic component of atmospheric aerosols. *Geophys. Res. Lett.*, 20:4079–4082, 2001.

[50] S. Fuzzi, M. C. Facchini, G. Orsi, J. A. Lind, W. Wobrock, M. Kessel, R. Maser, W. Jaeschke, K. H. Enderle, B. G. Arends, A. Berner, I. Solly, C. Kruisz, G. Reischl, S. Pahl, U. Kaminski, P. Winkler, J. A. Ogren, K. J. Noone, A. Hallberg, H. Fierlinger-Oberlinninger, H. Puxbaum, A. Marzorati, H. C. Hansson, A. Wiedensohler, I. B. Svenningsson, B. G. Martinsson, D. Schell, and H. W. Georgii. The Po Valley fog experiment 1989. an overview. *Tellus B*, 44:448–468, 1992.

[51] S. Fuzzi, M. C. Facchini, D. Schell, W. Wobrock, P. Winkler, B. G. Arends, M. Kessel, J. J. Mols, S. Pahl, T. Schneider, A. Berner, I. Solly, C. Kruisz, M. Kalina, H. Fierlinger, A. Hallberg, P. Vitali, L. Santoli, and G. Tigli. Multiphase chemistry and acidity of clouds at Kleiner-Feldberg. *J. Atmos. Chem.*, 19:87–106, 1994.

[52] J. H. C. Gash and W. J. Shuttleworth. Tropical deforestation:Albedo and the surface-energy balance. *Climatic Change*, 19:123–133, 1991.

[53] S. Ghan, R. Easter, E. Chapman, H. Abdul-Razzak, Y. Zhang, L. Leung, N. Laulainen, R. Saylor, and R. Zaveri. A physically based estimate of radiative forcing by anthropogenic sulfate aerosol. *J. Geophys. Res.*, 106:5279–5293, 2001.

[54] S. Ghan, R. Easter, J. Hudson, and F. M. Bron. Evaluation of aerosol indirect radiative forcing in MIRAGE. *J. Geophys. Res.*, 106:5317–5334, 2001.

[55] S. J. Ghan, C. C. Chuang, R. C. Easter, and J. E. Penner. A parameterization of cloud droplet nucleation .2. Multiple aerosol types. *Atmos. Res.*, 36(1-2):39–54, 1995.

[56] S. J. Ghan, C. C. Chuang, and J. E. Penner. A parameterization of cloud droplet nucleation. part I: Single aerosol species. *Atmos. Res.*, 30:197–222, 1993.

[57] S. J. Ghan, G. Guzman, and H. Abdul-Razzak. Competition between sea-salt and sulfate particles as cloud condensation nuclei. *J. Atmos. Sci.*, 55:3340–3347, 1998.

[58] S. J. Ghan, L. R. Leung, R. C. Easter, and H. Abdul-Razzak. Prediction of cloud droplet number in a general circulation model. *J. Geophys. Res.*, 102(D18):21777–21794, 1997.

[59] A. D. Gosman and A. Ideriah. TEACH-2E. Tech.Rep. FM-83-2, Univ. California Berkeley, 1976.

[60] I. Gultepe and G. A. Isaac. The relationship between cloud droplet and aerosol number concentrations for climate models. *Int. J. Climatol.*, 16(8):941–946, 1996.

[61] J. Hansen, M. Sato, and R. Ruedy. Radiative forcing and climate response. *J. Geophys. Res.*, 102:6831–6864, 1997.

[62] J. Y. Harrington, G. Feingold, and W. R. Cotton. Radiative impacts on the growth of a population of drops within simulated summertime arctic stratus. *J. Atmos. Sci.*, 57:766–785, 2000.

[63] N. Hatzianastassiou, W. Wobrock, and A. I. Flossman. The role of droplet spectra for cloud radiative properties. *Q.J.R.Meteorol.Soc.*, 123:2215–2230, 1997.

[64] D. A. Hegg. Impact of gas-phase HNO_3 and NH_3 on microphysical processes in atmospheric clouds. *Geophys. Res. Lett.*, 15:2201–2204, 2000.

[65] M. Hess, P. Koepke, and I. Schult. Optical properties of aerosols and clouds: The software package OPAC. *Bull. Am. Met. Soc*, 79:831–844, 1998.

[66] A. C. Hindmarsh. ODEPACK: A systemetized collection of ODE solvers. In R.S. Stepleman et al., editor, *Scientific Computing*, pages 55–64. North–Holland, New York, 1983.

[67] R. Hitzenberger and S. Tohno. Comparison of black carbon (BC) aerosols in two urban areas - concentrations and size distributions. *Atmos. Environ.*, 35:2153–, 2001.

[68] P. V. Hobbs, D. A. Bowdle, and L. F. Radke. Particles in the lower troposphere over the high plains of the United States, 2. Cloud condensation nuclei. *J. Clim. Meteorol.*, 24:1358–1369, 1985.

[69] W. A. Hoppel, G. M. Frick, and J. W. Fitzgerald. Deducing droplet concentration and supersaturation in marine boundary layer clouds from surface aerosol measurements. *J. Geophys. Res.*, 101(D21):26553–26565, 1996.

[70] J. G. Hudson. Effects of CCN concentrations on stratus clouds. *J. Aerosol Sci.*, 40(2):480–486, 1983.

[71] J. G. Hudson. An instantaneous CCN spectrometer. *J. Atmos. Ocean. Tech.*, 6:1055–1065, 1989.

[72] J. G. Hudson and A. D. Clarke. Aerosol and cloud condensation nuclei measurements in the Kuwait plume. *J. Geophys. Res.*, 97:14,533–14,536, 1992.

[73] J. G. Hudson and P. R. Frisbie. Surface cloud condensation nuclei and condensation nuclei measurements at Reno, Nevada. *Atmos. Environ.*, 25:2285–2299, 1991.

[74] J. G. Hudson, C. F. Rogers, and G. Keyser. Simultaneous operation of three CCN counters and an isothermal haze chamber at the 1980 International CCN workshop. *J. Rech. Atmos.*, 15:271–283, 1981.

[75] F. P. Incropera and D. P. DeWitt. *Fundamentals of heat and mass transfer*. John Wiley, New York, 2nd edition, 1985.

[76] Intergovernmental Panel on Climate Change (IPCC). *Climate Change (2001): The Scientific Basis*. Cambridge University Press, UK, 2001.

[77] J. B. Jensen and R. J. Charlson. On the efficiency of nucleation scavenging. *Tellus B*, 36:367–375, 1984.

[78] N. Kaneyasu and S. Murayama. High concentrations of black carbon over middle latitudes in the North Pacific Ocean. *J. Geophys. Res.*, 105:19881–19890, 2000.

[79] Y. J. Kaufman and R. S. Fraser. The effect of smoke particles on clouds and climate forcing. *Science*, 277:1636–1639, 1997.

[80] Y. J. Kaufman, P. V. Hobbs, V. W. Kirchhoff, P. Artaxo, M. D. King, and D. E. Ward. Smoke, Clouds, and Radiation - Brazil (SCAR-B) experiment. *J. Geophys. Res.*, S, 1998.

[81] Y. J. Kaufman and T. Nakajima. Effect of Amazon smoke on cloud microphysics and albedo - Analysis from satellite imagery. *J. Appl. Meteorol.*, 32:729–744, 1993.

[82] Y. J. Kaufman, A. Setzer, D. Ward, D. Tanré, B. N. Holben, P. Menzel, M. C. Pereira, and R. Rasmussen. Biomass burning airborne and spaceborne experiment in the Amazonas (BASE-A). *J. Geophys. Res.*, 97:14,581–14,599, 1992.

[83] J. T. Kiehl, T. L. Schneider, P. J. Rasch, M. C. Barth, and J. Wong. Radiative forcing due to sulfate aerosols from simulations with the National Center for Atmospheric Research Community Climate Model, Version 3. *J. Geophys. Res.*, 105:1441–1457, 2000.

[84] J. T. Kiehl. Climate change - Solving the aerosol puzzle. *Science*, 283(5406):1273, 1999.

[85] M. Kleeman, J. Schauer, and G. Cass. Size and composition distribution of fine particulate matter emitted from motor vehicles. *Environ. Sci. Technol.*, 34:1132–1142, 2000.

[86] H. Köhler. Zur kondensation des wasserdampfe in der atmosphäre. *Geofys. Publ.*, 2:3–15, 1921.

[87] H. Köhler. *Trans. Faraday Soc.*, 32:1152, 1936.

[88] M. Kulmala, P. Korhonen, T. Vesala, H. C. Hansson, K. Noone, and B. Svenningsson. The effect of hygroscopicity on cloud droplet formation. *Tellus B*, 48:347–360, 1996.

[89] M. Kulmala, A. Laaksonen, R. J. Charlson, and P. Korhonen. Clouds without supersaturation. *Nature*, 388:336–337, 1997.

[90] M. Kulmala, A. Laaksonen, P. Korhonen, T. Vesala, T. Ahonen, and J. C. Barrett. The effect of atmospheric nitric acid vapor on cloud condensation nucleus activation. *J. Geophys. Res.*, 98:22949–22958, 1993.

[91] V. I. Khvorostyanov and J. A. Curry. A simple analytical model of aerosol properties with account for hygroscopic growth. 1.Equilibrium size spectra and cloud condensation nuclei activity spectra. *J. Geophys. Res.*, 104:2175–2184, 1999.

[92] A. Laaksonen, J. Hienola, M. Kulmala, and F. Arnold. Supercooled cirrus cloud formation modified by nitric acid pollution of the upper troposphere. *Geophys. Res. Lett.*, 24:3009–3012, 1997.

[93] A. Laaksonen, P. Korhonen, M. Kulmala, and R. J. Charlson. Modification of the Köhler equation to include soluble trace gases and slightly soluble substances. *J. Aerosol Sci.*, 155:853–862, 1998.

[94] A. A. Lacis and J. E. Hansen. A parameterization for the absorption of solar radiation in the earth's atmosphere. *J. Aerosol Sci.*, 31:118–133, 1974.

[95] A. G. Laktionov. A constant-temperature method of determining the concentrations of cloud condensation nuclei. *Atmos. and Oceanic Phys.*, 8:672–677, 1972.

[96] G. G. Lala and J. E. Jiusto. An automatic light scattering CCN counter. *J. Appl. Meteorol.*, 16:413–418, 1977.

[97] J. Lelieveld, P. J. Crutzen, V. Ramanathan, M. O. Andreae, C. A. M. Brenninkmeijer, T. Campos, G. R. Cass, R. R. Dickerson, H. Fischer, J. A. de Gouw, A. Hansel, A. Jefferson, D. Kley, A. T. J. de Laat, S. Lal, M. G. Lawrence, J. M. Lobert, O. L. Mayol-Bracero, A. P. Mitra, T. Novakov, S. J. Oltmans, K. A. Prather, T. Reiner, H. Rodhe, H. A. Scheeren, D. Sikka, and J. Williams. The indian ocean experiment:

Widespread air pollution from south and southeast asia. *Science*, 291:1031–1036, 2001.

[98] D. Lide. *CRC Handbook of Chemistry and Physics*. CRC Press, Cleveland, Ohio, 2000.

[99] X. H. Liu and M. H. Wang. A parameterization of the efficiency of nucleation scavenging of aerosol particles and some related physicochemical factors. *Atmos. Environ.*, 30:2235–2341, 1996.

[100] G. Loglio, P. Pandolfini, U. Tesei, and B. Noskov. Measurements of interfacial properties with the axisymmetric bubble-shape analysis technique: effects of vibrations. *Colloids Surfaces A: Physicochem. Eng. Aspects*, 143:301–310, 1998.

[101] U. Lohmann and J. Feichter. Impact of sulfate aerosols on albedo and lifetime of clouds: A sensitivity study with the ECHAM4 GCM. *J. Geophys. Res.*, 102:13685–13700, 1997.

[102] U. Lohmann and J. Feichter. Can the direct and semi-direct aerosol effect compete with the indirect effect on a global scale? *Geophys. Res. Lett.*, 28(1):159–161, 2001.

[103] U. Lohmann, J. Feichter, C. C. Chuang, and J. E. Penner. Prediction of the number of cloud droplets in the ECHAM GCM. *J. Geophys. Res.*, 104(D8):9169–9198, 1999.

[104] M. Kulmala, A. Toivonen, T. Mattila and P. Korhonen Variations of cloud droplet concentrations and the optical properties of clouds due to changing hygroscopicity: A model study. *J. Geophys. Res.*, 103:16183–16195, 1998.

[105] N. A. Marley, J. S. Gaffney, C. Baird, C. A. Blazer, P. J. Drayton, and J. E. Frederick. An empirical method for the determination of the complex refractive index of size-fractionated atmospheric aerosols for radiative transfer calculations. *Aerosol Sci Technol.*, 34:535–549, 2001.

[106] G. Martin, D. Johnson, and A. Spice. The measurement and parameterization of effective radius of droplets in warm stratocumulus clouds. *J. Aerosol Sci.*, 51:1823–1842, 1994.

[107] B. Mason. *Principles of Geochemistry*. John Wiley, New York, 1966.

[108] B. J. Mason. *Physics of Clouds*. Oxford University Press, Oxford, 1957.

[109] T. Mattila, Y. Viisanen, H. Kokkola, A. Laaksonen, and M. Kulmala. *J. Aerosol Sci.*, 31:1109–1122, 2000.

[110] O. L. Mayol-Bracero, P. Guyon, B. Graham, G. Roberts, M. O. Andreae, S. Decesari, M. C. Facchini, S. Fuzzi, and P. Artaxo. Water-soluble organic compounds in biomass burning aerosols over Amazonia: 2. Apportionment of the chemical composition and importance of the polyacidic fraction. *J. Geophys. Res.*, LBA Special Issue, in press, 2002.

[111] P. McMurry. A review of atmospheric aerosol measurements. *Atmos. Environ.*, 34:1959–1999, 2000.

[112] A. I. Medalia, D. Rivin, and D. R. Sanders. A comparison of carbon black with soot. *Sci. Total Environ.*, 31:1–22, 1983.

[113] C. A. Miller and P. Neogi. *Interfacial Phenomena: Equilibrium and Dynamic Effects*. Marcel Dekker, New York, 1985.

[114] A. Nenes, R. J. Charlson, M. C. Facchini, M. Kulmala, A. Laaksonen, and J. H. Seinfeld. Can chemical effects on cloud droplet number rival the first indirect effect? *Geophys. Res. Lett.*, in press, 2002.

[115] A. Nenes, P. Y. Chuang, R. C. Flagan, and J. H. Seinfeld. A theoretical analysis of cloud condensation nucleus (CCN) instruments. *J. Geophys. Res.*, 106(D4):3449–3474, 2001.

[116] A. Nenes, W. C. Conant, and J. H. Seinfeld. Black carbon radiative effect on cloud microphysics and implications for the aerosol indirect effect: 2. Cloud microphysics. *J. Geophys. Res.*, in press, 2002.

[117] A. Nenes, S. Ghan, H. Abdul-Razzak, P. Y. Chuang, and J. H. Seinfeld. Kinetic limitations on cloud droplet formation and impact on cloud albedo. *Tellus B*, 53(2):133–149, 2001.

[118] S. Nichols. The dynamics of stratocumulus: aircraft observations and comparisons with a mixed layer model. *Q.J.R.Meteorol.Soc.*, 110:783–820, 1984.

[119] NOAA-ARL. HYSPLIT 4, hybrid single-particle lagrangian integrated trajectory model. Tech.rep., NOAA Air Resources Laboratory, Silver Spring, MD., 1997.

[120] T. Novakov, M. O. Andreae., R. Gabriel, T. W. Kirchstetter, O. L. Mayol-Bracero, and V. Ramanathan. Origin of carbonaceous aerosols over the tropical indian ocean: Biomass burning or fossil fuels? *Geophys. Res. Lett.*, 27:4061–4064, 2000.

[121] C. D. O'Dowd, J. A. Lowe, and M. H. Smith. Coupling sea-salt and sulphate interactions and its impact on cloud droplet concentration predictions. *Geophys. Res. Lett.*, 26:1311–1314, 1999.

[122] C. D. O'Dowd, M. H. Smith, and S. G. Jennings. Submicron particle, radon, and soot carbon characteristics over the northeast atlantic. *J. Geophys. Res.*, 98:1123–1135, 1993.

[123] S. P. Pandis, J. H. Seinfeld, and C. Pilinis. The smog-fog-smog cycle and acid deposition. *J. Geophys. Res.*, 95:18489–18500, 1984.

[124] S. V. Patankar. *Numerical Heat Transfer and Fluid Flow.* McGraw-Hill, New York, 1980.

[125] I. A. Podgorny, W. C. Conant, V. Ramanathan, and S. K. Satheesh. Aerosol modulation of atmospheric and surface solar heating over the tropical Indian Ocean. *Tellus B*, 52:947–958, 2000.

[126] M. Posfai, J. R. Anderson, P. R. Buseck, and H. Sievering. Soot and sulfate aerosol particles in the remote marine troposphere. *J. Geophys. Res.*, 104:21685–21693, 1999.

[127] H. R. Pruppacher and J. D. Klett. *Microphysics of Clouds and Precipitation.* Kluwer Academic Publishers, Boston, 2nd edition, 1997.

[128] R. F. Pueschel, C. C. Van Valin, R. G. Castillo, J. A. Kadlecek, and E. Ganor. Aerosols in polluted versus nonpolluted air masses: Long range transport and effects on clouds. *J. Clim. Appl. Meteorol.*, 25:1908–1917, 1986.

[129] B. K. Pun, C. Seigneur, D. Grosjean, and P. Saxena. Gas-phase formation of water-soluble organic compounds in the atmosphere: A retrosynthetic analysis. *J. Atmos. Chem.*, 35:199–223, 2000.

[130] V. Ramanathan, P. J. Crutzen, J. Lelieveld, A. P. Mitra, and coauthors. Indian Ocean Experiment: An integrated analysis of the climate forcing and effects of the great Indo-Asian haze. *J. Geophys. Res.*, 106:28369–28370, 2001.

[131] V. Ramanathan, P. J. Crutzen, J. T. Kiehl, and D. Rosenfeld. Aerosols, climate, and the hydrological cycle. *Science*, 294:2119–2124, 2001.

[132] J. S. Reid, P. V. Hobbs, R. J. Ferek, D. R. Blake, J. V. Martins, M. R. Dunlap, and C. Liousse. Physical, chemical, and optical properties of regional hazes dominated by smoke in Brazil. *J. Geophys. Res.*, 103:32,059–32,080, 1998.

[133] W. T. Roach, R. Brown, S. J. Caughey, J. A. Garland, and C. J. Readings. A field-study of nocturnal stratocumulus. 1. Mean structure and budgetsa field-study of nocturnal stratocumulus .1. mean structure and budgets. *Q.J.R.Meteorol.Soc.*, 102:103–123, 1976.

[134] G. Roberts. *Cloud condensation nuclei in the Amazon Basin: Their role in a tropical rainforest*. Ph.D. thesis, California Institute of Technology, Pasadena, CA, 2001.

[135] G. Roberts, A. Nenes, M. Andreae, and J. H. Seinfeld. Impact of biomass burning on cloud properties in the Amazon Basin. *J. Geophys. Res.*, in press, 2002.

[136] G. Roberts, J. Zhou, P. Artaxo, and M. Andreae. Cloud condensation nuclei in the Amazon Basin: "Marine" conditions over a continent? *Geophys. Res. Lett.*, 28:2807–2810, 2001.

[137] G. Roberts, J. Zhou, E. Swietlicki, P. Artaxo, and M. Andreae. Sensitivity of CCN spectra on chemical and physical properties of aerosol. *Geophys. Res. Lett.*, 28:2807–2810, 2001.

[138] D. Rosenfeld. TRMM observed first direct evidence of smoke from forest fires inhibiting rainfall. *Geophys. Res. Lett.*, 26:3105–3108, 1999.

[139] J. L. Ross, P. V. Hobbs, and B. Holben. Radiative characteristics of regional hazes dominated by smoke from biomass burning in Brazil: Closure tests and direct radiative forcing. *J. Geophys. Res.*, 103:31,925–31,941, 1998.

[140] L. Rotstayn. Indirect forcing by anthropogenic aerosols: A global climate model calculation of the effective-radius and cloud-lifetime effects. *J. Geophys. Res.*, 104:9369–9380, 1999.

[141] P. Saxena and L. M. Hildemann. Water-soluble organics in atmospheric particles: A critical review of the literature and application of thermodynamics to identify candidate compounds. *J. Atmos. Chem.*, 24:57–109, 1996.

[142] S. E. Schwartz and A. Slingo. In *Proc. NATO Advanced Res. Workshop: "Clouds, Chemistry and Climate"*. Springer Verlag, Berlin, 1996.

[143] J. H. Seinfeld and S. N. Pandis. *Atmospheric chemistry and physics: from air pollution to climate change.* John Wiley, New York, 1998.

[144] A. W. Setzer and M. C. Pereira. Amazon biomass burnings in 1987 and their tropospheric emissions. *Ambio*, 20:19–22, 1991.

[145] M. L. Shulman, M. C. Jacobson, R. J. Charlson, R. E. Synovec, and T. E. Young. Dissolution behaviour and surface tension effects of organic compounds in nucleating cloud droplets. *Geophys. Res. Lett.*, 23:277–280, 1996.

[146] A. M. Sinnarwalla and D. J. Alofs. A cloud nucleus counter with long available growth time. *J. Appl. Meteorol.*, 12:831–835, 1973.

[147] M. H. Smith, A. Jones, J. A. Lowe, and C. D. O'Dowd. Role of atmospheric aerosol in the indirect climate cooling mechanism. *12th Int.Conference on Clouds and Precipitation, Zurich*, 1996.

[148] J. Smolik, L. Dzumbova, J. Schwarz, and M. Kulmala. Evaporation of ventilated water droplet: connection between heat and mass transfer. *J. Aerosol Sci.*, 33(1):205–205, 2002.

[149] P. Squires and S. Twomey. The relation between cloud droplet spectra and the spectrum of cloud nuclei. In *Physics of Precipitation, in Geoph. Monogr. Ser.* 1960.

[150] B. Stevens, G. Feingold, W. R. Cotton, and R. L. Walco. Elements of the microphysical structure of numerically simulated nonprecipitating stratocumulus. *J. Aerosol Sci.*, 53(7):980–1006, 1996.

[151] I. N. Tang. Thermodynamic and optical properties of mixed-salt aerosols of atmospheric importance. *J. Geophys. Res.*, 102:1883–1893, 1997.

[152] O. B. Toon and T. P. Ackerman. Algorithms for the calculation of scattering by stratified spheres. *Appl. Opt*, 20:3657–3660, 1981.

[153] C. H. Twohy and J. G. Hudson. Measurements of cloud condensation nucleus spectra within maritime cumulus cloud droplets: Implications for mixing processes. *J. Appl. Meteorol.*, 34:815–833, 1995.

[154] S. Twomey. The nuclei of natural cloud formation. II. The supersaturation in natural clouds and the variation of cloud droplet concentration. *Geofisica pura e applicata*, 43:243–249, 1959.

[155] S. Twomey. Measurements of natural cloud nuclei. *J. Rech. Atmos.*, 1:101–105, 1963.

[156] S. Twomey. Pollution and the planetary albedo. *Atmos. Environ.*, 8:1251–1256, 1974.

[157] S. Twomey. The influence of pollution on the shortwave albedo of clouds. *J. Aerosol Sci.*, 34:1149–1152, 1977.

[158] US Geological Survey. Suwanee River certified FA standards. *Report 87-557*, 1979.

[159] K. von Salzen, H. G. Leighton, P. A. Ariya, L. A. Barrie, S. L. Gong, J. P. Blanchet, L. Spacek, U. Lohmann, and L. I. Kleinman. Sensitivity of sulphate aerosol size distributions and CCN concentrations over North America to SO_x emissions and H_2O_2 concentrations. *J. Geophys. Res.*, 105:9741–9765, 2000.

[160] K. T. Whitby. The physical characteristics of sulfur aerosols. *Atmos. Environ.*, 12:135–159, 1978.

[161] A. B. White, C. W. Fairall, and J. B. Snider. Surface-based remote sensing of marine boundary-layer cloud properties. *J. Aerosol Sci.*, 52:2827–2838, 1995.

[162] E. *et al.* Williams. Observational tests of the aerosol hypothesis for precipitation and electrification in Rondonia, Brazil. *J. Geophys. Res.*, LBA Special Issue, in press, 2002.

[163] Y. Yin, Z. Levin, T. Reisin, and S. Tzivion. The effects of giant cloud condensation nuclei on the development of precipitation in convective clouds - a numerical study. *Atmos. Res.*, 53:91–116, 2000.

[164] K. C. Young and A. J. Warren. A reexamination of the derivation of the equilibrium supersaturation curve for soluble particles. *J. Aerosol Sci.*, 49:1138–1143, 1992.

[165] S. Zappoli, A. Andracchio, S. Fuzzi, M. C. Facchini, A. Gelencser, G. Kiss, Z. Krivacsy, A. Molnar, E. Meszaros, H. C. Hansson, K. Rosman, and Y. Zebuhr. Inorganic, organic and macromolecular components of fine aerosol in different areas of Europe in relation to their water solubility. *Atmos. Environ.*, 33:2733–2743, 1999.

[166] Y. Zhang, R. C. Easter, S. J. Ghan, and H. Abdul-Razzak. Impact of aerosol size representation on modeling aerosol-cloud interactions. *J. Geophys. Res.*, in press, 2002.

[167] J. Zhou, E. Swietlicki, H. Hansson, and P. Artaxo. Sub-micrometer aerosol particle size distribution and hygroscopic growth measurements in the Amazonian rain forest during the wet season. *J. Geophys. Res.*, LBA Special Issue, in press, 2002.